

University of St Andrews



Full metadata for this thesis is available in
St Andrews Research Repository
at:

<http://research-repository.st-andrews.ac.uk/>

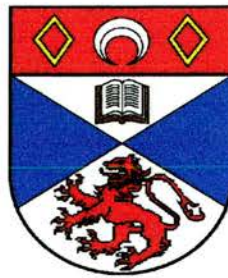
This thesis is protected by original copyright

Quantum Interference Effects: Electromagnetically Induced Transparency and Focusing

A thesis presented by

David J. Fulton, B.Sc

to the University of St Andrews in application for the degree of
Doctor of Philosophy



J.F. Allen Physics Research Laboratories

School of Physics and Astronomy

University of St Andrews

North Haugh

St Andrews KY16 9SS

Scotland

October 1996



Tu C230

Declarations

I, David James Fulton, hereby certify that this thesis, which is approximately 70,000 words in length, has been written by me, that it is the record of work carried out by me and that it has not been submitted in any previous application for a higher degree.

Date.. *31st Oct 96* Signature of candidate.

I was admitted as a research student in October 1993 and as a candidate for the degree of Ph.D in October 1994; the higher study for which this is a record was carried out in the University of St. Andrews between 1993 and 1996.

Date.. *31st Oct 96* Signature of candidate..

I hereby certify that the candidate has fulfilled the conditions of the Resolution and Regulations appropriate for the degree of Doctor of Philosophy in the University of St. Andrews and that the candidate is qualified to submit this thesis in application for that degree.

Date.....31 Oct 96..... Signature of supervisor.

In submitting this thesis to the University of St. Andrews I understand that I am giving permission for it to be made available for use in accordance with the regulations of the University Library for the time being in force, subject to any copyright vested in the work not being affected thereby. I also understand that the title and abstract will be published, and that a copy of the work may be made and supplied to any bona fide library or research worker.

Date.....31st Oct 96..... Signature of candidate.

Abstract

Theoretical and experimental studies of steady state quantum interference effects within an atomic vapour have been carried out. These include the effects of Electromagnetically Induced Transparency (E.I.T.), Electromagnetically Induced Focusing (E.I.F.) and inversionless lasing. Theoretical analysis was carried out using semi-classical density matrix models while experiments employed continuous-wave Ti:sapphire or Dye lasers within atomic rubidium.

An initial study of the properties of E.I.T. was carried out within Doppler broadened rubidium. Coherently induced transparencies were generated in three basic systems: V-type, lambda and cascade. This allowed a theoretical and experimental comparison between the three systems to be made.

The $5S_{1/2} - 5P_{3/2} - 5D_{5/2}$ cascade system proved the simplest in which to observe E.I.T., providing windows with depths $> 90\%$. Thus, a fundamental study of E.I.T. within this system was carried out. This included the effect of varying optical field parameters and of Zeeman splitting. Highlighted by this analysis was the fact that E.I.T. can provide novel high resolution two-photon spectroscopy techniques.

A unique non-dissipative cross focusing effect on the probe field was observed when the spatial profile's of the optical fields were considered. This was a direct result of the coherent interaction of the coupling field with the rubidium atoms and so was named Electromagnetically Induced Focusing. E.I.F. was shown, both theoretically and experimentally, to vary dramatically with changes in the system's physical parameters.

An examination of the effects of varying the field wavelength's within all three systems was theoretically carried out. This analysis showed that a Doppler broadened medium does not require matched wavelength optical fields in order to observe coherently induced transparency. It also highlighted the relative roles of E.I.T. and Autler-Townes splitting within an induced transparency.

A final study was carried out which theoretically predicts the presence of blue inversionless gain in a system which employed I.R. driving fields within atomic rubidium.

Acknowledgements

I would like to thank my supervisors Prof. Malcolm Dunn and Dr. Bruce Sinclair for their help, enthusiasm and experience during the period of this work. I would also like to acknowledge the large debt I owe to Dr. Sara Shepherd for all her patience and invaluable advice given from day one of Ph.D life, and for taking the time to read this thesis. A special thanks must also go to Dr. Richard Moseley who's insight proved the spark for much of the early work of this thesis, and for getting a job in time to let me go to America in his place. I would also like to thank Litsa Zekou and James Boon for joining our group last year and hopefully for continuing the experimental success of the group over the next few years.

The list of people who have contributed in one way or another to the completion of this thesis is extensive. I must thank the technical staff of the department for their time in deciphering my technical drawings and turning them into workable systems. I would also like to thank all the students and postdocs of the department, past and present, for making my time in St. Andrews so enjoyable, especially Sara, Richard, Steve, Matthew, Garry, Angus, Cameron, Gordon and Christian. Thanks also to Morag for lending me her printer, so enabling me to submit this century. I wish also to thank my family for their support, and Sunday dinners, over the last three years.

It goes without saying that I thank anyone who has joined me in a game of football in the last three years. Particularly, I thank the boys at St. Andrews Amateurs, A.C. Zimmers and more recently at the University Football Club and The Whey Pat for many memorable moments, both on and off the field of play. These have helped me retain my sanity when the things in the lab have felt like getting too much to bear. I would also like to thank Mark for being the only one willing to get out of his bed in time to book a five-a-side slot for the department. Thanks especially goes to Glasgow Rangers F.C. for winning the league every year I've been in St. Andrews. Here's hoping nothing changes in 1996-97 and we go on to win nine in a row...

Table Of Contents

Declaration

Abstract

Acknowledgements

Table Of Contents

Chapter 1): Introduction

1.1) Light In The 20th Century	1
1.2) Wave Mixing In Vapours	2
1.3) Quantum Interference And Electromagnetically Induced Transparency	4
1.4) Topics Related To Electromagnetically Induced Transparency	17
1.5) A Guide On What Is To Follow	27
References	29

Chapter 2): Theoretical Modelling Of Atomic Coherence Effects

2.1) Models For Examining A Three Level Atom	45
2.2) Employment Of Density Matrix Models	54
2.3) Modelling Atomic Systems For Inversionless Lasing	66
2.4) Moseley's N Level Rules	75
References	76

Chapter 3): Atomic Rubidium, Theoretical Rabi Frequencies And	
Experimental Apparatus	
3.1) Atomic Rubidium	78
3.2) Calculation Of Experimental Rabi Frequencies	86
3.3) Experimental Apparatus	91
Acknowledgement	105
References	106
Chapter 4): A Comparison Of Schemes For The Study Of Continuous-	
Wave Electromagnetically Induced Transparency	
4.1)Introducing Three Level E.I.T. Schemes	109
4.2) Theoretical Ideal Three Level Systems	111
4.3) Experimental Procedures	123
4.4) The V-type System	125
4.5) The Lambda System	133
4.6) A Cascade System	140
4.7) Comparing The Experimental Systems	143
References	145
Chapter 5): Two Photon And Zeeman Splitting Effects In Continuous-	
Wave Electromagnetically Induced Transparency	
5.1) An Outline Of Sub-Doppler E.I.T. Within The Cascade	
System	147
5.2) Two Photon Residual Doppler Width	149
5.3) Varying The Optical Field Parameters	151
5.4) Effect Of Coupling Field Detuning	160
5.5) A Population Comparison	163
5.6) A Theoretical Look At The Effects Of Introducing A	
Magnetic Field	167
5.7) An Experimental Look At The Effects Of Introducing A	
Magnetic Field	176
5.8) Implications Of Zeeman Splitting On Coherently	
Prepared Systems	180
References	183

Chapter 6): Electromagnetically Induced Focusing

6.1) An Introduction To The Spatial Consequences Of E.I.T.	186
6.2) Modelling Electromagnetically Induced Focusing	190
Acknowledgement	198
6.3) Experimental E.I.F. Results	212
6.4) Concluding Remarks On E.I.F.	219
References	222

Chapter 7): Wavelength Dependence Of Coherently Induced Transparency**In A Doppler-Broadened Medium**

7.1) An Introduction To Coupling Field Wavelength Effects	224
7.2) Modelling The Effects Of Wavelength Mismatch Within E.I.T. Systems	226
7.3) Experimental Effects Of Varying The Coupling Field Wavelength	249
7.4) Concluding Remarks	257
References	259

Chapter 8): Development Of A 422 nm Inversionless Gain System And Other Future Experiments

8.1) A Theoretical 422 nm Inversionless Gain System Within Atomic Rubidium	261
8.2) Other Future Experimental Work	279
References	283

Conclusions 284**Appendix A: Density Matrix Equations For Four Level Atomic Systems** 288**Appendix B: Publications, Presentations And Reviewed Papers** 292

Chapter 1

Introduction

1.1) Light In The 20th Century

All sources of light consist of matter that is excited in one way or another. The firefly excites its body matter by some obscure chemical process; the matter of the sun is excited by heat. However, ever since Heinrich Hertz demonstrated the validity of Maxwell's theory of electromagnetic radiation, it has been known that the ultimate source of radiation is an accelerated electric charge. The actual form of this radiation still remains a bit of a mystery to the modern physicist, since the wave particle duality of light remains unresolved. Classical Newtonian physics is unable to provide a complete explanation for the quantum nature of light interactions with matter. In 1905, Einstein showed how the photoelectric effect could be explained through a hypothesis of the corpuscular nature of electromagnetic radiation. By 1926, through the efforts of Bohr, Born, Heisenberg, Schrödinger, De Broglie, Pauli, Dirac and others quantum mechanics had become a well-verified theory and the quantum of radiation was named a "photon".

One of the main streams of thought in the early formulation of quantum theory was concerned with the explanation of atomic spectral lines. The interaction of electromagnetic radiation with atoms was discussed by Einstein [1] in 1917. This incoherent model allows for absorption, spontaneous and stimulated emission

associated with population changes of the atomic levels, and is characterised by the A and B coefficients [2]. Einstein's rate equation theory for the absorption and emission of light by an atom depends upon simple phenomenological considerations, but leads to correct predictions and so, is still used frequently today.

When, in 1814, Fraunhofer discovered that the solar spectrum contained numerous dark lines, the experimental study of the interaction of light and matter had begun. Nineteenth century scientists were able to show that the frequency positions of these dark lines were unique to an element, thus the connection between light and matter had been made. However, the nineteenth century scientist only had incoherent light sources to work with. With the development of the coherent laser source it has proved possible to study the effects that monochromatic coherent radiation has on atoms, so extending the initial work described by Einstein's rate equations. The rate equation theory breaks down in this regime thus semiclassical or fully quantum mechanical treatments of the systems must be carried out. With the introduction of coherent light sources came the possibility of studying quantum interference effects in atomic vapours. Coherent excitation allows optical transitions to be induced within an atom where the wavefunction describing the system retains its coherence [3]. Thus the atomic response holds a definite phase relationship to the oscillating field which induced the transition. The atom in the vapour is sufficiently isolated so as to retain this induced coherence for a period of time approaching that of the atomic level decay rate and so a variety of interesting phenomena have been observed. These include Rabi oscillations of atomic population [2], Autler-Townes splitting [4] and coherent population trapping [5].

1.2) Wave Mixing In Vapours

The first demonstration of a working laser source occurred in 1960. Since then, further work has provided high intensity coherent radiation sources for employment in light matter interaction experiments. The interaction of light with a medium can be described through the induced polarisation produced by the electric field, \mathbf{E} , of the electromagnetic wave. Expressing the polarisation, \mathbf{P} , as a power series allows a phenomenological description of many nonlinear optical effects:

$$\mathbf{P} = \epsilon_0 \chi^{(1)} \mathbf{E} + \epsilon_0 \chi^{(2)} \mathbf{E}^2 + \epsilon_0 \chi^{(3)} \mathbf{E}^3 + \dots \quad (1.1)$$

The first term in the series is the linear response with the first order electric susceptibility being labelled $\chi^{(1)}$ to distinguish it from higher order terms. This linear susceptibility leads to the concept of refractive index. Higher order terms in the power series describe the nonlinear response of the medium to the incident optical field, with the higher order susceptibilities providing a variety of useful and sometimes limiting processes. These wave mixing processes are coherent, and if vapours are employed as the nonlinear medium then close tuning to a resonance line substantially increases their efficiency. Second order susceptibility, $\chi^{(2)}$, processes are termed three-wave mixing nonlinear optical effects because power is transferred from two fundamental optical fields to generate a new optical field at one of the sum or difference frequencies. This group of $\chi^{(2)}$ nonlinear optical effects includes second harmonic generation (S.H.G.), sum frequency mixing (S.F.M.), difference frequency mixing (D.F.M.), parametric amplification and optical rectification. Second order $\chi^{(2)}$ processes are usually forbidden in isotropic media due to symmetry requirements on the potential energy of the electrons in the atomic medium [6]. Third order, $\chi^{(3)}$, nonlinear optical effects are allowed in isotropic media and describe a variety of four-wave mixing processes. These include third harmonic generation (T.H.G.), two-photon absorption, the Kerr effect and optical phase conjugation [7].

A vapour can be a useful medium for second-order nonlinear processes if the intrinsic symmetry is broken by some external means [8]. Sinclair gives a detailed review of $\chi^{(2)}$ three wave mixing in vapours [9]. Transverse electric or magnetic fields [10], high power pulsed excitation and noncollinear beams have all been used for this purpose [11](and references therein). With the symmetry broken three transitions are generally employed, in a closed atomic system, for resonant enhancement of the nonlinear susceptibilities. This implies that one of the transitions must be dipole forbidden thus, quadrupole or magnetic moments must be considered, along with their appropriate selection rules. Using this arrangement, nonlinear susceptibilities can be obtained that rival those achieved within crystals, but only over gigahertz tuning ranges [12]. Phase matching is still important and can be achieved via anomalous dispersion, buffer gas dispersion, noncollinear beams, periodic phase matching or intensity dependent refractive index. If achieved, the limiting factors are then absorption (strong for the fundamental radiation that is near resonance with the ground state transition),

saturation of the single or two-photon absorption, self-focusing, collisional dephasing and multi-photon ionisation.

Present day research at St. Andrews evolved from a study of magnetic field induced second harmonic generation [9, 11, 13, 14] and sum frequency mixing [12, 15, 16] experiments. Stabilised dye lasers were employed to probe the 3S-3P-4D transitions within sodium and gain high resolution measurements in order to test theoretical predictions. A modified titanium sapphire laser [15] was then incorporated into the experiment to allow the study of the 3S-3P-3D system which improved the generated signals since the 3S-3D quadrupole moment is just under seven times larger than the 3S-4D moment. The effect of different phase matching conditions in S.F.M. systems was then studied within sodium vapour on the 3S-3P-4P scheme [17]. This route differs from those previously studied since the quadrupole transition (3P-4P) is on one of the input transitions and a dipole allowed transition exists at the generated ultraviolet wavelength. The work in this system was then extended to examine interference effects between the excitation routes in resonant sum frequency mixing [18]. The two pathways considered were the two-step route, which resulted in the creation of a real intermediate population, and a direct two-photon excitation resonantly enhanced, but not populating, the intermediate level. A cancellation of $\sim 94\%$ of the maximum generated sum frequency mixing signal was reported in this work.

1.3) Quantum Interference And Electromagnetically Induced Transparency

1.3.1) Fano Interference and Population Trapping

The phenomenon of coherent excitation allows an atomic excitation transition to retain a definite phase relationship to that of the driving radiation field for a time on the scale of an atomic level decay rate. Thus if two coherent driving fields are set up within the one atomic system then interference between the two routes can arise. This is exactly the principle employed by Fano in the first coherence interference study [19]. He found that the interference of a discrete autoionised state with a continuum gave rise to a characteristically asymmetric peak in the excitation spectra. In fact a zero in the transition probability was found on one side of the excitation spectra. The concept of a phase relationship between the autoionised state and the continuum was developed which accounts for the observed spectra. A physical interpretation of this effect is that

the end product, photoionisation, is achieved by two separate routes, that of direct ionisation the other via the auto-ionisation state. It is coherent interference between these two routes which causes the observed effects.

Two route interference need not necessarily involve the continuum or an autoionised state. Two separate excitation routes to the same end product within a three level atomic system can produce coherent interference effects and thus, population trapping. A theoretical prediction of population trapping was made by the Pisa group in 1976. Their density matrix analysis showed that the generation of a coherence between two ground states of sodium could cause the "switching off" of the absorption from the ground state to an upper state [20]. This theoretical prediction was later confirmed within experiments carried out in sodium vapour [21, 22]. A multimode dye laser tuned to a D line resonance of sodium was used to coherently pump a sodium cell while an inhomogeneous magnetic field was simultaneously applied. When the splitting of the ground state was such that it equalled the mode spacing of the dye laser, a dark region occurred in the output fluorescence of the upper level. At this point of Raman resonance the population is trapped in the lower states hence, explaining the hole in the fluorescence signal.

Gray, Whitely and Stroud saw this population trapping effect as an added difficulty, to be circumvented, in order to extract as much of a ground state population of an atomic system as possible [23]. They had previously presented a complete and detailed treatment of three-level atoms interacting with two near-resonant monochromatic fields [24]. This fully quantum-electrodynamic explanation, dubbed "dressed state", is employed in a similar fashion to provide a theoretical analysis of the atomic system based on the D_1 line of sodium [23]. In this system the population trapping is explained via a mixing of the two lower levels creating one state decoupled from the excitation. Population is pumped into this state and so becomes trapped. Experimental confirmation of this phenomena was achieved using two dye lasers and an atomic beam. Their results clearly show a sharp interference feature which occurs at the two-photon resonance point within the lambda system employed. They found that the width of this feature in the upper state fluorescence signal increased with the strength of the applied optical fields. A theoretical paper by Dalton and Knight discusses the effects of field phase fluctuations on the coherently trapped population [25]. It is shown

that, unless the fields are critically cross-correlated, these phase fluctuations destroy the induced coherence within the system and so eliminate the effect of population trapping.

A continuation of the work on coherent population trapping tended to concentrate on maximising ion yields through multi-photon ionisation processes therefore, the transfer of atomic population was of prime interest [26]. An important analogy between the interference within atomic systems and that of Fano interference was made by Coleman and Knight [27]. The same authors also outlined how a strong laser field could produce a bound state embedded in the photo-ionisation continuum so altering ion yields. This idea was dubbed “laser induced continuum structure” or L.I.C.S. and has more recently been experimentally observed by two separate groups [28, 29].

1.3.2) Autler-Townes Splitting

The introduction of a strong resonant coherent field to an atomic medium causes atoms to experience an environment where the probability of stimulated emission exceeds that of the spontaneous emission probability. Under the continued action of the coherent field the driven population can be observed to experience regular sinusoidal oscillations between the two levels $|i\rangle$ and $|j\rangle$, termed Rabi oscillations [2, 3, 30], the frequency of which is referred to as the Rabi frequency, defined as:

$$\Omega = \frac{\mu_{ij}E}{\hbar} \quad (1.2)$$

where E is the amplitude of the coherent driving electric field, μ_{ij} the associated dipole matrix element and \hbar is related to Planck’s constant.

The presence of this coherent field also causes strong mixing of the atomic levels the result of which is a splitting of the levels, termed the ac-Stark effect. Autler and Townes first studied this effect in a microwave-optical field experiment in 1955 [4], and so the effect is also referred to as Autler-Townes splitting. The amount by which an atomic level is split, $\tilde{\Omega}$, depends upon the induced Rabi frequency and the detuning of the coherent field, such that:

$$\tilde{\Omega} = \sqrt{\Omega^2 + \Delta^2} \quad (1.3)$$

Figure 1.1 presents a schematic outline of Autler-Townes splitting where the optical field is initially exactly resonant, as in Figure 1.1(a), and then detuned by an amount Δ , as in Figure 1.1(b).

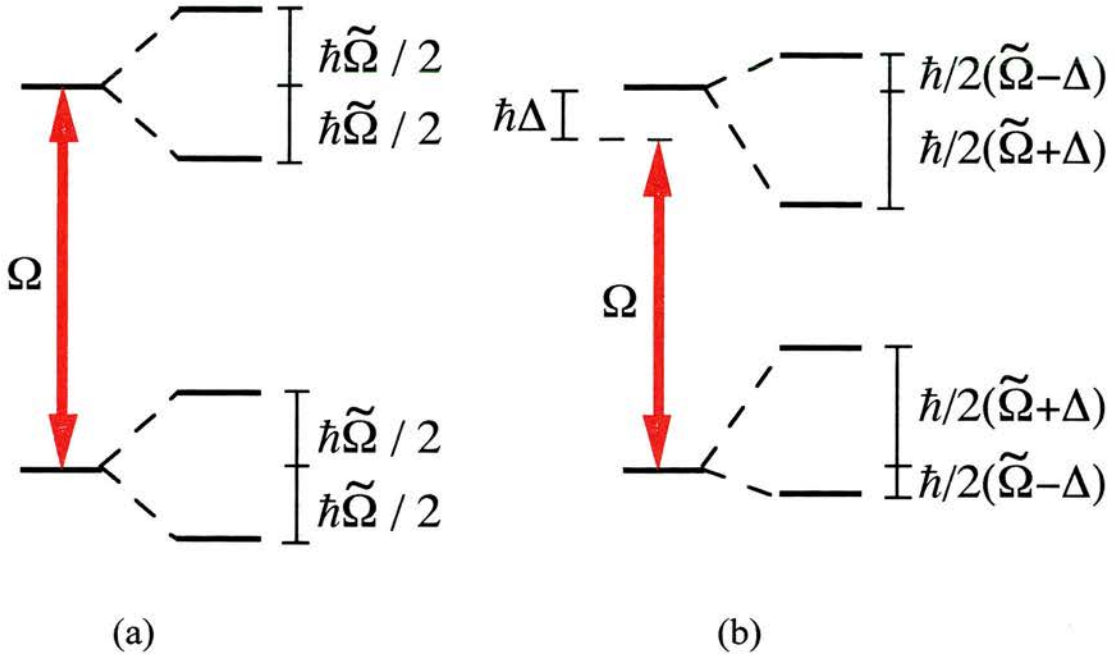


Figure 1.1: Schematic representation of Autler-Townes splitting, $\tilde{\Omega}$, for (a) a resonant driving field of Rabi frequency Ω and (b) the same driving field detuned by Δ from exact resonance.

The splitting of the levels can be seen to be symmetric about the bare state levels when the coherent field is resonant with the transition whereas, when the field is detuned from resonance the Autler-Townes splitting becomes asymmetric.

Since the first paper on Autler-Townes splitting various optical schemes have been analysed. Extensive theoretical work has continued in this field [3, 30, 31] and further experimental confirmation of these effects has been observed in atomic sodium [32, 33, 34] and neon gas [35, 36]. More recently Fisk, Bachor and Sandeman have published a series of three papers investigating the dynamic stark effect in a three level cascade system within a beam of atomic barium [37, 38, 39]. Barium was chosen as the atomic

medium since its most abundant isotope, ^{138}Ba , exhibits no intrinsic spin therefore, has no associated hyperfine structure. These three papers clearly show the effects of Autler-Townes splitting, coherent population trapping and, although not realised by the authors, the quantum interference effect (later named by Harris, see Section 1.3.3) Electromagnetically-Induced Transparency (E.I.T.). In fact it was not realised until the work of Harris that the absorption lineshape for transitions to an Autler-Townes doublet was not simply the addition of two, appropriately split, sub-components but that in fact between the components quantum interference was created. It is this quantum interference, which occurs in the frequency region between the Autler-Townes components, which creates the greatly reduced absorption feature even when the Autler-Townes splitting is less than the inhomogeneous linewidth so appearing as a narrow transparency within the absorption profile. Sub-Doppler E.I.T. features are apparent in the experimental traces of a coherent population trapping experiment, within the D_1 line of rubidium, carried out by Akulshin et al. [40]. However, this work again preceded that of Harris and so the connection to quantum interference and the effect of E.I.T. and its terminology was not made. The relative roles of Autler-Townes splitting and E.I.T. in a coherently induced transparency feature is dealt with in detail in Chapter 8 of this work.

1.3.3) Electromagnetically Induced Transparency

The viewpoint of quantum interference effects took a subtle change in 1989, following work contained in a theoretical paper by Harris [41]. The author considers a four level system and predicts the presence of interference in the absorption profile of lower level atoms if the two upper levels are purely lifetime broadened and decay to an identical continuum. These interference effects are shown to be absent in the stimulated emission profile of the upper level atoms, leading to the prediction of the possibility of laser amplification without a population inversion. Later the following year Imamoglu extended the above idea to show that a three state atomic system, where the upper two states have the same J and m_J quantum numbers and decay radiatively to the states of a single atomic level, is equivalent to that of the system of Harris [42]. This work revealed that atomic interference effects could be coherently induced without ionisation to the continuum taking place. The first explicit reference to Electromagnetically Induced Transparency (E.I.T.) occurred the following year when Harris et al.

theoretically proposed the employment of E.I.T. to enhance nonlinear optical processes [43]. The suggested scheme involved applying a strong coupling field between a metastable state and the upper state of an allowed transition to ground thus obtaining a resonantly enhanced third order susceptibility while simultaneously inducing transparency in the media.

The first experimental observations of E.I.T. were carried out by the Stanford group. Their initial experiment employed neutral strontium as the atomic medium, outlined in Figure 1.2, and pulsed dye lasers to generate the optical fields [44]. With most of the atomic population initially in state $|1\rangle$ the authors were able to prevent absorption on the autoionising transition from state $|1\rangle - |3\rangle$, where state $|3\rangle$ is an autoionising state found in the continuum. Normally the transmittance of a probe laser resonant with this transition (337.1 nm) would be of the order of $\exp(-20)$. However, application of the yellow coupling field at a wavelength of 570.3 nm, corresponding to the resonance wavelength between levels $|2\rangle$ and $|3\rangle$, caused the transmittance of the probe to increase to $\exp(-1)$. This change in transmittance due to the presence of a coupling field is the effect dubbed Electromagnetically Induced Transparency (E.I.T).

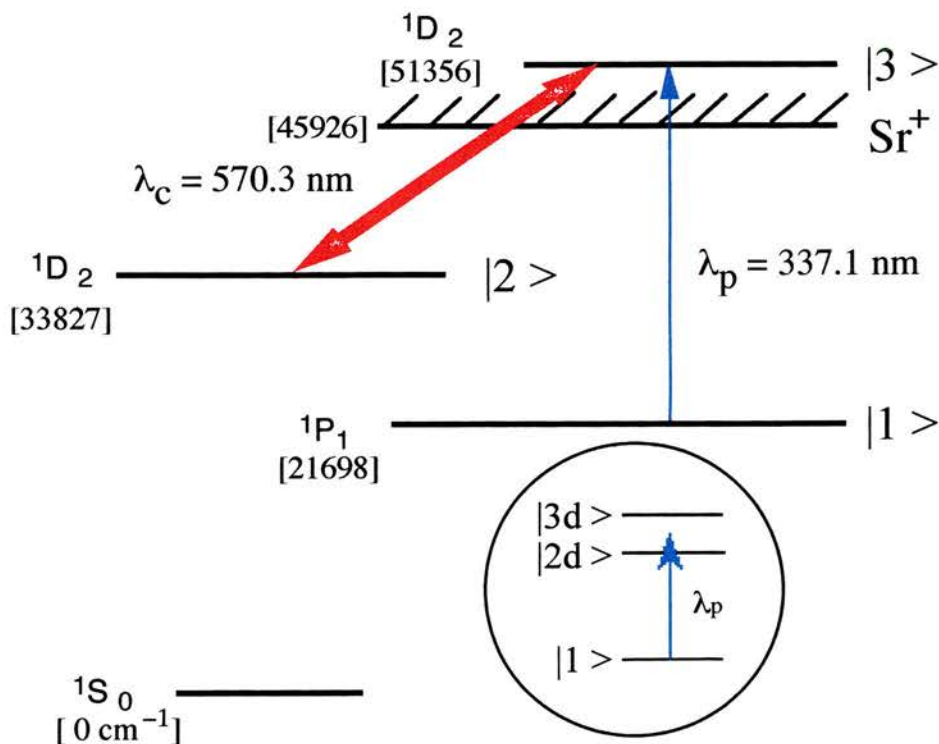


Figure 1.2:- Energy-level diagram of neutral Strontium employed by Boller et al. to observe experimental E.I.T. within neutral strontium. Inset: Dressed-state picture.

The physical explanation of this phenomenon is that when the probe laser is turned on in the presence of the coupling laser, ground-state atoms evolve to a steady state where a fraction of their population is in state $|2\rangle$. This coherently phased population produces a dipole moment of equal magnitude and opposite sign to the primary moment at the probe frequency, trapping the population in $|2\rangle$ and leaving $|3\rangle$ empty. Equivalently the transparency may be viewed as the interference in absorption between two ac-Stark split components of $|3\rangle$. The effect of the coupling field is essentially to create two dressed states, that is, states of the laser-atom system, shown as $|2d\rangle$ and $|3d\rangle$ in the inset of Figure 1.2. Destructive interference between the ground state transitions to these two levels prevents the absorption of photons whose wavelength lies exactly between the two dressed states.

Later Field et. al demonstrated the presence of E.I.T. in a second experiment in which the resonance transitions were broadened by collisions within the gas [45]. This experiment was based on a system within lead vapour which is shown schematically in Figure 1.3.

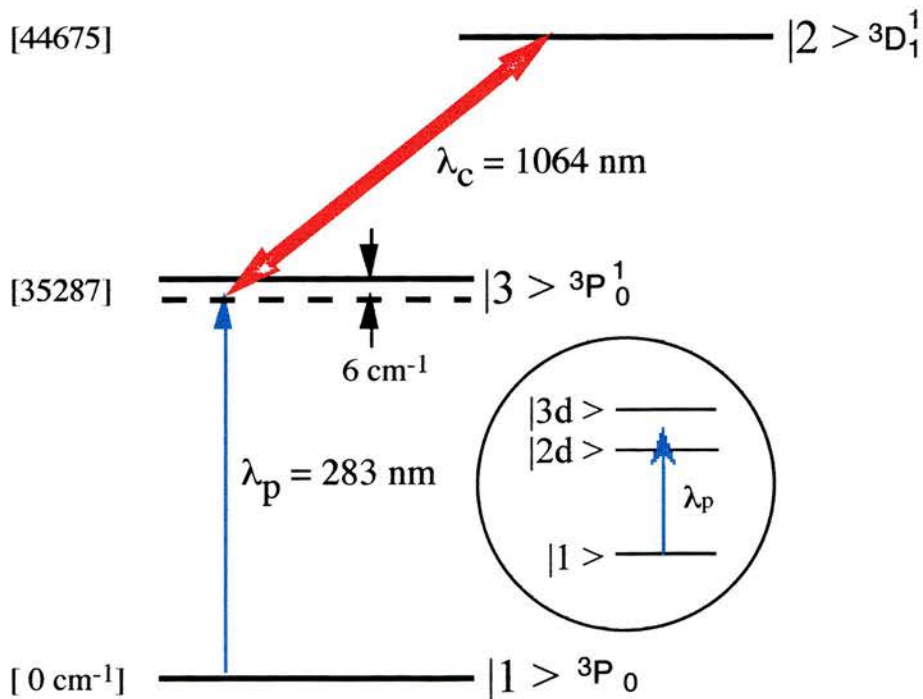


Figure 1.3: Energy level diagram of neutral lead employed by Field et al. to observe experimental E.I.T. within neutral lead. Inset: Dressed-state picture.

On this occasion the coupling field was generated by a pulsed, Q-switched, injection-seeded Nd:YAG laser whereas the probe field was a pulsed, frequency-doubled dye laser. The researchers were able to increase the transmission at 283 nm by at least a factor of $\exp(10)$, with nearly all the lead atoms remaining in the ground state. A review of both of the experiments described above and of other early work within the field of quantum interference is presented in a popular article by Levi [46].

1.3.4) Subsequent Work On E.I.T

Following the early studies at Stanford there has subsequently been a great deal of theoretical and experimental work carried out in the field of quantum interference. As well as the work at St. Andrews (see [47] for an introductory overview) there have been extensive studies carried out by various other groups. In Section 1.4, E.I.T. related topics which include its application to enhance nonlinear optics, the creation of phaseonium like media and production of inversionless lasing will be discussed. The remainder of this section contains a brief review of some of the fundamental studies of E.I.T. which have also been carried out.

After their initial work a series of papers have been written by the Stanford group dealing with various aspects of E.I.T. The dispersive properties experienced by a probe field during an E.I.T. window were considered by Harris et al. [48]. A theoretical prediction that a probe field pulse would propagate with an unusually slow group velocity was made, where modelling on a lead vapour system resulted in optical delay values some 250 times less than the speed of light. In a more recent publication [49] the authors describe the first experimental studies of the temporal dynamics and spatial behaviour of propagating E.I.T. pulses. For a weak probe and a strong coupling field they observed group velocities as slow as $c/165$ with an energy transmission of 55% and the observation of near diffraction-limited beam transmission in a medium which, without the coupling field present, was nearly optically impenetrable. In an experiment within caesium vapour O. Schmidt et al. have measured even lower group velocity values, below $c/3000$ [50]. These values correspond to a time delay of more than 200ns for a 2 cm caesium cell length, or equivalently to more than 60 m of free space propagation.

A set of papers concerning the mutual propagation of coupling and probe field pulses through a coherently prepared E.I.T. style medium have also been published. Harris points out that when an arbitrarily shaped pulse is applied to an ensemble of population-trapped atoms, the atoms will generate a matching pulse shape on the complementary transition and, after a characteristic propagation length, render themselves transparent [51]. Following on from this work, two theoretical papers were published which examined the propagation of optical field pulse pairs in an absorbing medium under single-photon and two-photon resonant lambda system conditions [52, 53]. Matched Gaussian pulses, at the two transition frequencies, were applied simultaneously to the medium. It was found that the probe laser experiences a front edge preparation loss as it produces a population trapped state, but is lossless thereafter. This process is described in terms of paired variables which are the normal modes for E.I.T. Continuing the work on pulse analysis Harris and Luo published a paper where they discussed the laser energy requirements necessary to initiate E.I.T. within a lambda system [54]. They found that the number of photons within the coupling field pulse must exceed the product of the number of atoms in the laser path times the ratio of the oscillator strengths of the probe and coupling field transitions. More recently in a publication by Buffa it has been proposed that E.I.T. could be employed to suppress laser induced collisional autoionisation [55]. Ionisation suppression levels of the order of 70% are predicted for dressing laser pulse intensities of a few tens of MW cm^{-2} .

A series of cw E.I.T experiments, some similar to those within this thesis, have been carried out in atomic rubidium by the group in Arkansas. Initially, by employing a Mach-Zehnder interferometer, the authors measured the dispersive properties experienced by a probe field resonant with the D_2 line of rubidium, in the presence of a strong coupling field on the $5P_{3/2} - 5D_{5/2}$ transition [56]. This work was published alongside the first paper outlining the effects of Electromagnetically Induced Focusing (E.I.F.) [57], see also Chapter 6. The Stanford group has also published a paper which deals with inherent focusing effects of E.I.T. [58]. Here they demonstrated a method for eliminating self-focusing and defocusing, within a lambda system, for a co-propagating pair of intense laser beams whose frequencies differ by a Raman resonance. The next paper in the Arkansas group series introduced a theoretical and experimental study of E.I.T. within an inhomogeneously broadened cascade medium [59]. By employing diode lasers the authors observed $\sim 64\%$ depth transparency features within these experiments. Diode lasers were again employed to study a lambda system based

on the D_1 line of rubidium [60]. The transient properties of E.I.T. within the previous two systems have also been studied by the same group [61]. Here they predict the damped oscillatory nature of the probe field absorption, to a steady state (transparent) value, after a coupling field is introduced to the system. Further discussion on this phenomenon is presented in Chapter 4 of this work. At the same time as the two-photon spectroscopy work of Chapter 5 was first published [62] the Arkansas group had similar work published outlining the possibilities of employing E.I.T. for hyperfine spectroscopy [63]. They adopt a more mathematical approach in their explanation of these effects, however their single experimental trace does agree completely with those contained within Chapter 5. The most recent paper published by the Arkansas group outlines a theoretical study of the interaction between laser fields and degenerate Zeeman sublevel atoms [64]. This formalism is employed to numerically investigate coherent population trapping schemes within the D_1 line of rubidium.

A paper by a group from Shanghai presents work on the experimental observation of cw E.I.T. within a sodium V-type system [65]. Their experimental results show that by employing a frequency stabilised dye laser the absorption coefficient at maximum coherence is reduced by $\sim 72\%$ of the maximum value. Lately Vemuri et al. have published two papers. The first examines the sub-Doppler resolution in an inhomogeneously broadened media [66] and the second carries out an analysis of sub-Doppler linewidths within inversionless amplification [67]. The authors quantify the linewidths of the coherently induced features within a lambda E.I.T. experiment and conclude that these depend critically on the detuning of the coupling field. These results agree well with the linewidths of the features observed in Section 5.4 of this work where the effects of coupling field detuning within a cascade E.I.T. experiment have been examined. Most recently homogeneously broadened cw E.I.T. has been observed within a rubidium atomic trap [68]. A schematic representation of this experiment is shown in Figure 1.4(a) with Figure 1.4(b) outlining the energy levels and field orientations employed by the authors to study a lambda E.I.T. system. As well as this lambda system a V-type system and a system utilising degenerate Zeeman sublevels of the ground state have also been studied. The most significant result from this paper is the fact that the perturbing effects of the magneto-optical trap (M.O.T.) are found to be small.

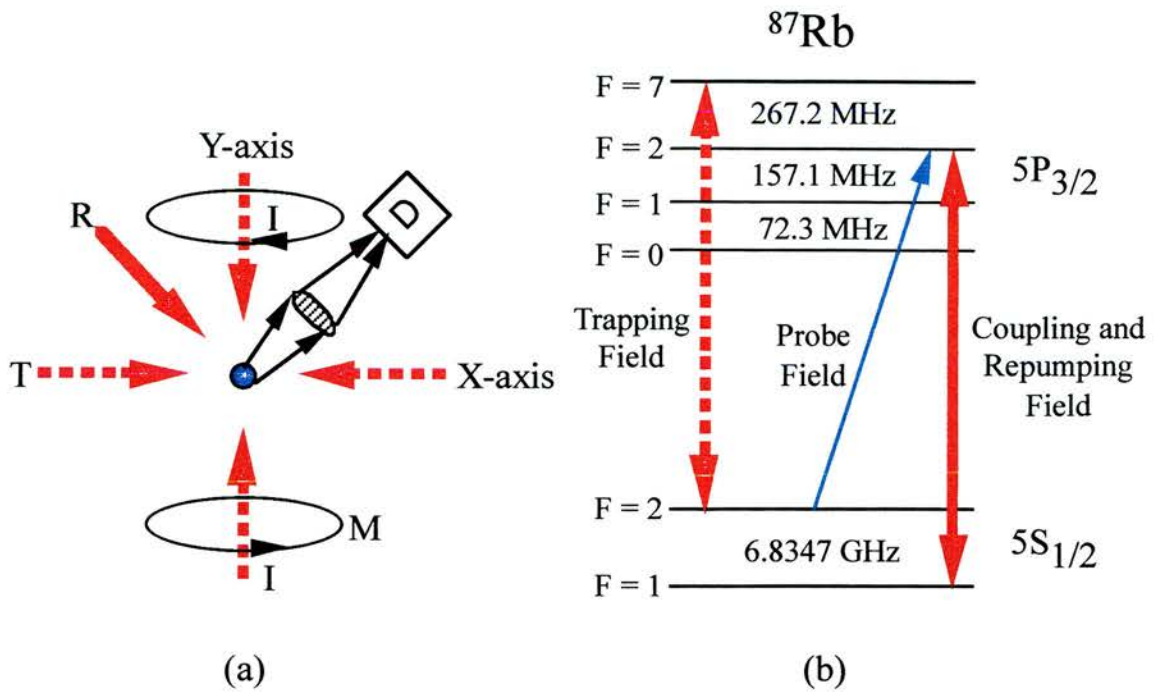


Figure 1.4: (a) Schematic diagram in the $x - y$ plane of the M.O.T. showing trapping fields T and repumping fields R . The trapping field on the z -axis is not shown. The magnetic coils M are coaxial with the y -axis and carry currents in an anti-Helmholtz configuration. (b) Energy-level diagram for trapping ^{87}Rb , showing also the coupling and probe beams for a lambda system experiment.

Results taken in the presence and absence of the M.O.T. (i.e. turned on or off) do not differ significantly thus, both agree well with theoretical predictions obtained from standard E.I.T. density matrix models for homogeneously-broadened samples.

Ever more exotic theoretical studies of E.I.T. have been carried out which, as yet have no experimental confirmation. A whole area of theoretical induced transparency effects have been studied whereby the coupling field has been removed and replaced by placing a single atom in an ultra-high finesse cavity [69, 70] (and references therein). By driving the two level atom from the side by an optical field, which can be single mode or multi-mode, it is found that the fluorescence from the atom is reduced in a similar fashion to that of E.I.T. This effect is again due to quantum interference where it is coherence of the driving field and the field resonating within the cavity which result in the observed phenomena.

The effects of phase fluctuations on E.I.T. in a V-type system have been analysed by Gong and Xu [71]. They show that for a coupling field with a finite linewidth, induced transparency and enhanced refractive index effects are substantially reduced. Harnessing the properties of E.I.T. to produce phase noise squeezing has also been predicted [72, 73]. Phase noise squeezing of the order of 50% is predicted on the probe field. Full quantum mechanical studies of E.I.T., where the electromagnetic fields are quantised, predict matched photon statistics [74] and a correlation of high frequency phase fluctuations [75]. More recently a full quantum treatment is carried out on the suppression of absorption and lasing without inversion in a three level system where a strong driving field is resonant with the two lower levels [76]. It is shown that because of the distinguishability of the states of the driving field that have different photon numbers, destructive interference is confined to occur within a finite region of the photon number space. This places a quantum mechanical restriction on the amount of induced transparency achievable in much the same way that the inclusion of a finite bandwidth of the driving field or spontaneous decay, limits the semiclassical theoretical predictions. Theoretical predictions have also been made that suggest that quantum interference effects could be employed to eliminate a spectral line in the spontaneous emission spectrum and spontaneous emission cancellation in steady state [77].

1.3.5) Quantum Interference In The Solid State

There has already been some limited quantum interference work carried out in the solid state, which is the obvious extension of the work in this thesis in order to develop more practical working systems for commercial use. Fröhlich et al. reported the observation of the optical stark effect within Cu_2O [78] and GaAs multiple-quantum-well structures (M.Q.W.S.) [79, 80]. Here a CO_2 laser was employed as the coupling field and the change in absorption was monitored using a tuneable dye laser.

Wei et al. have carried out experimental investigations of absorption and dispersion profiles of strongly driven transitions in two level systems with a weak probe [81], and in V-type systems with a strong probe [82]. The experiments were carried out within the nitrogen-vacancy colour centre in diamond where the coupling field was generated at 4.7 MHz or 5.4 MHz, by employing an R.F. source, and the probe field at 638 nm was provided by a cw-dye laser. The second paper in particular is of interest since the

authors set out to study the Autler-Townes doublet created by the coupling field. However, examination of the presented experimental results certainly suggest the possible presence of E.I.T. features.

The possibility of semiconductor lasers without a population inversion have been suggested by two groups. Zhao et al. proceed by introducing a coherent laser field to couple two electron subbands within a quantum well [83]. They predict that E.I.T. and light amplification without a population inversion of a weak probe beam within such a system should be possible. Imamoglu and Ram propose a radical new scheme for lasing without population inversion that utilises interference, not through the presence of a coupling field, but through the interactions of a unipolar double-quantum-well (D.Q.W.) intersubband transition [84]. The proposed system is outlined schematically in Figure 1.5(a).

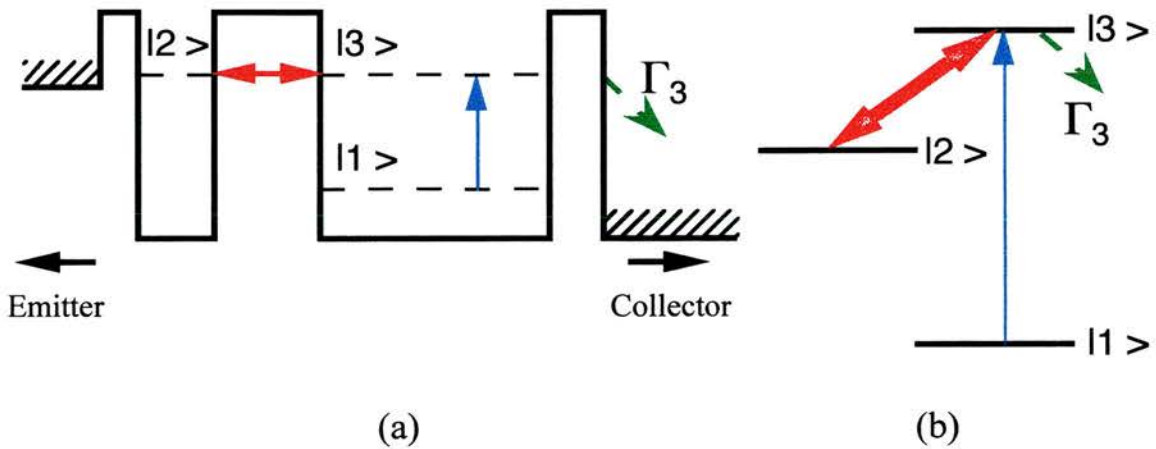


Figure 1.5: Bare state energy-level diagram for (a) the unipolar D.Q.W. structure and (b) the inversionless three level atomic scheme proposed by Imamoglu and co-workers.

The first subband, $|2\rangle$, of the narrow well is resonant with the second subband, $|3\rangle$, of the wide well, which in turn has a dipole allowed transition to the lower subband, $|1\rangle$. The authors show that this system directly corresponds to that originally proposed by Imamoglu and Harris [85], shown schematically in Figure 1.5(b), where an optical field was employed to generate the required coherence.

1.4) Topics Related To Electromagnetically Induced Transparency

1.4.1) The Enhancement Of Nonlinear Optics

Electromagnetically-induced transparency has some promising applications for nonlinear systems. Nonlinear effects are resonantly enhanced the closer one is to a transition resonance [86, 87]. This occurs because the higher order susceptibilities, on which the nonlinear effects depend, increase rapidly as an optical field is tuned onto resonance. This fact was realised by Harris and co-workers in one of their early papers where they considered the employment of E.I.T. to enhance a four wave mixing process within a gas [43], see Figure 1.6.

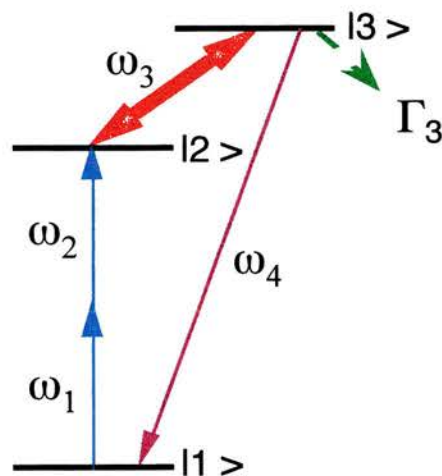


Figure 1.6: Four wave mixing scheme analysed by Harris et al. for the enhancement of nonlinear processes by E.I.T.

It was illustrated that by employing a strong coupling field on the $|2\rangle - |3\rangle$ transition, E.I.T. could be induced on the generated $|1\rangle - |3\rangle$ four wave mixing transition hence reducing the re-absorption of the generated field normally experienced. E.I.T. does not simultaneously reduce the nonlinear conversion process hence, the ratio of the nonlinear generation to re-absorption increases dramatically, by up to four orders of magnitude. Later, the same group showed that the predicted phase matching point at the centre of E.I.T. could be employed to enhance a four-wave mixing signal at 283 nm within atomic lead, even when the strong coupling field was off resonance [88]. Petch et al.

have also carried out an extensive theoretical study of the role that E.I.T. plays in resonant four wave mixing [89]. Their model incorporates the effects of driving and pump field phase fluctuations, Doppler broadening and phase matching conditions and so again predicts large enhancements in the four mixing efficiencies along with the simultaneous existence of gain. A similar mechanism is employed by Moseley et al. within a three wave sum-frequency mixing experiment, where strong absorption of the fundamental input wave is found to be the limiting factor on the conversion mechanism [90]. It was shown that when the second input field is strong enough to induce E.I.T. there is still a significant nonlinear conversion, and so the generated sum frequency mixing signal is significantly enhanced.

Near resonance experiments which employ E.I.T. to reduce re-absorption have also been employed to enhance second-harmonic generation. Experimental evidence for the enhancement of second-harmonic generation within hydrogen has been demonstrated by researchers in Toronto [91, 92]. A schematic outline of the atomic hydrogen system they employed is presented in Figure 1.7.

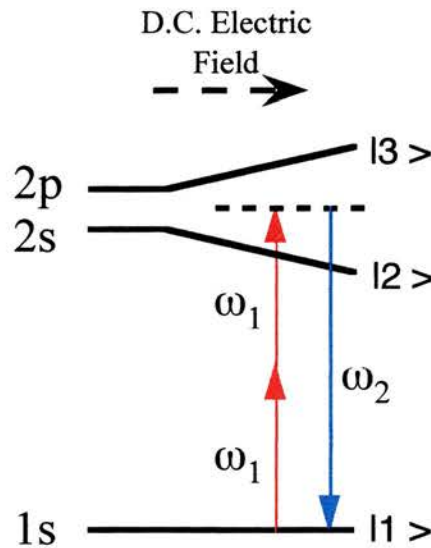


Figure 1.7: Energy levels of atomic hydrogen involved in the dc field induced generation of S.H.G. employed by Hakuta et. al.

The application of a dc electric field yields the same characteristics predicted by Harris et. al [43] for coupling with an electromagnetic field. This dc electric field is shown to couple the $2s$ and $2p$ states producing resonantly enhanced nonlinear susceptibility and

reduced absorption at the second-harmonic wavelength. The development of this experiment so as to replace the dc electric field with an optical frequency coupling field was later presented and again the separate behaviours of the linear and nonlinear susceptibilities was clearly demonstrated [93]. The properties of this hydrogen experiment were analysed by Gheri et al. who outlined that this experiment was capable of producing the second harmonic field with highly squeezed quantum fluctuations [94].

Various other theoretical papers have also been published with regards to these nonlinear four-wave mixing processes. These include the employment of additional external fields to enhance the nonlinear generation [95] and the effects of laser linewidths on the generated fields [96]. A theoretical paper proposing the control of optical bistability using E.I.T and quantum interference [97] is just one of the latest of an ever growing list of applications of E.I.T. to the field of nonlinear optics

1.4.2) Phaseonium

The term phaseonium refers to a medium which exhibits high refractivity without absorption via atomic coherence effects and was first outlined by Scully in 1991 [98], with a comprehensive study outlined the following year by Fleischhauer et al. [99]. The underlying principles are atomic coherence and quantum interference effects. For a coherently coupled scheme, the point of maximum transmission, within a resonance line, corresponds to a zero in the refractive index profile, although a large gradient is present. However, if a small fraction of the atoms are pumped into the upper state then the refractive index is seen to be large at the zero absorption point [100].

One of the theoretically suggested applications for an index enhanced material is a high-sensitivity magnetometer [101] which, in principle, has a quantum noise sensitivity rivalling that of a SQUID device ($\sim 10^{-10}$ G). Other possible applications include high resolution microscopes and improved laser particle accelerators [98] (and references therein). A more recent theoretical paper by Eberly et al. describes a propagation law for weak light pulses in a quantum-phase-clamped (phaseonium) medium [102]. They show that despite heavily overdamped evolution of the atomic density matrix elements

that couple to the optical fields, complex pulse shaping can be obtained in both space and time, and this reshaping is strongly quantum phase dependent.

The first, and to date only, experimental demonstration of a phaseonium medium was published by Zibrov et. al [103]. A conceptual foundation for their experiment can be obtained by considering the lambda system outlined in Figure 1.8(a). The coherent driving field with Rabi frequency Ω_c and weak coherent probe, Ω_p , allow the atom to be prepared in a coherent superposition of states $|b\rangle$ and $|c\rangle$. When the detunings of these two fields from their respective transitions are equal, E.I.T. is obtained. The incoherent pumping, r , alters the coherent superposition by pumping some of the population into other states. Depending upon the actual parameters this may result in gain, loss, or complete transparency for the probe field. A detailed theoretical analysis shows that at the point where the medium becomes transparent the resonant index of refraction has a large value and so a phaseonium medium has been created.

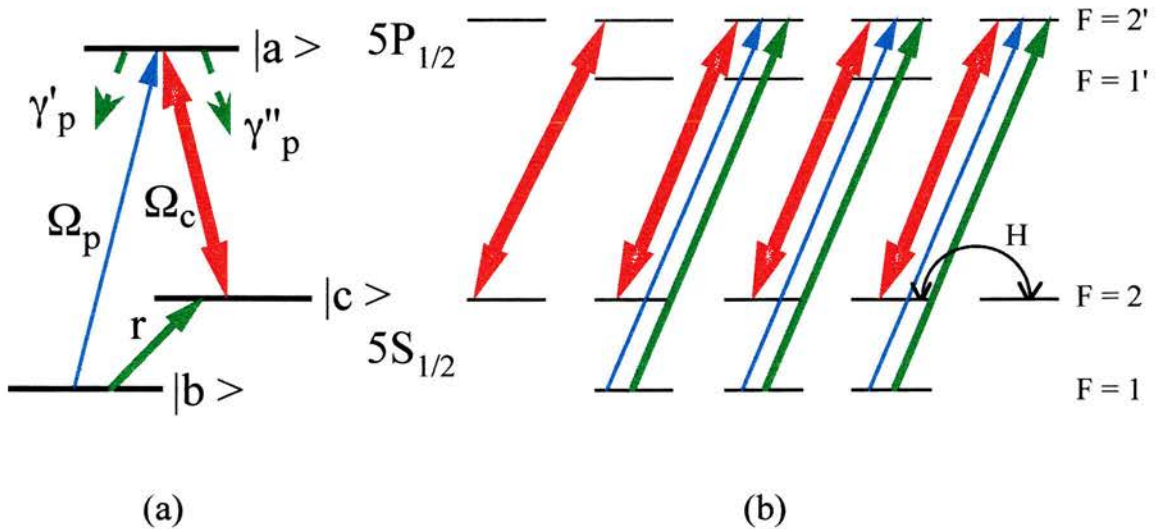


Figure 1.8: (a) Simplified three-level model for index enhancement. (b) The actual atomic level scheme of the D_1 line within ^{87}Rb and the optical fields employed by Zibrov et al. to create a phaseonium medium.

The actual atomic system employed by the authors, based on the D_1 line of rubidium, is presented in Figure 1.8(b). Here right circularly polarised coherent driving and probe fields, generated by extended cavity diode lasers at 794 nm, were tuned close

to the $|2\rangle - |2'\rangle$ and $|1\rangle - |2'\rangle$ transitions, respectively. To avoid the trapping of population in the state $F = 2, M_F = 2$ a weak magnetic field ($H \sim 2 \times 10^{-4}$ T) was employed, which mixed the populations of the magnetic hyperfine levels via Larmor precession.

1.4.3) Non - Inversion Lasers

1.4.3.1) An Introduction To Non-Inversion Lasers

It has long been believed that a population inversion is an inherent requirement in order to produce laser light. Laser systems work because of stimulated emission, an event in which an excited atom or molecule is induced by a photon to release that photon's identical twin. Arrange to have many atoms producing photons by stimulated emission, and a chain reaction is the result, with all the photons produced having the same wavelength and phase. Conventional laser systems achieve this effect by the creation of a population inversion between an excited level and a lower energy level. The difficulty in these schemes is that in order to generate a coherent laser field at a particular frequency, it is necessary to have incoherent pumping at a higher frequency, since both the levels involved in the lasing transition are excited levels. In other words, a conventional laser transforms incoherent energy into a coherent field at a lower frequency.

The question then arises, "Why should research groups pursue lasing without inversion when we already have plenty of lasers that operate with inversion?" The reason becomes obvious if one tries to imagine a system that would produce coherent X-ray or even a γ -ray light. It is rather difficult to create an inversion of population using incoherent pumping at or above these frequencies. This is due to the rapid decay rates associated with the highly energetic (X-ray or γ -ray emitting) states. Thus the road to higher-frequency lasers is not accessible via conventional means. For these reasons the past decade has seen a vast increase in the amount of literature published on the subject of lasers without a population inversion.

1.4.3.2) Driven Two-Level Systems

Some of the first schemes for lasing without inversion were based on the phenomenon of Rabi oscillations. If a two-level medium is driven by a strong, resonant coherent electric field, amplification without population inversion is possible at the beat frequencies of the atomic resonance and the Rabi oscillation. Such schemes were predicted independently by Rautian and Sobel'man [104] and by Mollow [105] and have since been verified experimentally [106, 107]. Thus, gain is possible away from the atomic resonance in the absence of population. This is achieved by a transfer of coherence from one field to another field. However, this transfer is realised without extraction of energy from the medium. A theoretical interpretation of this system has been presented by various groups [108, 109, 110].

1.4.3.3) Amplification Via Quantum Interference Mechanisms

Since the initial ground breaking work of Harris in 1989 [41] there have been many proposed systems for inversion gain which employ quantum interference. The basic principles of amplification without inversion are that small signal gain is produced with no population inversion in the bare states in the presence of all the appropriate coherent coupling and incoherent pump fields. The gain mechanism must also extract energy from the interaction medium and not simply be some complex wave mixing process. A comprehensive review of the field of lasing without inversion is presented by Mandel [111]. However, this is not the only review paper on this subject, significant theoretical reviews have also been published by other authors [112, 113, 114] and a whole volume of the journal "Quantum Optics" has also been dedicated to this topic [115]. Recently an interesting review paper was published by Lukin et al. [116]. As well as reviewing some of the basic principles of lasing without inversion this paper also reviews the first experiments to realise these effects, see Section 1.4.3.4. It then goes on to discuss the difficulties in extending these proof of principle experiments to ones that will be able to generate new shorter wavelength lasers. Although the previously referenced review papers, along with their included references, do not provide the complete literature review of this subject they do highlight many of the key points. Therefore, these papers serve as a good starting point for researchers wishing to begin a study of non-inversion lasing.

In short, the literature outlines two different mechanisms for amplification without a population inversion [117, 118]. The first class of mechanisms to be discussed are those which exhibit lasing without a population inversion in the bare states, but exhibit an associated population inversion between levels in the dressed state analysis [119]. It is proposed that this population inversion between the dressed states is a necessary, though not sufficient, condition for amplification [120]. The lasing medium in most of these devices, dubbed quantum beat lasers, consists of a three-level atom, with either a lower or upper state doublet. Generation of coherence between the closely spaced doublet leads to a modification of the atomic coherence of the optical transition thus producing gain [117, 121, 122, 123, 124, 125]. The second class of mechanism is one which appears to require neither a population inversion between eigenstates of the density matrix nor between the fully quantum mechanically treated dressed states [126, 127, 128, 129, 130, 131]. In these systems gain is achieved through the quantum interference effects between the dressed states.

1.4.3.3) Experimental Observation Of Non-Inversion Gain

The first experimental report of light amplification without population inversion was by Gao et. al. in 1992 [132]. The experiment was performed using sodium atoms whose hyperfine components $F = 2$ and $F = 1$ of the ground state, $3S_{1/2}$, were coupled to the excited state, $3P_{1/2}$, by an intense coherent pump field at 589.6 nm. A weak tuneable field probes the gain in the frequency domain near 589 nm. Under the appropriate conditions the weak probe beam was amplified in the presence of a Raman pulse. There has been much discussion over the interpretation of this experiment because the reported amplification was not accompanied by clear evidence of a lack of inversion. However, a more recent publication attempts to provide a theoretical framework for the interpretation of Gao et. al. experimental results [133]. This theoretical analysis of the gain properties of a four-level active medium, without population inversion and in the presence of a pulsed Raman field, follows on from previous work by the group [122]. More recently, light amplification without a population inversion in sodium vapour has been reported by the same authors where a long laser pulse has been employed as the driving field [134].

In 1993 the first clear-cut evidence of gain was reported by Nottelmann et. al. [135]. The authors used a scheme based on Zeeman coherence within samarium vapour, as shown in Figure 1.9.

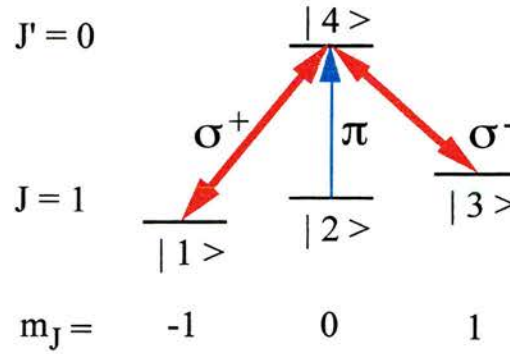


Figure 1.9: Nottelmann et. al. samarium energy level and excitation scheme for the production of non-inversion gain.

This system is a generalisation of the lambda-scheme, with three lower levels connected to one upper level. The samarium atoms are subjected to a static magnetic field which causes ground state hyperfine splitting. A low frequency ρ_{13} coherence is created by means of a periodic train of picosecond pulses, with R.F. period T_p , which excites the σ^+ and σ^- transitions and so provides the required source of quantum interference. A test picosecond pulse, similar to those of the σ train, follows the last pulse of the train after a delay of $T_p / 4$. Depending on the strength of the magnetic field the test pulse can either experience attenuation or gain. Gain, when present, is related to the population in the upper state, $|4\rangle$, therefore a populating picosecond pulse is sent into the system before the test pulse arrives. This populating pulse has its electric field polarised orthogonal to the σ pulses such that it drives the π transition without effecting either of the σ transitions.

The second experiment reporting pulsed gain was performed by Fry et. al., in 1993, where the authors employed dye lasers to generate their optical fields and the D_1 line of atomic sodium as their interaction medium [136]. Further evidence of pulsed gain has been presented by van der Veer et. al [137] using cadmium vapour in a magnetic field

driven by dye lasers pumped by a Q-switched Nd:YAG laser. In this experiment a V-type system rather than the usual lambda system was employed. An extensive theoretical study of the properties of a V-type system for the production of inversionless gain has been carried out by Zhu and co-workers. In an initial paper the authors examine the photon statistics within this V-type system [138]. This paper is then followed by an analysis of the transient and steady states of the system [139].

The first demonstration of steady-state gain due to quantum interference effects was carried out by Kleinfeld and Streater in 1994 [140]. They employed a potassium-helium mixture in a double V-type configuration as the gain medium, outlined in Figure 1.10. A fuller description of their theoretical analysis and experimental results from this system was published in a later paper [141].

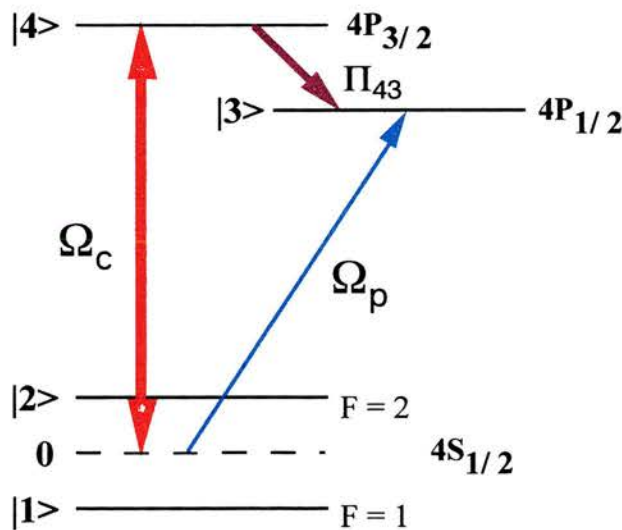


Figure 1.10: Kleinfeld and Streater potassium energy level diagram for generating cw gain. A helium buffer gas was present to collisionally transfer the required population from level $|4\rangle$ to level $|3\rangle$.

Here a strong coupling field, Ω_c , generated by a dye laser, was applied on the potassium D_2 line, while the probe field, Ω_p , generated by a Ti:sapphire laser, was scanned across the D_1 line. The presence of the coupling field produces a trapped population in a superposition of the ground states so resulting in the probe field experiencing an induced transparency at line centre. It is the presence of helium buffer gas which

provides the mechanism for transforming the induced transparency into inversionless gain. This gas acts to move population from level $|4\rangle$ to level $|3\rangle$ through inelastic collisions at a rate Π_{43} , and so provides the small amount of upper state population required for the observation of non-inversion gain. The authors noted that the induced inversionless gain feature could be enhanced by detuning the coupling field somewhat off resonance (typically $\sim 3\text{GHz}$).

The first experimental demonstration of laser oscillation without population inversion was demonstrated by Zibrov et al. in 1995 [142]. Here diode lasers were employed as the optical field sources in a V-type atomic configuration within the D_1 and D_2 lines of rubidium vapour. This system is discussed later in detail within Section 2.3.2. of this work. The same group later demonstrated cw amplification and laser oscillation without a population inversion for the first time in a complex lambda system within the sodium D_1 line [143], shown schematically in Figure 1.11.

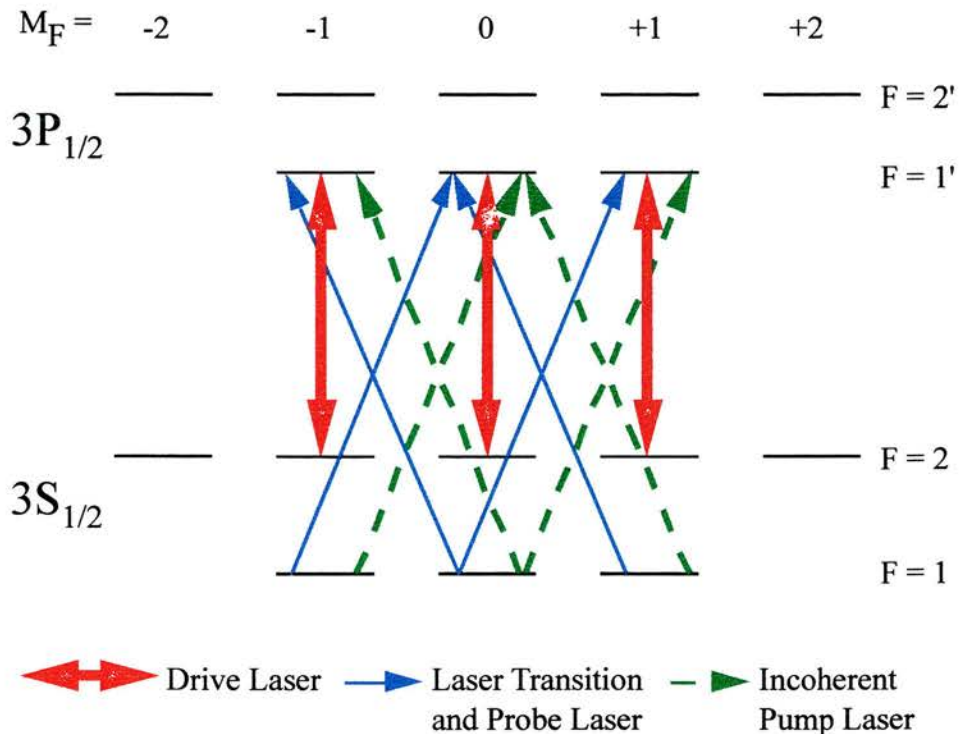


Figure 1.11: Relevant energy levels of sodium employed in Padmabandu et. al atomic beam experiment to generate laser oscillations without a population inversion.

This system is based on the simple three level lambda system and is closest to the concept proposed by Imamoglu, Field and Harris [127], which is theoretically analysed later in Section 2.3.1. This experiment employed a sodium atomic beam and so was also the first experiment to demonstrate laser oscillation within a beam apparatus.

A second experiment with an atomic beam has now been published by Sellin et al. [144]. In this experiment the authors study the production of laser gain with and without a population inversion in a doubly driven cascade-type atomic system. Single-mode, ring dye and Ti:sapphire lasers were employed to provide the required optical fields. In the inversionless regime, laser gain consistent with theory is experimentally demonstrated. Less commonly studied is the laser gain produced by coherent excitation when the employed fields produce atomic inversion. The authors also investigate gain in this regime, and find that the coherent fields act to magnify the amount of laser gain normally derivable from a given level of inversion. The ability of coherent excitation to enhance gain in the presence of inversion has obvious importance in terms of laser operation and is sure to be the subject of future theoretical and experimental investigation.

1.5) A Guide On What Is To Follow

This chapter has outlined some of the background work on the enormous field of physics dealing with the interaction of light with atoms. From the early experiments examining the spectrum of light within the sun's rays, to the complex mechanisms involved in quantum interference effects, the subject of atom-light interactions has long fascinated scientists. The work involved in the remainder of this thesis uncovers another piece of this ever growing complex puzzle, while helping to extend our understanding of the subject, now classified under the impressive heading of quantum optics.

Following the introduction are two theoretical chapters. The first, Chapter 2, outlines the theory behind amplitude state and density matrix models employed to help explain the observed phenomena within the following experimental chapters. Using these models a brief analysis of popularly studied E.I.T. and non-inversion laser systems is carried out. Chapter 3 continues with a theoretical introduction to atomic rubidium, which is the medium that all the experimental work of this thesis is carried out in. This

includes a brief explanation of the intrinsic structure involved with rubidium and an outline of how to calculate induced Rabi frequencies on particular dipole allowed transitions in the presence of Gaussian optical fields. Chapter 3 concludes with an outline of the experimental apparatus employed within following chapters.

Four experimental chapters then follow. The first of these, Chapter 4, introduces some of the fundamental concepts of E.I.T. and highlights some of the difficulties involved in observing theoretically predicted results, obtained from ideal three level atom models, within real experimental systems. A comparison of the practicalities of three of the most popularly studied systems is then made. Chapter 5 continues the work of the previous chapter to consider two photon and Zeeman splitting effects on E.I.T. windows within the cascade system. Novel spectroscopy techniques are discussed and the detrimental effects of magnetic fields to quantum interference highlighted. Chapter 6 extends the experimental work to consider the spatial consequences of employing Gaussian profiled cw optical fields within E.I.T. style experiments. It is found that novel focusing effects, dubbed Electromagnetically Induced Focusing (E.I.F.), occur and that these can be employed such that the focusing or propagation of one optical field is controlled by another. The final experimental chapter, Chapter 7, examines the relative roles of Autler-Townes splitting and E.I.T. in a coherently induced transparency feature within a Doppler broadened medium. The most important, and highly significant, result from this chapter is the fact that matched probe and coupling field wavelengths in Doppler broadened systems need not be found in order to observe quantum interference effects.

This last result opens a whole new area of research in the field of quantum interference. Some of these are theoretically discussed and modelled within Chapter 8. In this chapter the knowledge and experience gained over the course of this thesis is drawn together to present a novel system which predicts that the employment of I.R. Ti:sapphire lasers can produce non-inversion gain in the blue region of the electromagnetic spectrum. Other future experiments are also presented where it is proposed to replace the coupling optical field with an R.F. source. This would allow the R.F. control of the absorption and dispersion of an optical field which could be employed in many varying future applications.

References

- [1] **A. Einstein**, *On The Quanta Theory Of Radiation*, Phys. Z. 18, 121 (1917).
- [2] **R. Loudon**, *The Quantum Theory Of Light*, (Clarendon Press, Oxford, 2nd edition (1992)).
- [3] **B.W. Shore**, *The Theory Of Coherent Atomic Excitation*, (Wiley, New York (1990)).
- [4] **S.H. Autler and C.H. Townes**, *Stark Effect In Rapidly Varying Fields*, Phys. Rev. 100, 703 (1955).
- [5] **H.R. Gray, R.M. Whitley and C.R. Stroud Jr.**, *Coherent Trapping Of Atomic Population*, Optics Letters 3, 218 (1978).
- [6] **A. Yariv**, *Quantum Electronics*, (Wiley, New York (1975)).
- [7] **A. Yariv**, *Optical Electronics*, (Saunders College Publishing, Orlando, 4th Edition (1991)).
- [8] **N. Bloembergen**, *Nonlinear Optics*, (Benjamin, New York (1965)).
- [9] **B.D. Sinclair**, *Continuous-Wave Second-Harmonic Generation In Sodium Vapour*, PhD thesis, University of St. Andrews (1987).
- [10] **H. Uchiki, H. Nakatsuka and M. Matsuoka**, *Optical Second Harmonic Generation In Gases In Magnetic Field*, J. Phys. Soc. Japan 52, 3010 (1983).
- [11] **B.D. Sinclair and M.H. Dunn**, *Continuous-Wave Second Harmonic Generation In Sodium Vapour*, Phys. Rev. A 34, 3989 (1986).
- [12] **A.J. Poustie**, *Magnetic Field Induced Sum Frequency Mixing In Sodium Vapour*, PhD thesis, University of St. Andrews, (1990).

- [13] **M.H. Dunn**, *Continuous-Wave, Single-Frequency, Second Harmonic Generation In Sodium Vapour*, Opt. Commun 45 , 346 (1983).
- [14] **B.D. Sinclair and M.H. Dunn**, *Magnetic Field Gradients And Particle Density Effects In Second-Harmonic Generation In Sodium Vapour*, J. Mod. Opt. 35 , 517 (1988).
- [15] **S. Shepherd**, *Use And Development Of A CW Titanium Sapphire Laser For Nonlinear Optics*, PhD thesis, University of St. Andrews, (1993).
- [16] **R.R. Moseley**, *Sum Frequency Mixing And Quantum Interference In Three-Level Atoms*, PhD thesis, University of St. Andrews, (1994).
- [17] **S. Shepherd, R.R. Moseley, B.D. Sinclair and M.H. Dunn**, *Effects Of Different Phase-Matching Conditions In Sum-Frequency-Mixing Systems In Vapours*, Phys. Rev. A 49 , 3002 (1994).
- [18] **R.R. Moseley, S. Shepherd, D.J. Fulton, B.D. Sinclair and M.H. Dunn**, *Interference Between Excitation Routes In Resonant Sum-Frequency Mixing*, Phys. Rev. A 50 ,4339 (1994).
- [19] **U. Fano**, *Effects Of Configuration Interaction On Intensities And Phase Shifts*, Phys. Rev. 124 , 1866 (1961).
- [20] **E. Arimondo and G. Orriols**, *Nonabsorbing Atomic Coherences By Coherent Two-Photon Transitions In A Three-Level Optical Pumping*, Nuovo Cimento Lettere 17 , 333 (1976).
- [21] **G. Alzetta, A. Gozzini, L. Moi and G. Orriols**, *An Experimental Method For The Observation Of R.F. Transitions And Laser Beat Resonances In Oriented Na Vapour*, Il Nuovo Cimento B 36B , 5 (1976).

- [22] **G. Alzetta, L. Moi and G. Orriols**, *Nonabsorption Hyperfine Resonances In A Sodium Vapour Irradiated By A Multimode Dye-Laser*, *Il Nuovo Cimento B* 52B, 209 (1979).
- [23] **H.R. Gray, R.M. Whitley and C.R. Stroud Jr.**, *Coherent Trapping Of Atomic Populations*, *Optics Letters* 3, 218 (1978).
- [24] **R.M. Whitley and C.R. Stroud Jr.**, *Double Optical Resonance*, *Phys. Rev. A* 14, 1498 (1976).
- [25] **B.J. Dalton and P.L. Knight**, *Population Trapping And Ultranarrow Raman Lineshapes Induced By Phase-Fluctuating Fields*, *Opt. Commun.* 42, 411 (1982).
- [26] **P.M. Radmore and P.L. Knight**, *Population Trapping And Dispersion In A Three-Level System*, *J. Phys. B.* 15, 561 (1982).
- [27] **P.E. Coleman and P.L. Knight**, *Population Trapping In Photoionisation To Dressed Continuum States*, *J. Phys. B: At. Mol. Phys.* 15, L235 (1982).
- [28] **Y.L. Shao, D. Charalambidis, C. Fotakis, J. Zhang and P. Lambropoulos**, *Observation Of Laser-Induced Continuum Structure In Ionisation Of Sodium*, *Phys. Rev. Lett.* 67, 3669 (1991).
- [29] **S. Cavalieri, F.S. Pavone and M. Matera**, *Observation Of Laser-Induced Resonance In The Photoionisation Spectrum Of Sodium*, *Phys. Rev. Lett.* 67, 3673 (1991).
- [30] **P.L. Knight and P.W. Milonni**, *The Rabi Frequency In Optical Spectra*, *Phys. Rep.* 66, 22 (1980).
- [31] **S. Feneuille and M.G. Schweighofer**, *Conditions For The Observation Of The Autler-Townes Effect In A Two Step Resonance Experiment*, *J. De Physique* 36, 781 (1975).

- [32] **S.E. Moody and M. Lambropoulos**, *ac Stark Effect In Multiphoton Ionization*, Phys. Rev. A 15 , 1497 (1977).
- [33] **J.E. Bjorkholm and P.F. Liao**, *AC Stark Splitting Of Two-Photon Spectra*, Opt. Commun. 21 , 132 (1977).
- [34] **H.R. Gray and C.R. Stroud Jr.**, *Autler-Townes Effect In Double Optical Resonance*, Opt. Commun 25 , 359 (1978).
- [35] **C. Delsart and J.C. Keller**, *Observation Of The Optical Autler-Townes Splitting In Neon Gas With A Cascade Level Scheme*, J. Phys. B: Atom. Molec. Phys. 9 , 2769 (1976).
- [36] **C. Delsart and J.C. Keller**, *Effects Of Zeeman Degeneracy On Optical Dynamic Stark Splitting*, J. Phys. B: Atom. Molec. Phys. 13 , 241 (1980).
- [37] **P.T.H. Fisk, H.A Bachor and R.J. Sandeman**, *Investigation Of The Dynamic Stark Effect In A $J = 0 \rightarrow 1 \rightarrow 0$ Three-Level System. I. Experiment*, Phys. Rev. A 33 , 2418 (1986).
- [38] **P.T.H. Fisk, H.A Bachor and R.J. Sandeman**, *Investigation Of The Dynamic Stark Effect In A $J = 0 \rightarrow 1 \rightarrow 0$ Three-Level System. II. Theoretical Description*, Phys. Rev. A 33 , 2424 (1986).
- [39] **P.T.H. Fisk, H.A Bachor and R.J. Sandeman**, *Investigation Of The Dynamic Stark Effect In A $J = 0 \rightarrow 1 \rightarrow 0$ Three-Level System. III. The "Strong-Probe" Case*, Phys. Rev. A 34 , 4762 (1986).
- [40] **A.M. Akulshin, A.A. Celikov and V.L. Velichansky**, *Sub-Natural Absorption Resonances On The D_1 Line Of Rubidium Induced By Coherent Population Trapping*, Opt. Commun. 84 , 139 (1991).

- [41] **S.E. Harris**, *Lasers Without Inversion: Interference Of Lifetime-Broadened Resonances*, Phys. Rev. Lett. 62 , 1033 (1989).
- [42] **A. Imamoglu**, *Interference Of Radiatively Broadened Resonances*, Phys. Rev. A 40 , 2835 (1989).
- [43] **S.E. Harris, J.E. Field and A. Imamoglu**, *Nonlinear Optical Processes Using Electromagnetically Induced Transparency*, Phys. Rev. Lett. 64 , 1107 (1990).
- [44] **K.J. Boller, A. Imamoglu and S.E. Harris**, *Observation Of Electromagnetically Induced Transparency*, Phys Rev Lett 66 , 2593 (1991).
- [45] **J.E. Field, K.H. Hahn, and S.E. Harris**, *Observation Of Electromagnetically Induced Transparency In Collisionally Broadened Lead Vapour*, Phys. Rev. Lett. 67, 3062 (1991).
- [46] **B.G. Levi**, *Some Benefits Of Quantum Interference Become Transparent*, Physics Today, May edition, 17 (1992).
- [47] **M.H. Dunn**, *Electromagnetically Induced Transparency in Laser Sources and Applications*, editors A. Miller and D.M. Finlayson p. 411 (SUSSP / IOP, Bristol, (1996)).
- [48] **S.E. Harris, J.E. Field and A. Kasapi**, *Dispersive Properties Of Electromagnetically Induced Transparency*, Phys. Rev. A. 46 , R29 (1992).
- [49] **A. Kasapi, M. Jain, G.Y. Yin and S.E. Harris**, *Electromagnetically Induced Transparency : Propagation Dynamics*, Phys. Rev. Lett. 74 , 2447 (1995).
- [50] **O. Schmidt, R. Wynands, Z. Hussein and D. Meschede**, *Steep Dispersion And Group Velocity Below $c/3000$ In Coherent Population Trapping*, Phys. Rev. A 53 , R27 (1996).

- [51] **S.E. Harris**, *Electromagnetically Induced Transparency With Match Pulses*, Phys. Rev. Lett. 70, 552 (1993).
- [52] **S.E. Harris**, *Normal Modes For Electromagnetically Induced Transparency*, Phys. Rev. Lett. 72, 52 (1994).
- [53] **J.H. Eberly, M.L. Pons and H.R. Haq**, *Dressed-Field Pulses In An Absorbing Medium*, Phys. Rev. Lett. 72, 56 (1994).
- [54] **S.E. Harris and Z.F. Luo**, *Preparation Energy For Electromagnetically Induced Transparency*, Phys. Rev. A 52, R928 (1995).
- [55] **R. Buffa**, *Suppression Of Laser-Induced Collisional Autoionisation Through Electromagnetically Induced Transparency*, Phys. Rev. A 53, 607 (1996).
- [56] **M. Xiao, Y. Li, S. Jin and J. Gea-Banacloche**, *Measurement Of Dispersive Properties Of Electromagnetically Induced Transparency In Rubidium Atoms*, Phys. Rev. Lett. 74, 666 (1995).
- [57] **R.R. Moseley, S. Shepherd, D.J. Fulton, B.D. Sinclair and M.H. Dunn**, *Spatial Consequences Of Electromagnetically Induced Transparency: Observation Of Electromagnetically Induced Focusing*, Phys. Rev. Lett. 74, 670 (1995).
- [58] **M. Jain, A.J. Merriam, A. Kasapi, G.Y. Yin and S.E. Harris**, *Elimination Of Optical Self-Focusing By Population Trapping*, Phys. Rev. Lett. 75, 4385 (1995).
- [59] **J. Gea-Banacloche, Y. Li, S. Jin and M. Xiao**, *Electromagnetically Induced Transparency In Ladder-Type Inhomogeneously Broadened Media: Theory and Experiment*, Phys. Rev. A 51, 576 (1995).
- [60] **Y. Li and M. Xiao**, *Observation Of Quantum Interference Between Dressed States In An Electromagnetically Induced Transparency*, Phys. Rev. A 51, 4959 (1995).

- [61] **Y. Li and M. Xiao**, *Transient Properties Of An Electromagnetically Induced Transparency In Three-Level Atoms*, Optics Letters 20, 1489 (1995).
- [62] **R.R. Moseley, S. Shepherd, D.J. Fulton, B.D. Sinclair and M.H. Dunn**, *Two-Photon Effects In Continuous-Wave Electromagnetically-Induced Transparency*, Opt. Commun 119, 61 (1995).
- [63] **S. Jin, Y. Li, M. Xiao**, *Hyperfine Spectroscopy Of Highly-Excited Atomic States Based On Atomic Coherence*, Opt. Commun. 119, 90 (1995).
- [64] **H.Y. Ling, Y. Li and M. Xiao**, *Coherent Population Trapping And Electromagnetically Induced Trapping In Multi-Zeeman-Sublevel Atoms*, Phys. Rev. A 53, 1014 (1996).
- [65] **Y. Wang, G. Xu, C. Ye, J. Zhao, S. Zhou and Y.Liu**, *Observation Of Transparency And Population Trapping Due To Atomic Coherence Effects*, Phys. Rev. A 53, 1160 (1996).
- [66] **G. Vemuri, G.S. Agarwal and B.D.N. Rao**, *Sub-Doppler Resolution In Homogeneously Broadened Media Using Intense Control Fields*, Phys. Rev A 53, 2842 (1996).
- [67] **G. Vemuri, G.S. Agarwal and B.D.N. Rao**, *Analysis Of Sub-Doppler Linewidths In Inversionless Amplification*, Phys. Rev. A 54, 1 (1996).
- [68] **S.A. Hopkins, E. Usadi, H.X. Chen and A.V. Durrant**, *Electromagnetically Induced Transparency Of Laser-Cooled Rubidium Atoms In Three-Level Lambda And Vee-Type Systems*, (received pre-print, submitted Opt. Commun (September 1996)).
- [69] **P.M. Alsing, D.A. Cardimona and H.J. Carmichael**, *Suppression Of Fluorescence In A Lossless Cavity*, Phys. Rev A 45, 1793 (1992).

- [70] **D.A. Cardimona, K. Koch and P.M. Alsing**, *Field-Cancellation By A Two-Level Atom In A Multimode Cavity Driven By A Time-Dependent Field*, (reviewed paper for Phys Rev A, proposed publication (January 1997)).
- [71] **S. Gong and Z. Xu**, *The Effect Of Phase Fluctuation On Absorption And Dispersion In A V Medium*, Opt. Commun. 115, 65 (1995).
- [72] **K.M. Gheri and D.F. Walls**, *Squeezed Lasing Without Inversion Or Light Amplification By Coherence*, Phys. Rev. A 45, 6675 (1992).
- [73] **M. Fleishhauer, U. Rathe and M.O. Scully**, *Phase-Noise Squeezing In Electromagnetically Induced Transparency*, Phys. Rev A 46, 5856 (1992).
- [74] **G.S. Agarwal**, *Coherent Population Trapping States Of A System Interacting With Quantised Fields And The Production Of The Photon Statistics Matched Fields*, Phys. Rev. Lett. 71, 1351 (1993).
- [75] **M. Fleishhauer**, *Correlation Of High-Frequency Phase Fluctuations In Electromagnetically Induced Transparency*, Phys. Rev. Lett. 72, 989 (1994).
- [76] **H. Lee**, *Quantum Theory Of Electromagnetically Induced Suppression Of Absorption And Inversionless Lasing In A Three-Level System*, J. Opt. Soc. Am. B 12, 449 (1995).
- [77] **S. Zhu and M.O. Scully**, *Spectral Line Elimination And Spontaneous Emission Cancellation Via Quantum Interference*, Phys. Rev. Lett. 76, 388 (1996).
- [78] **D. Fröhlich, A. Nöthe and K. Reimann**, *Observation Of The Resonant Optical Stark Effect In A Semiconductor*, Phys. Rev. Lett. 55, 1335 (1985).
- [79] **D. Fröhlich, K. Reimann and R. Wille**, *Optical Stark Effect Of Excitons In Semiconductors*, J. Lumines. 38, 235 (1987).

- [80] **D. Fröhlich, R. Wille, W. Schlapp and G. Weimann**, *Optical Quantum-Confined Stark Effect In GaAs Quantum Wells*, Phys. Rev. Lett. 59, 1748 (1987).
- [81] **C. Wei and N.B. Manson**, *Experimental Investigations Of The Absorption And Dispersion Profiles Of A Strongly Driven Transition: Two Level System With A Weak Probe*, Phys. Rev A 49, 4751 (1994).
- [82] **C. Wei, N.B. Manson and J.P.D. Martin**, *Experimental Investigations Of Absorption And Dispersion Profiles Of A Strongly Driven Transition: V-Shaped Three-Level System With A Strong Probe*, Phys. Rev A 51, 1438 (1995).
- [83] **Y. Zhao, D. Huang and C. Wu**, *Electric-Field-Induced Quantum Coherence Of The Intersubband Transition In Semiconductor Quantum Wells*, Optics Letters 19, 816 (1994).
- [84] **A. Imamoglu and R.J. Ram**, *Semiconductor Lasers Without Population Inversion*, Optics Letters 19, 1744 (1994).
- [85] **A. Imamoglu and S.E. Harris**, *Lasers Without Inversion: Interference Of Dressed Lifetime-Broadened States*, Optics Letters 14, 1344 (1989).
- [86] **R. Salomaa and S. Stenholm**, *Two-Photon Spectroscopy: Effects Of A Resonant Intermediate State*, J. Phys. B: Atom. Molec. Phys. 11, 1795 (1975).
- [87] **J.E. Bjorkholm and P.F. Liao**, *Line Shape And Strength Of Two-Photon Absorption In An Atomic Vapour With A Resonant Or Nearly Resonant Intermediate State*, Phys. Rev. A 14, 751 (1976).
- [88] **M. Jain, G.Y. Yin, J.E. Field and S.E. Harris**, *Observation Of Electromagnetically Induced Phase Matching*, Optics Letters 18, 998 (1993).
- [89] **J.C. Petch, C.H. Keitel, P.L. Knight and J.P. Marangos**, *The Role Of Electromagnetically Induced Transparency In Resonant Four Wave Mixing Schemes*, Phys. Rev. A 53, 543 (1996).

- [90] **R.R. Moseley, B.D. Sinclair and M.H. Dunn**, *Enhanced Conversion Efficiency In Three-Wave Mixing Via Electromagnetically Reduced Fundamental Wave Absorption*, Opt. Commun. 101 , 139 (1993).
- [91] **K. Hakuta, L. Marmet and B.P. Stoicheff**, *Electric-Field-Induced Second-Harmonic Generation With Reduced Absorption In Atomic Hydrogen*, Phys. Rev. Lett. 66 , 596 (1991).
- [92] **K. Hakuta, L. Marmet and B.P. Stoicheff**, *Nonlinear Optical Generation With Reduced Absorption Using Electric-Field Coupling In Atomic Hydrogen*, Phys. Rev. A 45 , 5152 (1992).
- [93] **G.Z. Zhang, K. Hakuta and B.P. Stoicheff**, *Nonlinear Optical Generation Using Electromagnetically Induced Transparency In Atomic Hydrogen*, Phys. Rev. Lett. 71 , 3099 (1993).
- [94] **K.M. Gheri, C. Saavedra and D.F. Walls**, *Intracavity Second-Harmonic Generation Using An Electromagnetically Induced Transparency*, Phys Rev. A 4 , 48 (1993).
- [95] **G.S. Agarwal and S.P. Tewari**, *Large Enhancement In Nonlinear Generation By External Electromagnetic Fields*, Phys. Rev. Lett. 56 , 1811 (1986).
- [96] **P.A. Lakshmi and S. Swain**, *Effects Of Laser Linewidths On Nonlinear Optical Processes Exploiting Electromagnetically Induced Transparency*, J. Mod. Opt. 38 , 2031 (1991).
- [97] **W. Harshwardhan and G.S. Agarwal**, *Controlling Optical Bistability Using Electromagnetic-Field-Induced Transparency And Quantum Interferences*, Phys. Rev. A 53 , 1812 (1996).
- [98] **M.O. Scully**, *Enhancement Of The Index Of Refraction Via Quantum Coherence*, Phys. Rev. Lett. 67 , 1855 (1991).

- [99] **M. Fleischhauer, C.H. Keitel, M.O. Scully, C. Su, B.T. Ulrich and S.Y. Zhu**, *Resonantly Enhanced Refractive Index Without Absorption Via Atomic Coherence*, Phys. Rev. A 46 , 1468 (1992).
- [100] **M.O. Scully**, *From Lasers And Masers To Phaseonium And Phasers*, Phys. Rep. 219 , 191 (1992).
- [101] **M.O. Scully and M. Fleischhauer**, *High-Sensitivity Magnetometer Based On Index-Enhanced Media*, Phys. Rev. Lett. 69 , 1360 (1992).
- [102] **J.H. Eberly, A. Rahman and R. Grobe**, *Index Of Refraction For An Optical Medium With Clamped Quantum Phase*, Phys. Rev. Lett. 76 , 3687 (1996).
- [103] **A.S. Zibrov, M.D. Lukin, L. Hollberg, D.E. Nikonov, M.O. Scully, H.G. Robinson and V.L. Velichansky**, *Experimental Demonstration Of Enhanced Index Of Refraction Via Quantum Coherence In Rb*, Phys. Rev. Lett. 76 , 3935 (1996).
- [104] **S.G. Rautian and I.I. Sobel'man**, *Photo-Dissociation Of Molecules As A Method Of Obtaining A Medium With The Negative Absorption Coefficient*, Zh. éksp. teor. Fiz. 41 , 2018 (1961) (English Translation, Soviet Phys. JETP 14 , 328 (1962)).
- [105] **B.R. Mollow**, *Stimulated Emission And Absorption Near Resonance For Driven Systems*, Phys. Rev. A 5 , 2217 (1972).
- [106] **F.Y. Wu, S. Ezekiel, M. Ducloy and B.R. Mollow**, *Observation Of Amplification In A Strongly Driven Two-Level Atomic System At Optical Frequencies*, Phys. Rev. Lett. 38 , 1077 (1977).
- [107] **Y. Zhu, Q. Wu, S. Morin and T.W. Mossberg**, *Observation Of A Two-Photon Gain Feature In The Strong-Probe Absorption Spectrum Of Driven Two-Level Atoms*, Phys. Rev. Lett. 65 , 1200 (1990).

- [108] **H.K. Holt**, *Gain Without Population Inversion In Two-Level Atoms*, Phys. Rev. A 16 , 1136 (1977).
- [109] **N. Lu**, *The Coherently Pumped Laser: The Simplest System For Lasers Without Inversion*, Opt. Commun. 73 , 479 (1989).
- [110] **M. Lewenstein, Y. Zhu and T.W. Mossberg**, *Two-Photon Gain And Lasing In Strongly Driven Two-Level Atoms*, Phys. Rev. Lett. 64 , 3131 (1990).
- [111] **P. Mandel**, *Lasing Without Inversion: A Useful Concept ?*, Contemp. Phys. 34 , 235 (1993).
- [112] **O. Kocharovskaya**, *Amplification And Lasing Without Inversion*, Phys. Rep. 219, 175 (1992).
- [113] **E. Arimondo**, *Is There A Fundamental Difference Between Lasing Without Inversion And Parametric Oscillation ?*, Phys. Rep. 219 , 203 (1992).
- [114] **M.O. Scully and M. Fleischhauer**, *Lasers Without Inversion*, Science 263 , 337 (1994).
- [115] **Various**, *Atomic Coherence And Interference*, Quantum Opt. 6 , 201 (1994).
- [116] **M.D. Lukin, M.O. Scully, G.R. Welch, E.S. Fry, L. Hollberg, G.G. Padmabandu, H.G. Robinson and A.S. Zibrov**, *Lasing Without Inversion: The Road To New Short-Wavelength Lasers*, Laser Phys. 6 , 436 (1996).
- [117] **O. Kocharovskaya, P. Mandel and Y.V. Radeonychev**, *Inversionless Amplification In A Three-Level Medium*, Phys. Rev. A 45 , 1997 (1992).
- [118] **C.H. Keitel, O.A. Kocharovskaya, L.M. Narducci, M.O. Scully, S.Y. Zhu and M.S. Doss**, *Two Mechanisms For Inversionless Amplification In Four-Level Atoms With Raman Pumping*, Phys. Rev. A 48 , 3196 (1993).

- [119] **P. Mandel and O. Kocharovskaya**, *Inversionless Amplification In A Multilevel System*, Phys. Rev. A 47 , 5003 (1993).
- [120] **M.O. Scully, S.H. Zhu and A. Gavriclides**, *Degenerate Quantum Beat Laser: Lasing Without Inversion And Inversion Without Lasing*, Phys. Rev. Lett. 62 , 2813 (1989).
- [121] **P. Mandel and O. Kocharovskaya**, *Inversionless Amplification Of A Monochromatic Field By A Three-Level Medium*, Phys. Rev. A 46 , 2700 (1992).
- [122] **L.M. Narducci, M.O. Scully, C.H. Keitel, S.Y. Zhu and H.M. Doss**, *Physical Origin Of The Gain In A Four-Level Model Of A Raman Driven Laser Without Inversion*, Opt. Commun. 86 , 324 (1991).
- [123] **A. Karawajczyk, J. Zakrzewski and W. Gawlik**, *Dressed-Atom Model Of Lasing Without Inversion In The Double- Λ Configuration*, Phys. Rev. A 45 , 420 (1992).
- [124] **Z.F. Luo and Z.Z. Xu**, *Lasing Without Inversion And Coherence In Dressed States*, Phys. Rev. A 45 , 8292 (1992).
- [125] **A.S. Manka, C.H. Keitel, S.Y. Zhu, M. Fleischhauer, L.M. Narducci and M.O. Scully**, *Quantum Theory Of Laser Emission From Driven Three-Level Atoms*, Opt. Commun 94 , 174 (1992).
- [126] **S.E. Harris and J.J. Macklin**, *Lasers Without Inversion: Single Atom Transient Response*, Phys. Rev. A 40 , 4135 (1989).
- [127] **A. Imamoglu, J.E. Field and S.E. Harris**, *Lasers Without Inversion: A Closed Lifetime Broadened System*, Phys. Rev. Lett. 66 , 1154 (1991).
- [128] **G.B. Prasad and G.S. Agarwal**, *Light Amplification By Coherence Effects - A Double Resonance Model For Lasers Without Inversion*, Opt. Commun. 86 , 409 (1991).

- [129] **M. Fleischhauer, C.H. Keitel, L.M. Narducci, M.O. Scully, S.Y. Zhu and M.S. Zubairy**, *Lasing Without Inversion: Interference Of Radiatively Broadened Resonances In Dressed Atomic Systems*, *Opt. Commun.* 94, 599 (1992).
- [130] **Y. Zhu**, *Lasing Without Inversion In A Closed Three-Level System*, *Phys. Rev. A* 45, R6149 (1992).
- [131] **Y. Zhu, O.C. Mullins and M. Xiao**, *Inversionless Laser From A Closed Multilevel System*, *Phys. Rev. A* 47, 602 (1993).
- [132] **J. Gao, C. Guo, X. Guo, G. Jin, P. Wang, J. Zhao, H. Zhang, Y. Jiang, D. Wang and D. Jiang**, *Observation Of Light Amplification Without Population Inversion In Sodium*, *Opt. Commun* 93, 323 (1992).
- [133] **H.M. Doss, L.M. Narducci, M.O. Scully and J. Gao**, *Theoretical Analysis Of A Four-Level Laser Without Inversion Driven By A Pulsed Raman Field*, *Opt. Commun.* 95, 57 (1993).
- [134] **J.Y. Gao, H.Z. Zhang, H.F. Cui, X.Z. Guo, Y. Jiang, Q.W. Wang, G.X. Jin and J.S. Li**, *Inversionless Light Amplification In Sodium*, *Opt. Commun.* 110, 590 (1994).
- [135] **A. Nottelmann, C. Peters and W. Lange**, *Inversionless Amplification Of Picosecond Pulses Due To Zeeman Coherences*, *Phys. Rev. Lett.* 70, 1783 (1993).
- [136] **E.S. Fry, X. Li, D. Nikonov, G.G. Padmabandu, M.O. Scully, A.V. Smith, F.K. Tittel, C. Wang, S.R. Wilkinson and S.Y. Zhu**, *Atomic Coherence Effects Within The Sodium D_1 Line: Lasing Without Inversion Via Population Trapping*, *Phys. Rev. Lett.* 70, 3235 (1993).
- [137] **W.E. van der Veer, R.J.J. van Diest and A. Dönszelmann**, *Experimental Demonstration Of Light Amplification Without Population Inversion*, *Phys. Rev. Lett.* 70, 3243 (1993).

- [138] **Y. Zhu, A.I. Rubiera and M. Xiao**, *Inversionless Lasing And Photon Statistics In A V-type Atomic System*, Phys. Rev. A 53 , 1065 (1996).
- [139] **Y. Zhu**, *Lasing Without Inversion In A V-type System: Transient And Steady-State Analysis*, Phys. Rev. A 53 , 2742 (1996).
- [140] **J.A. Kleinfeld and A.D. Streater**, *Observation Of Gain Due To Coherence Effects In A Potassium-Helium Mixture*, Phys. Rev. A 49 , R4301 (1994).
- [141] **J.A. Kleinfeld and A.D. Streater**, *Gain And Coherence Effects Induced By Strong cw-Laser Coupling In Potassium-Rare-Gas Mixtures*, Phys. Rev. A 53 , 1839 (1996).
- [142] **A.S. Zibrov, M.D. Lukin, D.E. Nikonov, L. Hollberg, M.O. Scully, V.L. Velichansky and H.G. Robinson**, *Experimental Demonstration Of Laser Oscillation Without Population Inversion Via Quantum Interference In Rb*, Phys. Rev. 75 , 1499 (1995).
- [143] **G.G. Padmabandu, G.R. Welch, I.N. Shubin, E.S. Fry, D.E. Nikonov, M.D. Lukin and M.O. Scully**, *Laser Oscillation Without Population Inversion In A Sodium Atomic Beam*, Phys. Rev. Lett. 76 , 2053 (1996).
- [144] **P.B. Sellin, G.A. Wilson, K.K. Meduri and T.W. Mossberg**, *Observation Of Inversionless Gain And Field-Assisted Lasing In A Nearly Ideal Three-Level Cascade-Type Atomic System*, Phys. Rev. A 54 , 2402 (1996).

Chapter 2

Theoretical Modelling Of Atomic Coherence Effects

In this chapter two methods of developing three level atomic models are introduced. The first is a state amplitude model which provides fundamental insight into the quantum interference mechanisms involved on a single atom scale. Practically in the laboratory atomic densities up to 10^{17} atoms m^{-3} are achieved and as such the amplitude model no longer offers the best way of modelling the atomic systems. For these systems density matrix models are employed which prove to be an elegant method for dealing with large ensembles of atoms. Following this introduction to density matrices two sections follow showing how these models predict the presence of quantum coherence effects. The first deals with E.I.T. within three different systems while the second continues this work and considers inversionless gain in two popularly discussed systems. The chapter ends with a brief section discussing Moseley's N level rules which provide an efficient method for directly deriving a system's density matrix without having to carry out a full derivation from first principles.

2.1) Models For Examining A Three Level Atom

2.1.1) A State Amplitude Model

In this section a state amplitude model is outlined which describes the evolution of state amplitudes for the case of a single three level atom subject to two, near-resonant, radiation fields. From these amplitudes the associated probability densities can be readily deduced. This allows inferences to be made about the state populations for a collection of such atoms, the polarisations associated with the atom and hence its effect on the radiation fields themselves. This approach is useful for gaining insight into the origins of absorption, gain, dispersion and particularly E.I.T. as outlined by Dunn [1]. However, such an approach becomes somewhat clumsy when averaging over large numbers of atoms excited at different times, as occurs in real physical situations, or when Doppler broadening is taken into account. In this situation it is more appropriate to work with a density matrix approach, see section 2.1.2. The density matrix is a more powerful computational tool when ensemble averages are involved, however insight is lost in the black-box thereby created. Section 4.2.1 presents some of the results of Dunn's amplitude state model, therefore for completeness an outline of the derivation of this model is presented below.

In Figure 2.1 a schematic outline of a simple three level cascade atom used as the basis of the following model is shown.

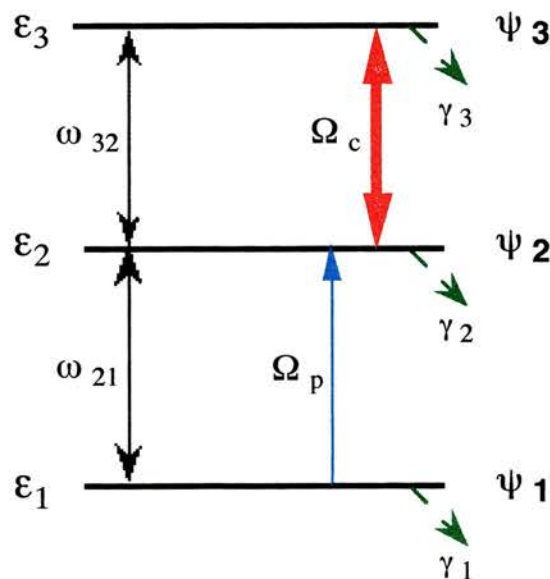


Figure 2.1:- Schematic of the cascade three level atom employed within the state amplitude model.

The three levels have energies ϵ_1 , ϵ_2 and ϵ_3 , associated eigenfunctions ψ_1 , ψ_2 and ψ_3 respectively as well as associated spontaneous decay rates (which decay to levels outside the system not explicitly considered here) γ_1 , γ_2 and γ_3 respectively. The Rabi field strengths of the radiation fields between the two pairs of states are Ω_c for the coupling field (between state $|2\rangle$ and $|3\rangle$) and Ω_p for the probe field (between state $|1\rangle$ and $|2\rangle$).

The quantum mechanical treatment of the atom takes as its starting point the time dependent Schrödinger equation [2].

$$H \Psi(\mathbf{r},t) = i\hbar \frac{\partial \Psi(\mathbf{r},t)}{\partial t} \quad (2.1)$$

Here $\Psi(\mathbf{r},t)$ is the overall wavefunction of the atom and H the Hamiltonian of the system. The Hamiltonian, H , is made up of two components, namely that associated with the isolated atom, but including the phenomenological damping introduced through the population decay rates, and that describing the additional energy of the atom as a result of the interaction with the two time-varying radiation fields. The latter is treated in terms of the electric dipole approximation. The total Hamiltonian is then given by :

$$H = H_0 + exE_p \cos(\omega_p t) + exE_c \cos(\omega_c t) \quad (2.2)$$

where ω_p and ω_c are the angular frequencies and E_p and E_c the electric field amplitudes of the probe radiation field and the coupling radiation field respectively, e is the electronic charge and x the (generalised) position of the electron in the atom.

In this approach the wavefunction of the atom subject to the radiation fields is written in terms of the unperturbed eigenfunctions, but where the associated coefficients are allowed to be time-dependent namely:

$$\Psi(\mathbf{r},t) = a_1(t) \psi_1 + a_2(t) \psi_2 \exp(-i\omega_{21}t) + a_3(t) \psi_3 \exp(-i\omega_{31}t) \quad (2.3)$$

where ω_{21} and ω_{31} are the angular frequencies of the resonant transitions. By employing the procedure outlined below the time evolution of the state amplitudes of this model can be found :

- The above expressions for the Hamiltonian, H given by equation (2.2), and the wavefunction, $\Psi(\mathbf{r},t)$ given by equation (2.3), are substituted into the time dependent Schrödinger equation, equation (2.1).
- Employing the orthonormality properties of the basis set. i.e.

$$\langle \psi_i | \psi_i^* \rangle = \int_{-\infty}^{\infty} \psi_i \psi_i^* d\tau = 1 \quad (2.4)$$

$$\langle \psi_i | \psi_j^* \rangle = \int_{-\infty}^{\infty} \psi_i \psi_j^* d\tau = 0 \quad (2.5)$$

allows three coupled time-dependent equations for $a_1(t)$, $a_2(t)$ and $a_3(t)$ to be recovered by multiplying the resultant equation by ψ_1^* , ψ_2^* and ψ_3^* respectively, and then integrating over the whole of space.

- For his model Dunn invokes the rotating wave approximation [2, 3] which allows the effects of high frequency terms to be neglected. A further assumption is that the two radiation fields are on exact resonance with their associated transitions, i.e. $\omega_p = \omega_{21}$ and $\omega_c = \omega_{32}$. These assumptions provide a simplified form of the equations obtained for $a_1(t)$, $a_2(t)$ and $a_3(t)$ but are adequate for the purpose of examining the fundamental nature of E.I.T. It is reasonably straight forward to generalise the expressions obtained to the non-resonant case [4, 5], although not done so here.

The three coupled equations, obtained by the method outlined above, describing the state amplitudes $a_1(t)$, $a_2(t)$ and $a_3(t)$ are given below:

$$\dot{a}_1 = -i\Omega_p a_2 - \gamma_1 a_1 \quad (2.6)$$

$$\dot{a}_2 = -i\Omega_p a_1 - i\Omega_c a_3 - \gamma_2 a_2 \quad (2.7)$$

$$\dot{a}_3 = -i\Omega_c a_2 - \gamma_3 a_3 \quad (2.8)$$

where

$$\Omega_p = \frac{\mu_{12} E_p}{2\hbar} \quad (2.9)$$

$$\Omega_c = \frac{\mu_{23} E_c}{2\hbar} \quad (2.10)$$

are half-Rabi frequencies for the probe and coupling field transitions respectively. μ_{12} and μ_{23} are the associated dipole matrix elements for the two transitions.

These three coupled equations are the basis of the discussion of Section 4.2.1. Although physically meaningful analytical solutions of the above equations are not possible, it is reasonably straight forward to solve them numerically for the situations of interest. This was carried out by Dunn and some of these results are presented in Section 4.2.1. In addition to the requirement to follow the time evolution of the state amplitudes of the three level atom, equations (2.6) - (2.8), it is also useful to describe the influence of the atom on the two radiation fields. This is achieved by way of the associated polarisation terms defined as:

$$P_p = \mu_{12} \int_{-\infty}^t a_1^*(t, t_0) a_2(t, t_0) dt_0 \quad (2.11)$$

$$P_c = \mu_{23} \int_{-\infty}^t a_2^*(t, t_0) a_3(t, t_0) dt_0 \quad (2.12)$$

where the associated absorption or gain is given by $\text{Im}(P)/\epsilon_0 E$.

2.1.2) A Semiclassical Density Matrix Formulation Of Quantum Mechanics

2.1.2.1) Introducing Density Matrices And The Liouville Equation

Moving from a single atom model to one which deals with a large ensemble of atoms, as found in a Doppler broadened medium, requires a more elegant mathematical formalism than the previously presented state amplitude model. Large scale atomic coherence and quantum interference effects such as electromagnetically-induced transparency, and related topics, can be modelled semiclassically, using density matrix theory [6, 7, 8]. The density matrix formalism is a method of computing expectation values of operators in cases where the precise wavefunction is unknown. A brief introduction of the density matrix formalism and notation is presented below. A full discussion can be obtained from one of the above referenced texts.

Consider the atomic wavefunction defined as a superposition of a basis set, $\psi_n(\mathbf{r}, t)$, usually the unperturbed states of an isolated atom, weighted by the probability amplitudes of each element of the basis set, $a_n(t)$:

$$\Psi(\mathbf{r}, t) = \sum_n a_n(t) \psi_n(\mathbf{r}, t) \quad (2.13)$$

The density matrix elements, ρ_{nm} , are bilinear combinations of these weighted probability amplitudes, hence are observables defined as:

$$\rho_{nm} = \overline{a_m^* a_n} \quad (2.14)$$

where the type of averaging indicated above by a bar is what is known as the ensemble average. It follows from equation (2.14) that $\rho_{nm} = \rho_{mn}^*$ and so by definition ρ is an Hermitian matrix. Another important result is the trace normalisation condition:

$$\text{tr}(\rho) \equiv \sum_k \rho_{kk} = \sum_k a_k^* a_k = 1 \quad (2.15)$$

which follows directly from the normalisation condition of $\Psi(\mathbf{r}, t)$, in equation 2.13.

The wavefunction of each system in the ensemble satisfies equation 2.1 the time dependent Schrödinger equation. This is the starting point in the derivation of the Liouville equation [6, 8], which describes the evolution with time of the density matrix elements:

$$\begin{aligned} \frac{\partial \rho_{ij}}{\partial t} &= -\frac{i}{\hbar} [\hat{H}, \rho]_{ij} \\ &= -\frac{i}{\hbar} \sum_{k=1}^n (H_{ik} \rho_{kj} - \rho_{ik} H_{kj}) \end{aligned} \quad (2.16)$$

In the following three level models the Hamiltonian, \hat{H} , includes an interaction term, H_I , which corresponds to electric dipole interactions induced in the atom by the applied optical fields. Therefore, for an electric dipole transition with matrix elements $\mu_{ij} = \int \psi_i^* H_I \psi_j^* dV$, the Hamiltonian is of the form:

$$\begin{aligned} H &= H_0 + H_I \\ &= H_0 - \mu_{ij} \mathbf{E}(z, t) \end{aligned} \quad (2.17)$$

H^0 again is the free atom Hamiltonian, while the interaction term $H_I = -\hat{\mu}\mathbf{E}(z,t)$.

The array elements comprising the density matrix characterise particular observables. Diagonal elements, ρ_{kk} , represent the average populations of state k , or more precisely they give the average probability of finding an atom, within the ensemble, in state k . The off diagonal elements are termed coherences. They are related to the radiating electric dipoles of the ensemble. Thus, the induced polarisation, $P(t)$, is given by [6]:

$$P(t) = N\mu_{ij}\rho_{ij} \quad (2.18)$$

for an ensemble of N elements. From a macroscopic perspective the polarisation of a medium is related to the electric field via the susceptibility, χ :

$$\begin{aligned} P(t) &= \epsilon_0 \chi E \\ &= \epsilon_0 (\chi' - i\chi'')E \end{aligned} \quad (2.19)$$

where ϵ_0 is the permittivity of free space. It can be shown that the real part of χ , χ' , is proportional to the refractive index variation near the resonance, while the imaginary part, χ'' , is related to the absorption (or gain) experienced by the electric field. The overall result of this atomic polarisation is to change the phase delay experienced by the electric field, per unit length, from k to $k + \Delta k$, where:

$$\Delta k = \frac{k\chi'(\omega)}{2n^2} \quad (2.20)$$

as well as to cause the amplitude to vary exponentially with distance according to $\exp(\gamma/2)z$ where z is the distance propagated and:

$$\gamma(\omega) = -\frac{k\chi''(\omega)}{n^2} \quad (2.21)$$

where n is the index of refraction far from resonance. Equating (2.18) and (2.19) relates the density matrix to the susceptibility such that :

$$\chi'(\omega) = \frac{2N\mu_{ij}^2 \text{Re}(\rho_{ij})}{\epsilon_0 \hbar \Omega_R} \quad (2.22)$$

and

$$\chi''(\omega) = -\frac{2N\mu_{ij}^2}{\epsilon_0\hbar} \frac{\text{Im}(\rho_{ij})}{\Omega_R} \quad (2.23)$$

where $\Omega_R = \mu_{ij}E/2\hbar$, again is the Rabi frequency induced by the optical field [2]. It should be noted that this definition of Rabi frequency is actually half of the normal definition employed by most authors. The reason for choosing this definition is that it greatly simplifies the form of the density matrices outlined later in this chapter. In the following numerical models doubling the input Rabi frequency restores the consistency between experiment and theory.

The main interest of this work is in the use of continuous wave lasers to experimentally study the coherent effects induced in an atom. Thus, using the density matrix formalism, an analysis of the steady state condition can be carried out, in a similar fashion to that done by Brewer and Hahn [9]. Their cascade system is solved analytically, leading to very complex solutions. These solutions do not take into account the effects of Doppler broadening which must be added numerically. Therefore, the following systems are solved by totally numerical means, incorporating Doppler broadening by integrating over the Doppler profile.

2.1.2.2) The Addition Of Phenomenological Terms

Population Decay Rates

The use of a density matrix has the advantage over a probability amplitude approach since it allows the simple addition of phenomenological terms. These terms are introduced to account for decay, dephasing or incoherent pump mechanisms, which occur within the system. Decay phenomena are added by appending a term of the form $-\Gamma_{ji} \rho_{jj}$ to the diagonal elements to describe spontaneous emission out of level j . A corresponding positive term is then added to the receiving level i , if that level lies within the system of study, such that equation (2.16) now takes the forms :

$$\frac{\partial \rho_{jj}}{\partial t} = -\frac{i}{\hbar} [\hat{H}, \rho]_{jj} - \Gamma_{ji} (\rho_{jj} - \rho_{jj}^0) \quad (2.24a)$$

$$\frac{\partial \rho_{ii}}{\delta t} = -\frac{i}{\hbar} [\hat{H}, \rho]_{ii} + \Gamma_{ji} (\rho_{ij} - \rho_{ij}^0) \quad (2.24b)$$

where Γ_{ji} is the decay rate and ρ_{ij}^0 is the thermal equilibrium value of the density matrix elements given by:

$$\rho_{ij}^0 = \frac{\exp\left(-\frac{H_{ij}^0}{k_B T}\right)}{\text{tr}\left[\exp\left(-\frac{H^0}{k_B T}\right)\right]} \quad (2.25)$$

where k_B is Boltzmann's constant, T the temperature in Kelvin and H^0 the free atom Hamiltonian i.e. the Hamiltonian that describes the atom in the absence of any applied optical fields.

Coherence Dephasing Rates

Off-diagonal density matrix elements also decay towards thermal equilibrium values at rates given by :

$$\gamma_{ij} = \frac{1}{2}(\Gamma_{ii} + \Gamma_{jj}) + \gamma_{\text{deph}} \quad (2.26)$$

where γ_{deph} takes account of the macroscopic dephasing rates due to collisions that act on the system without causing important population decay [10, 11]. The rule of thumb for establishing the Γ_{ii} terms is that any spontaneous population decay rate that removes population from either level i or j contributes half its value to the coherence dephasing rate γ_{ij} on that particular transition. Population decay rates which add to the population in either level i or j have no contribution to the coherence dephasing rate γ_{ij} . With these terms in mind the coherence dephasing rate on an atomic transition is accounted for by adding the correct form of equation (2.26) to the appropriate Liouville equation.

Incoherent Pump Rates

Incoherent pumps such as discharges or flashlamps can also be incorporated into the density matrix model by adding phenomenological terms to the Liouville equation. These terms are mainly present when inversionless lasing systems are being considered since it is required that a small amount of population is put into the upper lasing level. Conceptually, it is simpler to employ incoherent pump sources than coherent sources. However, as will be discussed briefly in Section 2.3 and in more detail in Chapter 8, incoherent pumps would appear to be the more practical solution as well, since the addition of coherent pump sources act to destroy the coherences already present in the system. Incoherent pump terms can be added to the Liouville equation in two different forms.

The first form considers the effect of excitation by collisions induced in a discharge. These are accounted for by the addition of terms which remove population from the lower level of excitation and adds it to the upper level in a non-reversible manner. Consider the incoherent excitation of population from level $|1\rangle$ to level $|2\rangle$. The related Liouville equation must be altered such that:

$$\frac{\partial \rho_{11}}{\delta t} = -\frac{i}{\hbar} [\hat{H}, \rho]_{11} - \Pi_{12} \rho_{11} \quad (2.27a)$$

$$\frac{\partial \rho_{22}}{\delta t} = -\frac{i}{\hbar} [\hat{H}, \rho]_{22} + \Pi_{12} \rho_{11} \quad (2.27b)$$

where Π_{12} is the incoherent pump rate. For excitation via a thermal incoherent radiation bath, transitions can be stimulated in both directions and so the terms become:

$$\frac{\partial \rho_{11}}{\delta t} = -\frac{i}{\hbar} [\hat{H}, \rho]_{11} + R_{12}(\rho_{22} - \rho_{11}) \quad (2.28a)$$

$$\frac{\partial \rho_{22}}{\delta t} = -\frac{i}{\hbar} [\hat{H}, \rho]_{22} - R_{12}(\rho_{22} - \rho_{11}) \quad (2.28b)$$

where R_{12} is related to the incoherent radiation intensity. It should be noted that the dephasing between the levels is raised by the introduction of incoherent pumps. To account for this an additional $R_{12} / 2$ term must be added to the coherence dephasing rates each time either component of the incoherent pump rate's index appears in the

index of the coherence dephasing rate. i.e. for this particular system $R_{12} / 2$ should be added to both the γ_{23} and γ_{13} coherence dephasing rates, due to the presence of the 2 and then the 1 respectively in the indices of the coherence dephasing rates. However a full R_{12} term should be added to the γ_{12} coherence dephasing rate, once for each component of the “12” index.

2.2) Employment Of Density Matrix Models

2.2.1) The Cascade Configuration

Consider the three level model shown in Figure 2.2, which is closed with regard to the atomic basis set, that is, the lifetime broadening occurs by radiative decay to other states within the same system. Two optical fields, at angular frequencies ω_p (the probe field) and ω_c (the coupling field), are near resonant with the transitions at ω_{12} and ω_{23} respectively. They are assumed to be sufficiently separate such that only one field interacts with each transition.

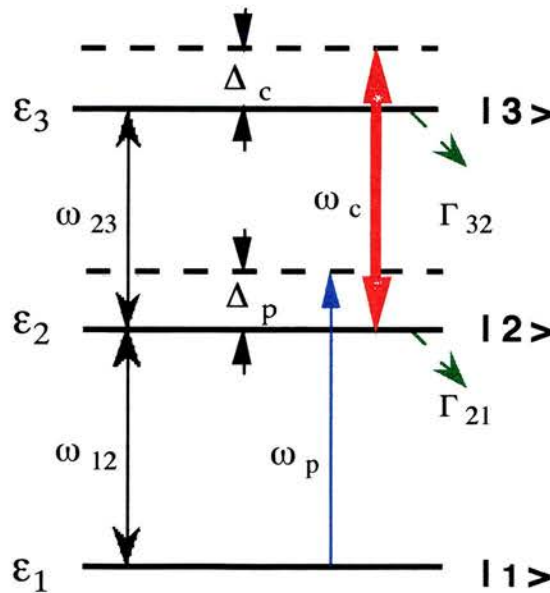


Figure 2.2: Schematic of a closed cascade three level atom.

Level $|3\rangle$ decays at a rate Γ_{32} to level $|2\rangle$ which, in turn decays to level $|1\rangle$ at rate Γ_{21} . The derivation employed here assumes that the Rabi frequencies involved are much smaller than the corresponding laser frequencies. Atomic selection rules require that transitions $|1\rangle - |2\rangle$ and $|2\rangle - |3\rangle$ are dipole allowed whereas, transition $|1\rangle - |3\rangle$ is dipole forbidden. Therefore, not all the matrix elements of $\hat{\mu}$ can have non-zero values in the electric dipole approximation. For the cascade system we have:

$$\mu_{12} = \langle 1|\mu|2\rangle \neq 0 = \mu_{21} \quad (2.29a)$$

$$\mu_{23} = \langle 2|\mu|3\rangle \neq 0 = \mu_{32} \quad (2.29b)$$

$$\mu_{13} = \langle 1|\mu|3\rangle = 0 = \mu_{31} \quad (2.29c)$$

The electric fields are defined as:

$$E_j(z,t) = \frac{E_j^0}{2} \left\{ \exp\left[i(\omega_j t - k_j z)\right] + \text{c.c.} \right\} \quad \text{for } j = p, c \quad (2.30)$$

and the respective Rabi frequencies are given by:

$$\Omega_p = \frac{\mu_{12} E_p^0}{2\hbar} \quad (2.31a)$$

$$\Omega_c = \frac{\mu_{23} E_c^0}{2\hbar} \quad (2.31b)$$

The applied optical field frequencies, ω_p and ω_c , have exact detunings from their respective atomic resonances given by:

$$\Delta_p = \omega_p - \omega_{12} - k_p V_z \quad (2.32a)$$

$$\Delta_c = \omega_c - \omega_{23} - k_c V_z \quad (2.32b)$$

where $k_i V_z$ are the Doppler shift contributions to the detuning, caused by an atom moving with a z-component of velocity V_z . It is the steady-state magnitude of the induced atomic dipoles that is of interest, so optical frequency oscillations of ρ_{ij} are removed by the transformations [12]:

$$\rho_{12} = \tilde{\rho}_{12} \exp[i(\omega_p t - k_p z)] \quad (2.33)$$

$$\rho_{23} = \tilde{\rho}_{23} \exp[i(\omega_c t - k_c z)] \quad (2.34)$$

$$\rho_{13} = \tilde{\rho}_{13} \exp[i\{(\omega_p + \omega_c)t - (k_p + k_c)z\}] \quad (2.35)$$

Using the Liouville equation, (2.16), the rates of change of the density matrix elements can be derived, yielding nine simultaneous equations. Terms oscillating rapidly, at around $2\omega_i$, are removed under the rotating wave approximation [3], since they average to zero for an integration time of anything over a few optical cycles. Thus, the solutions for the cascade system are:

$$\dot{\rho}_{11} = i\Omega_p(\tilde{\rho}_{21} - \tilde{\rho}_{12}) + \Gamma_{21}\rho_{22} \quad (2.36)$$

$$\dot{\rho}_{22} = i\Omega_p(\tilde{\rho}_{12} - \tilde{\rho}_{21}) + i\Omega_c(\tilde{\rho}_{32} - \tilde{\rho}_{23}) - \Gamma_{21}\rho_{22} + \Gamma_{32}\rho_{33} \quad (2.37)$$

$$\dot{\rho}_{33} = i\Omega_c(\tilde{\rho}_{23} - \tilde{\rho}_{32}) - \Gamma_{32}\rho_{33} \quad (2.38)$$

$$\dot{\tilde{\rho}}_{12} = -i(\Delta_p - i\gamma_{12})\tilde{\rho}_{12} + i\Omega_p(\rho_{22} - \rho_{11}) - i\Omega_c\tilde{\rho}_{13} \quad (2.39)$$

$$\dot{\tilde{\rho}}_{23} = -i(\Delta_c - i\gamma_{23})\tilde{\rho}_{23} + i\Omega_c(\rho_{33} - \rho_{22}) + i\Omega_p\tilde{\rho}_{13} \quad (2.40)$$

$$\dot{\tilde{\rho}}_{13} = -i(\Delta_p + \Delta_c - i\gamma_{13})\tilde{\rho}_{13} + i\Omega_p\tilde{\rho}_{23} - i\Omega_c\tilde{\rho}_{12} \quad (2.41)$$

These along with the complex conjugates of (2.39), (2.40) and (2.41) completely describe the final state of the density matrix. For ease of calculation it is convenient to convert the six complex equations above into nine real simultaneous equations. This is done by defining:

$$\tilde{\rho}_{ij} = \rho_{ij}^r + i\rho_{ij}^i \quad (2.42a)$$

and

$$\tilde{\rho}_{ij}^* = \rho_{ij}^r - i\rho_{ij}^i \quad (2.42b)$$

where $\rho_{ij}^r = \text{Re}(\tilde{\rho}_{ij})$ and $\rho_{ij}^i = \text{Im}(\tilde{\rho}_{ij})$. Population conservation, however, implies the trace normalisation:

$$\rho_{11} + \rho_{22} + \rho_{33} = 1 \quad (2.43)$$

This removes one degree of freedom from the system. Hence, in the steady-state, all the time derivatives may be set equal to zero and the system can be represented in matrix form $\mathbf{A}\underline{x} = \underline{b}$, shown by Matrix 2.1.

Matrix 2.1: *A closed three level cascade system.*

$$\begin{bmatrix}
 -\Gamma_{21} & \Gamma_{32} & 0 & 0 & 0 & -2\Omega_p & 0 & 2\Omega_c \\
 0 & -\Gamma_{32} & 0 & 0 & 0 & 0 & 0 & -2\Omega_c \\
 0 & 0 & \gamma_{12} & 0 & 0 & -\Delta_p & -\Omega_c & 0 \\
 0 & 0 & 0 & \gamma_{13} & 0 & -\Omega_c & -(\Delta_p + \Delta_c) & \Omega_p \\
 0 & 0 & 0 & 0 & \gamma_{23} & 0 & \Omega_p & -\Delta_p \\
 -2\Omega_p & -\Omega_p & \Delta_p & \Omega_c & 0 & \gamma_{12} & 0 & 0 \\
 0 & 0 & \Omega_c & (\Delta_p + \Delta_c) & -\Omega_p & 0 & \gamma_{13} & 0 \\
 \Omega_c & -\Omega_c & 0 & -\Omega_p & \Delta_c & 0 & 0 & \gamma_{23}
 \end{bmatrix}
 \begin{bmatrix}
 \rho_{22} \\
 \rho_{33} \\
 \rho_{12}^r \\
 \rho_{13}^r \\
 \rho_{23}^r \\
 \rho_{12}^i \\
 \rho_{13}^i \\
 \rho_{23}^i
 \end{bmatrix}
 =
 \begin{bmatrix}
 0 \\
 0 \\
 0 \\
 0 \\
 0 \\
 -\Omega_p \\
 0 \\
 0
 \end{bmatrix}$$

The detunings experienced by an atom are changed by the Doppler shift associated with its motion. The velocity distribution is assumed Maxwellian giving the fraction of atoms whose z component of velocity lies between V_z and $V_z + dV_z$ as:

$$f(V_z) = \frac{\exp\left(\frac{-V_z}{u}\right)}{\sqrt{\pi}} \frac{dV_z}{u} \quad (2.44)$$

where $u \equiv \left(\frac{2k_B T}{M}\right)^{1/2}$

and k_B is Boltzmann's constant, T the temperature in Kelvin and M the atomic mass. Therefore for each density matrix element we must integrate over the velocity distribution via:

$$\bar{\rho}_{ij} = \int_{-\infty}^{\infty} f(V_z) \rho_{ij}(V_z) dV_z \quad (2.45)$$

2.2.1.1) Implementation Of A Density Matrix Model

The implementation of the density matrix models was carried out in two different environments. Initially a solution to the above matrix was carried out on SPARC workstations with the algorithms coded in Fortran 77. The basic algorithm is outlined below :

Algorithm 1: *Fortran 77 implemented on SPARC workstations.*

- .1 Initialise values for Ω_i , Γ_{ji} , γ_{ij} , λ_i , Δ_c , T etc.
- .2 Calculate the thermal constant term u.
- .3 Loop over probe field detuning from $-\Delta_p$ to Δ_p in small steps.
 - .3.1 Loop over velocity groups from -v to v in small steps.
 - .3.1.1 Initialise matrix elements to zero.
 - .3.1.2 Calculate Maxwell-Boltzmann integration correction term
 - .3.1.3 Calculate the Doppler modified detuning values.
 - .3.1.4 Enter the non-zero matrix elements i.e. elements of **A** and **b**.
 - .3.1.5 Solve the matrix system repeatedly using LU factorisation with partial pivoting, and iterative refinement of **A** [13].
 - .3.1.6 Update velocity dependent arrays for the relevant parameters. This involves reading in the calculated value of \underline{x} from the previous step, multiplied by the appropriate Maxwell-Boltzmann integration correction term.
 - .3.2 Increment velocity v.
 - .3.3 Integrate the velocity dependent arrays of 3.1.6 over all group velocities in order to account for Doppler broadening. Integration is carried out using a third-order finite difference formulae with error estimates according to a method outlined by Gill and Miller [14].

.4 Increment probe field detuning Δ_p .

.5 End program.

This algorithm was capable of calculating a probe field scan of one thousand data points including the integration over one thousand velocity points for each probe detuning in a time of around ninety minutes. This is obviously very time consuming and so full calculations were usually only implemented when presentation quality results were required. On a daily basis, less accurate (hence less smooth) curves could be tolerated and so faster processing times were achieved. A good initial picture of a new system could be obtained in the homogeneous regime, where Doppler broadening effects were neglected. This reduced the running time of the model to less than a minute. To achieve similar, but not identical, Doppler broadened curves required inclusion of all the steps of Algorithm 1, increasing the coupling field Rabi frequencies and extra computer time as previously discussed.

These time constraints became more and more of a problematic feature as systems of greater complexity were studied i.e. four atomic levels and three optical fields. For this reason a second solution involving Power Macintosh workstations running Mathematica 2.2 was employed to decrease the running times of these density matrix models. Mathematica is a general computer software system and language which allows numerical, symbolic and graphical calculations to be carried out [15]. It is the fact that Mathematica handles symbolic calculations which is the key to its ability to dramatically reduce the running time of a density matrix calculation. The solution algorithm can then be modified, see Algorithm 2, such that the probe field detuning loop (Step .3 of Algorithm 1) can be simplified, dramatically reducing the running time. This is achieved because the step involving the LU factorisation, which is calculated at every numerical velocity value v , is effectively replaced with a single step which involves one inversion of a matrix (usually 8×8), while retaining v as an algebraic term within the optical field detuning terms.

Algorithm 2: *Mathematica 2.2 implemented on Power Macintosh workstations.*

- .1 Initialise values for $\Omega_i, \Gamma_{ji}, \gamma_{ij}, \lambda_i, \Delta_c, T$ etc.
- .2 Calculate the thermal constant term u and the Maxwell-Boltzmann integration correction term.
- .3 Input the density matrix elements, \mathbf{A} , and the solution vector elements, \underline{b} such that matrix equation $\mathbf{A}\underline{x} = \underline{b}$ can be solved.
- .4 Find the inverse of matrix \mathbf{A} (all numerical values except the homogeneous probe field detuning term and the velocity v within the Doppler shifted detuning terms) such that the matrix equation can be solved for \underline{x} i.e. $\underline{x} = \mathbf{A}^{-1} \underline{b}$
- .5 Set up the group velocity array to go from $-v$ to v in small steps
- .6 Select relevant density matrix element of \underline{x} and loop over homogeneous probe field detuning in small steps.
 - .6.1 Employ Simpson's Rule to integrate density matrix element over all group velocities.
- .7 Plot density matrix element or else put into a form which can be exported to KaleidaGraph.
- .8 End program.

Moving from Algorithm 1 to 2 decreased the running time of the most accurate calculations by around a factor of ten i.e. to about ten to fifteen minutes. Homogeneous calculations now execute in a matter of seconds rather than minutes. These dramatic time improvements enabled more complicated systems (15x15) to be examined in detail, see the work of Section 2.3 and Chapter 8.

Figure 2.3 shows the imaginary and real components of ρ_{12} , for a coupling field strength of 160 MHz, as a function of probe field detuning. These components correspond to the relative absorption and refractive index experienced by the probe field, respectively. An electromagnetically-induced transparency feature can clearly be

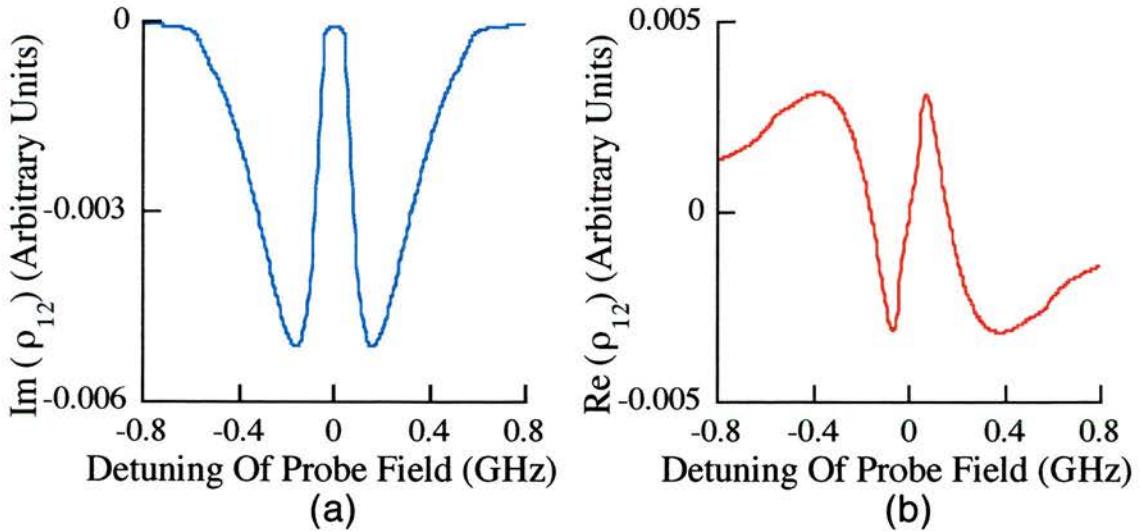


Figure 2.3: (a) Imaginary and (b) Real components of ρ_{12} (probe field) for an ideal closed cascade system, incorporating the effects of Doppler broadening, with coupling field and probe field strengths of 160 MHz and 1 MHz respectively.

2.2.2) The Lambda Configuration

Consider now the three level model shown in Figure 2.4, which is in the so called lambda (Λ) configuration. The system is again presumed to be closed with regards to the atomic basis set. In this system two optical fields at angular frequencies ω_p (the probe field) and ω_c (the coupling field), are near resonant with the transitions at ω_{13} and ω_{23} respectively. Again, they are assumed to be sufficiently different in frequency such that only one field interacts with each transition. Level $|3\rangle$ decays to both level $|1\rangle$ and level $|2\rangle$ at the rates Γ_{31} and Γ_{32} , respectively. The atomic selection rules are such that the dipole allowed transitions are now $|1\rangle - |3\rangle$ and $|2\rangle - |3\rangle$ and the dipole forbidden transition is $|1\rangle - |2\rangle$.

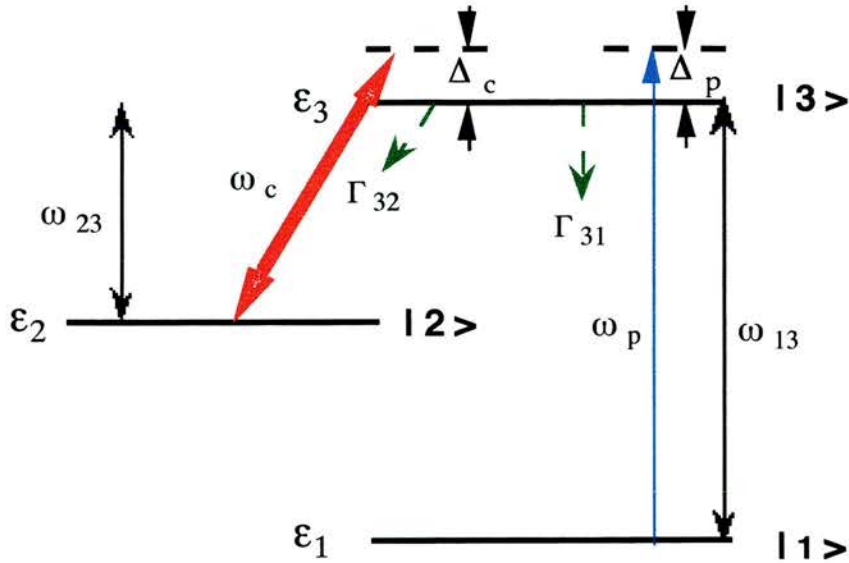


Figure 2.4: Schematic of a closed lambda three level atom.

Thus, for this configuration it is required that the dipole matrix elements, μ_{ij} , take the following values:

$$\mu_{12} = \langle 1 | \mu | 2 \rangle = 0 = \mu_{21} \quad (2.46a)$$

$$\mu_{23} = \langle 2 | \mu | 3 \rangle \neq 0 = \mu_{32} \quad (2.46b)$$

$$\mu_{13} = \langle 1 | \mu | 3 \rangle \neq 0 = \mu_{31} \quad (2.46c)$$

This system has been the source of much study in the atomic coherence effects of E.I.T. and inversionless lasing since in its ideal form, where level $|2\rangle$ is assumed metastable, the population decay rate Γ_{21} , and hence the coherence dephasing rate γ_{12} , are both approximately equal to zero. The same density matrix derivation is employed for the lambda configuration as was previously used for the cascade configuration, resulting in the matrix system represented by Matrix 2.2. The detunings experienced by an atom again change due to the Doppler shift associated with its motion, thus, using equations (2.44) and (2.45), the matrix system is again solved numerically. Figure 2.5 shows the real and imaginary components of ρ_{13} , for a coupling field strength of 160 MHz, in this lambda system.

Matrix 2.2: A closed three level lambda system.

$$\begin{bmatrix} 0 & -\Gamma_{32} & 0 & 0 & 0 & 0 & 0 & -2\Omega_c \\ 0 & (\Gamma_{32} + \Gamma_{31}) & 0 & 0 & 0 & 0 & 2\Omega_p & 2\Omega_c \\ 0 & 0 & \gamma_{12} & 0 & 0 & \Delta_c - \Delta_p & -\Omega_c & -\Omega_p \\ 0 & 0 & 0 & \gamma_{13} & 0 & -\Omega_c & -\Delta_p & 0 \\ 0 & 0 & 0 & 0 & \gamma_{23} & \Omega_p & 0 & -\Delta_c \\ 0 & 0 & \Delta_p - \Delta_c & \Omega_c & -\Omega_p & \gamma_{12} & 0 & 0 \\ -\Omega_p & -2\Omega_p & \Omega_c & \Delta_p & 0 & 0 & \gamma_{13} & 0 \\ \Omega_c & -\Omega_c & \Omega_p & 0 & \Delta_c & 0 & 0 & \gamma_{23} \end{bmatrix} \begin{bmatrix} \rho_{22} \\ \rho_{33} \\ \rho_{12}^i \\ \rho_{13}^i \\ \rho_{23}^i \\ \rho_{12}^r \\ \rho_{13}^r \\ \rho_{23}^r \end{bmatrix} = \begin{bmatrix} 0 \\ 0 \\ 0 \\ 0 \\ 0 \\ 0 \\ -\Omega_p \\ 0 \end{bmatrix}$$

where

$$\Delta_p = \omega_p - \omega_{13} - k_p V_z \quad (2.47)$$

$$\Omega_p = \frac{\mu_{13} E_p^0}{2\hbar} \quad (2.48)$$

and the remaining symbols represent the previously defined variables

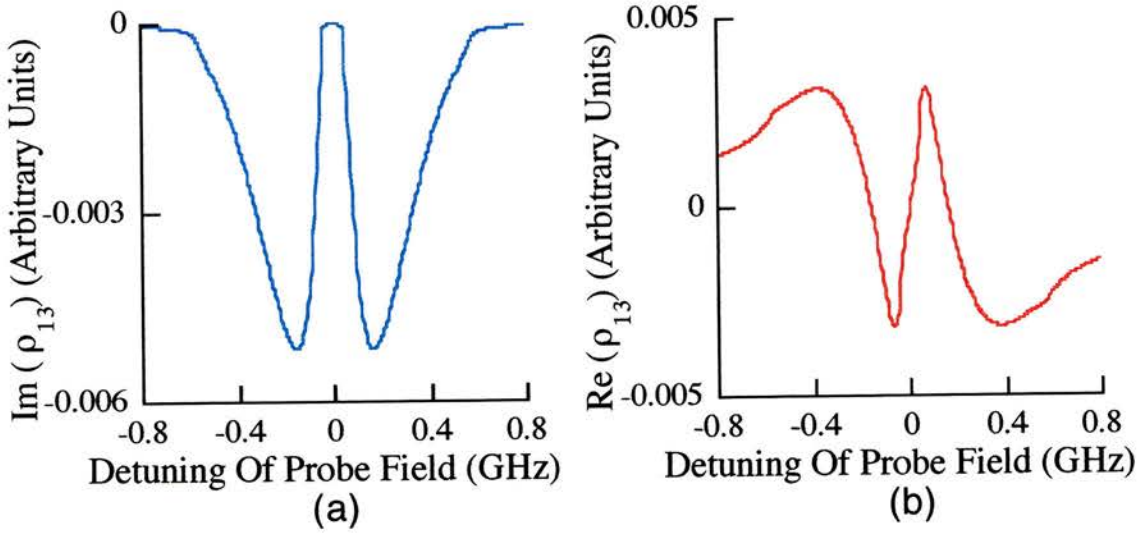


Figure 2.5: (a) Imaginary and (b) Real components of ρ_{13} (probe field) for an ideal closed lambda system, incorporating the effects of Doppler broadening, with coupling field and probe field strengths of 160 MHz and 1 MHz respectively.

Electromagnetically induced transparency can again be seen, shown in the absorption curve (imaginary part of ρ_{13}) of Figure 2.5(a). The refractive index (real part of ρ_{13}) of the probe field is again dramatically altered as it is scanned across the transparency feature. It should be noted that in the strong field regime, where the optical field strengths are greater than the saturation intensities for the various transitions, the lambda system acts in an analogous way to the cascade system and as such much of the mathematics can be transferred directly between the two.

2.2.3) The V-type Configuration

The third closed system that has been modelled is the so called V-type system, shown in Figure 2.6.

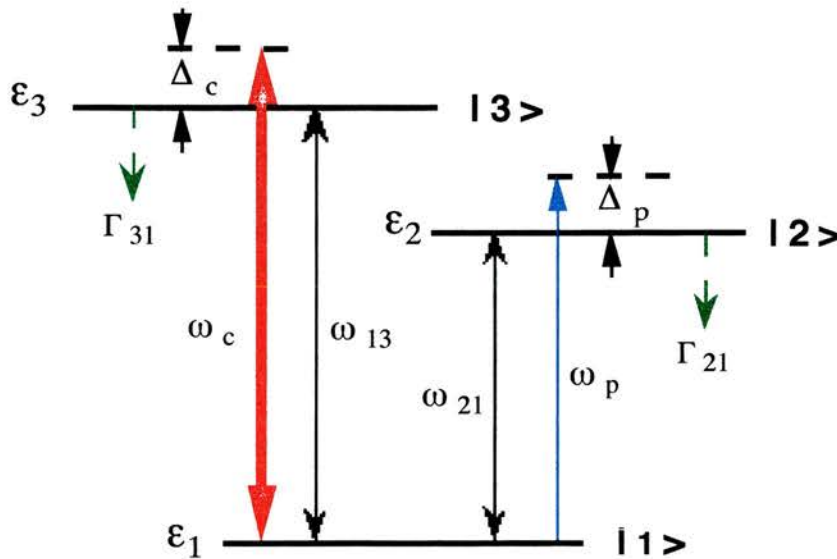


Figure 2.6: Schematic of a closed V-type three level atom.

The V-type system employs two optical fields at angular frequencies ω_p (the probe field) and ω_c (the coupling field), which are near resonant with the transitions at ω_{12} and ω_{13} respectively. Once again, the assumption that the levels are sufficiently frequency separated such that only one field interacts with each transition, is made. Levels $|3\rangle$ and $|2\rangle$ decay at a rates Γ_{31} and Γ_{21} , respectively, to level $|1\rangle$. The dipole allowed transitions for this system are now the $|1\rangle - |2\rangle$ and $|1\rangle - |3\rangle$ transitions and the dipole forbidden transition now being from levels $|2\rangle - |3\rangle$. Atomic selection rules

the dipole forbidden transition now being from levels $|2\rangle - |3\rangle$. Atomic selection rules for this configuration now require that the dipole matrix elements, μ_{ij} , take the following values:

$$\mu_{12} = \langle 1 | \mu | 2 \rangle \neq 0 = \mu_{21} \quad (2.49a)$$

$$\mu_{23} = \langle 2 | \mu | 3 \rangle = 0 = \mu_{32} \quad (2.49b)$$

$$\mu_{13} = \langle 1 | \mu | 3 \rangle \neq 0 = \mu_{31} \quad (2.49c)$$

Again the density matrix derivation is employed, as was used previously for the lambda and cascade systems. The resulting matrix system has the form shown in Matrix 2.3.

Matrix 2.3: *A closed three level V-type system.*

$$\begin{bmatrix} \Gamma_{21} & 0 & 0 & 0 & 0 & 2\Omega_p & 0 & 0 \\ 0 & \Gamma_{31} & 0 & 0 & 0 & 0 & 2\Omega_c & 0 \\ 0 & 0 & \gamma_{12} & 0 & 0 & -\Delta_p & 0 & -\Omega_c \\ 0 & 0 & 0 & \gamma_{13} & 0 & 0 & -\Delta_c & \Omega_p \\ 0 & 0 & 0 & 0 & \gamma_{23} & \Omega_c & \Omega_p & -(\Delta_c - \Delta_p) \\ -2\Omega_p & -\Omega_p & \Delta_p & 0 & -\Omega_c & \gamma_{12} & 0 & 0 \\ -\Omega_c & -2\Omega_c & 0 & \Delta_c & -\Omega_p & 0 & \gamma_{13} & 0 \\ 0 & 0 & \Omega_c & -\Omega_p & (\Delta_c - \Delta_p) & 0 & 0 & \gamma_{23} \end{bmatrix} \begin{bmatrix} \rho_{22} \\ \rho_{33} \\ \rho_{12}^r \\ \rho_{13}^r \\ \rho_{23}^r \\ \rho_{12}^i \\ \rho_{13}^i \\ \rho_{23}^i \end{bmatrix} = \begin{bmatrix} 0 \\ 0 \\ 0 \\ 0 \\ 0 \\ -\Omega_p \\ -\Omega_c \\ 0 \end{bmatrix}$$

where

$$\Delta_c = \omega_c - \omega_{13} - k_c V_z \quad (2.50)$$

$$\Omega_c = \frac{\mu_{13} E_c^0}{2\hbar} \quad (2.51)$$

and the remaining symbols represent the previously defined variables, of the cascade system. Once more the detunings experienced by the atom are altered due to the Doppler shift associated with its motion. Therefore, using equations (2.44) and (2.45), the matrix system is again solved numerically.

Figure 2.7 shows the real and imaginary components of ρ_{12} , for a coupling field strength of 160 MHz, in the V-type system. Once again electromagnetically-induced transparency can be seen in the absorption curve, Figure 2.7(a). The refractive index of the probe field again shows dramatic modulation as it is scanned across the transparency feature.

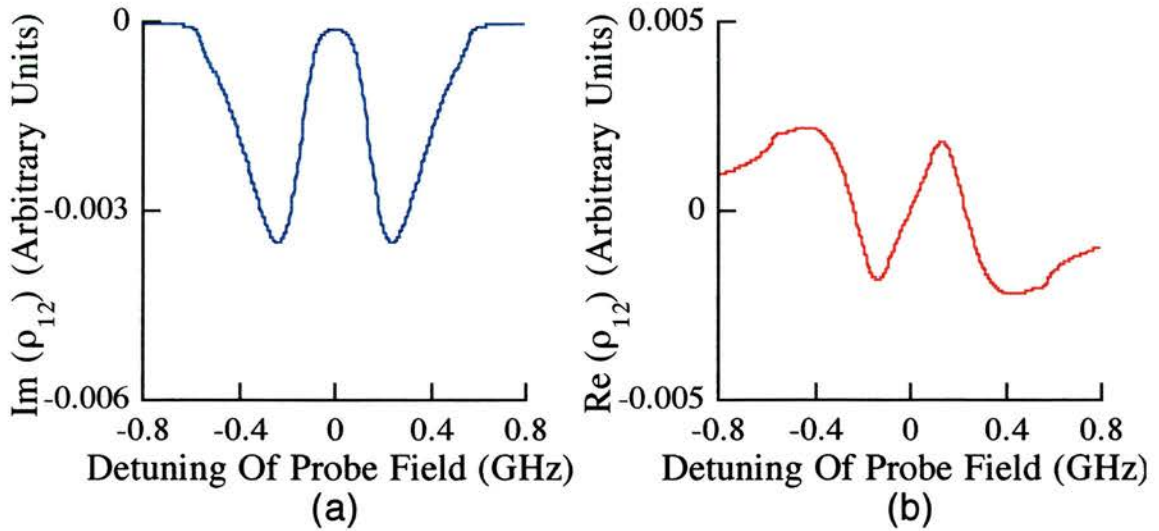


Figure 2.7: (a) Imaginary and (b) Real components of ρ_{12} (probe field) for an ideal closed V-type system, incorporating the effects of Doppler broadening, with coupling field and probe field strengths of 160 MHz and 1 MHz respectively.

2.3) Modelling Atomic Systems For Inversionless Lasing

This section outlines how some of the previously discussed density matrix models can be extended to model inversionless gain systems [16]. Two systems will be discussed in turn. The first is based on the lambda system outlined in Section 2.2.2 and was first discussed theoretically in this way by Imamoglu et. al [17]. The second system discussed presents a theoretical model of the first cw inversionless lasing system to be experimentally observed. This experiment based on atomic rubidium was carried out by Zibrov et al. [18]. The results from this model are used to back up the analysis of Chapter 8 which theoretically presents a new 422 nm inversionless lasing system.

2.3.1) Inversionless Gain In A Three Level Lambda System

A model laser system [17], based on the lambda configuration, can also be studied through the density matrix approach. The proposed laser operates by enhancing the electromagnetically induced interference produced by the presence of a strong coupling field on the $|2\rangle - |3\rangle$ transition, see Figure 2.4. The system is pumped by a thermal incoherent radiation bath, which has a different intensity (temperature) on the $|1\rangle - |3\rangle$ transition than on the $|2\rangle - |3\rangle$ transition. Each transition is spectrally broad compared to the decay rates, the detunings or the Rabi frequencies. The related matrix system for this gain system without a population inversion is given by Matrix 2.4.

Matrix 2.4: A closed lambda system with two incoherent pumps R_{13} and R_{23} employed to produce gain without a population inversion.

$$\begin{bmatrix} R_{23} & -R_{23} - \Gamma_{32} & 0 & 0 & 0 & 0 & 0 & -2\Omega_c \\ R_{13} - R_{23} & \begin{pmatrix} R_{23} + 2R_{13} \\ + \Gamma_{32} + \Gamma_{31} \end{pmatrix} & 0 & 0 & 0 & 0 & 2\Omega_p & 2\Omega_c \\ 0 & 0 & \gamma_{12} & 0 & 0 & \Delta_c - \Delta_p & -\Omega_c & -\Omega_p \\ 0 & 0 & 0 & \gamma_{13} & 0 & -\Omega_c & -\Delta_p & 0 \\ 0 & 0 & 0 & 0 & \gamma_{23} & \Omega_p & 0 & -\Delta_c \\ 0 & 0 & \Delta_p - \Delta_c & \Omega_c & -\Omega_p & \gamma_{12} & 0 & 0 \\ -\Omega_p & -2\Omega_p & \Omega_c & \Delta_p & 0 & 0 & \gamma_{13} & 0 \\ \Omega_c & -\Omega_c & \Omega_p & 0 & \Delta_c & 0 & 0 & \gamma_{23} \end{bmatrix} \begin{bmatrix} \rho_{22} \\ \rho_{33} \\ \rho_{12} \\ \rho_{13} \\ \rho_{23} \\ \rho_{12} \\ \rho_{13} \\ \rho_{23} \end{bmatrix} = \begin{bmatrix} 0 \\ R_{13} \\ 0 \\ 0 \\ 0 \\ 0 \\ -\Omega_p \\ 0 \end{bmatrix}$$

where the pumping rates are defined as:

$$R_{23} \equiv \Gamma_{32} \left\{ \exp\left[\frac{\hbar(\omega_3 - \omega_2)}{k_B T_{23}}\right] - 1 \right\}^{-1} = \Gamma_{32} \bar{n}_{23} \quad (2.52)$$

$$R_{13} \equiv \Gamma_{31} \left\{ \exp\left[\frac{\hbar(\omega_3 - \omega_1)}{k_B T_{13}}\right] - 1 \right\}^{-1} = \Gamma_{31} \bar{n}_{13} \quad (2.53)$$

and T_{23} and T_{13} are the temperatures of the pumping thermal radiation fields at $\omega_3 - \omega_2$ and $\omega_3 - \omega_1$. The terms \bar{n}_{23} and \bar{n}_{13} are the average number of thermal photons per mode at these frequencies.

As outlined by the authors the necessary and sufficient condition for amplification or gain without a population inversion in any atomic basis set is given by the inequality presented below :

$$\frac{\Gamma_{32}}{2\gamma_{12}} > \frac{\Gamma_{31}}{R_{13}} \frac{\Omega_c^2 + \frac{1}{2}R_{23}\gamma_{23}}{\Omega_c^2} > \frac{\Omega_c^2 + \frac{1}{2}(\Gamma_{32} + R_{23})\gamma_{23}}{\Omega_c^2} \quad (2.54)$$

If the first inequality is satisfied then there is net gain within the atomic system the source of which may include a population inversion. However, simultaneously satisfying the second inequality provides proof of the absence of a population inversion thus, any gain present occurs as a direct result of the atomic coherence effects. In Figure 2.8 typical results from this Doppler broadened model are presented where both optical fields are assumed to be in the infrared (~ 780 nm), $\Gamma_{31} = 1$ MHz , $\Gamma_{32} = 100$ MHz and level $|2\rangle$ is assumed metastable such that there is no Γ_{21} spontaneous decay. Figures 2.8(a), (c) and (e) show the absorption experienced by the probe field as a function of probe field detuning. Figures 2.8(b), (d) and (f) represent the corresponding population values within the three level system : ρ_{11} shown as a red solid line; ρ_{22} as a green dashed line; and ρ_{33} as a blue solid line marked with crosses.

Examination of equations (2.52) and (2.53) along with the inequality (2.54) shows that in order to produce inversionless gain it is also necessary that $R_{13}\Gamma_{32} > R_{23}\Gamma_{31}$. This is most easily achieved by the simple introduction of a small R_{13} term, relative to the coupling field Rabi frequency Ω_c , which alters the E.I.T. feature of Figure 2.5 to produce inversionless gain. This is born out in Figure 2.8(a) and (b) where positive absorption can be observed, with around 65 % of the population still remaining in level $|1\rangle$ of the system, when R_{13} has a value as small as only to equal twice that of the probe field Rabi frequency. The argument for inversionless gain is substantiated by calculating the values of the various terms of the inequality (2.54), ($500 > 5 > 1.01$) for the atomic parameters of Figure 2.8(a) and (b).

Inversionless gain does not however increase indefinitely as R_{13} continues to increase, as shown by the following two graphs of Figure 2.8.

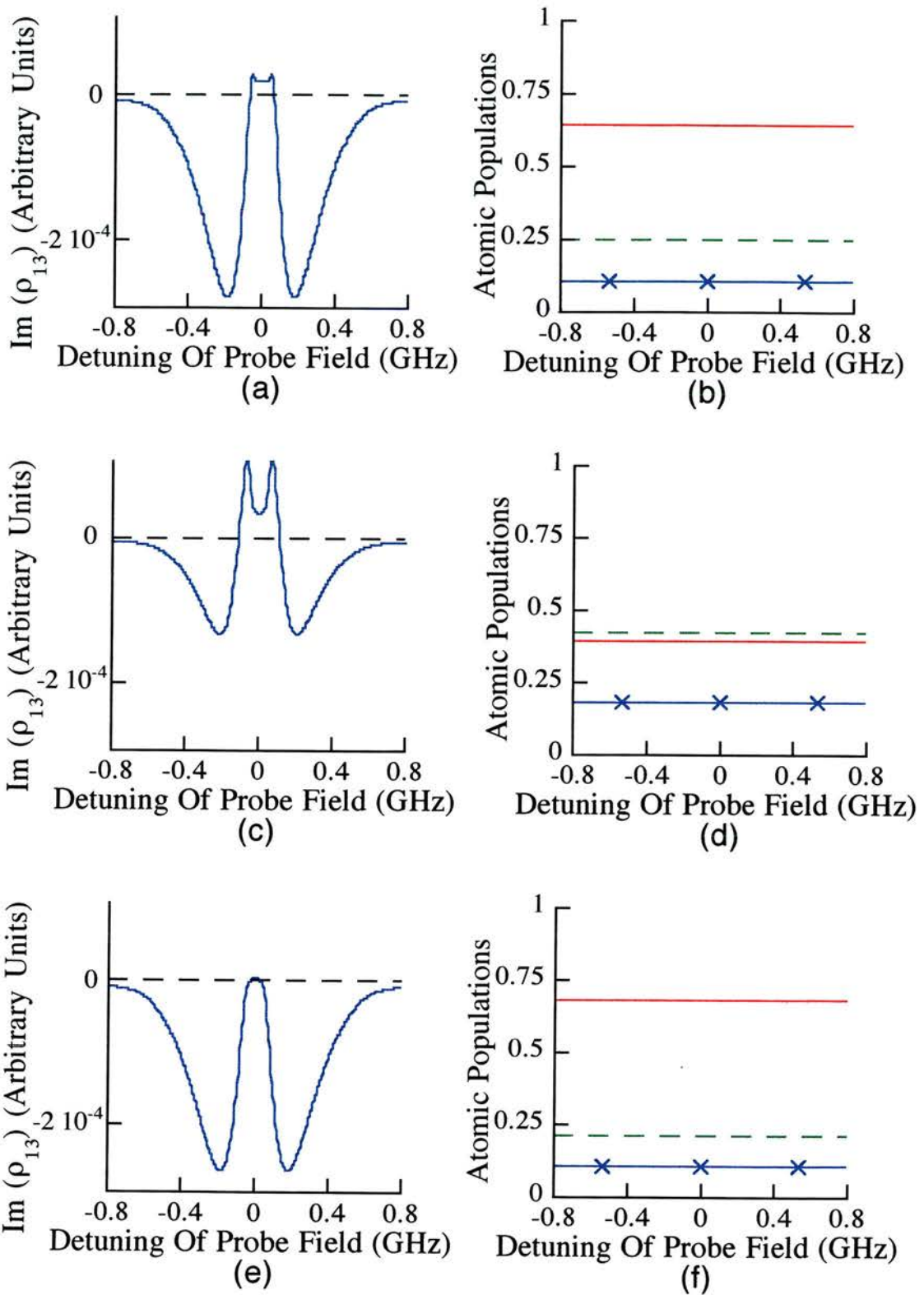


Figure 2.8 : Probe field absorption curves with the corresponding population levels for three different runs of the model corresponding to Matrix 2.4. Population in ρ_{11} shown as a red solid line, ρ_{22} as a green dashed line and ρ_{33} as a blue solid line marked with crosses. $\Omega_c = 160$ MHz, $\Omega_p = 0.1$ MHz and $\Delta_c = 0$ MHz. In (a) $R_{13} = 2\Omega_p$, $R_{23} = 0$ MHz, (c) $R_{13} = 10\Omega_p$, $R_{23} = 0$ MHz and (e) $R_{13} = 2\Omega_p$, $R_{23} = 150\Omega_p$.

Although Figure 2.8(c) still shows a large gain feature, examination of the population levels shown in Figure 2.8(d) reveals that less than 50 % of the population now remains in level $|1\rangle$, having been excited in large by the incoherent pump R_{13} . Thus, by the definition of Imamoglu et al. [17] this constitutes a population inversion and so the inequality (2.54) no longer holds ($100 > 1 > 1.01$). Further increases of R_{13} simply acts to empty level $|1\rangle$ to a larger extent, leading to greater inversion in the atomic population.

The introduction of R_{23} as expected from inspection of the inequality 2.54 acts in general against the production of inversionless gain. This is born out in the density matrix model where a typical result is presented in Figure 2.8(e) with the corresponding populations in Figure 2.8(f). In this case the model was run with the same parameters as for Figure 2.8(a) except for the fact that an R_{23} term of value $150 \Omega_p$ is now present. Comparison with Figure 2.8(a) and (b) shows that the gain feature has been significantly reduced with no real significant redistribution of population. The explanation of this effect lies within the gain mechanism of this lambda system [19]. An atom in state $|3\rangle$ experiencing spontaneous decay to state $|1\rangle$ becomes transparent to the probe field on a time scale given by the inverse decay rate of this transition. It is therefore removed from contributing to the gain mechanism within the system. However, an atom which decays from level $|3\rangle$ to level $|2\rangle$ produces gain. Therefore, when $\Gamma_{32} \gg \Gamma_{31}$ an atom, which is initially pumped by incoherent radiation from state $|1\rangle$ to state $|3\rangle$, is more likely to decay spontaneously to state $|2\rangle$ to then be recycled by the coupling field so allowing multiple spontaneous excitations of state $|2\rangle$ before decaying back to state $|1\rangle$ and providing transient loss. Introducing an R_{23} term effectively reduces the number of $|2\rangle - |3\rangle$ gain cycles experienced by the atom before loss is experienced by the spontaneous decay to level $|1\rangle$. Thus the overall effect of R_{23} is to reduce the inversionless gain observed within this lambda system.

2.3.2) Modelling Inversionless Gain Within An Atomic Rubidium V-type System

Recently, the first laser oscillation without a population inversion was demonstrated experimentally in a V-type ^{87}Rb atomic configuration within the D_1 and D_2 lines of rubidium vapour [18]. Figure 2.9 presents a schematic energy level diagram of the

atomic system employed for this experiment. As can be seen from this figure the probe field is resonant with the D₁ line of rubidium ($5S_{1/2}$ ($F = 1$) - $5P_{1/2}$) while the coupling field is resonant with the D₂ line ($5S_{1/2}$ ($F = 1$) - $5P_{3/2}$). A third coherent laser source is present which is also resonant with the D₁ transition. However, this pump source interacts with the second ground state hyperfine level, $5S_{1/2}$ ($F = 2$), and as such serves two separate purposes. In the absence of the pump field almost all of the population will be optically pumped into the $5S_{1/2}$ ($F = 2$) state. Thus, the pump field acts to destroy this optical pumping mechanism by populating the $5P_{1/2}$ level, and thus level $5S_{1/2}$ ($F = 1$), via spontaneous decay. Since the pump field puts a small population in the $5P_{1/2}$ level it also provides the gain mechanism which converts the V-type E.I.T. feature into inversionless gain.

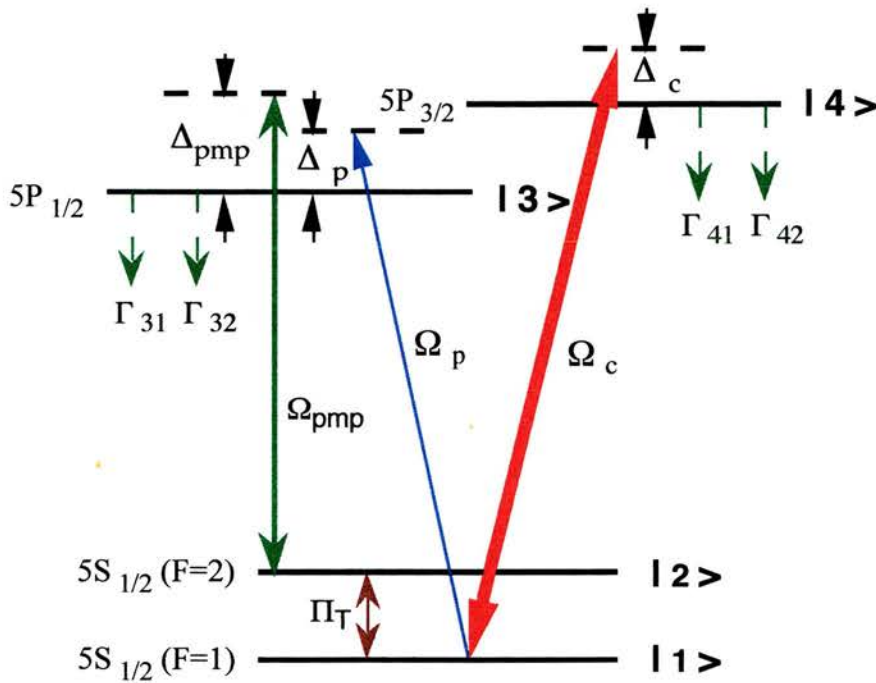


Figure 2.9: Schematic energy level diagram of the ^{87}Rb V-type system employed for inversionless lasing.

The authors provide the following expression for the gain coefficient, G , for the weak probe field on the $5S_{1/2}$ ($F = 1$) - $5P_{1/2}$ transition :

$$\begin{aligned}
G &= \frac{3\lambda^2 N L \Gamma_{31}}{4\pi} \frac{\text{Im}(\rho_{13})}{\Omega_p} \\
&= \frac{3\lambda^2 N L \Gamma_{31}}{4\pi} \times \frac{\left(\rho_{33}^0 - \rho_{11}^0\right) + \frac{|\Omega_c|^2}{\gamma_{34} \gamma_{14} (\rho_{11}^0 - \rho_{44}^0)}}{\gamma_{13} + \frac{|\Omega_c|^2}{\gamma_{34}}}
\end{aligned} \tag{2.55}$$

where ρ_{ii}^0 is the population of level i calculated to the zeroth order in the probe field, γ_{ij} again represents the relaxation rate of the density matrix element ρ_{ij} , N is the density of the atoms, L is the cell length and λ is the probe field wavelength.

Examination of the second equality in equation (2.55) shows that there are two contributions from upper level coherences which act to modify the usual gain or absorption profiles. The first corresponds to the well documented Stark effect [20] and is responsible for the $|\Omega_c|^2$ term in the denominator of this V-type configuration. However, another important effect also occurs as a result of the second term, which is proportional to $|\Omega_c|^2$, in the numerator of equation (2.55). This term is a direct result of the quantum interference effects within the atomic system which act to modify the properties of this V-type system. It follows from equation (2.55) that absorption interferes destructively if $\rho_{11}^0 - \rho_{44}^0 > 0$. This leads to a reduction in the absorption and so an enhancement of the gain. As a result the whole field can be amplified even if $\rho_{33}^0 - \rho_{11}^0 < 0$.

It should be noted that the authors developed two models in order to theoretically study this system. Both are density matrix models but the first deals with the simplified four level, three field system of Figure 2.9 while the second takes into account all the relevant Clebsh-Gordan and Racah coefficients, field polarisations and Zeeman sub-levels. This results in a 32-level density matrix model whose results, though more accurate, are very similar to those obtained from the simpler four level model. Therefore, starting from the Liouville equation once more a four level density matrix model for this system has been derived, see Matrix A.1 in Appendix A.

Using this matrix the graphs of Figure 2.10 have been generated where the optical pump field equals that of the coupling field such that $\Omega_c = \Omega_{\text{pmp}} = 300$ MHz, $\Omega_p = 1$ MHz and $\Delta_c = \Delta_{\text{pmp}} = 0$ MHz with all other parameters chosen to correspond to atomic rubidium (see Chapter 3). Figure 2.10(a) shows the probe field transmission as a function of probe field detuning with Figure 2.10(b) showing the corresponding populations within the system. Two distinct regions of gain can clearly be observed on the probe field absorption curve either side of exact probe resonance. Confirmation of the inversionless nature of this gain is obtained from the population traces of Figure 2.10(b). Examination of these population curves shows that $\sim 56\%$ of the population remains within the ground state hyperfine levels, with $\sim 34\%$ remaining solely in state $|1\rangle$. The two upper state levels each contain $\sim 22\%$ of the population and as such the generated gain experienced by the probe field must be of a non-inverted nature in this bare state model.

It should be noted that the nature of inversionless gain appears to depend on type of optical pump employed. In Section 2.3.1 where the pump is of an incoherent nature the gain appears as a modified induced transparency. However, in Section 2.3.2 where the pump is of a coherent nature the gain appears in two separate regions. The explanation of this phenomenon lies in the fact that along with modifying the population equations of the density matrix a coherent pump also modifies the coherence equations. However, employing an incoherent pump simply modifies the population equations and so does not significantly alter the relative coherences induced by the coupling field. This point is further examined in Chapter 8 where incoherent and coherent pump fields are employed in turn to produce inversionless gain within the same atomic system.

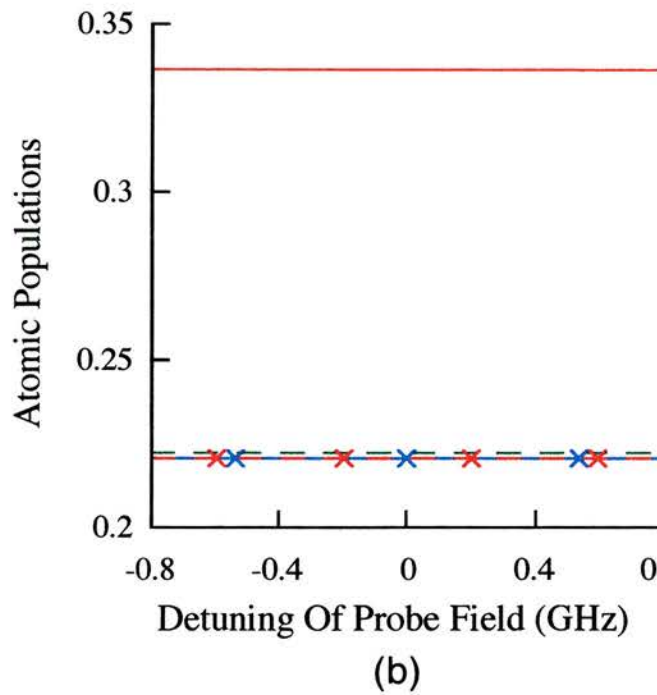
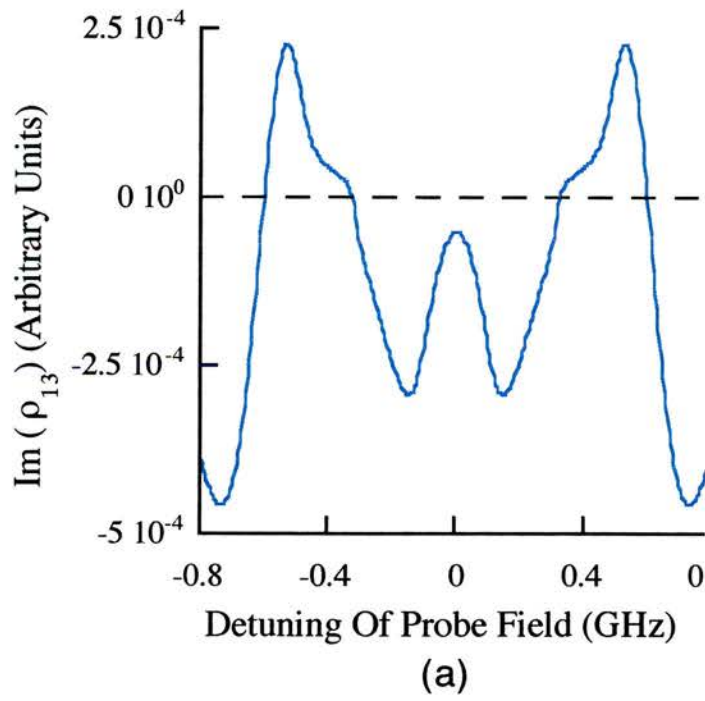


Figure 2.10: Probe field absorption curve (a) with the corresponding population levels (b) for the model corresponding to Matrix A.1. Population in ρ_{11} shown as a red solid line, ρ_{22} as a green dashed line, ρ_{33} as a blue solid line marked with crosses and ρ_{44} as a red dashed line marked with crosses. $\Omega_c = \Omega_{pmp} = 300$ MHz, $\Omega_p = 1$ MHz and $\Delta_c = \Delta_{pmp} = 0$ MHz.

2.4) Moseley's N Level Rules

The derivation of the above density matrices from first principles can be very time consuming, especially when any more than three atomic levels are being considered. After dealing with many of these density matrix problems Moseley observed that certain empirically derived rules could be created [21]. Employing these rules allows a system matrix to be written down directly, without reference to the original Liouville equation, and so saves a full and time consuming derivation each time a new system is considered. Moseley's N level rules allow the construction of the $N^2 - 1$ real simultaneous equations which describe the steady state of an arbitrary N level atom subjected to a number of coherent electromagnetic fields (up to a maximum of N - 1) while implicitly employing the rotating wave approximation [3]. The full potential of these rules can only be realised if they are used with care and an appreciation of the full derivation process from first principles. However, with this understanding in place these rules serve as a very useful and elegant way of deriving a particular system's density matrix.

References

- [1] **M.H. Dunn**, *Electromagnetically Induced Transparency* in Laser Sources and Applications, editors A. Miller and D.M. Finlayson p.411 (SUSSP / IOP, Bristol, (1996)).
- [2] **R. Loudon**, *The Quantum Theory Of Light*, 2nd edition (Oxford University Press, Oxford (1991)).
- [3] **I.I. Rabi, N.F. Ramsey and J. Schwinger**, *Use Of Rotating Coordinates In Magnetic resonance problems*, Rev. Mod. Phys. 26 , 167 (1954).
- [4] **J.E. Bjorkholm and P.F. Liao**, *Line Shape And Strength Of Two-Photo Absorption In An Atomic Vapour With A Resonant Or Nearly Resonant Intermediate State*, Phys. Rev. A 14 , 751 (1976).
- [5] **S.E. Harris, J.E. Field and A. Imamoglu**, *Nonlinear Optical Processes Using Electromagnetically Induced Transparency*, Phys. Rev. Lett. 64 , 1107 (1990).
- [6] **A. Yariv**, *Quantum Electronics*, (Wiley, New York (1975)).
- [7] **R. Tolman**, *The Principles Of Statistical Mechanics*, (Clarendon Press, Oxford (1938)).
- [8] **B. Shore**, *The Theory Of Coherent Atomic Excitation*, (John Wiley & Sons, New York (1990)).
- [9] **R.G. Brewer and E.L. Hahn**, *Coherent Two-Photon Processes : Transient And Steady-State Cases*, Phys. Rev. A 11 , 1641 (1975).
- [10] **J.E. Field, K.H. Hahn and S.E. Harris**, *Observation Of Electromagnetically Induced Transparency In Collisionally Broadened Lead Vapour*, Phys. Rev. Lett. 67 , 3062 (1991).

- [11] **R. Salomaa and S. Stenholm**, *Two-Photon Spectroscopy : Effects Of A Resonant Intermediate State*, J. Phys. B: Atom. Molec. Phys. 11 , 1795 (1975).
- [12] **N. Bloembergen**, *Nonlinear Optics*, (Benjamin, New York (1965)).
- [13] **J.H. Wilkinson and C. Reinsch**, *Handbook For Automatic Computation*, Vol 2. (Springer-Verlag, New York (1971)).
- [14] **P.E. Gill and G.F. Miller**, *An Algorithm For The Integration Of Unequally Spaced Data*, Comput. J. 15 , 80 (1972).
- [15] **S. Wolfram**, *Mathematica: A System For Doing Mathematics By Computer*, Second Edition (Addison-Wesley, Reading (1993)).
- [16] **P. Mandel**, *Lasing Without Inversion: A Useful Concept ?*, Contemp. Phys 34 , 235 (1993).
- [17] **A. Imamoglu, J.E. Field and S.E. Harris**, *Lasers Without Inversion: A closed Lifetime Broadened System*, Phys. Rev. Lett. 66 , 1154 (1991).
- [18] **A.S. Zibrov, M.D. Lukin, D.E. Nikonov, L. Hollberg, M.O. Scully, V.L. Velichansky and H.G. Robinson**, *Experimental Demonstration Of Laser Oscillation Without Population-Inversion Via Quantum Interference In Rb*, Phys. Rev. Lett. 75 , 1499 (1995).
- [19] **S.E. Harris and J.J. Macklin**, *Lasers Without Inversion: Single-Atom Transient Response*, Phys. Rev. A 40 , 4135 (1989).
- [20] **S.H. Autler and C.H. Townes**, *Stark Effect In Rapidly Varying Fields*, Phys. Rev. 100 , 703 (1955).
- [21] **R.R. Moseley**, *Sum Frequency Mixing And Quantum Interference In Three- Level Atoms*, Ph.D thesis, University of St. Andrews (1994).

Chapter 3

Atomic Rubidium, Theoretical Rabi Frequencies And Experimental Apparatus

This chapter briefly introduces the idea of atomic structure with particular reference to rubidium which is the medium in which all the experimental work of the following chapters is carried out. An initial look at fine and hyperfine structure is included which provides information about the resonant frequencies between different energy levels of rubidium. A section then follows on the theoretical calculation of Rabi frequencies induced on allowed dipole transitions. With these values in mind a discussion of the various laser sources employed to generate these resonant frequencies then follows. The chapter goes on to discuss other relevant experimental apparatus before finishing with a section on the design of a rubidium atomic beam to be used in future experimental work.

3.1) Atomic Rubidium

Rubidium was discovered in 1861 by R.W. Bunsen and G. Kirchoff in Heidelberg, Germany. It is a soft, highly reactive member of the alkali metal group of the periodic table, and exists as two natural isotopes, ^{85}Rb and ^{87}Rb . Rubidium is widely distributed throughout nature, but it only occurs in small amounts, its abundance in the earth's crust

being 310 parts per million (this compares with gold whose abundance is only 0.0011 p.p.m.). The main source of rubidium is through the electrolysis of carnallite, the hydrate chloride of magnesium and potassium. Rubidium ignites spontaneously in air and reacts violently with water, hence its applications are limited. However, rubidium is most suitable as a medium for atomic coherence experiments since many of its resonant transitions are accessible to Ti:sapphire, dye or diode laser sources. Being an alkali metal, rubidium also has the advantage of one unpaired electron in its outermost shell and therefore can be studied extensively with the theoretical models of the previous chapter. Some of the more relevant properties of rubidium are listed below in Table 3.1:-

Table 3.1:- Atomic properties of rubidium.

Atomic Property	Value
Atomic Number	37
Atomic Weight	85.4678 a.m.u.
Crystal Structure	Body Centred Cubic
Physical Property	Value
Melting Point	38.89 ° C
Boiling Point	686 ° C
Density @ 20 ° C	1.532 g cm ⁻³
Natural Isotope Mass No.	%
85	72.17
87	27.83

The main disadvantage of employing rubidium to experimentally study atomic coherence effects is the fact that its energy levels are not single levels but are in fact complicated combinations of many energy sublevels. The presence of this fine and hyperfine structure is due to mechanisms which remove the degeneracy of the sublevels. The creation of fine and hyperfine structure is outlined in great detail in many texts [1, 2, 3, 4]. Therefore, for the purpose of this work a brief summary of the most relevant characteristics are outlined below.

3.1.1) Fine Structure:-Spin Orbit Coupling

The fine structure within an atom is the result of the interaction of the intrinsic spin of an electron with the magnetic moment arising from its own orbital angular momentum about the nucleus, S and L respectively, since the outer shell contains only a single electron. For this reason fine structure effects, or spin orbit coupling as it is popularly known, are strongest in the lowest orbital angular momentum states, L , since these orbits keep the electron, on average, in closer proximity to the nucleus. It should be noted however, that for the lowest energy orbital angular state, $L = 0$, there is no spin orbit coupling effect.

These two angular momentum quantum numbers, L and S , couple together to produce the spin orbit interaction quantum numbers, J and m_J . Each angular momentum state, L , is split by the spin-orbit coupling into a number of J states ranging in number from $L+S$ to $|L - S|$. Each of these J states is again composed of a number of sub-levels, categorised by the m_J number, which itself ranges from J to $-J$ (in units of one). In rubidium, where $S = 1/2$, the orbital angular momentum states (L) are each split into two by the spin, except in the lowest state, where $L=0$. Since spin orbit coupling effects are inversely proportional to the average radial distance of the electron from the nucleus its effects produce significant fine structure on the P and D states of rubidium but becomes much less significant in higher orbital angular momentum states. In one electron systems the $J = L - S$ and $J = L + S$ states are separated by ΔE_F where ΔE_F is related to the fine structure constant, ξ_F , by [4]:

$$\Delta E_F = \frac{\xi_F}{2} (2L + 1) \quad (3.1)$$

Some of the more relevant fine structure constants for rubidium [5] are presented below in Table 3.2 along with the corresponding fine level energy separations. Negative values indicate an inversion of the fine states such that the lower valued $J = L - S$ state actually occurs at a higher energy than the $J = L + S$ state.

Table 3.2:- Fine level structure constants for rubidium along with corresponding energy separations.

Level	ξ_F / GHz	$\Delta E_F / \text{GHz}$
5P	4748.8	7123.2
4D	-5.3	-13.2
6P	1549.0	2323.5
5D	35.5	88.7
7P	701.3	1052.0
6D	27.1	67.8
5F	-0.09	-0.3
8P	376.9	565.4
7D	18.1	45.3

3.1.2) Hyperfine Structure:

Hyperfine structure can be explained in terms of the properties of the angular momentum of the nucleus. In 1924 Pauli suggested that a nucleus has a total angular momentum, which is labelled by the quantum number I . This quantum number may have integral or half-integral values, like the total angular momentum quantum number J . The reason for this is that a nucleus is a compound structure of nucleons, protons and

neutrons, each of which have intrinsic spin $1/2$ and may take part in orbital motion within the nucleus. For atomic rubidium the nuclear spin varies between the two isotopes $I = 5/2$ for ^{85}Rb and $I = 3/2$ for ^{87}Rb . Also attributed to the nucleus, in addition to its spin, are electromagnetic multipole moments of higher order than electric monopole. The interaction between these moments and the electromagnetic field produced at the nucleus by the orbiting electrons is responsible for hyperfine structure.

The quantum number $\mathbf{F} = \mathbf{I} + \mathbf{J}$ describes the total angular momentum of the atom. A corresponding splitting, analogous to fine splitting, into hyperfine structure levels labelled by F , which are $m_F = (2F+1)$ -fold degenerate then occurs. In the lowest level, where there is no spin-orbit coupling as $L = 0$ and $J = 1/2$, hyperfine structure can be said to directly replace fine structure and the mathematics are directly analogous with the substitutions of $J \rightarrow F$, $L \rightarrow J$ and $S \rightarrow I$ [1]. For states where there is spin-orbit coupling ($L \geq 1$) the hyperfine structure provides further structure but on a smaller scale to that of the previously discussed fine structure.

For $J = 1/2$ states the two hyperfine structure states, $F = I + 1/2$ and $F = I - 1/2$, are displaced by ΔE_{HF} which is related to the hyperfine dipole constant, ξ_{HF} , by [1]:

$$\Delta E_{\text{HF}} = \frac{\xi_{\text{HF}}}{2} [F(F+1) - I(I+1) - J(J+1)] \quad (3.2)$$

When $J > 1/2$ the effects of electric quadrupole interactions must be taken into account such that the structure depends also on the quadrupole hyperfine constant, Q_{HF} , and is defined as [1]:

$$\Delta E_{\text{HF}} = \frac{\xi_{\text{HF}}}{2} \kappa + \frac{Q_{\text{HF}}}{4} \frac{\frac{3}{2} \kappa(\kappa+1) - 2I(I+1)J(J+1)}{I(2I-1)J(2J-1)} \quad (3.3)$$

where

$$\kappa = F(F+1) - J(J+1) - I(I+1) \quad (3.4)$$

A review of the measurements of the hyperfine structure of free, naturally occurring, alkali atoms has been carried out by E. Arimondo et al. [6]. Some of these values for rubidium have been tabulated below in Table 3.3. Negative values of ξ_{HF}

indicate an inversion of the F states such that lower valued F states occur at higher energies than those of the higher valued F states.

Table 3.3:- Some hyperfine structure constants for rubidium.

Isotope	⁸⁵ Rb		⁸⁷ Rb	
	$\xi_{\text{HF}} / \text{MHz}$	$Q_{\text{HF}} / \text{MHz}$	$\xi_{\text{HF}} / \text{MHz}$	$Q_{\text{HF}} / \text{MHz}$
5S _{1/2}	1011.9		3417.3	
5P _{1/2}	120.7		406.2	
5P _{3/2}	25.0	25.9	84.8	12.5
5D _{3/2}	4.18	<5	14.4	3.5
5D _{5/2}	-2.12	No value	-7.4	<5
6S _{1/2}	239.3		809.1	
6P _{1/2}	39.1		132.6	
6P _{3/2}	8.2	8.2	27.7	4.0

In Figure 3.1 a schematic energy level diagram is presented which shows the fine structure of rubidium from the 5S_{1/2} ground state up to the 7D_{5/2} excited state. Also included are some of the optical wavelengths which can be generated by the laser sources described in Section 3.3. The fact that rubidium has an intrinsic nuclear spin results in complex sub-level structure. Since two separate isotopes exist naturally, each having its own values for I, ξ_{HF} and Q_{HF} , the splitting of the sub-level structure differs significantly. Figure 3.2 presents a second schematic energy level diagram of rubidium which again shows the 5S_{1/2} ground state and the first two excited states, 5P_{1/2} and 5P_{3/2}, but the hyperfine and magnetic hyperfine levels are now included. It is obvious from this second diagram that when the effects of nuclear spin are taken into account

full explanation of how to calculate 3j and 6j-symbols is beyond the scope of this work, however detailed descriptions of these can be found in the following texts [2, 3, 7].

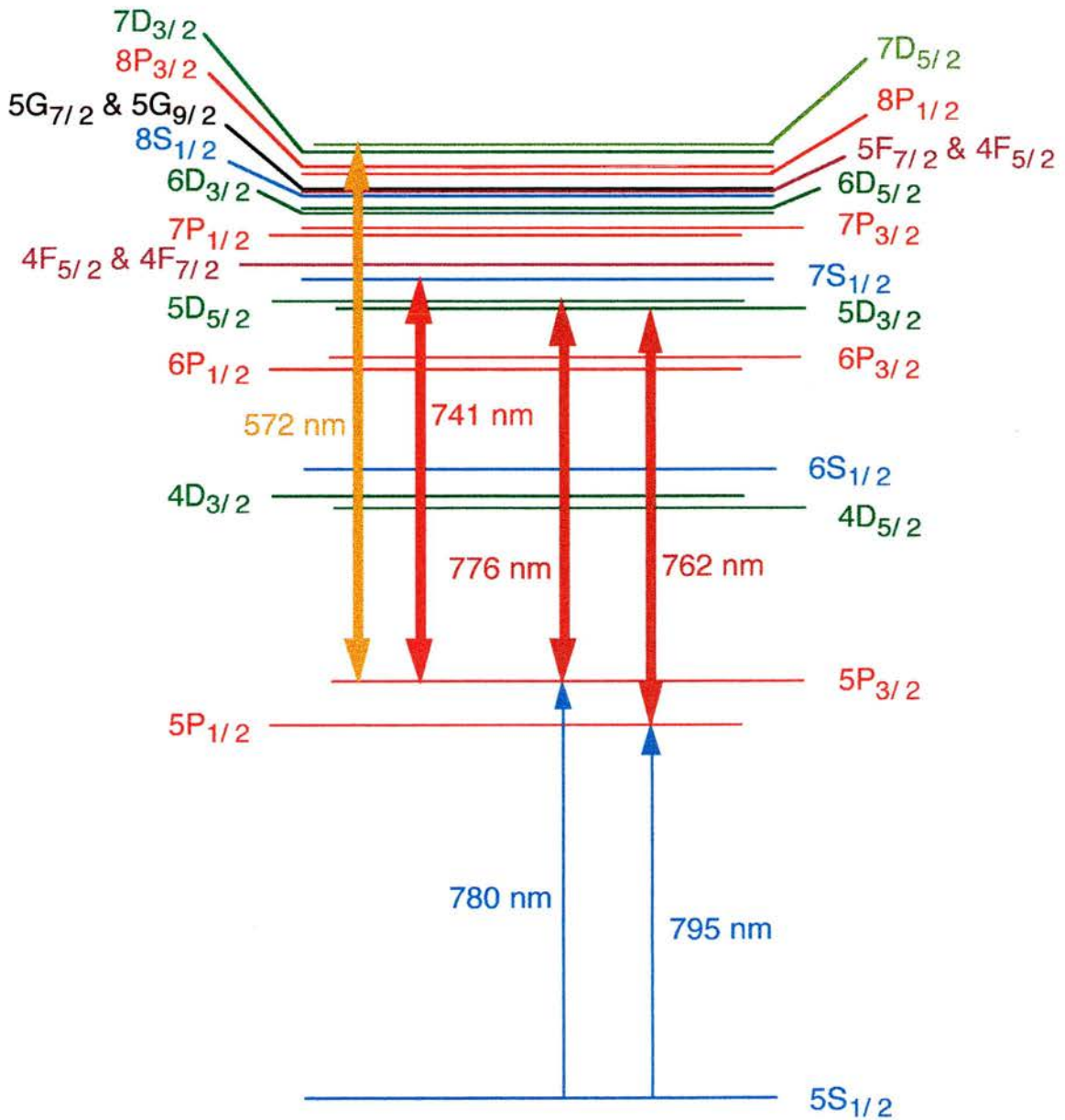


Figure 3.1:- Schematic energy level diagram of the fine states within rubidium from the $5S_{1/2}$ ground state to the $7D_{5/2}$ excited state. The arrows represent some of the optical transitions accessible by the available laser sources.

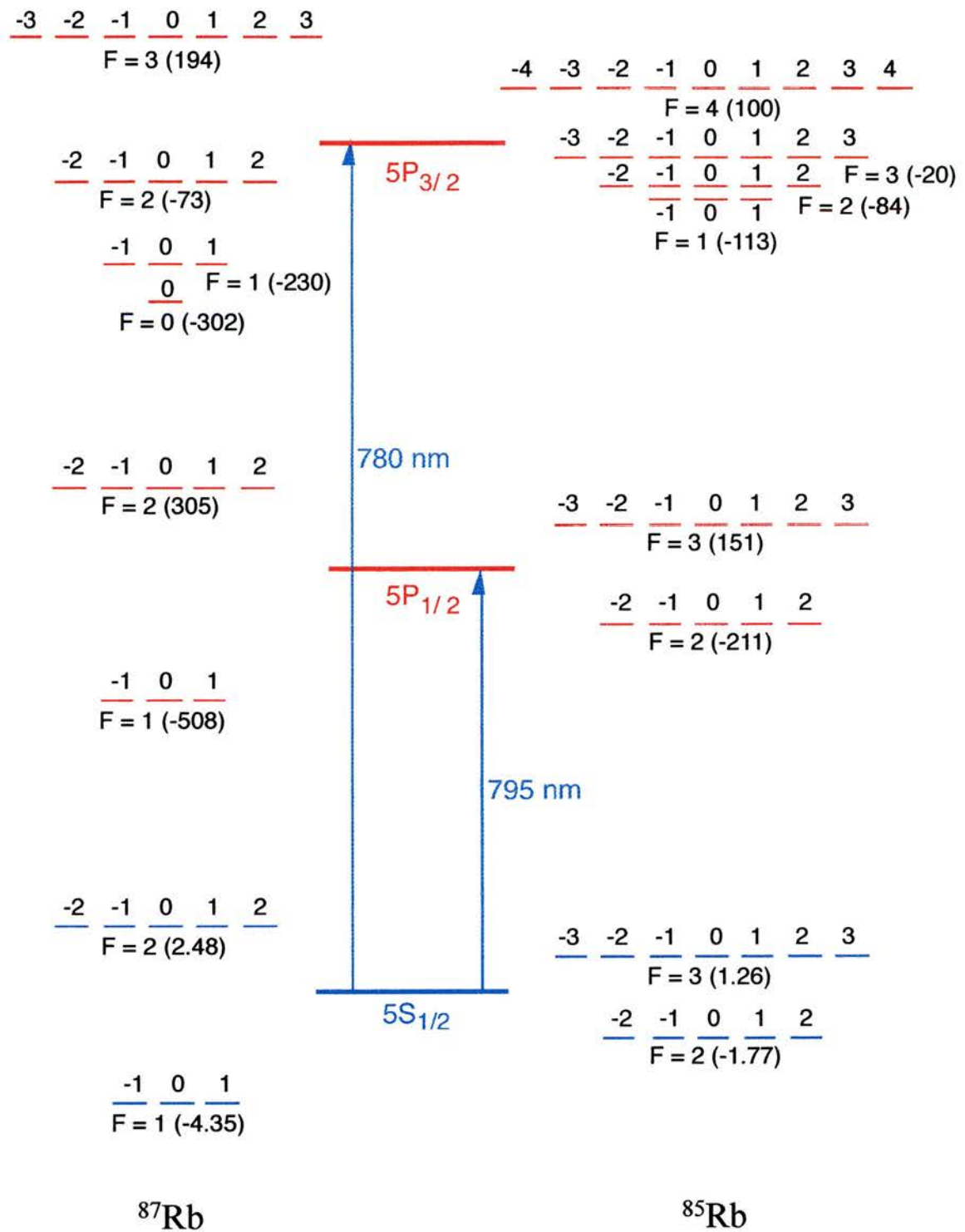


Figure 3.2:- Schematic energy level diagram of the hyperfine and magnetic hyperfine states within the $5S_{1/2}$ ground state and the first two excited states, $5P_{1/2}$ and $5P_{3/2}$, of rubidium. The relevant splittings of the levels from the fine state energy level are also indicated. It should be noted that the unit of splitting in the ground state is GHz whereas it is MHz in the excited states.

3.2) Calculation Of Experimental Rabi Frequencies

Consider a linearly polarised coherent optical field interacting with a two level atom as shown in Figure 3.3(a).

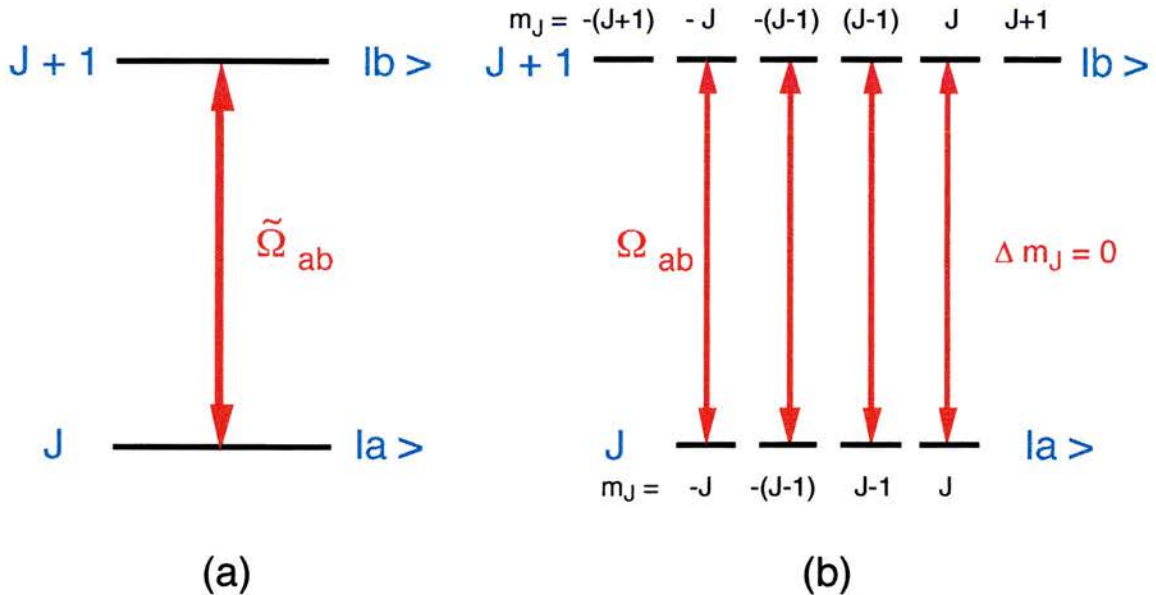


Figure 3.3:- (a) A schematic two level atom, with total angular momentum J for the lower state $|a\rangle$ and $J+1$ for the upper state $|b\rangle$ interacting with a linearly polarised optical field. (b) The same system as (a) but with the degeneracy m_J of the system taken into consideration.

Under the action of the radiation field population is removed from the ground state into the excited state. However, unlike in a rate equation analysis, a coherently driven population change does not saturate when the two states have equal populations. Instead the population continues to flow out of the ground state into the excited state, until all the population resides in the excited state. As more population moves out of the ground state, fewer atoms are available to absorb further photons, thus the absorption process decreases. Conversely, stimulated emission becomes increasingly significant as the population in the excited state grows. Once the population is completely inverted, population transfer takes place through stimulated emission and so the population begins to repopulate the ground state. Eventually all of the population again resides in the ground state and so this whole process is then ready to be repeated.

The frequency at which the population coherently oscillates between the two levels is known as the Rabi frequency [8].

Turning now to the degenerate two-level system of Figure 3.3(b) then each pair of sublevels that are linked by the selection rule, $\Delta m_j = 0$, have a distinct Rabi frequency. Thus it can be seen that there is no single Rabi frequency appropriate to a degenerate two-level transition. With this in mind it is useful to define a root-mean-square (r.m.s.) Rabi frequency $\tilde{\Omega}_{ab}$ for such a degenerate transition :

$$\left(\tilde{\Omega}_{ab}\right)^2 = \sum_{M_a M_b} (\Omega_{ab})^2 \quad (3.5)$$

The subscript on Ω_{ab} implies specification of magnetic quantum numbers, whereas the average $\tilde{\Omega}_{ab}$ has no dependence upon magnetic quantum numbers. Employing the summation properties of 3j-symbols and by defining the optical field phase as ϕ Shore [3] uses the r.m.s. value to express the actual Rabi frequency as:

$$\Omega_{ab} = \tilde{\Omega}_{ab} \frac{\sqrt{3}}{2\pi} e^{i\phi} (-1)^{J_>-M_a} \sum_q (-1)^q \varepsilon_{-q} \begin{pmatrix} J_a & 1 & J_b \\ -M_a & q & M_b \end{pmatrix} \quad (3.6)$$

where the 2π term in the denominator is present to give the Rabi frequency as a pure frequency value, $J_>$ is the larger value of J_a or J_b and ε_{-q} refers to the polarisation state of the optical field. There are several alternative ways of expressing the r.m.s. Rabi frequency that provide connections with other spectroscopic parameters. Following Condon and Shortley [4] the obtained expression is:

$$\left|\tilde{\Omega}_{ab}\right|^2 = \frac{(\lambda_{ab})^3}{4\pi^2 \hbar c} I \varpi_b A_{ba} \quad (3.7)$$

where λ_{ab} is the wavelength of the transition $|a\rangle - |b\rangle$ (m), I is the intensity of the optical field (Wm^{-2}), ϖ_b is the degeneracy of $|b\rangle$, A_{ba} is the Einstein A coefficient, \hbar is Planck's constant divided by 2π and c is the speed of light in vacuum.

3.2.1) Determination Of Coupling Field Intensity I

At first glance it may be expected that the value for the intensity, I , in equation (3.7) should be obtained by simply dividing the total power of the coupling field by the cross sectional area at the centre of the cell (πw_c^2 , where w_c is the waist size of the coupling field). However, taking this value as the average intensity interacting with the probe field leads to Rabi frequencies significantly less than those achieved experimentally. The reason for this is the Gaussian nature of the optical fields, see Figure 3.4, which shows a schematic representation of the overlap between the two normalised Gaussian field profiles where w_p represents the waist size of the probe field.

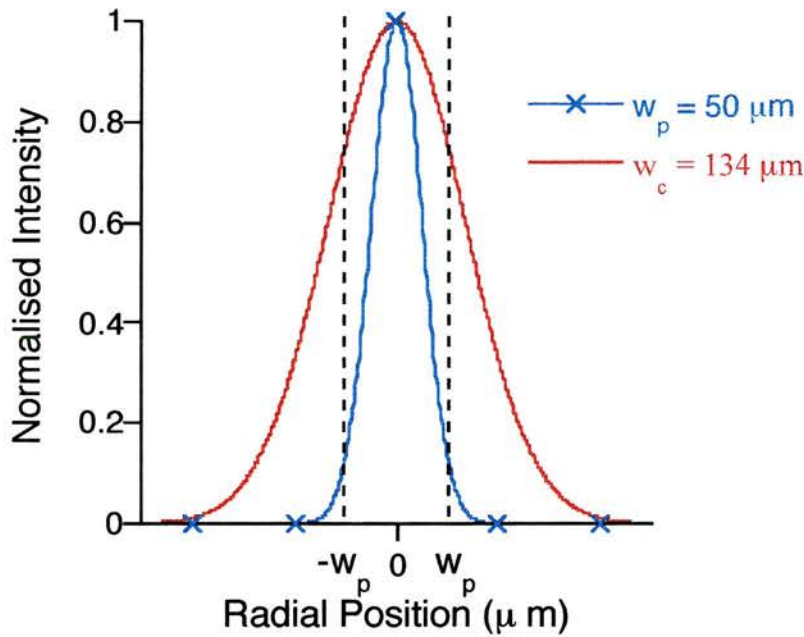


Figure 3.4:- Schematic representation of the overlap region between a normalised probe field and a normalised coupling when the probe field is such that it is contained spatially within the coupling field.

Since the probe is contained fully within the coupling field it is expected that the average intensity of the coupling field within the probe field cross-section will be much higher than the first approximation stated above. To provide a more accurate value of

the coupling field intensity inducing the corresponding Rabi frequency the total intensity of the coupling field between $-w_p$ and w_p must be calculated. This is achieved by considering the following expression for the total power contained in a Gaussian field of waist w_f :

$$P_T = I_{\max} \int_0^{2\pi} \int_0^{\infty} \exp\left(\frac{-2r^2}{w_f^2}\right) r \, dr \, d\theta \quad (3.8)$$

Employing the substitution $u = r^2$ provides the following expression for the power of the coupling field, P_c :

$$P_c = \frac{I_{\max} \pi w_c^2}{2} \quad (3.9)$$

The corresponding coupling field power within the probe field area, P_p , is then found by solving the expression :

$$P_p = I_{\max} \int_0^{2\pi} \int_0^{w_p} \exp\left(\frac{-2(r^2)}{w_c^2}\right) r \, dr \, d\theta \quad (3.10)$$

where I_{\max} is as given in equation (3.9). Thus, by dividing this value by the cross-sectional area of the probe field (πw_p^2) a more accurate value for the coupling field intensity is obtained :

$$I = \frac{P_c}{\pi w_p^2} \left[1 - \exp\left(-\frac{2w_p^2}{w_c^2}\right) \right] \quad (3.11)$$

For a coupling field power of 0.3 W, $w_c = 134 \, \mu\text{m}$ and $w_p = 50 \, \mu\text{m}$ the calculated intensity of the coupling field is $9.28 \, \text{MWm}^{-2}$ which compares to the first approximated value of $5.32 \, \text{MWm}^{-2}$.

3.2.2) An Example Rabi Frequency Calculation

An example calculation employing equations (3.6) and (3.7) is carried out for the $5P_{3/2} - 5D_{5/2}$ transition within rubidium as outlined in Figure 3.5. This is the most frequently employed coupling field transition for cascade systems within the following chapters.

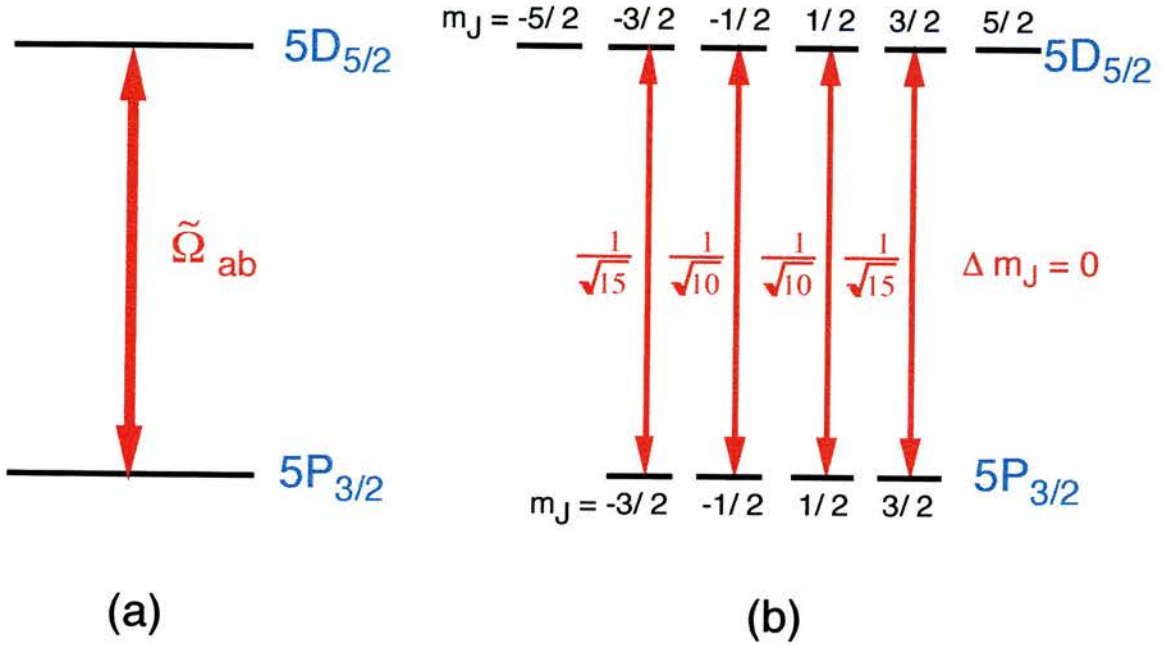


Figure 3.5:- (a) A schematic two level representation of the $5P_{3/2} - 5D_{5/2}$ transition within rubidium interacting with a linearly polarised optical field. In (b) the same system is presented but with the degeneracy m_J of the system taken into consideration. The appropriate m_J values for each level are marked along with the relative dipole strengths of the allowed m_J transitions ($\Delta m_J = 0$).

The appropriate relative dipole matrix elements for the allowed m_J transitions within Figure 3.5(b) are marked on the diagram. These were calculated using the 3j-symbol function of the mathematical package Mathematica [9]. Using the following values : $\lambda_c = 775.7650$ nm, $\varpi_b = 6$, $A_{ba} = 2.288 \cdot 10^6$ s⁻¹, $\hbar = 1.05 \cdot 10^{-34}$ Js, $c = 2.998 \cdot 10^8$ ms⁻¹ and $P_T = 175$ mW then the calculated values of I and $\tilde{\Omega}_{ab}$ are 5.42 MWm⁻² and 1453.7 MHz respectively. The calculated Rabi frequencies on each of the allowed Δm_J transitions are tabulated below :

Table 3.4:- Calculated Rabi frequencies on the allowed $5P_{3/2} - 5D_{5/2} \Delta m_j$ transitions within rubidium.

$5P_{3/2}$	$5D_{5/2}$	3j-symbol	Ω_{ab} / MHz
-3/2	-3/2	$1/\sqrt{15}$	375.3
-1/2	-1/2	$1/\sqrt{10}$	459.7
1/2	1/2	$1/\sqrt{10}$	459.7
3/2	3/2	$1/\sqrt{15}$	375.3

The values calculated above compare reasonably well with the experimentally observed value of 250 MHz (See Chapter 7). Within the experiment it is an intricate combination of all the m_j three level systems which contribute to the overall Rabi splitting observed. Overlap of the optical fields along the length of the cell is the main source of discrepancy between the theoretically calculated and experimentally realised results. Beam overlap is reduced due to the effects of E.I.F (see Chapter 6) and diffraction. The above calculation is carried out at the centre of the cell where the two optical field have their tightest waists. However, at the cell ends the profiles of the beams are quite different thus explaining why the calculated values are higher than those experimentally observed.

3.3) Experimental Apparatus

The optical fields required for the atomic coherence experiments described in this work were generated by laser sources. It is the steady-state response of the atoms that was of interest here, thus it was required that the lasers be continuous-wave in operation. All the sources used have a narrow spectral linewidth, and so satisfy the requirement for monochromatic radiation and allow sub-Doppler resolution in the vapour systems.

3.3.1) Pump Lasers

The primary source of power for the lasers in this work were continuous-wave, mainframe argon-ion lasers. The first, a Spectra-Physics 2030 laser [10], was employed to pump either a Spectra-Physics 380D dye laser or a Schwartz Ti:sapphire laser. The 2030 argon-ion laser can produce up to 20 W of power, when operating on all lines, or 8.5 W on single line operation at 514.5 nm. It was usual to run the laser multiline, so producing 10 W of TEM₀₀ output power, for pumping either of the above mentioned lasers. The second pump laser source was a Spectra-Physics 2080 laser with BeamLok™ [11], which was used to pump a Microlase MBR-110 Ti:sapphire laser. This laser can also produce up to 20 W of power, when operating on all lines, or 9 W on single line operation at 514.5 nm. Usually it was run multiline, with 7 W of TEM₀₀ output power produced for pumping the Microlase Ti:sapphire. It was found that it was important to ensure that the mode of the pump lasers were as close to TEM₀₀ as possible, to allow optimum mode matching between the pump and the circulating laser beams.

3.3.2) Optical Field Sources

Three different lasers were used to supply the coherent optical fields required for these experiments within rubidium. The scanning laser source, normally employed as the probe field, was provided by a Microlase MBR-110 Ti:sapphire. Figure 3.6 shows a schematic of the Microlase Ti:sapphire, bow-tie cavity arrangement, which includes a unidirectional device and a solid etalon, to ensure single-frequency operation. The Microlase Ti:sapphire also incorporates frequency stabilisation via side-of-fringe locking to an external, temperature controlled confocal etalon. Excellent passive stability is also realised due to the laser being mounted in a machined monolithic block. This provides a commercial system which is a continuous-wave, frequency-stabilised, single-mode scanning system with a linewidth < 200 kHz which can scan up to 30 GHz [12]. With reference to the experiments of the following chapters the Microlase Ti:sapphire would produce output powers of ~1.4 W, at 780 nm for 10 W pump power. However, it is found that high powers reduce the scanning properties of the laser. The maximum threshold power level for good scanning of the Microlase Ti:sapphire is

found to be ~ 400 mW. At this power level it proved possible to scan the system, over the normal frequency widths of 6 GHz or 10 GHz.

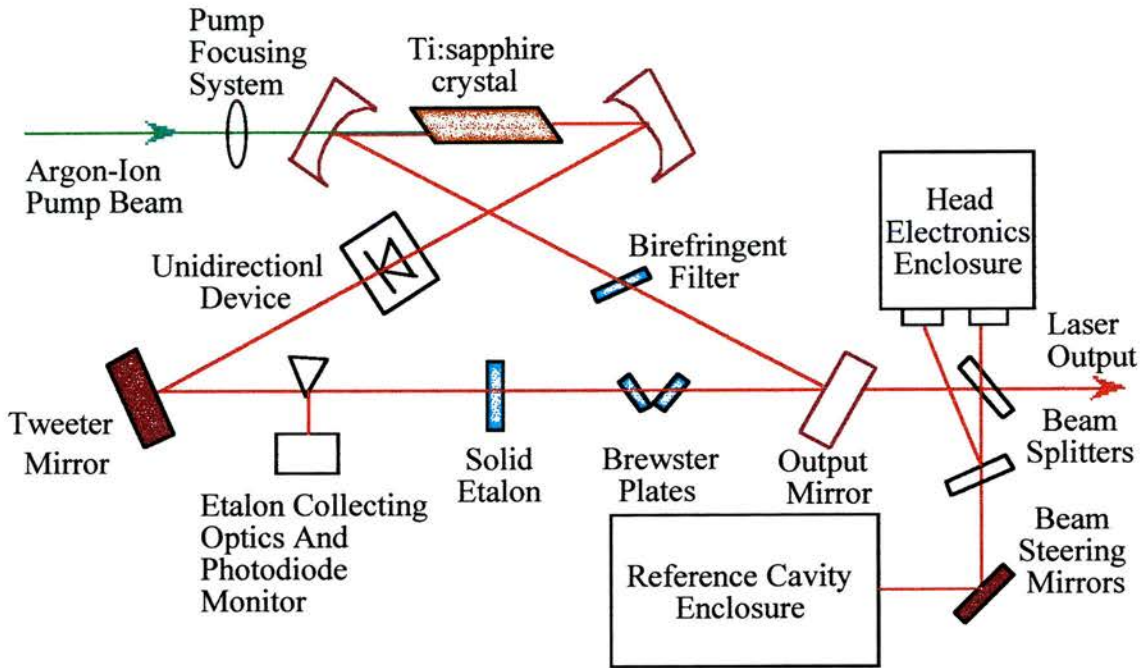


Figure 3.6:- Schematic of the Microlase MBR-110 Ti:sapphire laser.

The second optical field source was a modified Schwartz Electro Optic Titan CW Ti:sapphire laser [13, 7]. This laser source was mainly employed to provide a continuous-wave, single-mode coupling field for the experiments of the following chapters. The basic design of the modified laser resembles that of the Microlase Ti:sapphire laser and is schematically displayed in Figure 3.7. Again the system has a bow-tie configuration with a unidirectional device and a solid etalon present to provide single-frequency operation. The Brewster plates were an optional feature within this cavity, providing a mechanism for shifting the operating wavelength of the laser by a few tens of megahertz before a solid etalon mode hop occurs. No commercial scanning or stabilisation system was included but a free-running linewidth of < 5 MHz has been measured. The system was capable of producing 1.3 W of single frequency light. at ~ 800 nm.

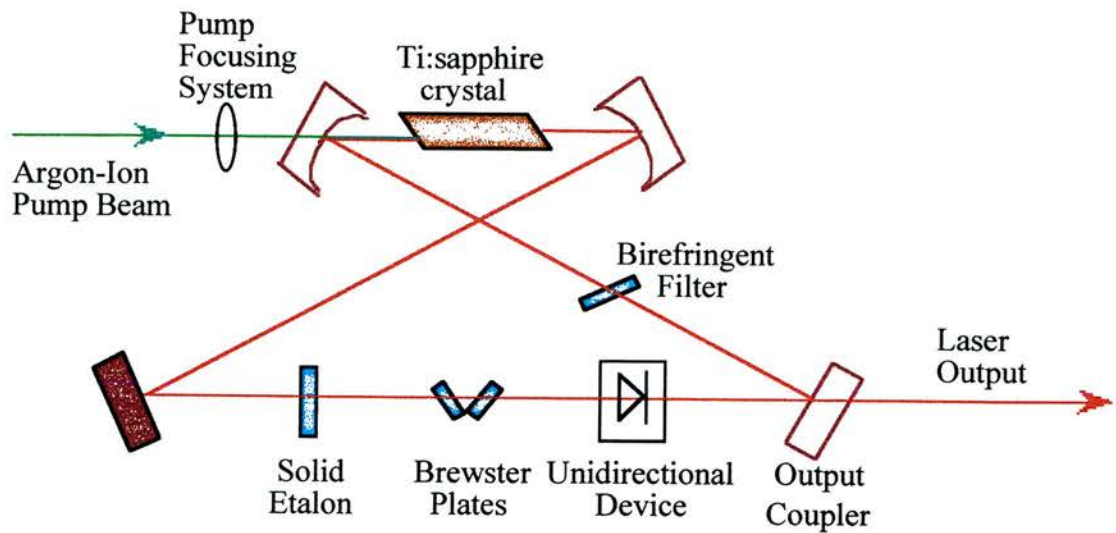


Figure 3.7:- Schematic of the modified Schwartz Electro Optic Titan-CW

The third optical field source employed for the experiments of Chapter 7 was a Spectra Physics 380D Ring Dye Laser. In these experiments the dye laser replaced the Schwartz Ti:sapphire providing a coupling field source at 572 nm. The dye laser was a continuous-wave, frequency-stabilised, single-mode scanning system with a linewidth of less than 1 MHz which could scan up to 30 GHz under commercial electronic control [14]. Figure 3.8 shows a schematic of the dye, bow-tie cavity, which includes a unidirectional device and an air-spaced etalon, to ensure single-frequency operation.

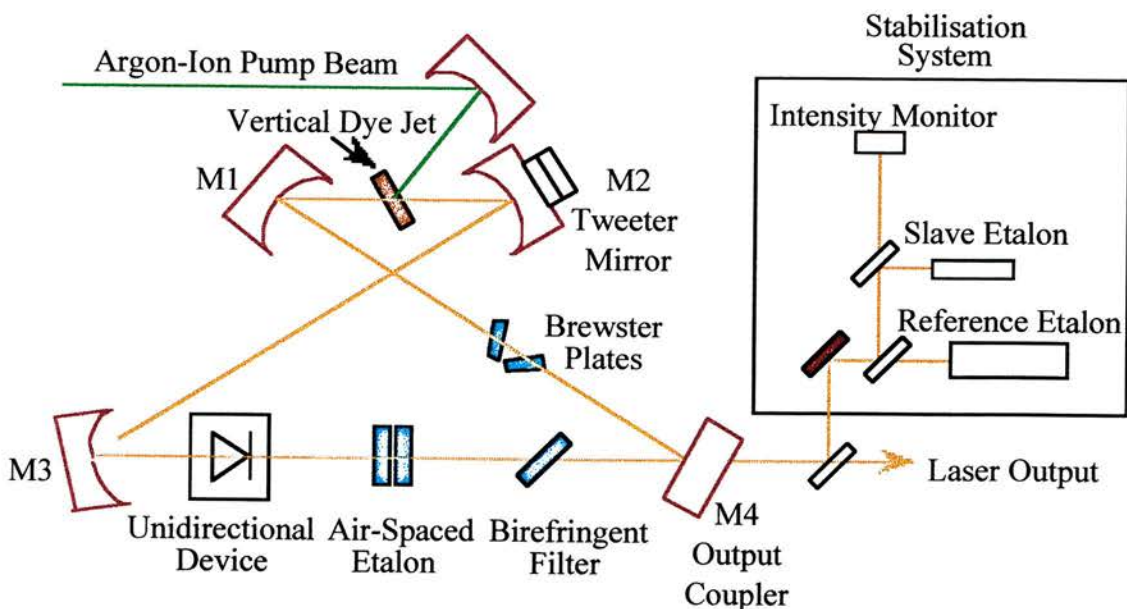


Figure 3.8:- Schematic of the Spectra-Physics 380D Ring Dye Laser

The lasing medium was Rhodamine 6G dye dissolved in ethylene glycol, which has a typical operating lifetime of around 6 weeks. With 7 W all line argon-ion pumping, the dye laser produced up to 250 mW at 572 nm.

3.3.3) Other Experimental Apparatus

Single-frequency operation of the lasers was monitored using piezo spaced, voltage-ramped, confocal Fabry-Perot interferometers of free spectral range 1.5 GHz. These confocal signals were used to provide 1.5 GHz frequency markers during laser scans.

Absolute wavelengths of the lasers were measured using a Kowalski-style travelling wave meter. This wavemeter uses a double Michelson interferometer arrangement, with a scanning arm, to provide wavelength readings accurate to 1 part in 10^6 . The counting of fringes is carried out simultaneously on the input incident laser field and on a temperature stabilised helium-neon laser. The number of fringes obtained for the helium laser is used as the standard since the wavelength of this laser is known (633 nm). By comparing the number of fringes counted for the incident laser field with that of the helium-neon, a wavelength reading is obtained. The accuracy obtained by this wavemeter was sufficient to set the lasers to within an etalon mode of the relevant atomic transition, typically to within a few GHz.

The rubidium vapour used in these experiments was present in the form of a cell of length 2 cm or 10 cm and diameter 2.5 cm. These cells were purchased from Ophos Instruments Inc. who evacuated them to 10^{-6} torr before filling them with rubidium and then sealing the cells. These cells allowed the atomic vapour to be easily heated to the required temperature, and so provided a means for altering the vapour density. A calculation of the vapour density within the cell can be obtained by using the empirical relation of Miles and Harris [15]:

$$N = \frac{9.66084 \times 10^{24}}{T} \exp\left[-\frac{a}{T} + d\right] \quad (3.12)$$

where N is in units of atoms m^{-3} , T is the temperature in degrees Kelvin and the empirical constants a and d have the values 9140.07 and 16.0628 respectively for

rubidium. This vapour density expression is valid for pressures around 1 torr (as is typical in this work).

Magnetic field coils, required for Zeeman splitting within the experiments of Chapter 5, were produced by Newport type A magnets placed around the cell. These had pole pieces of length 10 cm and provided fields calibrated at 0.045 T amp^{-1} up to a value of 0.4 T.

Results from all the following experiments were recorded on a 486 PC (Elonex PC-433) usually via phase sensitive detection methods. Filtered Hamamatsu photomultiplier tubes or photodiodes, were used to detect the chopped probe field and related fluorescence signals. The use of a few hundred hertz frequency chopper and a phase sensitive detector provided noticeable improvement in the signal-to-noise ratio of the detected signals. Neural density filters or graduated wheels allowed control of the input optical fields powers. The analogue to digital conversion required between experiment and PC is achieved via a 12-bit 16-channel board (Amplicon Liveline PC30AT) and a multichannel connection box. Amplicon Dash-300 software allowed the immediate storage of experimental data.

A schematic diagram showing the basic outlay of the experimental equipment is shown in Figure 3.9. Modifications to the direction of propagation of the applied optical fields is carried out between different experiments. This is easily achieved by changing the configuration of the beam steering mirrors, which, as presently shown, are in a counter-propagating arrangement.

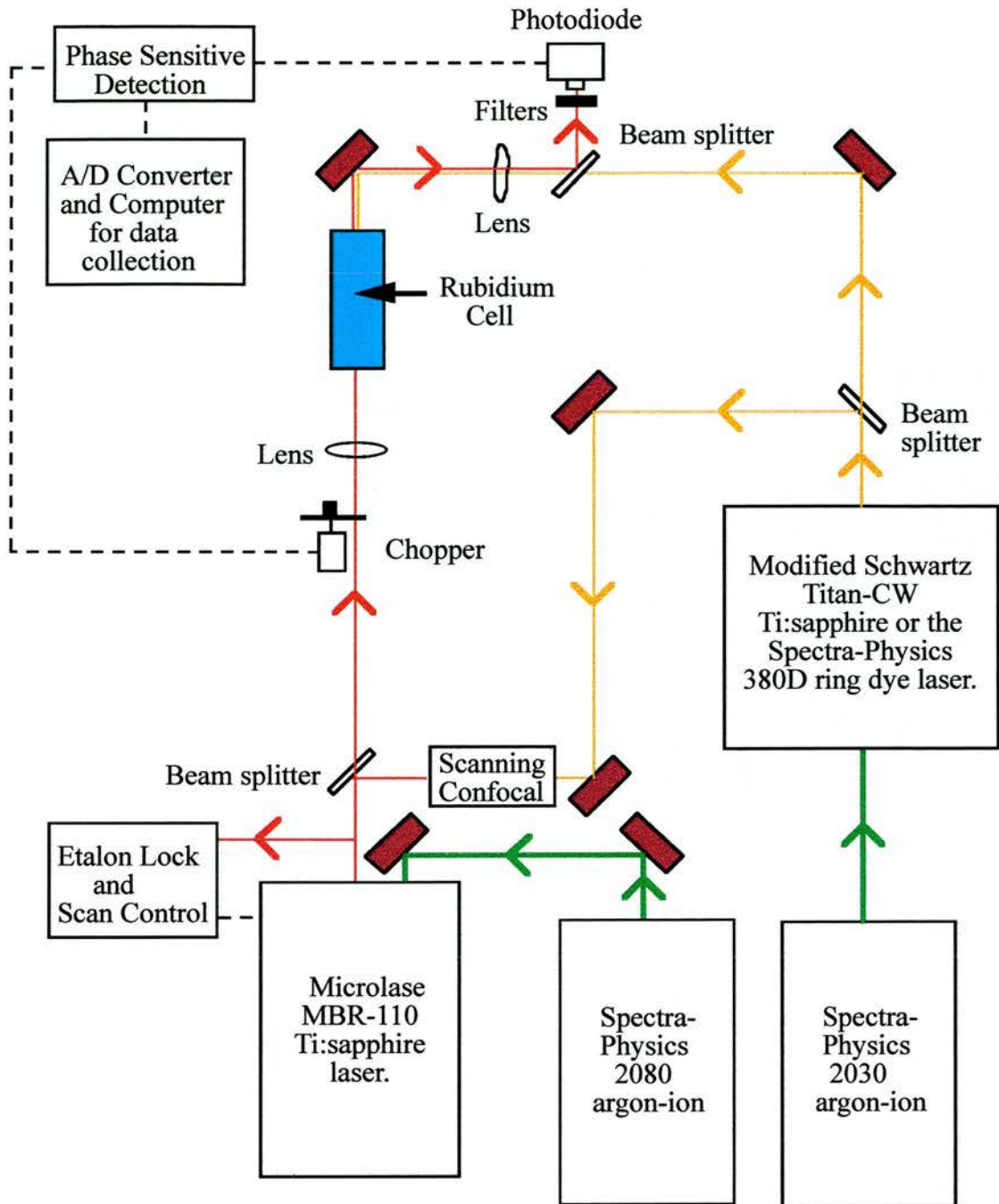


Figure 3.9:- Schematic of apparatus employed for atomic coherence experiments.

3.3.4) Experimental Apparatus For Future Work

3.3.4.1) An Atomic Beam

Historical Perspective

The subject of atomic or molecular beams is the study of directed beams of neutral particles at such low pressures that the effects of particle collisions are for the most part negligible. The earliest atomic-beam experiments were performed by Dunoyer [16]. He heated sodium, in an evacuated glass chamber, until it vaporised and then watched for a deposit to form at the far end of the chamber. The deposit was of the form expected, based on the assumption that the sodium atoms travel in straight lines in an evacuated tube.

Subsequent to Dunoyer's pioneering work, many different experiments based on molecular-beam methods have been performed. Of particular significance are the experiments carried out by Stern and his collaborators in the nineteen-twenties and early thirties [17, 18]. Their work laid down many of the principles of molecular-beam techniques which are followed even to the present day.

The development of molecular and atomic beams allowed, for the first time, precision measurements and concise studies within molecular and atomic structures. They provided a means for studying gas kinetics, for measuring the spins and magnetic moments of both atoms and nuclei and for examining the radio frequency spectrum of molecules and atoms. Experimental procedures for studying the above quantities are described extensively by Ramsey [19], along with atomic-beam design principles and techniques, which are still used today. However, some improvements in the atom sources have been made. These include: demountable ovens, for ease in replenishing the atom source[20]; three-stage beam sources, which greatly increase the intervals required between refilling [21, 22]; and the addition of a second oven stage to increase beam purity [21]. Referring to a recent caesium atomic beam design [23] it can be seen that the designs of atomic beams have not changed significantly in the last twenty-five years. Except for a more compact oven design, this atomic beam incorporates all the main features summarised by Ramsey [19].

Why An Atomic Beam Instead Of A Vapour Cell ?

Much of the theoretical analysis for atomic coherence experiments is carried out on ideal homogeneous two or three level systems [24, 25]. However, in an atomic vapour cell this ideal system is far from being the case. It is in fact very difficult, if not impossible to isolate an individual two or three level system, thus the whole ensemble must be examined at once. The thermal motion of the atoms within the cell causes Doppler broadening of the system, which may result in the desired observation being obscured or reduced. Replacement of the atomic vapour cell by an atomic beam is a reasonably simple method for reducing the effects of Doppler broadening while simultaneously allowing the study of clean two or three level systems. The observation of the predicted two-photon gain in a strongly driven two-level atom, [25], was simplified by the use of a barium atomic beam within the experiment [26]. Also, a very good approximation of an isolated three-level atom was obtained, using a sodium atomic beam, for the observation of the Autler-Townes effect [27] and more recently within a laser oscillation without population inversion experiment [28].

The St. Andrews Atomic Beam

An atomic beam system must be constructed within an evacuated chamber [29, 30], the low ambient pressure ensuring a sufficiently long mean free path of the atoms. In this section, the designed vacuum chamber, as well as the elements comprising the atomic beam apparatus are described. A schematic diagram of the atomic beam apparatus is shown in Figure 3.10.

The vacuum chamber comprises of five stainless steel sections: an oven chamber, two six-arm cross pieces, a T-piece and a liquid nitrogen tank. Stainless steel flanges, containing either copper or viton gaskets are found at the end of each section. These flanges are bolted together to form an effective vacuum tight seal. To allow the entry and exit of Ti:sapphire laser beams (~760-800 nm) to the interaction region, quartz windows are mounted on the two side arms (perpendicular to the atomic beam axis) of each of the six-arm sections. Quartz optical flats are fitted to the top arm of each six-arm section, to allow observation of fluorescence signals from the interaction regions.

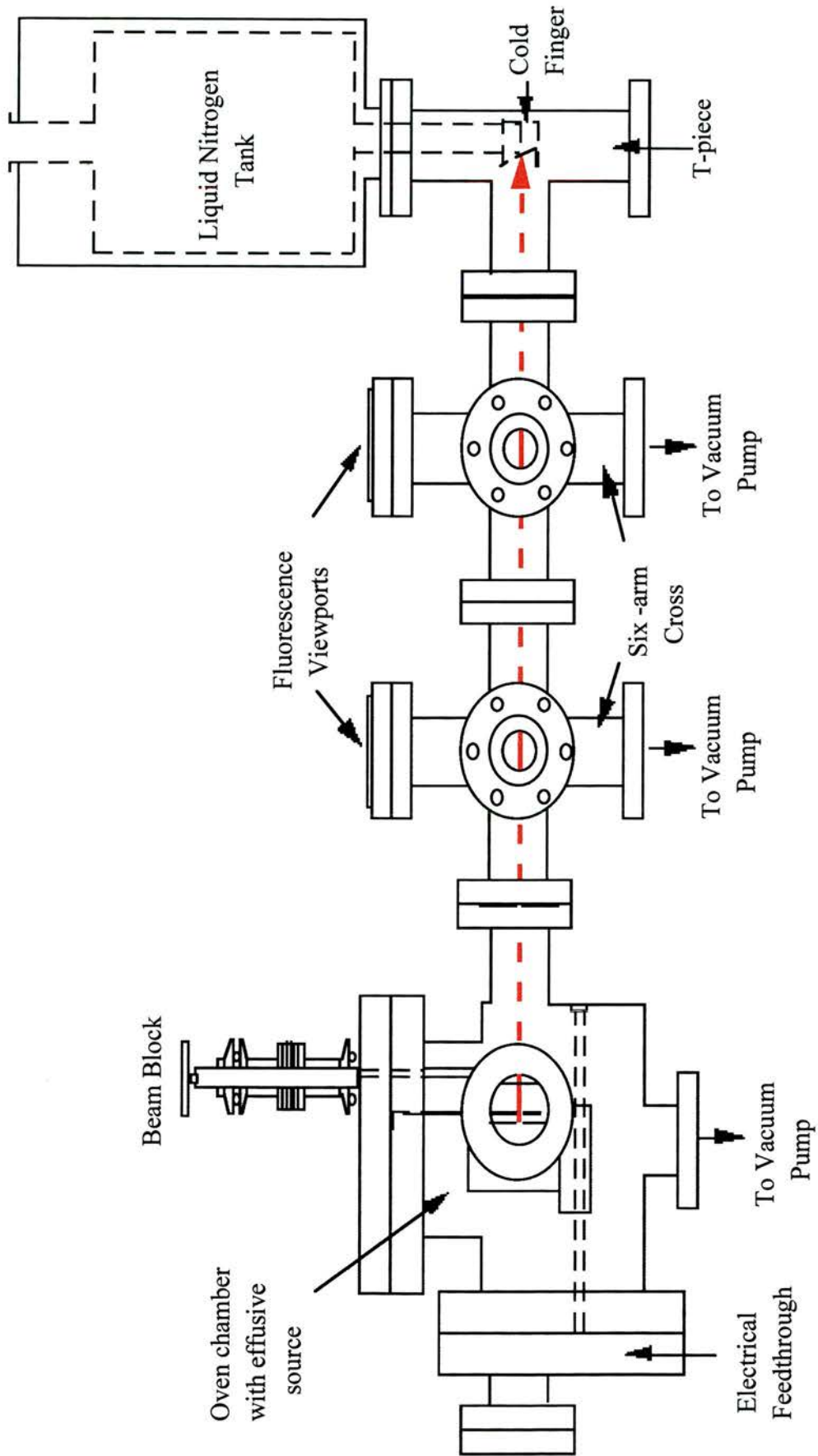


Figure 3.10:- Schematic diagram of the atomic beam

Electrical connections for the atom source inside the oven chamber are supplied by means of a vacuum feedthrough, mounted in an adapter section situated behind the oven.

A schematic diagram of the proposed pumping arrangement to be employed is shown in Figure 3.11. Two diffusion pumps are fitted, one under the oven chamber, the other under the interaction regions of the six-arm pieces. Initially the whole vacuum system will be pumped down from atmospheric pressure by an Edwards rotary pump, which will also serve as a backing pump for the diffusion pumps. It is expected that the pressure in the system, with the atomic beam running, will be of the order 10^{-6} - 10^{-7} mbar.

The rubidium forming the atomic beam is emitted from a small stainless steel oven, acting as an effusive source. The oven assembly is shown in Figure 3.12. The oven has an aperture cut in it, 1 mm in diameter and 1 mm thick. This aperture has to be correctly aligned with two 5 mm diameter apertures, used for collimating the beam. The first aperture is located in a plate attached to the lid of the oven chamber, the second is located in the flange between the oven chamber and the first six-arm piece. Alignment is achieved by the use of a He-Ne laser which is directed into the vacuum chamber and steered along the atomic beam axis. The oven is then correctly positioned by the use of the translation stage, on which it sits. Attaching the translation stage to steel rods in the oven chamber allows the alignment to be optimised. The oven does not in fact sit directly on the translation stage but rests on a ceramic bead, and is fastened in position by a ceramic knife edge, thus reducing heat conduction from the oven. An integral part of the oven lid is a rod with a baffle attached to its end. Movement of this baffle prevents clogging of the oven aperture. A copper washer ensures a good seal between the lid and the oven. The heating element is made up of a stainless steel sleeve, which fits tightly over the oven, wrapped around which are several turns of Thermocoax heating wire. Small stainless steel bands, spot-welded onto the sleeve hold the Thermocoax wire in place. A stainless steel radiation shield is placed over the oven to reduce heat losses and so improve the oven efficiency. The temperature of the oven is monitored by a thermocouple, which is attached to the translation stage and slotted into a small depression in at the rear of the oven. The Thermocoax wire is specified to have a line resistance of $5.5 \Omega \text{m}^{-1}$ and operate safely up to temperatures of $600 \text{ }^\circ\text{C}$.

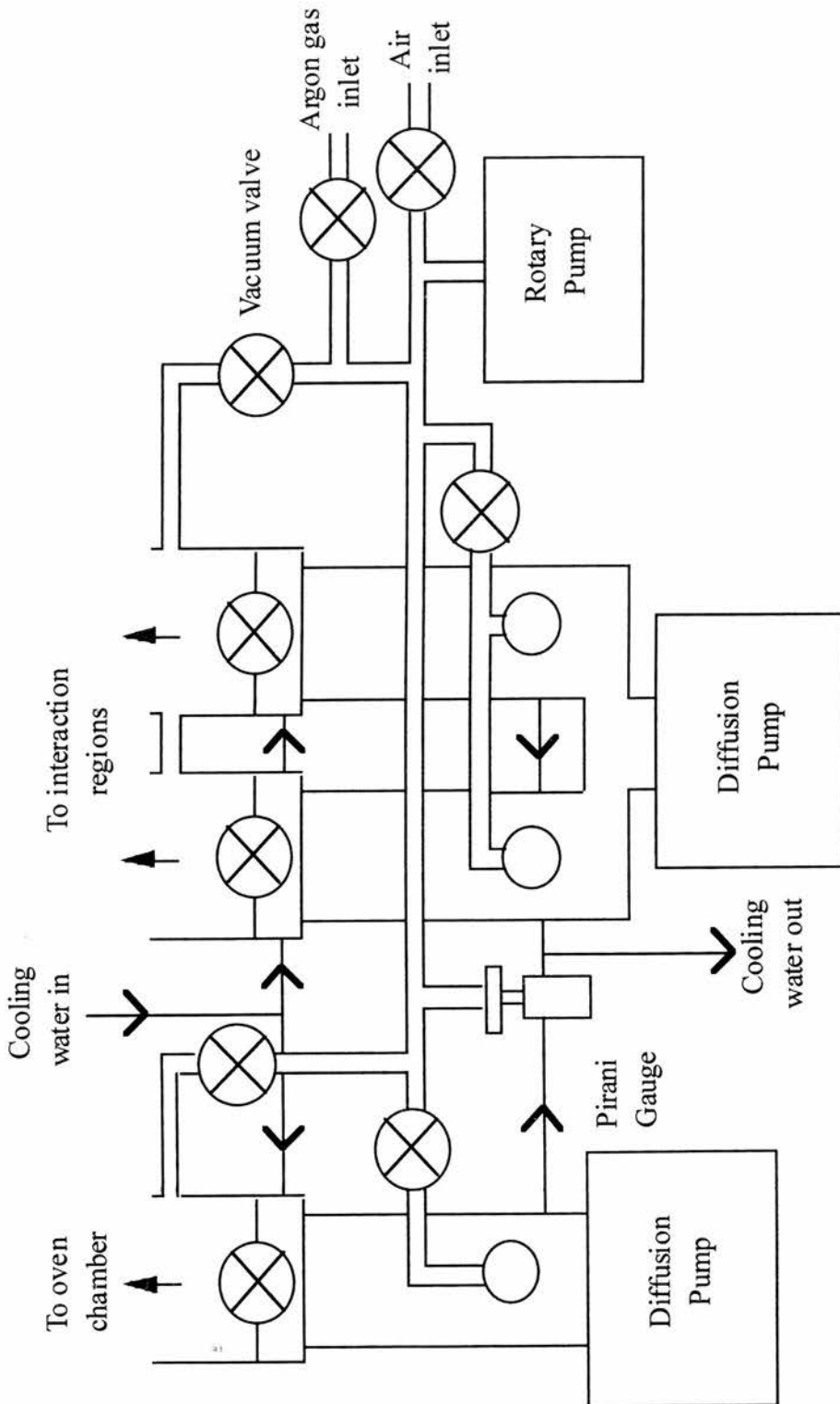


Figure 3.11:- Schematic diagram of vacuum pumping arrangement for the atomic beam

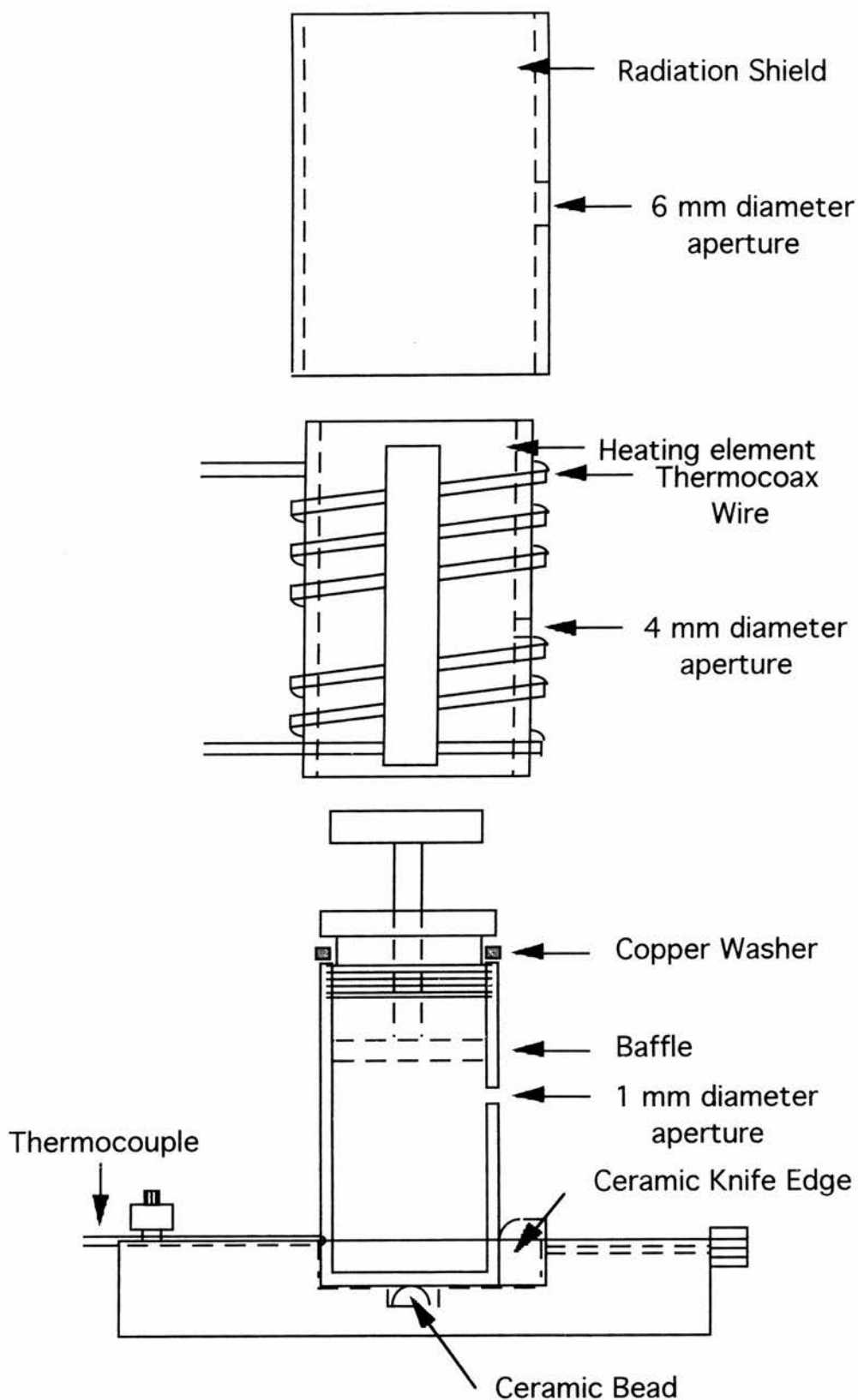


Figure 3.12:- Schematic diagram of oven assembly.

With a driving voltage of ~ 20 V it is expected that the oven will be easily heated to ~ 230 °C, as is required.

The rubidium is supplied in glass ampoules containing 1 g of the pure metal. One of these is loaded into the oven, broken and sealed inside the vacuum system. This is all done under a stream of argon gas since, in air, an oxide layer forms quickly on the metal surface, contaminating the sample and also preventing the formation of a beam.

A beam block, shown in Figure 3.11, which is operated from outside the vacuum chamber by means of a threaded bellows, simply allows the experimenter to tell whether the beam is propagating along the chamber or not. When lowered into the beam it can be assumed that no rubidium atoms are reaching the copper cold finger, directly from the oven source.

The melting point of rubidium is 38.8 °C and so it has a comparatively high vapour pressure at room temperature (1.2×10^{-7} mbar). This means that rubidium atoms reaching the T-piece of the vacuum chamber, would linger in this area before being pumped out or condensing on the chamber walls. Thus, a steady state cloud of rubidium atoms would build up and so the atomic beam quality would deteriorate. To prevent this cloud from forming, a liquid nitrogen copper cold finger has been constructed. The cold finger is shown in the schematic diagram of Figure 3.11. With the cold finger at temperatures ~ -150 °C, the rubidium atoms from the atomic beam condense on the angled face, thereby preventing the formation of a background cloud.

To date the atomic beam has not been tested within an experimental context. The construction of the beam and vacuum system has now been completed. The system has passed initial vacuum tests but still requires further testing with all the quartz windows in place.

Acknowledgements

I would like to acknowledge the much needed advice received in the design of this atomic beam. My thanks go to Dr. P Ewart and Dr. I. Hughes, of the Clarendon Laboratories, Oxford, for permitting me to examine their atomic beam and thereafter providing invaluable consultation time. I would also like to thank Mr. R.H. Mitchell, Senior Scientific Officer at the University of St. Andrews, for his help and experience with the vacuum technology and cryogenics involved in this atomic beam. Finally I would like to thank Mr. J. Lindsay and Mr. J. Clark for the construction of the atomic beam.

References

- [1] **G.K. Woodgate**, *Elementary Atomic Structure*, Second Edition (Clarendon Press, Oxford (1980)).
- [2] **M. Weissbluth**, *Atoms And Molecules*, Student Edition (Academic Press Inc., London (1978)).
- [3] **B.W. Shore**, *The Theory Of Coherent Atomic Excitation*, (Wiley, New York (1990)).
- [4] **E.U. Condon and G.H. Shortley**, *The Theory Of Atomic Spectra*, (University Press, Cambridge (1953)).
- [5] **Charlotte E. Moore**, *Atomic Energy Levels*, Vol. 2 (National Bureau Of Standards, Washington, (1949)).
- [6] **E. Arimondo, M. Inguscio and P. Violino**, *Experimental Determination Of The Hyperfine Structure In The Alkali Atoms*, Rev. Mod. Phys. 49, 31 (1977).
- [7] **S. Shepherd**, *Use And Development Of A CW Titanium Sapphire Laser For NonLinear Optics*, PhD thesis, University of St. Andrews (1993).
- [8] **I.I. Rabi**, Space Quantisation In A Gyating Magnetic Field, Phys. Rev. 51, 652 (1937).
- [9] **S. Wolfram**, *Mathematica: A System For Doing Mathematics By Computer*, (Addison-Wesley, 2nd Edition, Reading (1993)).
- [10] **Spectra-Physics**, *Model 2030 and 2035 High Power Ion Lasers Instruction Manual*, (1988).
- [11] **Spectra-Physics**, *BeamLokTM 2060 and 2080 Ion Laser User's Manual*, (1992).
- [12] **Microlase Optical Systems**, *MBR-110 Ti:sapphire Laser Operator's Manual: Part I*, (1993).

- [13] **Schwartz Electro Optics**, *Titan-CW Series Preliminary Operator's Manual*.
- [14] **Spectra-Physics**, *Model 380D Frequency Stabilised Dye Laser Instruction Manual*, (1979).
- [15] **R.B. Miles and S.E. Harris**, *Optical Third-Harmonic Generation In Alkali Metal Vapours*, IEEE J. Quantum Electron. QE-9 , 470 (1973).
- [16] **L. Dunoyer**, *The Kinetic Theory Of Gases And The Realisation Of A Material Radiation Of Thermal Origin*, Comptes Rendus 152 , 592 (1911).
- [17] **O. Stern**, *Transformation Of Atoms Into Radiation*, Zeits. f. Physik 39 , 751 (1929).
- [18] **F. Knauer and O. Stern**, *Intensity Measurements Of Molecular Radiation From Gases*, Zeits. f. Physik 53 , 766 (1929).
- [19] **N.F. Ramsey**, *Molecular Beams*, (Oxford University Press, Oxford (1956)).
- [20] **H. Yasunga**, *Calibrated Source Of Atomic Cesium Beams*, Rev. Sci. Instrum. 47 , 726 (1976).
- [21] **M. Lambropoulos and S.E. Moody**, *Design Of A Three-Stage Alkali Beam Source*, Rev. Sci. Instrum. 48 , 131 (1977).
- [22] **G.M. Carter and D.E. Pritchard**, *Recirculating Atomic Beam Oven*, Rev. Sci. Instrum. 49(1) , 120 (1978).
- [23] **G.S. Tompa, J.L. Lopes and G. Wohlrab**, *Compact Efficient Modular Cesium Atomic Beam Oven*, Rev. Sci. Instrum. 58(8) , 1536 (1987).
- [24] **R.M. Whitley and C.R. Stroud Jr.**, *Double Optical Resonance*, Phys. Rev. A 14 , 1498 (1976).

- [25] **M. Lewenstein, Y. Zhu and T.W. Mossberg**, *Two-Photon Gain And Lasing In Strongly Driven Two-Level Atoms*, Phys. Rev. Lett. 64, 3131 (1990).
- [26] **Y. Zhu, Q. Wu, S. Morin and T.W. Mossberg**, *Observation Of A Two-Photon Gain Feature In The Strong-Probe Absorption Spectrum Of Driven Two-Level Atoms*, Phys. Rev. Lett. 65, 1200 (1990).
- [27] **H.R. Gray and C.R. Stroud Jr.**, *Autler-Townes Effect In Double Optical Resonance*, Opt. Commun. 25, 359 (1978).
- [28] **G.G. Padmabandu, G.R. Welch, I.N. Shubin, E.S. Fry, D.E. Nikonov, M.D. Lukin and M.O. Scully**, *Laser Oscillation Without Population Inversion In A Sodium Atomic Beam*, Phys. Rev. Lett. 76, 2053 (1996).
- [29] **J. Strong**, *Procedures In Experimental Physics*, (Prentice Hall Inc., New York (1938)).
- [30] **A. Guthrie and R.K. Wakerling**, *Vacuum Equipment And Techniques*, (McGraw-Hill Book Co., New York (1949)).

Chapter 4

A Comparison Of Schemes For The Study Of Continuous-Wave Electromagnetically Induced Transparency

This chapter introduces some of the fundamental concepts of E.I.T. and presents some of the difficulties that arise when trying to observe E.I.T. experimentally in a Doppler broadened medium. The chapter begins with a brief resume of previously employed schemes for observing E.I.T. Next follows a theoretical comparison between the three most popular schemes for observing E.I.T. This includes a brief summary of results reported from a single atom model followed by a more in-depth analysis of results from homogeneously broadened density matrix models. An experimental investigation and comparison of E.I.T. between the three basic schemes within rubidium vapour is then presented.

4.1) Introducing Three Level E.I.T. Schemes

Interest has grown in E.I.T. since the first realisation that a dipole allowed transition could be rendered transparent due to the presence of a strong optical field interacting with a second connected dipole allowed transition [1]. A variety of systems have been studied both theoretically and experimentally [2, 3], however, the three systems of Figure 4.1 are by far the most popular.

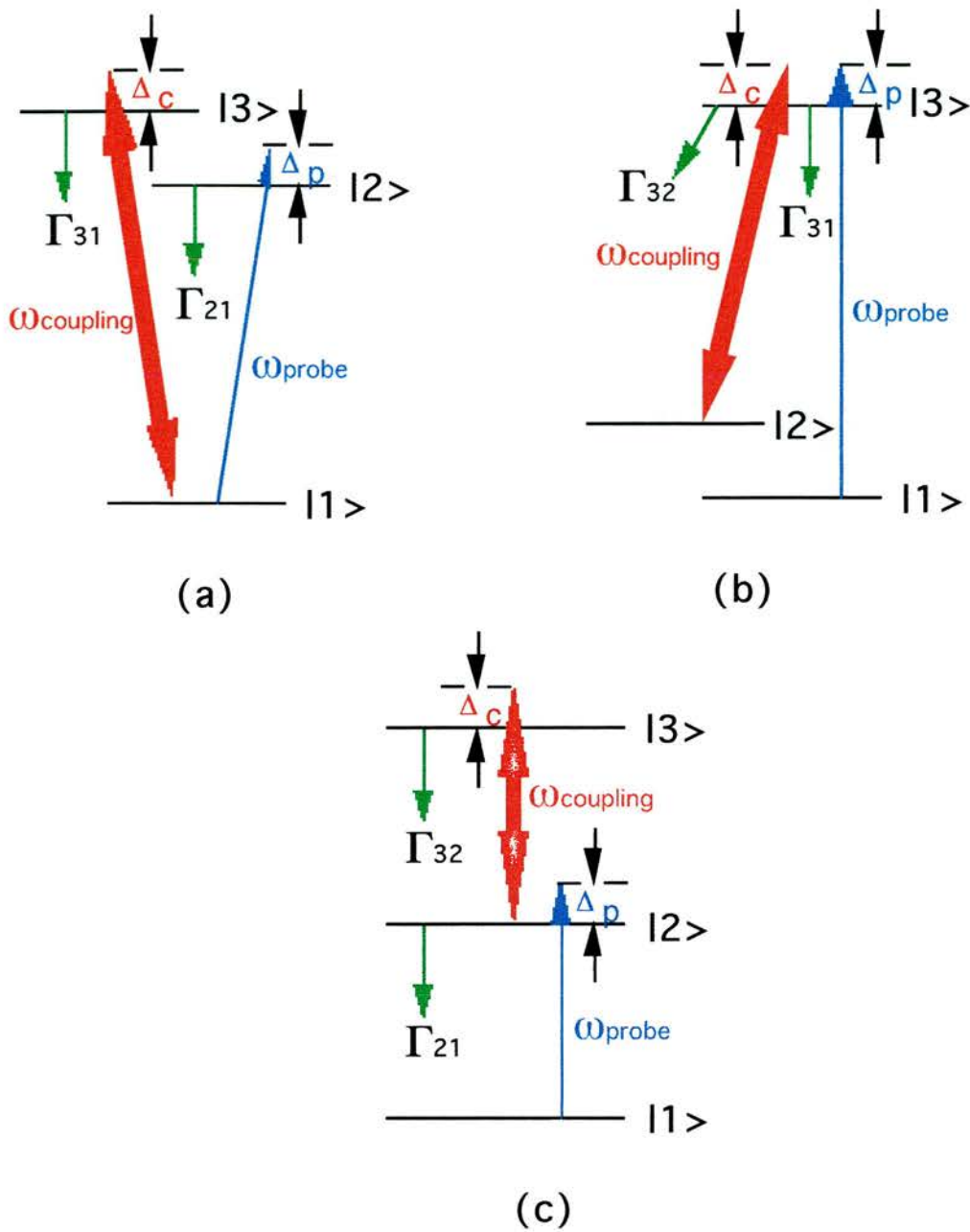


Figure 4.1:- Schematic energy level diagrams showing the ideal three level atoms, with relevant population decay values (Γ_i). Also shown are the probe field and coupling field transitions and detunings, ω_p , ω_c , Δ_p and Δ_c respectively for: (a) the V-type system, (b) the lambda system, and (c) the cascade system.

The first, Figure 4.1(a), is termed a V-type system. An initial theoretical and experimental comparison between V-type E.I.T., coherent population trapping, and multilevel optical pumping was discussed in papers by Weiss, Sander et. al. [4, 5]. They employed continuous-wave diode lasers to produce coherent electromagnetic fields, with output powers of ~ 10 mW, to explore a system within rubidium.

The second scheme is the so called lambda system, shown in Figure 4.1(b), which in fact was the one employed for the first experimental observation of E.I.T. [6]. This scheme was also used in the earlier work by Gray, Whitley and Stroud for their study of the "problematic" effects of coherent trapping of atomic populations [7], and in the continuous-wave coherence experiment of Akulshin, Celikov and Velichansky [8]. Although these authors were observing coherent population trapping effects, their experiments show distinctive E.I.T. features. However, this work was prior to the first discussion of E.I.T. by S.E. Harris and co-workers [1, 6], thus the connection to E.I.T., and its terminology, was not made. Extensive theoretical work has since been carried out on the lambda system [9, 10].

The final scheme, termed a cascade system, is shown in Figure 4.1(c). It was first shown to be experimentally viable for observing E.I.T. by Field, Hahn and Harris [11] when lead vapour was rendered transparent by the application of pulsed laser sources. This scheme has been the source of extensive study by the St. Andrews group. The bulk of the following chapters are devoted to E.I.T. and related effects within this scheme. This chapter will merely highlight some important characteristics of the cascade system and so allow a comparison of the three schemes to be carried out.

4.2 Theoretical Ideal Three Level Systems

The induced transparency on a probe field in each system of Figure 4.1 can be considered to be the result of destructive interference between two *possible* paths for absorption: direct absorption to the upper probe field state and indirect absorption to the same state which first involves transfer of population to an intermediate state and back. For the cascade system and the lambda system the population transfer processes are damped away over a period of time (the time scale of this effect will be discussed in

section 4.2.2) leaving the population trapped in a coherent superposition of states. However, the V-type system is seen to produce E.I.T. without trapping any population. Both of these mechanisms leading to E.I.T. are discussed in section 4.2.1.

In order to observe E.I.T. the two applied optical fields must satisfy the following two-photon field detuning criteria :

$$\Delta_p \pm \Delta_c = 0 \quad (4.1)$$

where the + sign corresponds to cascade systems and the - sign to lambda and V-type systems. Equation (4.1) is an obligatory but not defining condition for the observation of E.I.T. Induced Rabi frequencies and decay rates also make an important contribution, more of which shall be discussed in section 4.2.2. In order to best satisfy equation (4.1) for all velocity groups in a Doppler broadened medium it is required that the applied optical fields co-propagate for lambda and V-type systems while they must counter-propagate for cascade systems. When the two-photon condition is met the velocity groups experience E.I.T. at the similar probe frequencies (a small variation remains due to different Doppler shifts occurring as a result of the small wavelength mismatch of the optical fields). If however, the two-photon condition is not satisfied then all the velocity groups experience E.I.T. at different probe frequencies. Thus, when we integrate across all the velocity groups the E.I.T. experienced by one velocity group at one particular frequency is masked by the absorption experienced by the other groups.

4.2.1) E.I.T. Within Single Atom Three Level Systems

By employing the single atom state amplitude model described in Section 2.1.1, Dunn outlines two separate mechanisms for producing E.I.T [12]. The first describes the physical process of E.I.T. within the lambda and cascade systems (Figure 4.1(b) and Figure 4.1(c) respectively). Consider a cascade system with the population initially all in level $|1\rangle$. The state amplitudes of this system are described by the following three coupled equations:-

$$\dot{a}_1 = -i\Omega_p a_2 - \gamma_1 a_1 \quad (4.2)$$

$$\dot{a}_2 = -i\Omega_p a_1 - i\Omega_c a_3 - \gamma_2 a_2 \quad (4.3)$$

$$\dot{a}_3 = -i\Omega_c a_2 - \gamma_3 a_3 \quad (4.4)$$

where Ω_c and Ω_p are the Rabi frequencies of the coupling and probe field respectively and γ_i are open system population decay rates as described in Section 2.1.1.

In Figures 4.2 - 4.3 a red arrow represents the presence of the coupling field and a blue arrow the presence of the probe field. The moduli of the three states along with the imaginary component of the polarisation experienced on the probe field transition are all plotted against time (all values are in arbitrary units). The imaginary component of the polarisation is a direct measure of the absorption experienced by the probe field. The time averaged value of this quantity over the effective lifetime of the atom is a measure of the total net effect of the radiation field on the atom. A negative value would indicate gain and a positive value absorption. The value of this time average is included in each of the polarisation diagrams.

The presence of a strong coupling field in the cascade system is shown to dramatically reduce the absorption experienced by the weak probe field, see Figure 4.2. The time average of the imaginary component of the probe transition polarisation has been reduced by a factor of 20 from the case where no coupling field was present. This is simply the phenomena of E.I.T. A notable feature is that as time progresses the state amplitudes a_1 , a_2 and a_3 (and hence the associated populations) experience damped harmonic motion and so tend to steady state values, see Figure 4.2. How long the state amplitudes take to reach a steady state is dealt with in more detail in Section 4.2.2.1 below. Population is seen to be trapped in a coherent superposition state of levels $|1\rangle$ and $|3\rangle$ with the amplitude of state $|2\rangle$ tending to zero. Examination of equations (4.2)-(4.4) provides the explanation for this E.I.T. process. Amplitude is being fed into state $|2\rangle$ from state $|3\rangle$ by the coupling field (as described by the second term on the right of equation (4.3)) which over a period of time is exactly equal in magnitude but in anti-phase with the amplitude that is being fed into state $|2\rangle$ from state $|1\rangle$ by the probe field (first term on the right hand side of equation (4.3)).

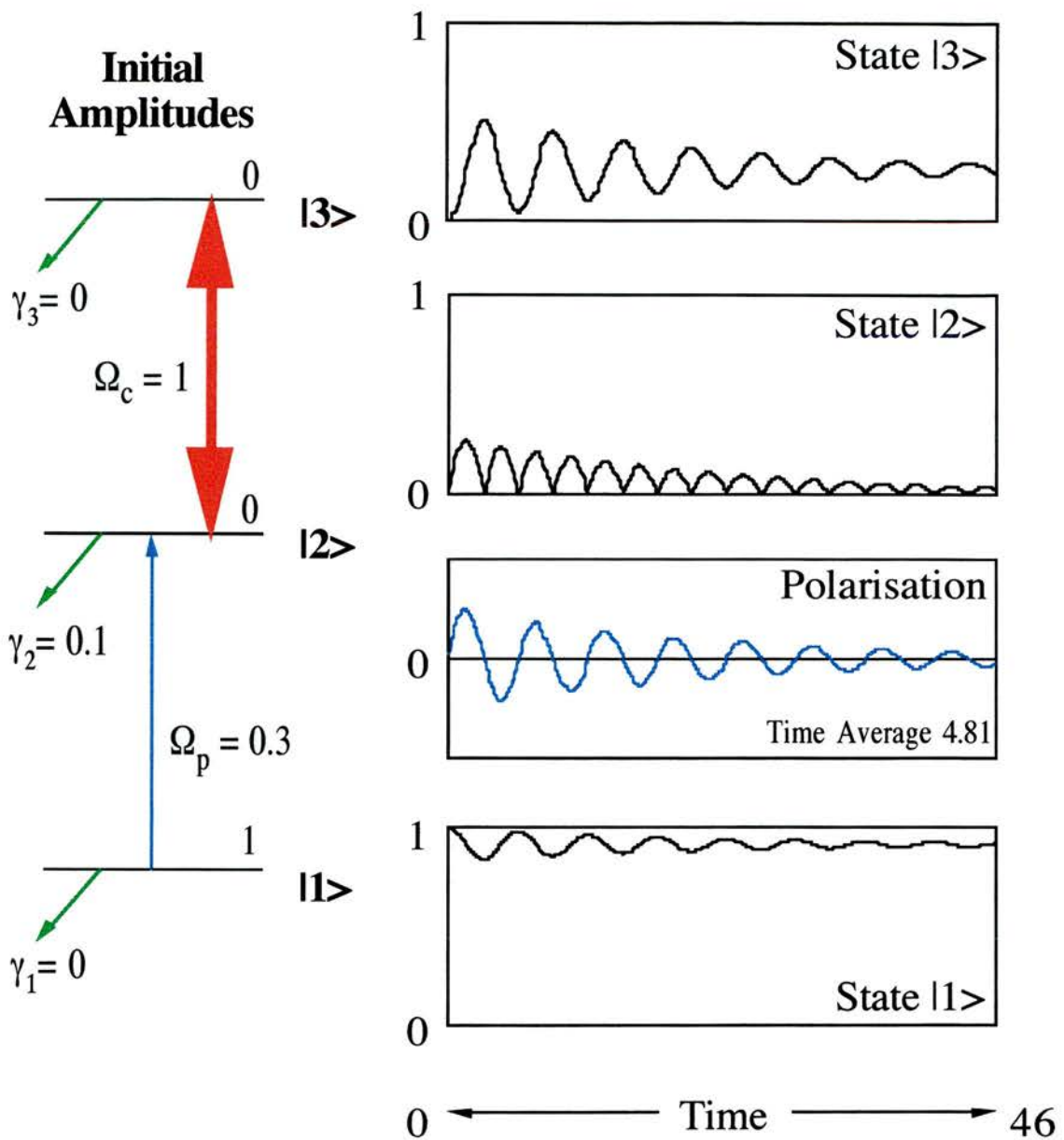


Figure 4.2:- Three level amplitude model results for a cascade system. All parameters are given in arbitrary units. The coupling strength between states $|2\rangle$ and $|3\rangle$ is 1.0, and between states $|1\rangle$ and $|2\rangle$ is 0.3. The only non-zero population decay rate is that from state $|2\rangle$ having a value of 0.1. The moduli of the state amplitudes a_1 , a_2 and a_3 are plotted as functions of time. Also plotted as a function of time is the imaginary component of the polarisation for the probe field transition $|1\rangle - |2\rangle$, shown in blue.

Thus, there is no net effect on the amplitude of state $|2\rangle$ and so the probe field polarisation tends towards zero. A relation between the magnitudes of the state amplitudes of states $|1\rangle$ and state $|3\rangle$ is obtained for the steady state regime by neglecting population decay terms and by setting $\dot{a}_2 = 0$ in equation (4.3). Thus:

$$a_1 = -\frac{\Omega_c}{\Omega_p} a_3 \quad (4.5)$$

From equation (4.5) it is clearly seen that the magnitudes of the trapped state amplitudes are directly related to the ratio of the induced Rabi frequencies. Thus if the optical fields induce Rabi frequencies in the ratio 1:10 ($\Omega_c:\Omega_p$) then the trapped state amplitudes are found to be in the ratio 1:10 ($a_1:a_3$). Equivalently the trapped state populations would then be in the ratio 1:100 ($\langle a_1 \rangle:\langle a_3 \rangle$).

E.I.T. within the lambda system is seen to be totally analogous to that of the cascade system. Here the probe field couples state $|1\rangle$ and $|3\rangle$ while the coupling field couples states $|2\rangle$ and $|3\rangle$. As can be seen from Figure 4.3 a trapped population is rapidly established in a coherent superposition of states $|1\rangle$ and $|2\rangle$. This results in little decay occurring from state $|3\rangle$ and so there is very little absorption of the probe field i.e. E.I.T. has been induced on the probe transition.

Turning now to the V-type system, see Figure 4.1(a), it is seen that unlike the lambda and cascade systems there is no trapped population formed by the coherent superposition of the uncoupled amplitude states. Figure 4.4 highlights the fact that E.I.T. is observed in the V-type system in that there is little amplitude transfer to state $|2\rangle$ from state $|1\rangle$ hence, the magnitude of the associated time average of the polarisation on probe field transition is small. However, it is apparent that in the V-type system a trapped population is not formed. Amplitude rapidly oscillates between states $|1\rangle$ and $|3\rangle$ due to the coupling field. This leads to the cancellation of the amplitude transfer between states $|1\rangle$ and $|2\rangle$ because the rapidly changing amplitude in state $|1\rangle$ causes the sign of the polarisation on the state $|1\rangle - |2\rangle$ transition to rapidly cycle. This polarisation quickly averages over time to be close to zero.

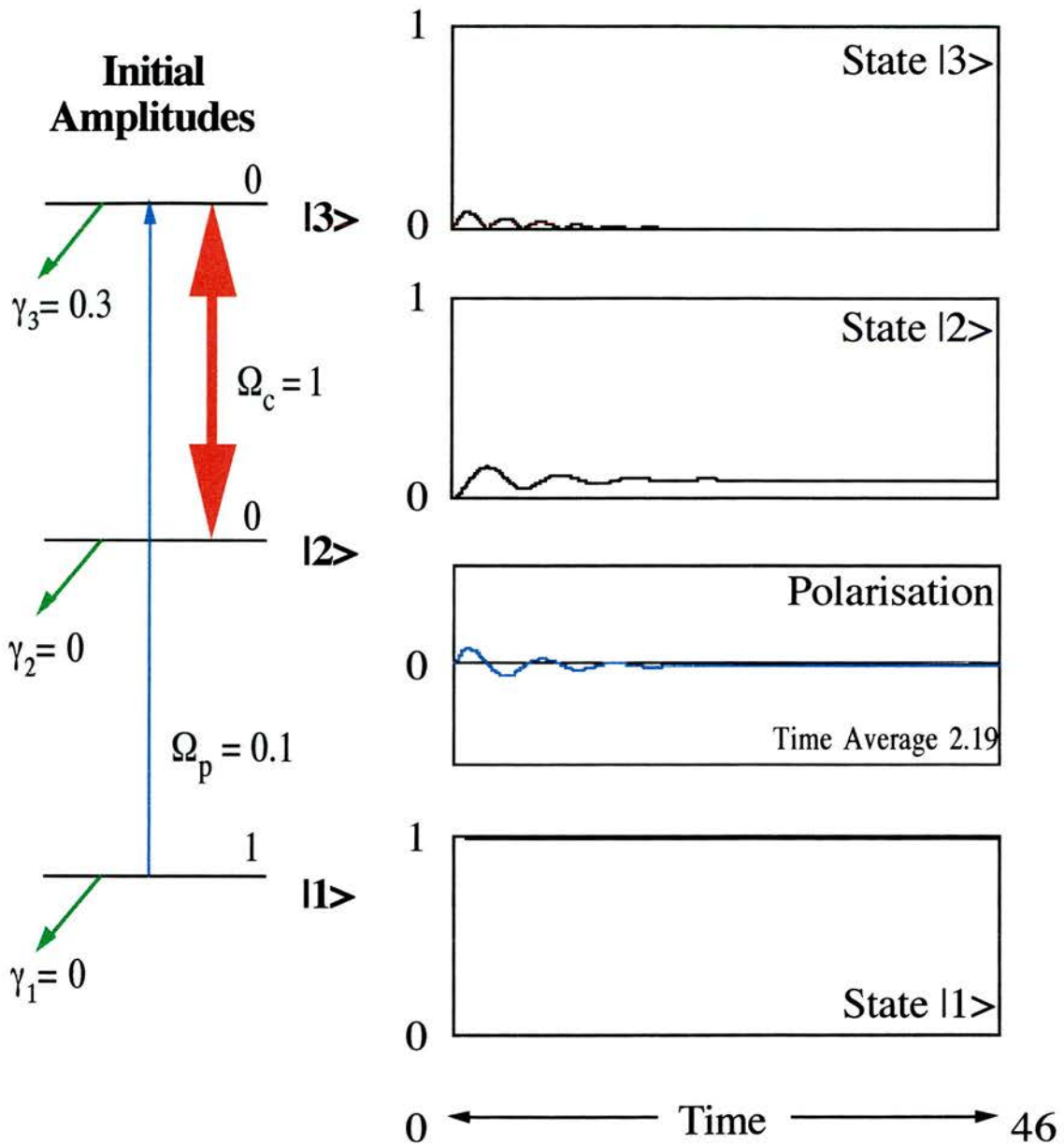


Figure 4.3:- Three level amplitude model results for a lambda system. All parameters are given in arbitrary units. The coupling strength between states $|2\rangle$ and $|3\rangle$ is 1.0, and between states $|1\rangle$ and $|3\rangle$ is 0.1. The only non-zero population decay rate is that from state $|3\rangle$ having a value of 0.3. The moduli of the state amplitudes a_1 , a_2 and a_3 are plotted as functions of time. Also plotted as a function of time is the imaginary component of the polarisation for the probe field transition $|1\rangle - |3\rangle$, shown in blue.

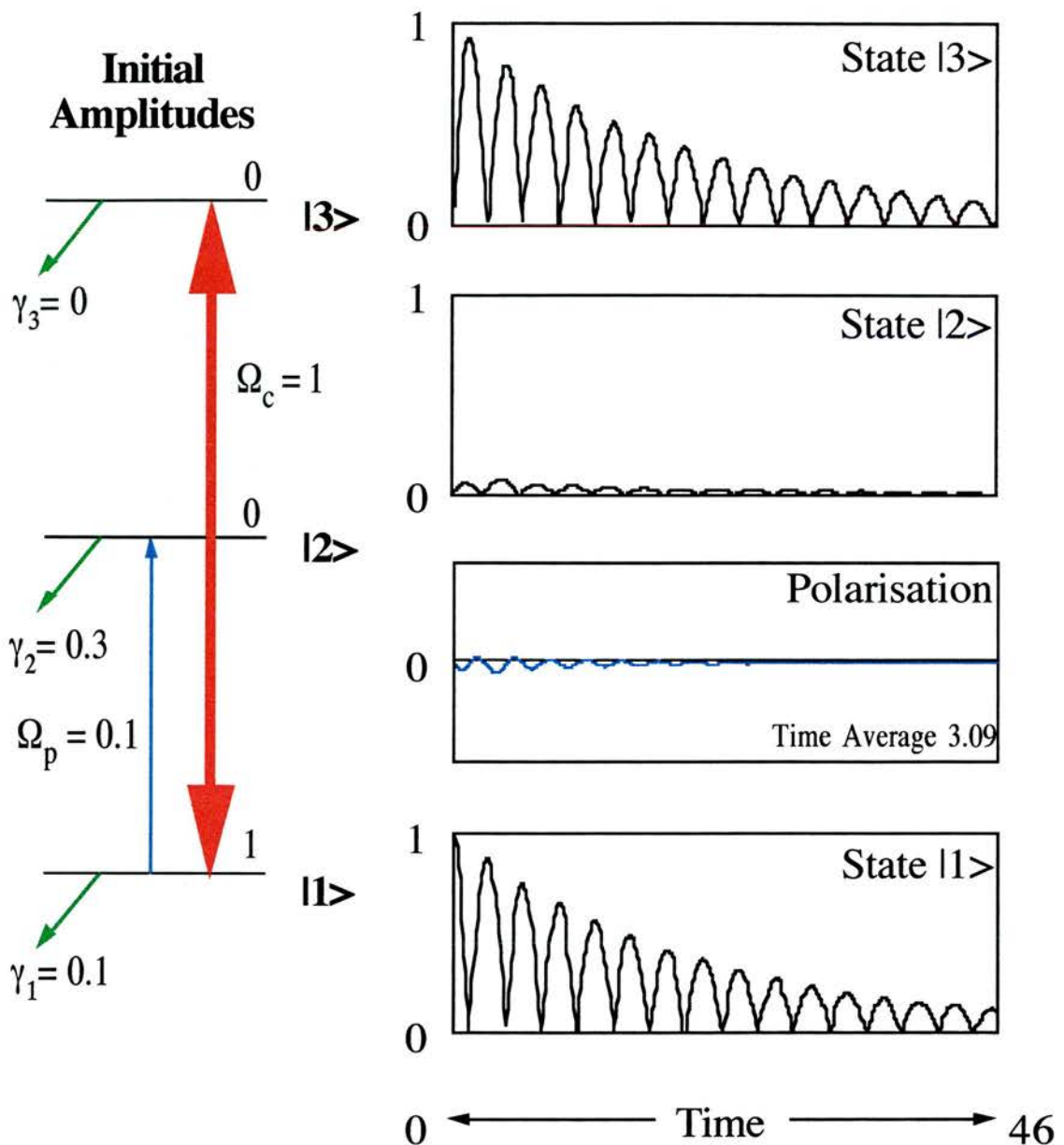


Figure 4.4:- Three level amplitude model results for a V-type system. All parameters are given in arbitrary units. The coupling strength between states $|1\rangle$ and $|3\rangle$ is 1.0, and between states $|1\rangle$ and $|2\rangle$ is 0.1. The population decay rates from states $|1\rangle$, $|2\rangle$ and $|3\rangle$ are 0.1, 0.3 and 0 respectively. The moduli of the state amplitudes a_1 , a_2 and a_3 are plotted as functions of time. Also plotted as a function of time is the imaginary component of the polarisation for the probe field transition $|1\rangle - |2\rangle$, shown in blue.

In the absence of the coupling field, absorption of the probe field would allow the atom to leave the system by the more rapid decay route from state $|2\rangle$, so resulting in net absorption. However, the rapid oscillations in the sign of the polarisation (Ω_c) effectively block this route for the atom and so it may only leave the system via the lower state $|1\rangle$, even though this has a lower decay rate than state $|2\rangle$, 0.1 as compared with 0.3. In so doing, the atom leaves the three level system without having extracted a photon from the probe field, and absorption is once more reduced. No trapped populations are involved in this system but E.I.T. still occurs as the result of destructive interference between the direct absorption pathway on the $|1\rangle - |2\rangle$ probe field transition, and the absorption pathway to state $|2\rangle$ which first experience amplitude beating with the $|1\rangle - |3\rangle$ coupling field transition.

4.2.2) E.I.T. Within An Ensemble Of Three Level Systems

4.2.2.1) An Estimate Of The Transient Response Time Of E.I.T.

An outline of the density matrix models employed to study systems containing large numbers of atoms (10^{17} atoms m^{-3}) has already been presented in Chapter 2. These models provide solutions for the three level ensemble systems once they have attained a steady state i.e. the non transient regions of the state amplitudes in the single atom models. This begs the questions:

- i) Typically, how long do we expect these transient regions to last ?
- ii) After the coupling field is turned on, how fast can the atomic medium become transparent to the probe field ?
- iii) Is this response time of this induced transparency limited by the atomic decay rates or by the Rabi frequency of the coupling field (Ω_c) ?

Li and Xiao [13] present some answers to these question through an examination of the relevant density matrix equations for the cascade system, which were explicitly derived in Section 2.2.1. By assuming that the two applied optical fields are exactly on resonance ($\Delta_c = \Delta_p = 0$) and that $\Omega_c \gg \gamma_{13}$ a solution for the time evolution of ρ_{21} is obtained:

$$\rho_{21}(t) = \rho_{21}(0) \exp\left(-\frac{\gamma_{12}}{2} t\right) \left(\cos\frac{\Omega}{2} t + \frac{\gamma_{12}}{\Omega} \sin\frac{\Omega}{2} t \right) \quad (4.6)$$

where $\Omega = \left(\Omega_c^2 - \gamma_{12}^2\right)^{1/2}$

It is obvious that, when $\Omega_c \gg \gamma_{12}$, equation (4.6) describes a damped harmonic oscillator with initial amplitude $\rho_{21}(0)$, frequency Ω , and damping rate γ_{12} . Thus, the authors show that at $\gamma_{12} t \approx 10$ the probe field reaches a steady state and the transient gain region has passed. For the cascade system employed for the majority of our experimental work (the $5S_{1/2}$ - $5P_{3/2}$ - $5D_{5/2}$ system within rubidium) $\gamma_{12} = 20$ MHz, thus our transient region will be of the order of $0.5 \mu\text{s}$. Since the Rabi frequency of the coupling field is much larger than the decay rate of the excited state of the system, the response time in which the optically dense medium becomes transparent (or negative absorption is obtained from the initial opaqueness) is limited by the Rabi frequency of the coupling field, not by the decay rate γ_{12} of the system. Since Rabi frequencies of several hundred megahertz can be achieved with focused Ti:sapphire lasers the response time for a rubidium medium to change from highly absorptive to transparent is on a nanosecond timescale. This optical switching of the probe field could be realised experimentally by switching the coupling field on and off with an electro-optic modulator or a Pockels cell.

4.2.2.2) A Comparison Of Ideal Systems

The following experiments deal with coherent effects induced on atomic systems due to the application of optical fields which are produced by employing continuous-wave lasers. The time scales involved in the experimental observations are far greater than those of the transient response regions. Therefore, the density matrix formalism provides a powerful, and accurate tool for carrying out a theoretical analysis on an ensemble of atoms. A simplified theoretical density matrix analysis is presented below which allows further comparisons between the three ideal E.I.T. systems to be made. For the purpose of this comparison we have assumed that:

- i) The three atomic systems are homogeneous. i.e. We neglect the effects of Doppler broadening.
- ii) All dipole allowed transitions have equal population decay rates (to which the coherence dephasing rates are directly related) and equal dipole transition matrix elements.
- iii) All dipole forbidden transitions have zero valued population decay rates.

In each system the coupling field is set to induce a Rabi frequency of 10 MHz, and the probe field a Rabi frequency of 1 MHz on their respective transitions. All non-zero population decay rates, Γ_{ij} , are set to 10 MHz. With these assumptions the coherence dephasing rates of the dipole forbidden transitions are (referring to Figure 4.1):

$$\text{i) V-type System:} \quad \gamma_{23} = \frac{1}{2}(\Gamma_{21} + \Gamma_{31}) \quad (4.7)$$

$$\text{ii) Lambda system} \quad \gamma_{12} = 0 \quad (4.8)$$

$$\text{iii) Cascade system} \quad \gamma_{13} = \frac{1}{2}\Gamma_{32} \quad (4.9)$$

The strength of an E.I.T window is strongly dependent on the coherence dephasing rate of the dipole forbidden transition. Therefore it is expected that, with all the other parameters being equal, the ideal lambda system will produce the best E.I.T. window and the ideal V-type system the poorest. However, E.I.T. is not the only source of increased transparency in these ideal models. Within the V-type system, E.I.T. cannot be isolated from an increased probe field transmission, induced by the coupling field saturating the $|1\rangle - |3\rangle$ transition. Also, the lambda system is complicated by population being optically pumped into level $|2\rangle$ by the probe field. However, population trapped due to optical pumping, within the lambda system, is normally reduced by the presence of the coupling field, since it acts to re-pump population out of level $|2\rangle$ back into the system. Thus, the presence of a coupling field causes the maximum absorption experienced by the probe field, in a lambda system, to be enhanced.

Three different curves, for each system, have been generated from these ideal three level models and are shown in Figure 4.5.

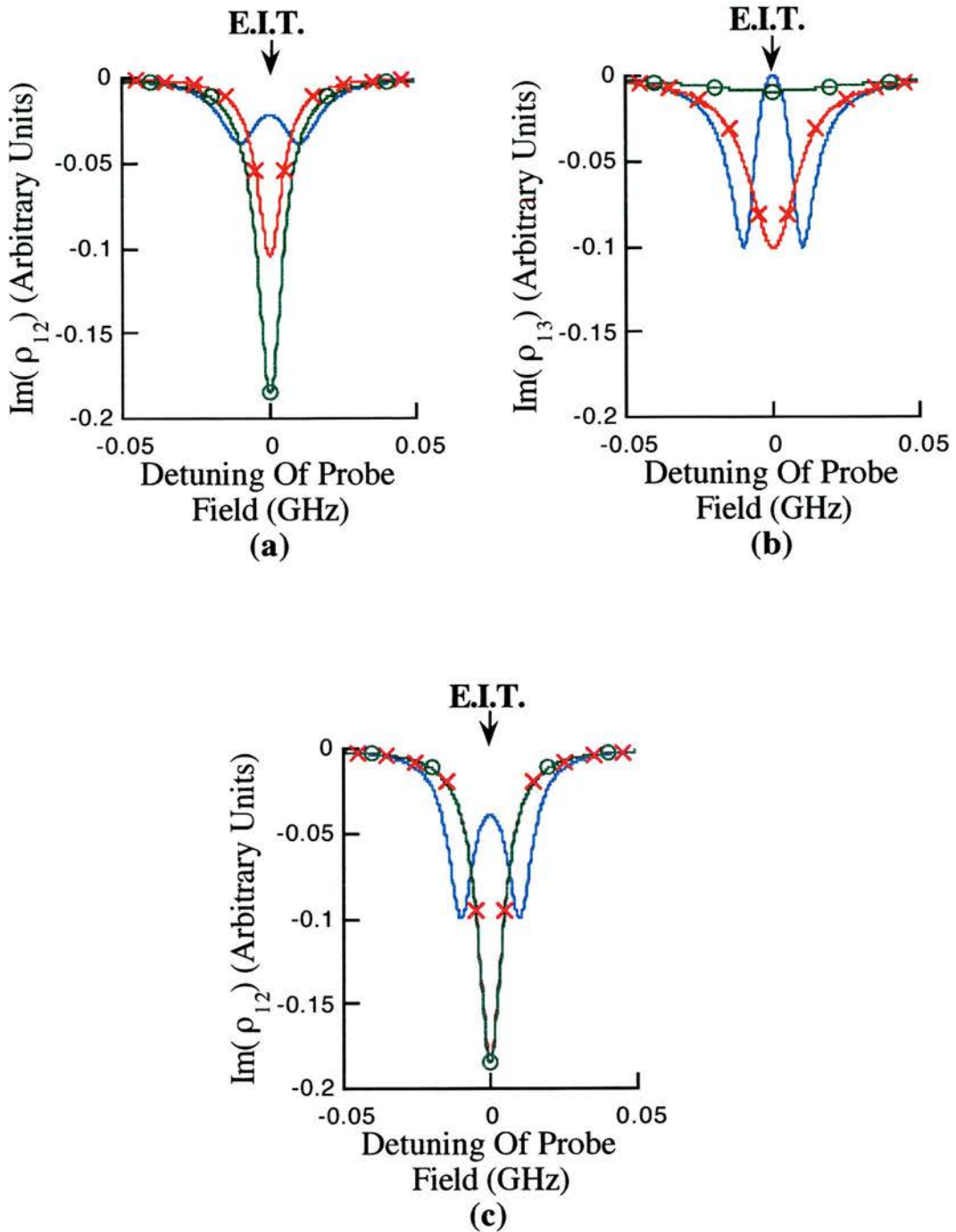


Figure 4.5:- $\text{Im}(\rho_{12})$ or $\text{Im}(\rho_{13})$ (proportional to probe field absorption) versus the detuning of the probe field for the ideal three level (a) V-type, (b) lambda and (c) cascade systems. Probe field Rabi frequency of 1 MHz, coupling field Rabi frequency of 10 MHz. All the non-zero population decay rates are set to be 10 MHz. Blue lines show absorption lineshapes including E.I.T. Red lines marked with red crosses are those with 10 GHz constant dephasing rate terms added to the uncoupled transitions. Green lines marked with green circles are those with 10 GHz constant dephasing rate terms added to both uncoupled and coupling field transitions.

In this figure the imaginary component of ρ_{12} for the V-type and cascade systems, and ρ_{13} for the lambda system, which are directly related to the absorption experienced by the probe field, have been plotted against the detuning of the probe field. The blue solid lines show the absorption lineshapes generated for each system, in the presence of all the induced transparency mechanisms. The greatest transparency depth can be seen to occur in the lambda system and is simply due to the effect of E.I.T. However, the V-type system is seen to produce a transparency window of greater depth than the cascade system, since this window is a result of the combination of E.I.T. and coupling field saturation. The E.I.T. windows can be artificially removed by increasing the dephasing rate on the uncoupled transition in each system. This is achieved by adding a constant dephasing rate term of 10 GHz to equations (4.7) - (4.8). Three curves incorporating this change are represented by the red lines marked with red crosses in Figure 4.5. It is seen that the maximum absorption of the probe field in the V-type and lambda systems is less than in the cascade system due to coupling field saturation effects and population trapping within level $|2\rangle$, respectively. A more realistic alteration to the ideal models is to dephase particular atomic levels rather than just single transitions. i.e. level $|3\rangle$ in the V-type and cascade system, and level $|2\rangle$ in the lambda system. This results in the dephasing of all the coherence terms related to this level, and so the coupling field transition as well as the uncoupled transition must be artificially dephased. This is the case represented by the green lines marked by green circles in Figure 4.5. By increasing the dephasing rate on the coupling field transition the interaction between the optical field and the atom is effectively reduced. Thus, the effects of coupling field saturation within the V-type system and optical re-pumping within the lambda system are reduced by increasing the related dephasing rate. An analysis of the density matrix equations used to derive the cascade model (See Section 2.2.1) reveals that the absorption of the coupling field is given by:

$$\rho_{23}^i = \frac{\Omega_c(\rho_{33} - \rho_{22}) + \Omega_p \rho_{13}^r - \Delta_c \rho_{23}^r}{\gamma_{23}} \quad (4.10)$$

Thus, when the coupling field is on exact resonance ($\Delta_c = 0$) and is much stronger than the probe field ($\Omega_c \gg \Omega_p$) then:

$$\rho_{23}^i = \frac{\Omega_c(\rho_{33} - \rho_{22})}{\gamma_{23}} \quad (4.11)$$

From equation (4.11) it can be seen that an artificial increase of the dephasing rate on the coupling field transition produces the same effect as a reduction of the coupling field power.

In practise, a complete comparison between the three schemes is hindered because three systems with identical atomic parameters do not exist. For this reason, population decay rates, coherence dephasing rates and dipole matrix elements between levels $|1\rangle$, $|2\rangle$ and $|3\rangle$ for each system of Figure 4.1, will vary, affecting the E.I.T. realised in each. Also the energy levels involved with the dipole forbidden transitions can never have zero valued population decay rates. This is because these forbidden lines may still occur through transitions other than electric dipole transitions and further dephasing may be induced through collisional mechanisms [14]. Interaction with only three levels within an atomic structure is itself difficult because each level usually has associated structure. It is found that optical pumping between hyperfine ground states greatly complicates the interpretation of experimental results within the V-type and lambda systems. However, by varying the experimental procedures between systems, it is often possible to get round these complicating optical pumping characteristics. A further limitation of our ideal three level models is the assumption that the levels are purely homogeneously broadened. The following experiments are carried out in vapour cells and so inhomogeneous Doppler broadening of the systems is experienced. The effects of Doppler broadening can usually be reduced by careful experimental planning. All these factors are taken into account when discussing the practicalities of each system for further experimental work.

4.3) Experimental Procedures

The optical fields for the following experiments were produced by the two single-frequency, linearly polarised, continuous-wave Ti:sapphire ring lasers described in Chapter 3, which were pumped by separate mainframe argon-ion lasers. The scanning optical field source was produced by the Microlase MBR-110 Ti:sapphire laser, while the non-scanning source was provided by the modified Schwartz Electro-Optic Titan Ti:sapphire laser. Measurements on the Schwartz non-scanning laser

indicated a linewidth and drift of approximately 5 MHz over the time of one scan of the Microlase laser. The choice of which laser provided the probe optical field and which the coupling optical field depended on what system was being studied. Wavelengths as well as probe and coupling fields orientations were also system dependent and are described for each system in sections 4.4, 4.5 and 4.6, respectively. The probe field was usually attenuated via neutral density filters to $< 50 \mu\text{W}$ within a spot size of waist $100 \mu\text{m}$ to avoid saturation and self-focusing effects [15]. The coupling laser provided up to 600 mW of power within a spot size of waist $150 \mu\text{m}$. It was however attenuated via neutral density filters to $\sim 5 \text{ mW}$ for the V-type and lambda systems since power broadening hindered the interpretation of these experimental results. The two laser fields were linearly polarised in the same plane except for the case of the lambda system experiments. Here the wavelengths of the applied optical fields were so close that orthogonally polarised lasers fields had to be employed so as to avoid the coupling field masking the probe field at the detector. Orthogonal polarisation of the laser fields was achieved by rotating the coupling field with a half wave plate. The coupling field was then filtered out before reaching the detector by the use of linear polarising cubes. The filtering out of the coupling field in the V-type system experiments was achieved by simply employing a rubidium D_1 or D_2 line interference filter.

The rubidium vapour was contained within a 10 cm long quartz cell at a temperature of $45 \text{ }^\circ\text{C}$ providing a density of $10^{17} \text{ atoms m}^{-3}$. When the beams were focused, lenses were chosen such that the confocal parameters for both fields matched the length of the vapour cell and the probe field propagated within the spatial profile of the coupling field. For the V-type and lambda systems the laser fields co-propagated through the cell, but they counter-propagated for the cascade system experiments, so as to satisfy the two-photon condition of equation (4.1). The probe field was detected by a large-area photodiode in all three systems, in order to reduce the effects of electromagnetically-induced focusing (See Chapter 6). For the cascade and two-photon lambda systems a 422 nm fluorescence signal ($6P - 5S_{1/2}$) was also monitored at right angles to the optical field propagation direction, using a filtered photomultiplier tube (R.C.A. IP28, with Schott Glass BG38 filters). This signal monitored the population of the $5D_{5/2}$ level via cascade decay. Phase-sensitive detection was used for both of these diagnostic signals to raise the signal-to-noise ratio. Single-mode operation was

monitored by the 1.5 GHz confocal etalons, and absolute wavelengths measured by the Kowalski style travelling wave meter (See Chapter 3).

4.4) The V-Type System

The V-type system used for this theoretical and experimental study employs the D_1 line (794 nm) and D_2 line (780 nm) of rubidium, as shown in Figure 4.6. The energy level structure of ^{87}Rb is shown in Figure 4.6(a) and that of ^{85}Rb in Figure 4.6(b). Both of these systems were studied experimentally, in order to test our theoretical predictions. An experimental analysis of the V-type system was carried out by scanning the frequency of the coupling field, while employing a static frequency probe field as described by Weiss, Sander et. al. [4, 5]. Here the coupling field was focused using a 40 cm lens, and was scanned upwards in frequency across the $5S_{1/2}$ - $5P_{3/2}$ transition while the probe laser was focused with a 50 cm lens and was set to be resonant with the $5S_{1/2}$ - $5P_{1/2}$ transition. The diagnostic observed in this experiment was the variation of the probe field transmission due to the presence of the scanning coupling field.

An initial examination of Figure 4.6 clearly shows that the applied optical fields do not interact solely with a simple three level V-type system. Due to the inherent nuclear spin component within rubidium there is associated hyperfine within the system. This structure leads to complicating optical pumping mechanisms which act to alter the transmission of the probe field. Therefore, it is clear that careful interpretation of the experimental results is required in order to filter out those effects which are truly a result of the presence of E.I.T.

In practice there are four mechanisms induced by the coupling field that can alter the transmission of the probe field. These are outlined schematically in Figure 4.7. Mechanism 1, shown in Figure 4.7(a), is that of E.I.T. within an ideal V-type system. Next follows the system for coupling field saturation, termed mechanism 2, represented by Figure 4.7(b). Here the coupling field causes a distribution of the population between levels $|1\rangle$ and $|3\rangle$ which acts to increase the transmission of the probe field, as previously described in Section 4.2.2.2. A further complicating factor which can also act to mask the observation of E.I.T. in this V-type system, is optical pumping.

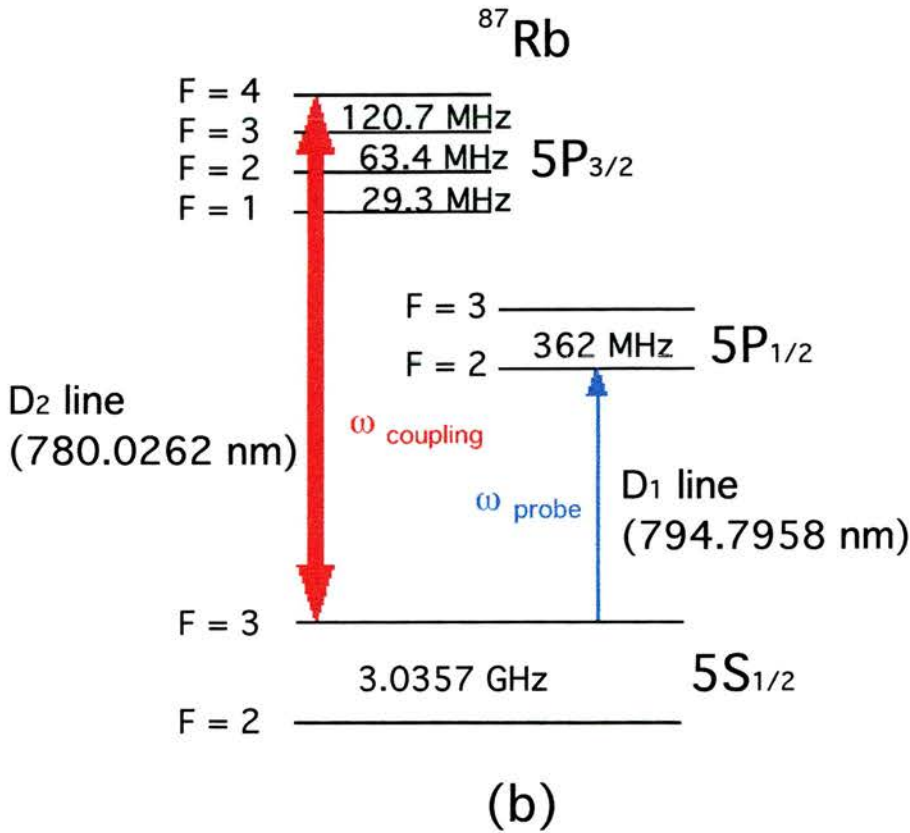
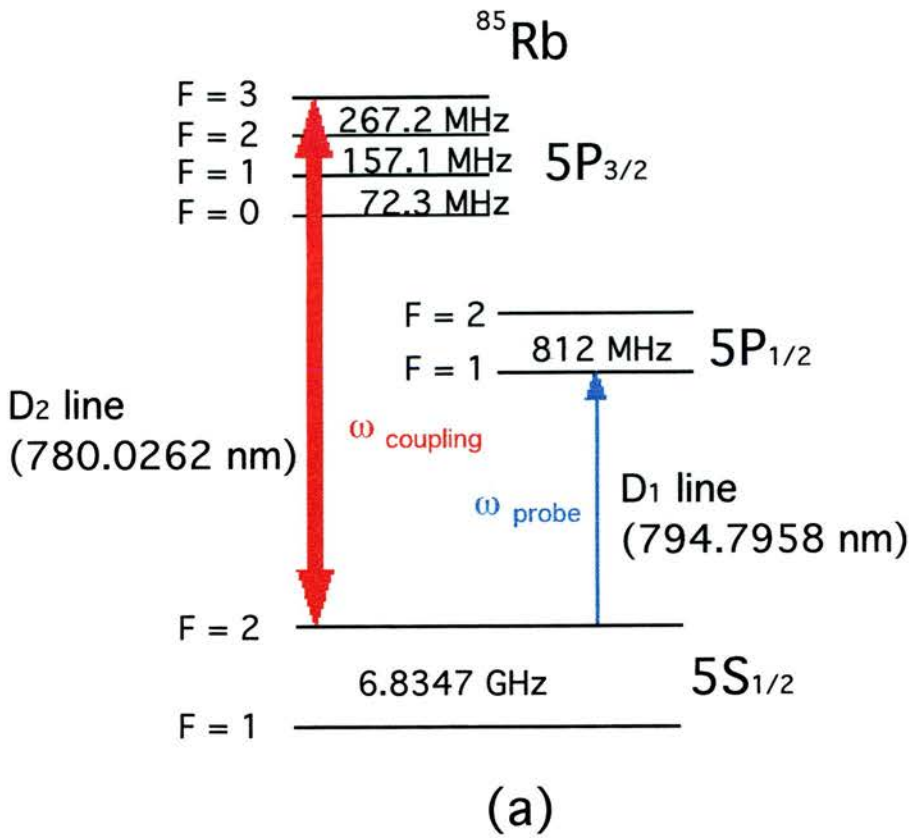


Figure 4.6:- A partial energy level diagram of rubidium showing the scheme employed for the V-type system experiment within (a) the ^{87}Rb isotope and (b) the ^{85}Rb isotope.

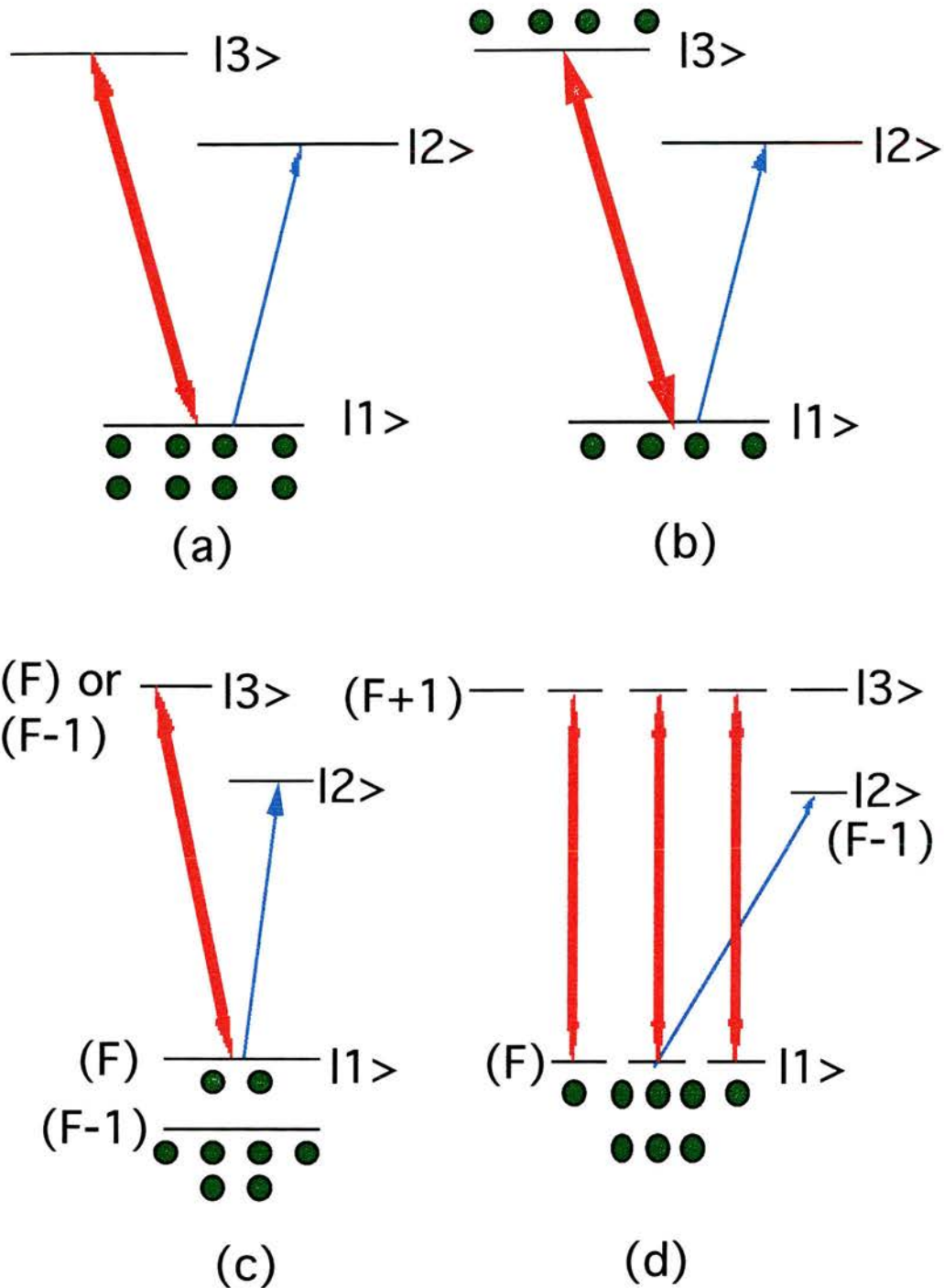


Figure 4.7:- Schematic diagrams representing the four simultaneously occurring mechanisms in this V-type system:- (a) Mechanism 1, V-type system required for the observation of E.I.T. (b) Mechanism 2, coupling field saturation (c) Mechanism 3, optical pumping between ground state hyperfine levels (d) Mechanism 4, optical pumping between magnetic hyperfine sub-levels. Two headed red arrows represent the coupling field while single headed blue arrows the probe field.

There are in fact two velocity selective optical pumping mechanisms in our V-type system. The first, mechanism 3, involves optical pumping between ground state hyperfine levels, as shown in Figure 4.7(c). Atomic selection rules for electric dipole allowed transitions say that $\Delta F = 0, \pm 1$ for both excitation and decay [14]. Thus, with an initial ground state level of hyperfine quantum number F , optical pumping into the $F-1$ ground state occurs if level $|3\rangle$ has a hyperfine quantum number F or $F-1$. As an example consider ^{85}Rb , as shown in Figure 4.6(a), where the probe field is resonant with the $D_1 (F = 3 \rightarrow 2, 3)$ line. When the coupling field is resonant with the $D_2 (F = 3 \rightarrow 2, 3)$ line optical pumping depopulates the ground state of the probe transition, whereas on the $D_2 (F = 3 \rightarrow 4)$ resonance this hyperfine optical pumping is no longer dipole allowed. Being able to remove the hyperfine optical pumping mechanism has obvious benefits when trying to isolate the effects of E.I.T in a V-type system as will be seen in the following experimental results. A point to note is that the hyperfine optical pumping mechanism is never one hundred percent efficient due to collisional and thermal redistribution of the population within the ground state hyperfine levels.

The second optical pumping mechanism, termed mechanism 4, occurs between magnetic hyperfine sub-levels. Since linearly polarised optical fields are employed the magnetic hyperfine selection rule is $\Delta m_F = 0$ with respect to a quantisation axis parallel to the propagation of the optical fields [16]. If the coupling field is resonant with the $D_2 (F \rightarrow F+1)$ transition, so as to remove ground state hyperfine optical pumping effects, then mechanism 4 is only distinguishable when the probe field is simultaneously resonant with a $D_1 (F \rightarrow F-1)$ transition, shown schematically in Figure 4.7(d). Since the relative dipole matrix elements favour magnetic hyperfine optical pumping routes which end in lower $|m_F|$ valued states [16], optical pumping then occurs within the ground state manifold from states with higher $|m_F|$ values to those with lower ones. Effectively the probe field experiences an increased ground state population thus producing increased absorption of the probe on top of which E.I.T. can be imprinted. If however the probe field is on a $D_1 (F \rightarrow F, F+1)$ transition this increased probe field absorption is not experienced. Even although optical pumping between the magnetic hyperfine sub-levels of the ground state still occurs the atomic selection rules always allow the probe field to interact with all the ground state sub-levels. Hence the probe

field is always able to interact with all the ground state population no matter how it is distributed.

It should be noted that the hyperfine optical pumping mechanism can also be removed if we employ the (F-1) ground state hyperfine level of Figure 4.7(c). Now the hyperfine optical pumping mechanism would be absent if the coupling field is resonant with a D_2 (F-1 \rightarrow F-2) transition (not shown in Figure 4.7(c)) in a similar fashion as described above. However, the conditions required to generate the beneficial magnetic hyperfine optical pumping, mechanism 4, can no longer be satisfied and so a reduced transmission background is not created to aid the observation of E.I.T.

In Figure 4.8 an experimental trace of the probe field transition versus the scanning of the coupling field for ^{85}Rb is presented. The first cluster of three peaks corresponds to the case where the probe field is velocity selected into resonance with the $5S_{1/2}$ (F=3) - $5P_{1/2}$ (F=3) transition, while the coupling field is scanned upwards in frequency across the $5S_{1/2}$ (F=3) - $5P_{3/2}$ transition. The probe field is then velocity selected into resonance with the $5S_{1/2}$ (F=3) - $5P_{1/2}$ (F=2) transition as the coupling field continues to scan, and so produces the second cluster of three peaks 362 MHz away corresponding to the hyperfine splitting of the $5P_{1/2}$ level. The splitting of the three power broadened peaks in both clusters corresponds to the hyperfine splitting within the $5P_{3/2}$ level i.e. 63.4 MHz and 120.7 MHz. All six peaks can be explained through different combinations of the four mechanisms described in Figure 4.7. The four peaks marked by vertical lines correspond to the case when mechanisms 1, 2 and 3 are present. The contributions of all these mechanisms act to increase the transmission of the probe field and as a result E.I.T. cannot be resolved. The peak marked by the black arrow comprises of mechanisms 1 and 2. Again both act to increase the probe field transparency, and so E.I.T. cannot be resolved, but this increased transmission is not as large as the previous case since no optical pumping between the ground state hyperfine levels is present. The final peak, marked by a red arrow, consists of mechanisms 1, 2 which act to increase the probe field transmission and mechanism 4 which acts to reduce it. Therefore, since the coupling field saturation effect and E.I.T. are of opposite sign and smaller linewidth than that of the magnetic hyperfine level optical pumping they appear imprinted on a reduced transparency background.

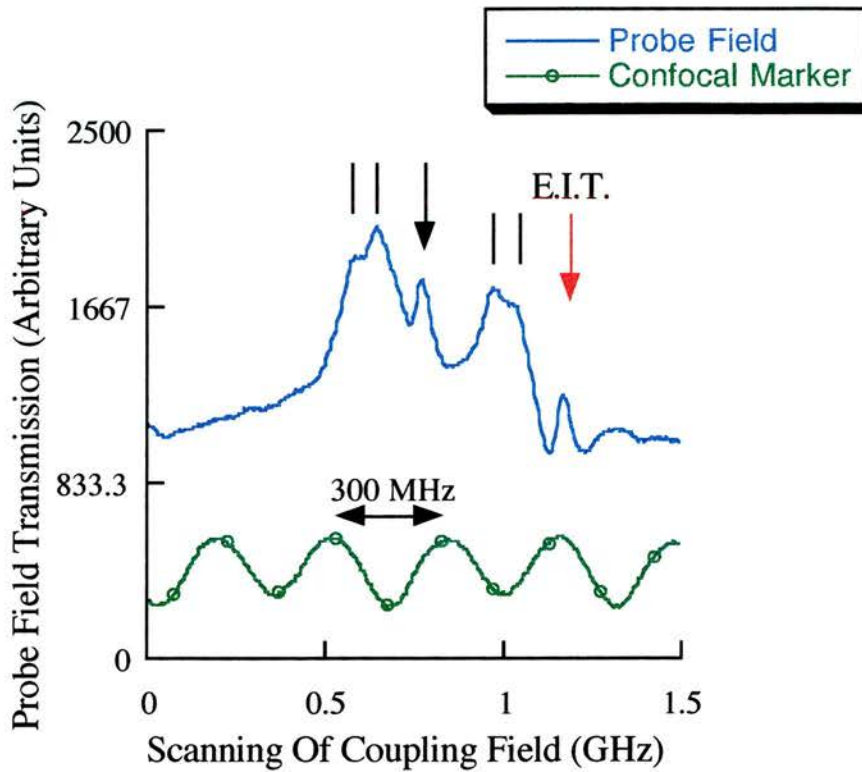


Figure 4.8:- The probe field transmission recorded versus the scanning of the coupling field for the ^{85}Rb V-type system experiment. Vertical lines mark the frequency position of peaks dominated by mechanism 3. The black arrow marks the frequency position of peak 3, which does not suffer/benefit from the effects of mechanism 3/4. The red arrow marks the frequency position of the E.I.T. feature. A 300 MHz confocal signal is also present as a frequency reference.

It has been pointed out by F. Sander et al. [5] that theoretically this transparency window cannot solely be accounted for by coupling field saturation, since its depth is much greater than would be expected for this process alone. The increased transparency depth is thus E.I.T.: a reasonably narrow, 35 MHz, feature which clearly increases the transmission of the probe field.

Confirmation of the contribution of E.I.T. is found by examining the coupling field power dependence of these peaks. In Figure 4.9 the second cluster of three peaks are examined in more detail for ^{87}Rb i.e. the probe field is set on the $5S_{1/2}$ ($F=2$) - $5P_{1/2}$ transition while the coupling field is scanned across the $5S_{1/2}$ ($F=2$) - $5P_{3/2}$ transition. Three probe field transmission traces are presented, where the coupling field has been

quartered in power between each trace. Quartering the power corresponds to halving the Rabi frequency. Since E.I.T. is directly proportional to the coupling field Rabi frequency it is expected that the contribution to transparency of E.I.T. will fall rapidly as the coupling field power is reduced. Reducing the coupling field power also reduces the optical pumping mechanisms but will not greatly affect coupling field saturation if there is still sufficient power to saturate the coupling field transition. Examining Figure 4.9 it can be seen that the overall probe field transmission is reduced as the coupling field power is quartered. This cannot solely be accounted for by less efficient hyperfine optical pumping since the E.I.T. peak, marked by a red arrow, does not experience this mechanism. Coupling field saturation is still present thus the fall off must be the result of reduced E.I.T. as well as reduced hyperfine optical pumping where present.

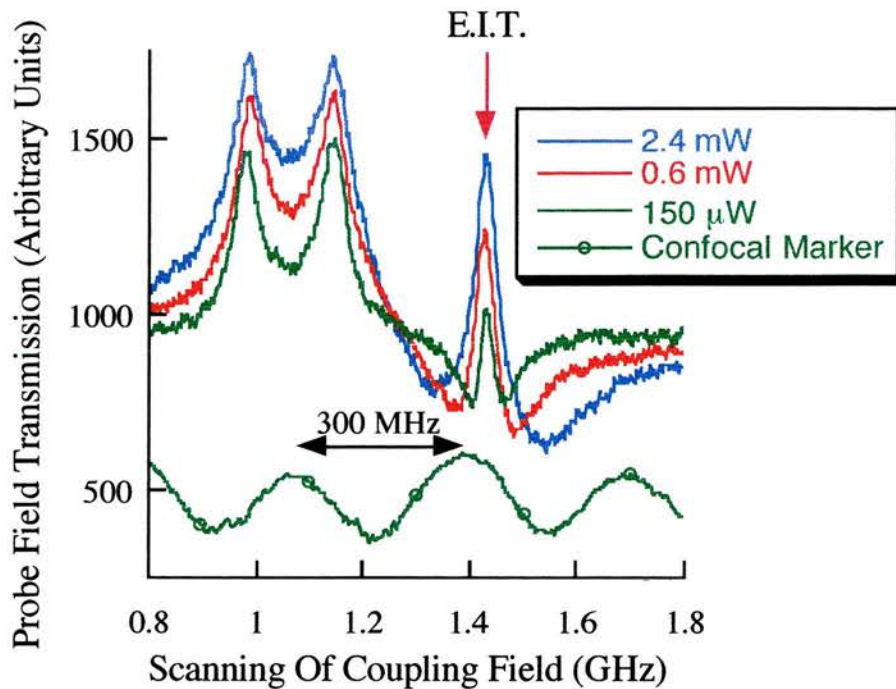


Figure 4.9:- Three probe field transmission curves recorded versus a scan of the coupling field for an ^{87}Rb , V-type system experiment. The probe field is set on the $5S_{1/2}$ ($F=2$) - $5P_{1/2}$ transition while the coupling field is scanned across the $5S_{1/2}$ ($F=2$) - $5P_{3/2}$ transition. The frequency position of the three E.I.T. features is marked by a red arrow. A 300 MHz confocal signal is also present as a frequency reference.

A final point to note is that E.I.T. can never be distinguished from optical pumping in the V-type system if the two optical fields are swapped over, such that the scanning coupling field is on the $5S_{1/2} (F=3) - 5P_{1/2}$ transition and the probe field on the $5S_{1/2} (F=3) - 5P_{3/2}$ transition. Optical pumping between the hyperfine ground states, mechanism 3, can never be eliminated in this system and so E.I.T. will always be masked by this effect. An experimental curve, shown in Figure 4.10 for ^{87}Rb , confirms this point. The trace shows strong optical pumping features on all six peaks which act to mask any E.I.T. Again the structure of the $5P_{3/2}$ and $5P_{1/2}$ levels can be clearly resolved. However, the larger hyperfine splitting of the ^{87}Rb isotope is reflected in Figure 4.10 since the two clusters of three peaks are now split by 812 MHz corresponding to the hyperfine splitting of the $5P_{1/2}$ level. The three peaks within each cluster also show greater resolution since they are now separated by 157 MHz and 267 MHz corresponding to the hyperfine splitting of the $5P_{3/2}$ level.

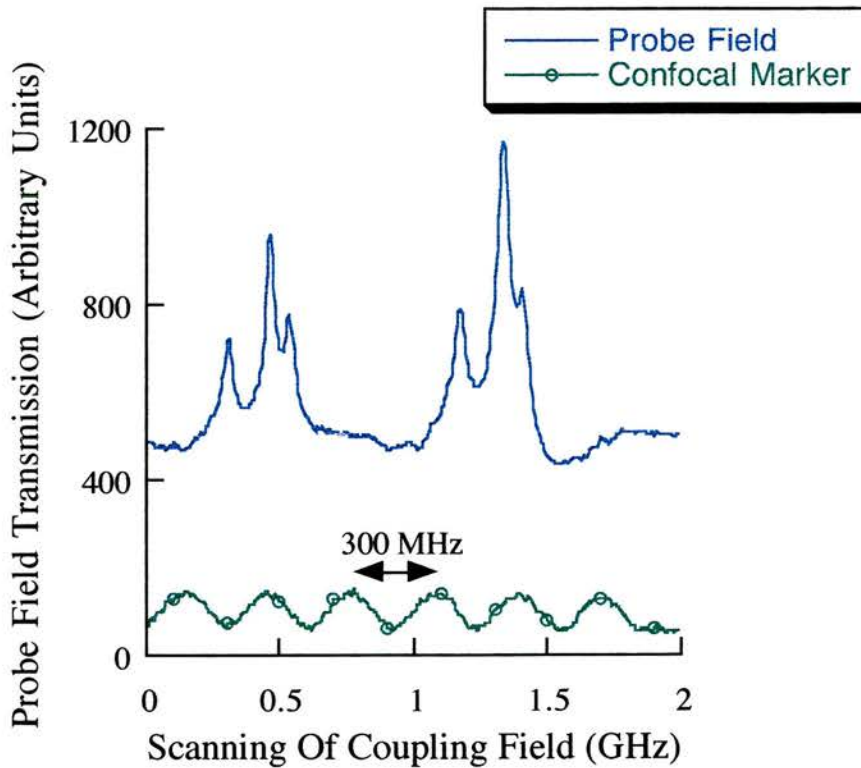


Figure 4.10:- A probe field transmission curve recorded versus a scan of the coupling field for an ^{87}Rb V-type system experiment. The probe field is set on the $5S_{1/2} (F=2) - 5P_{3/2}$ transition while the coupling field is scanned across the $5S_{1/2} (F=2) - 5P_{1/2}$ transition. The coupling field has a power of 165 mW. A 300 MHz confocal signal is also present as a frequency reference.

4.5) The Lambda System

For the purpose of a comparison of schemes two different lambda systems have been studied. The first system employs a single-photon probe field set on the $5S_{1/2} - 5P_{1/2}$ transition, and the second system employs a novel two-photon probe field resonant with the $5S_{1/2} - 5D_{5/2}$ transition. In the single-photon probe scheme the coupling field is resonant with the $5S_{1/2}$ hyperfine level thus optical pumping is present. Moving to a two-photon probe field system removes the effects of optical pumping which complicate the observation of E.I.T., since the coupling field is no longer resonant with the ground state. Each system is taken in turn and the feasibility of each for observing E.I.T. is examined.

4.5.1.) A Lambda System Employing A Single-Photon Probe Field

This lambda system is based on the D_1 line of ^{85}Rb , $5S_{1/2} - 5P_{1/2}$. The hyperfine splitting of the $5P_{1/2}$ levels, 362 MHz, is not sufficient to allow either of these to be isolated as the upper state for an ideal lambda system thus a double lambda system is in fact present. However, as will be shown below, both induce E.I.T. at the same probe field frequency. The energy level configurations involved in this system are shown in Figure 4.11. The probe field was set to be resonant with the $5S_{1/2}$ ($F=2$) - $5P_{1/2}$ transitions, while the coupling field was scanned across the $5S_{1/2}$ ($F=3$) - $5P_{1/2}$ transition. The optical fields were unfocused and co-propagate so as to satisfy the two-photon condition of equation 4.1. Since the coupling field was resonant with a ground state level it was expected that strong optical pumping would be experienced between the ground state hyperfine levels, in a similar fashion to that described above for the V-type system. However, unlike the V-type system, the effect of optical pumping and E.I.T. on the probe field transmission are always of opposite sign.

A four level density matrix analysis has been carried out on this lambda system which predicts the effects of both hyperfine optical pumping and E.I.T. Figure 4.12 presents the result of this four level model. Shown in Figure 4.12(a) is a theoretical trace of the probe field transmission versus coupling field detuning. This curve can be seen to consist of three reduced transmission components, separated by 362 MHz, which are the result of the optical pumping between the ground state hyperfine levels.

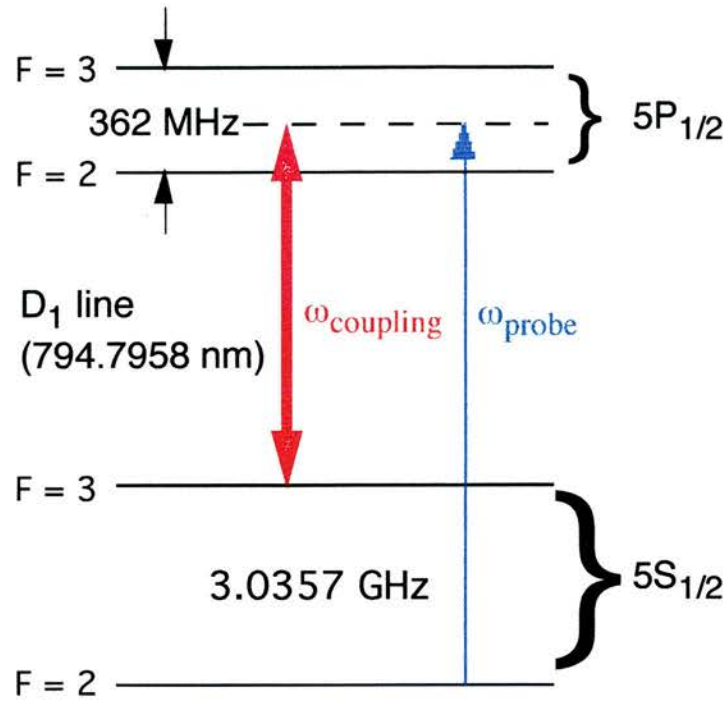


Figure 4.11:- A partial energy level diagram of rubidium showing the scheme employed for the single-photon probe lambda system experiment.

The middle feature also consists of an E.I.T. feature imprinted on top of the reduced probe field transmission background.. This corresponds to the case represented by the partial energy level diagram in Figure 4.12(c), where both of the optical fields are simultaneously velocity shifted into resonance with both the upper state $5P_{1/2}$ hyperfine levels, thus producing E.I.T. This occurs when the applied optical fields are separated in frequency by the splitting of the ground state levels. Figure 4.12(b) and (d) show the partial energy level diagrams for the other two reduced transmission features. These correspond to the cases when the two optical fields are separated by the ground state ($5S_{1/2}$) hyperfine splitting minus or plus the hyperfine splitting of the upper state ($5P_{1/2}$) respectively. Both arise from simultaneous velocity shifts of both optical fields into different upper state hyperfine levels. Since the two optical fields no longer share a common upper level the conditions for E.I.T. are not met, and so the transmission features consist simply of optical pumping between ground state hyperfine levels.

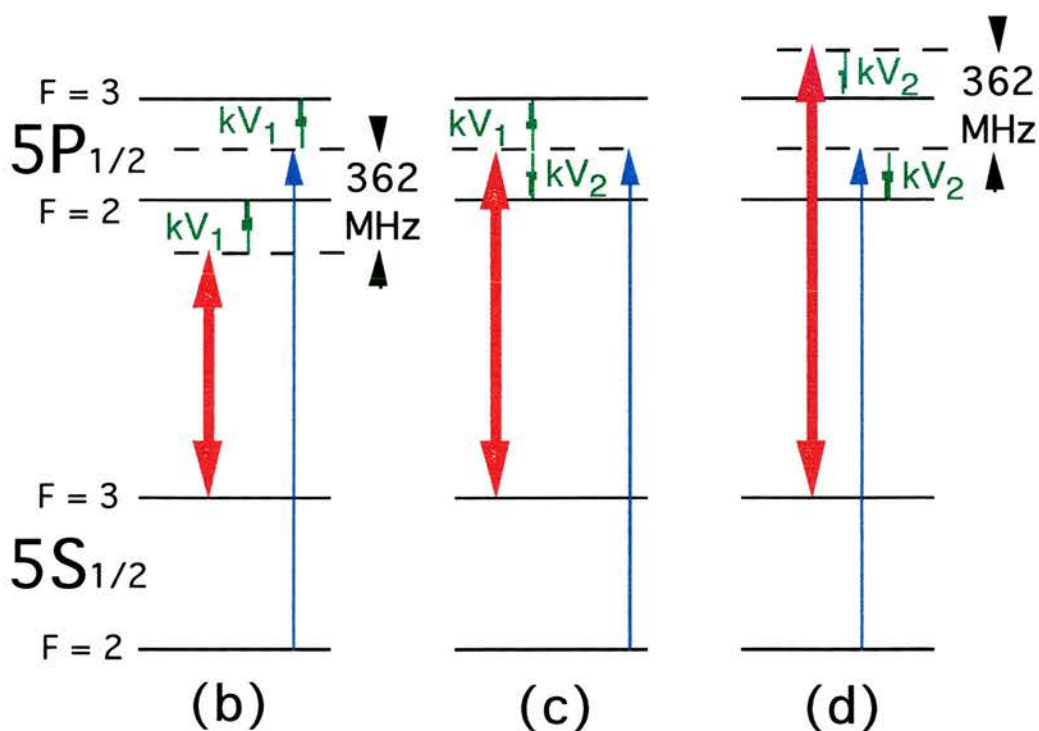
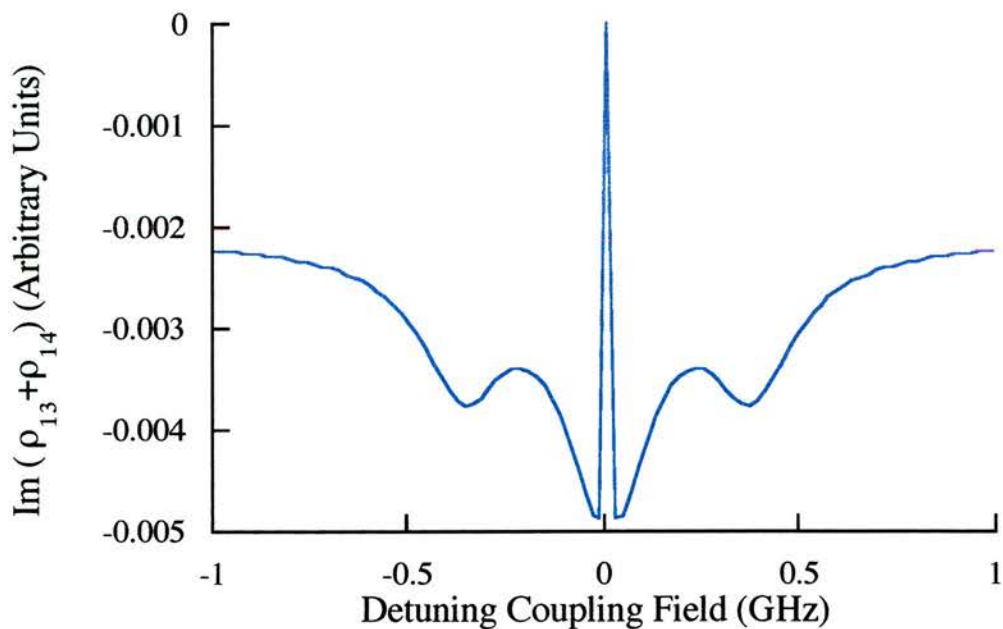


Figure 4.12:- (a) $Im(\rho_{13} + \rho_{14})$ (proportional to probe field absorption) versus the detuning of the coupling field for the single-photon lambda systems within ^{85}Rb vapour. Probe field Rabi frequency of 1 MHz on the $5S_{1/2}$ ($F=2$) - $5P_{1/2}$ transition, coupling field Rabi frequency of 20 MHz on the $5S_{1/2}$ ($F=3$) - $5P_{1/2}$ transition. The three observed probe field transmission features, correspond to the partial energy diagrams shown in Figure 4.12(b), (c) and (d), respectively.

Experimental traces of the probe field transmission versus the coupling field detuning are shown in Figure 4.13.

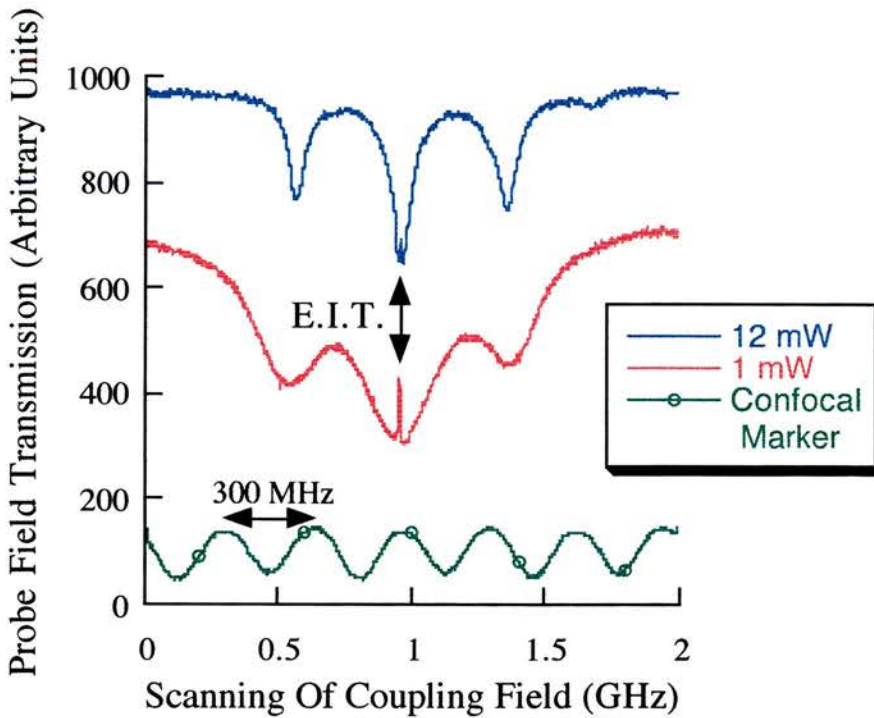


Figure 4.13:- Two probe field transmission curves recorded versus a scan of the coupling field for the ^{85}Rb , single-photon probe lambda system experiment. The probe field is set on the $5S_{1/2}$ ($F=2$)- $5P_{1/2}$ transition while the coupling field is scanned across the $5S_{1/2}$ ($F=3$) - $5P_{1/2}$ transition. The frequency position of the two E.I.T. features is marked by a double headed arrow. A 300 MHz confocal signal is also present as a frequency reference.

The two traces differ in the fact that the coupling field is a factor of ten greater in the second trace than in the first. As predicted both traces show three reduced probe transmission features due to optical pumping, with E.I.T. imprinted on the second of these. The three optical pumping features are indeed separated by the hyperfine splitting (362 MHz) of the $5P_{1/2}$ upper transition. Comparing the two curves the effects of power broadening can clearly be seen, with the higher powered 12 mW coupling field trace having significantly broader features than those of the 1 mW coupling field trace. Taking the coupling field to higher powers in order to enhance E.I.T. causes the

power broadening to dominate and a loss of resolution is the result. As is expected the degree of optical pumping and the depth of the E.I.T. window can be seen to fall off with the power reduction of the coupling field.

4.5.2.) A Lambda System Employing A Two-Photon Probe Field

The second lambda system studied is based on the $5S_{1/2} - 5P_{3/2} - 5D_{5/2}$ scheme within rubidium. These energy levels are employed as a lambda system by setting the coupling field to be resonant with the $5P_{3/2} - 5D_{5/2}$ transition while employing a two-photon scanning probe field on the $5S_{1/2} - 5D_{5/2}$ transition. This novel two-photon probe field is employed so as to provide a lambda system which does not have the coupling field resonant with the ground state, thus does not suffer from optical pumping between ground state hyperfine levels. In this experiment the incoherent fluorescence from the $6P - 5S_{1/2}$ transition is monitored at right angles to the direction of the optical field propagation. This fluorescence is directly proportional to the population present in the $5D_{5/2}$ level since spontaneous decay moves population from $5D_{5/2}$ to $6P$ at a rate of 2.6 MHz. This compares with the alternative spontaneous decay route from $5D_{5/2}$ to $5P$ of 1.6 MHz. Since the $6P$ fluorescence provides a diagnostic for monitoring the $5D_{5/2}$ population then the presence of E.I.T. may be inferred through the observation of dips in the fluorescence signal. This scheme, with the appropriate optical field wavelengths, is shown in Figure 4.14.

The normal orientation for two-photon spectroscopy experiments is that the two-photon transition is induced by the interaction of two counter-propagating photons [17]. With counter-propagating probe field photons all the atomic velocity groups are simultaneously resonant with the two-photon transition, hence this transition is termed Doppler free and the resolution is limited by the natural linewidth of the transition. However, with this field geometry it proved impossible to resolve any dips in the $6P$ fluorescence signal since the fluorescence features exhibited too narrow a linewidth, ~ 2.6 MHz, for the lasers to be able to resolve. Therefore a co-propagating probe field and coupling field geometry was chosen, giving a two-photon Doppler linewidth of ~ 760 MHz for the probe transition [18], which is reflected in the fluorescence curves. With this probe field orientation it proved possible to observe dips in the fluorescence

signal, thus inferring the presence of E.I.T., shown by the experimental traces of Figure 4.15.

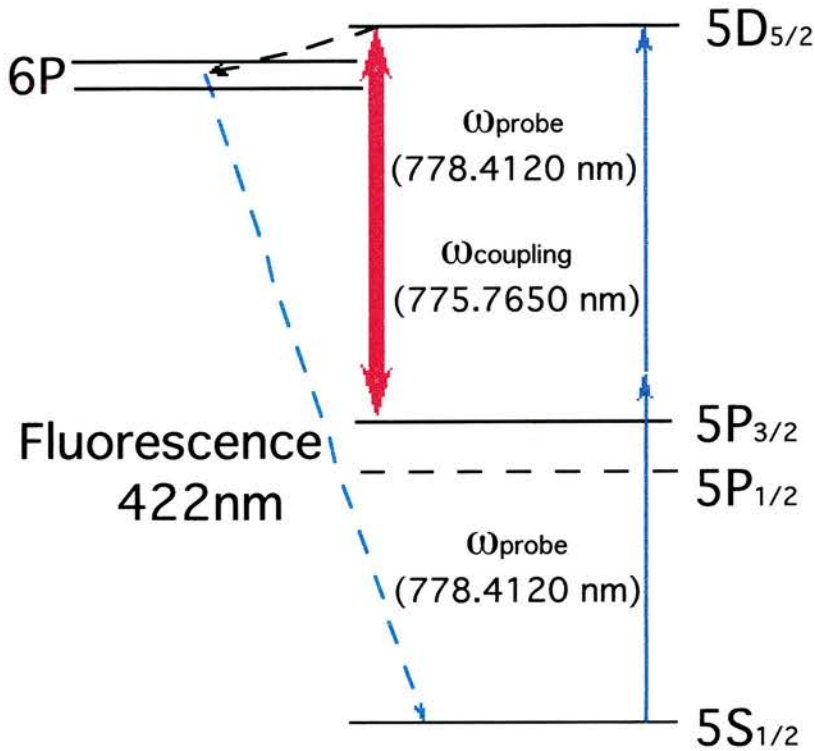


Figure 4.14:- A partial energy level diagram of rubidium showing the scheme employed for the two-photon probe lambda system experiment.

The transparency window observed in this system is relatively broad, 300 MHz, and not of any great depth, $\sim 10\%$. This width is the result of E.I.T. windows at slightly different probe frequency positions, due to the various velocity groups coming into two-photon resonance with each of the hyperfine levels in the $5P_{3/2}$ state. A major restriction on the strength of the E.I.T. window in this system is the fact that the uncoupled transition ($5S_{1/2} - 5P_{3/2}$) is in fact dipole allowed, and so will inherently produce strong dephasing of this transition. This dephasing is therefore not zero as given by equation (4.8) but in fact has the significant value of 20 MHz. The net result is that less E.I.T. is produced than would be if the uncoupled transition was non-dipole allowed, as described in section 4.2.2. Also included in Figure 4.15 is the 6P fluorescence signal in the absence of the coupling field (circled marked blue line). Here it is seen that the maximum fluorescence is significantly less than for the case where the coupling field is present. The reason for this is that the population of the $5D_{5/2}$ level

can decay to the $5S_{1/2}$ ground state by employing either the $6P$ or the $5P_{3/2}$ level as an intermediate state. Now, with the coupling field on, any population that decays into the $5P_{3/2}$ level is quickly re-excited back to the $5D_{5/2}$ level. Thus the preferential decay route is the one involving the $6P$ level, and so the fluorescence signal is increased in the presence of the coupling field.

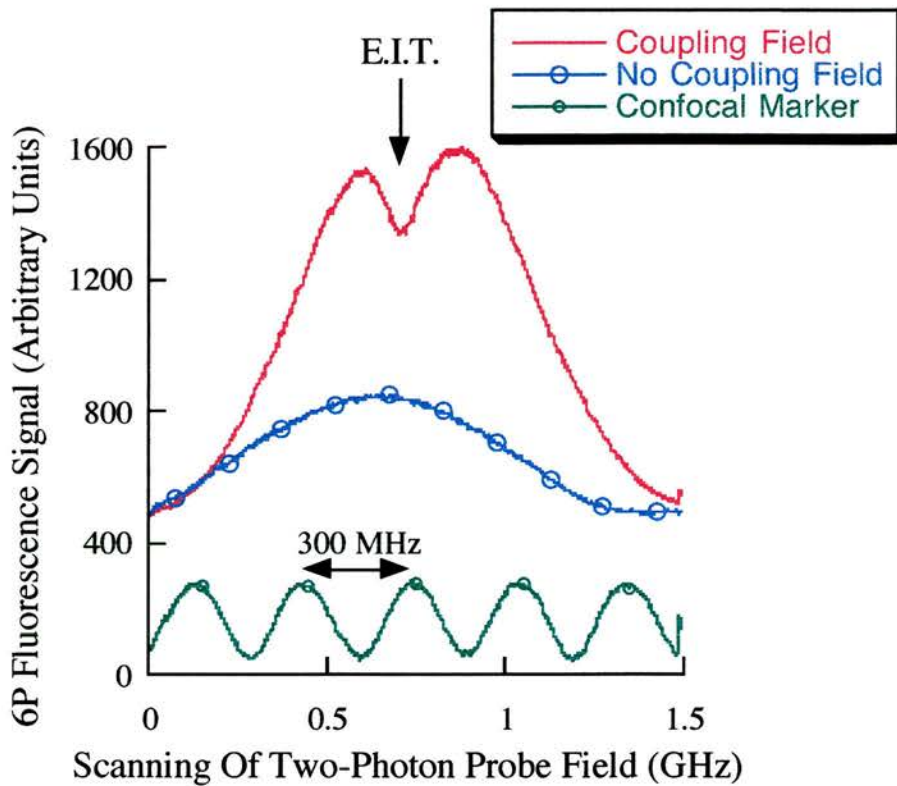


Figure 4.15:- A $6P$ (422 nm) fluorescence signal curve recorded versus a scan of the two-photon probe field, for ^{85}Rb , in the two-photon probe lambda system experiment. Fluorescence with coupling field, ~ 300 mW, present is represented by the red solid line and absent by the circle marked blue line. The two-photon probe field is scanned across the $5S_{1/2}$ ($F=3$) - $5D_{5/2}$ transition while the coupling field is resonant with the $5P_{3/2}$ - $5D_{5/2}$ transition. The frequency position of the E.I.T. features is marked with an arrow. A 300 MHz confocal signal is also present as a frequency reference.

4.6) A Cascade System

The cascade system studied here employed the $5S_{1/2}$ - $5P_{3/2}$ - $5D_{5/2}$ energy levels within rubidium as shown in Figure 4.16. A scanning probe field was resonant with the $5S_{1/2}$ - $5P_{3/2}$ transition, while a coupling field of fixed frequency was resonant with the $5P_{3/2}$ - $5D_{5/2}$ transition. The condition for E.I.T. of equation (4.1) was satisfied in this system by employing counterpropagating optical fields. The observation of E.I.T. was carried out by monitoring the transmission of the probe field. Both lasers were focused into the 10 cm long rubidium cell, the coupling field by a 50 cm lens and the probe field by a 40 cm lens. It should be noted that this system does not involve any complicating optical pumping mechanisms, since the coupling field was not resonant with the ground state, and, by definition, the probe field was of a low enough power that it did not produce large scale population movement.

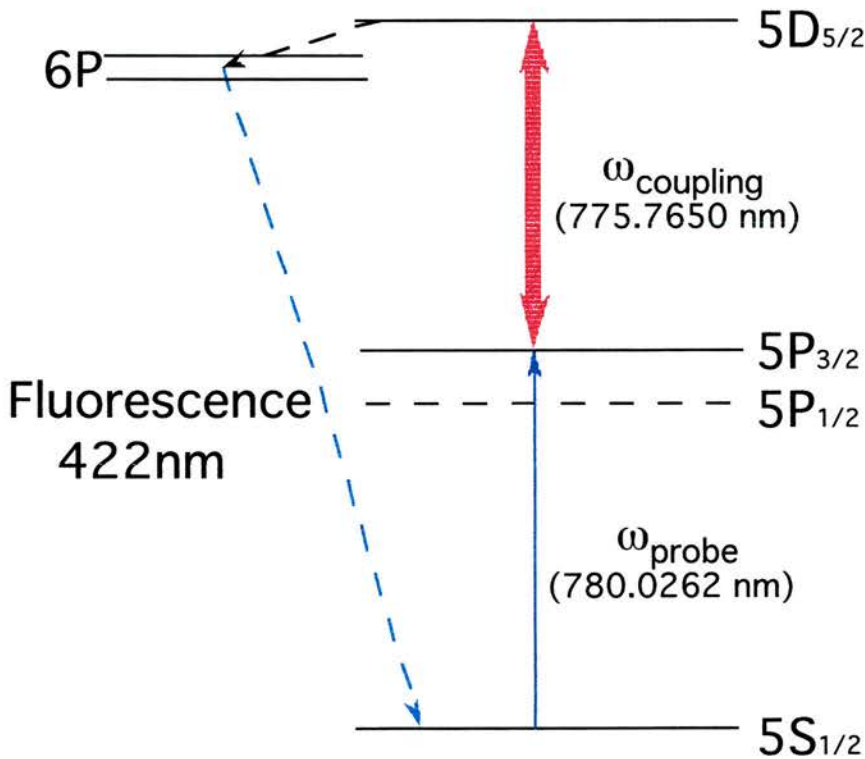


Figure 4.16:- A partial energy level diagram of rubidium showing the scheme employed for the cascade system experiment.

A theoretical prediction for the observation of E.I.T. within this system, using a three level density matrix model, is shown in Figure 4.17, where the imaginary

component of ρ_{12} , which is proportional to the probe field absorption, has been plotted against probe field detuning. When the two optical fields are on exact resonance the medium can be seen to be rendered non-dissipative to both optical fields. E.I.T. has turned off population movement on the lower transition and so there is no population available for absorption by the coupling field.

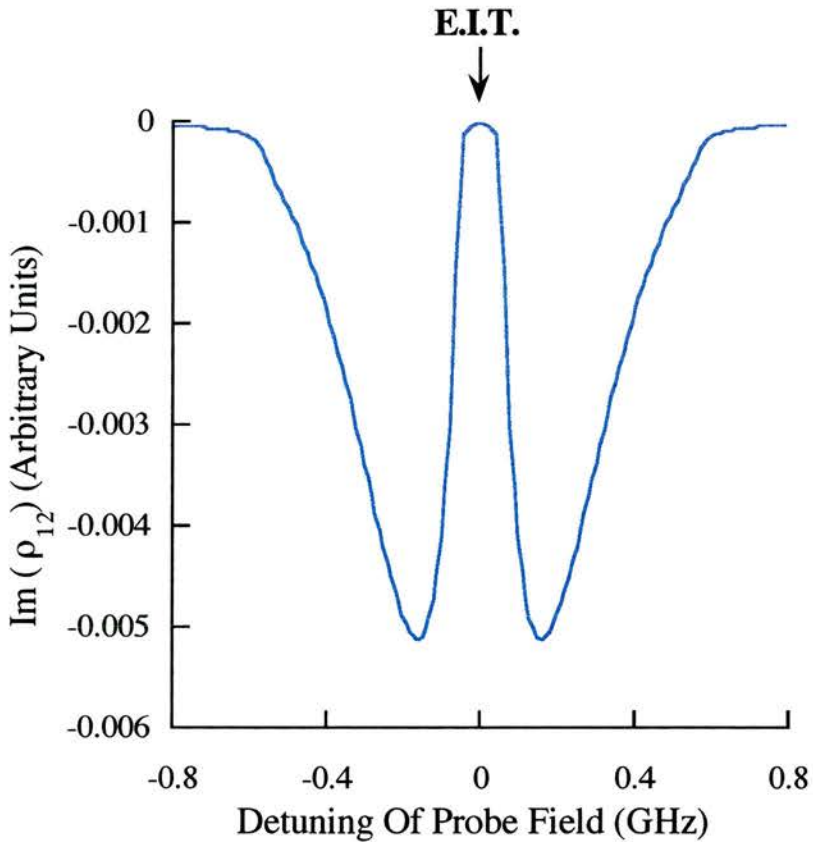


Figure 4.17:- $Im(\rho_{12})$ (proportional to probe field absorption) versus the detuning of the probe field, for ^{85}Rb vapour, within the cascade system. The frequency position of the E.I.T. window is marked by an arrow. Probe field Rabi frequency of 1 MHz on the $5S_{1/2} - 5P_{3/2}$ transition, coupling field Rabi frequency of 160 MHz on the $5P_{3/2} - 5D_{5/2}$ transition.

In Figure 4.18 an experimental trace showing E.I.T. within the ^{87}Rb $5S_{1/2}$ ($F=2$) - $5P_{3/2} - 5D_{5/2}$ and ^{85}Rb $5S_{1/2}$ ($F=3$) - $5P_{3/2} - 5D_{5/2}$ systems is presented. It can be seen

that E.I.T. windows of $\sim 70\%$ depth have been produced experimentally within this system.

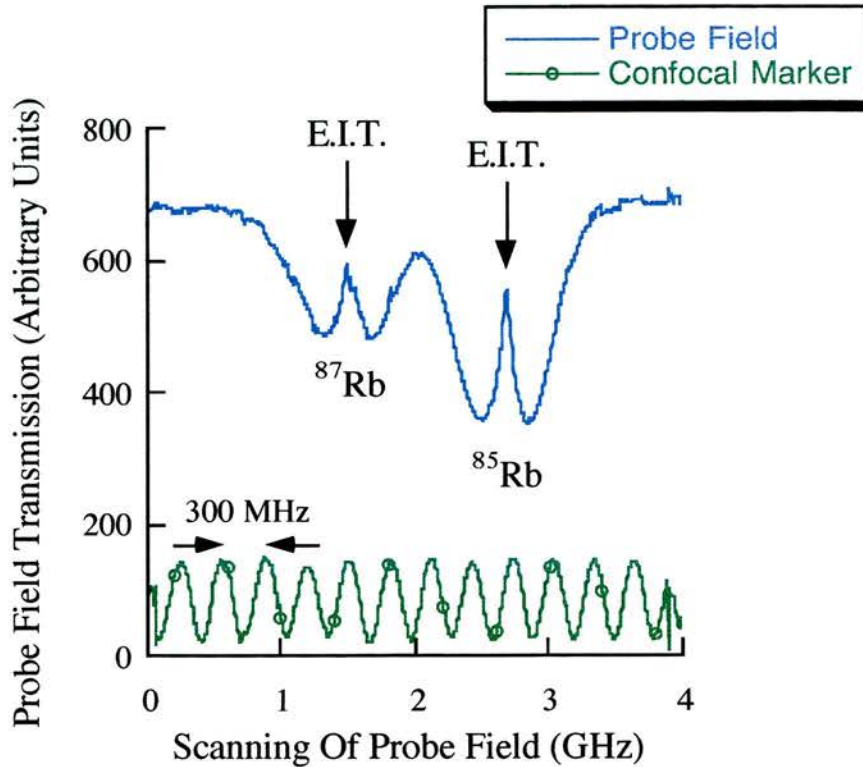


Figure 4.18:- A probe field transmission curve recorded versus a scan of the probe field for rubidium, within the cascade system experiment. The probe field is scanned across the $5S_{1/2} (F=2) - 5P_{3/2}$ transition for ^{87}Rb and across the $5S_{1/2} (F=3) - 5P_{3/2}$ transition for ^{85}Rb , while the coupling field is resonant with the $5P_{3/2} - 5D_{5/2}$ transition. Coupling field power ~ 600 mW. The frequency positions of the two E.I.T. features are marked by arrows. A 300 MHz confocal signal is also present as a frequency reference.

More recently improved E.I.T. has been observed with window depths, of $>90\%$, in this cascade system, when the 10 cm vapour cell was replaced by a 2 cm cell (See Chapter 5). Coupling field power levels and detuning effects on this E.I.T. window are also studied extensively in Chapter 5, and so are not examined here. The spatial profile of the coupling field gives rise to varying Rabi frequencies across the probe field. This accounts for electromagnetically-induced focusing effects, studied in detail in Chapter 6, and for the reduced level of transparency observed here experimentally as compared with theoretical predictions which do not take this into account.

4.7) Comparing The Experimental Systems

The observation of E.I.T. within rubidium is much more complicated than is suggested by theoretical modelling using ideal three level systems. These simple models imply that a lambda system should produce the best E.I.T. and the poorest E.I.T should occur in the V-type system. This is a direct result of the dephasing rates on the related uncoupled transitions. The amplitude model also suggest that there are in fact two different mechanisms for producing E.I.T. The cascade and lambda systems exhibit population trapping after a characteristic period of time which has been shown to be related to the spontaneous atomic decay rates. For rubidium this is of the order of half a microsecond. The V-type system however exhibits E.I.T. without ever trapping population. Here the mechanism for E.I.T. involves a combination of amplitude beating and quantum interference effects. Since a large ensemble of atoms is being studied (10^{17} atoms m^{-3}) experimental confirmation of these two separate mechanisms for E.I.T. is not possible within our experimental system. For all three systems it is possible to switch the medium from being optically opaque to optically transparent on a time scale set by the induced Rabi frequency of the coupling field. Thus, if the coupling field Rabi frequency is of the order of a few hundred megahertz this switching is on a nanosecond time scale.

Many complicating factors exist in practical experiments as have been discussed above. These are found to mask the presence of E.I.T., and so alter the ideal picture. A major complicating factor which appears in two of the above systems, but not in the cascade system, is that of optical pumping between hyperfine ground state levels. This occurs because the coupling field is resonant with one of the ground state hyperfine levels, inducing large scale population movement. In the lambda single-photon system described, this optical pumping mechanism always works against E.I.T. This reduces the induced transparency within the medium, but allows E.I.T. to be experimentally resolved. For the V-type system optical pumping between hyperfine levels works with E.I.T. when present, making it impossible to resolve the E.I.T feature. However, if rendering the medium transparent at the probe wavelength is the desired effect, then this latter optical pumping mechanism is a favourable process. This is not the case for the second optical pumping mechanism discussed in context with the V-type system i.e. optical pumping between ground state magnetic hyperfine sub-levels. The presence of this mechanism provides a reduced transparency feature on top of which any

transparency increasing mechanisms can be observed. Within the above V-type system there were always two transparency increasing mechanisms which can never be resolved completely, E.I.T. and coupling field saturation. Thus, an experimental examination of isolated E.I.T. is far more difficult in the V-type system than in either of the other two systems. It should be noted that both E.I.T. and coupling field saturation mechanisms are also present when optical pumping between hyperfine ground states takes place. However, hyperfine optical pumping tends to be the dominant process, thus E.I.T. and coupling field saturation are masked by this effect.

The two-photon probe lambda system provided a possible solution for observing lambda E.I.T. within rubidium. Although this system did remove the complications of optical pumping between hyperfine ground state levels, suffered by the single-photon lambda system, it did provide new difficulties. The two-photon probe field is difficult to detect by direct absorption thus inferences of the presence of E.I.T. had to be made through a fluorescence diagnostic. Also the uncoupled transition was in fact dipole allowed thus the levels of E.I.T. obtained were always significantly less than the ideal system.

These features highlight the importance of trying to find an E.I.T. system which employs a coupling field that is not resonant with the ground state. This is exactly the case found within the above cascade system. With counter-propagating optical fields, and no large scale optical pumping mechanisms, the cascade system proved by far the easiest system for the uncomplicated observation of E.I.T. This does not imply that the other systems should be totally discarded. With better matched confocal parameters and shorter cells, better E.I.T. may be produced within either of the other two systems. A second solution to simplify the observation of E.I.T. within V-type and lambda systems would be to find a medium which does not have any intrinsic nuclear spin and thus no hyperfine structure. One possible candidate would be to use barium as the atomic interaction medium. However, barium brings its own practical problems i.e. it requires higher temperatures, increased Doppler broadening etc. In practice it has proven easiest to observe isolated E.I.T. within the cascade system. This allows a detailed study of E.I.T., and some of its related effects, to be undertaken without the complicating factors involved in the V-type and lambda systems. These studies are discussed in detail in the remaining chapters of this work.

References

- [1] **S.E. Harris, J.E. Field and A. Imamoglu**, *Nonlinear Optical Processes Using Electromagnetically Induced Transparency*, Phys. Rev. Lett. 64, 1107 (1990).
- [2] **O. Kocharovskaya, P. Mandel and Y.V. Radeonychev**, *Inversionless Amplification In A Three-Level Medium*, Phys. Rev. A. 45, 1997 (1992).
- [3] **O. Kocharovskaya**, *Amplification And Lasing Without Inversion*, Physics Reports 219, 175 (1992).
- [4] **A. Weiss, F. Sander and S.I. Kanorsky**, *Reduction Of Opacity By Quantum Interference In A Three-Level System*, IEEE Technical Digest, 5th European Quantum Electronics Conference '94 (Optical Society Of America, Washington D.C.), 252 (1994).
- [5] **F. Sander, A. Weiss, S. I. Kanorsky, T.W. Hänsch, M. Fleischhauer and M.O. Scully**, *Observation Of V-type CW-Induced Transparency: Beyond Population Trapping*, (Unpublished Preprint), (1994).
- [6] **K.J. Boller, A. Imamoglu, and S.E. Harris**, *Observation Of Electromagnetically Induced Transparency*, Phys. Rev. Lett 66, 2593 (1991).
- [7] **H.R. Gray, R.M. Whitley and C.R. Stroud Jr.**, *Coherent Trapping Of Atomic Populations*, Optics Letters 3, 218 (1978).
- [8] **A.M. Akulshin, A.A. Celikov and V.L. Velichansky**, *Sub-Natural Absorption Resonances On The D_1 Line Of Rubidium Induced By Coherent Population Trapping*, Opt. Commun. 84, 139 (1991).
- [9] **O.A. Kocharovskaya, F. Mauri and E. Arimondo**, *Lasers Without Population Inversion And Coherent Trapping*, Opt. Commun. 84, 393 (1991).

- [10] **A.D. Wison-Gordon**, *Gain In A Three-Level Λ System Driven By A Single Pump*, Phys. Rev. A 48, 4639 (1993).
- [11] **J.E. Field, K.H. Hahn and S.E. Harris**, *Observation Of Electromagnetically Induced Transparency In Collisionally Broadened Lead Vapour*, Phys. Rev. Lett. 67, 3062 (1991).
- [12] **M.H. Dunn**, *Electromagnetically Induced Transparency in Laser Sources and Applications*, editors A. Miller and D.M. Finlayson p.411 (SUSSP / IOP, Bristol, (1996)).
- [13] **Y. Li and M. Xiao**, *Transient Properties Of An Electromagnetically Induced Transparency In Three-Level Atoms*, Optics Lett. 20, 1489 (1995).
- [14] **B. Shore**, *The Theory Of Coherent Atomic Excitation*, Vol. 2, (Wiley, New York, (1990)).
- [15] **J.E. Bjorkholm and A. Ashkin**, *CW Self-Focusing And Self-Trapping Of Light In Sodium Vapour*, Phys. Rev. Lett. 32, 129 (1974).
- [16] **W. Happer**, *Optical Pumping*, Rev. Mod. Phys. 44, 169 (1972).
- [17] **V.S. Letokhov and V.P. Chebotayev**, *Nonlinear Laser Spectroscopy*, Springer-Verlag, (Berlin Heidelberg New York (1977)).
- [18] **A. Yariv**, *Optical Electronics*, Fourth Edition, (Saunders College Publishing, New York. (1991)).

Chapter 5

Two Photon And Zeeman Splitting Effects In Continuous-Wave Electromagnetically Induced Transparency

Continuing on from the comparison of schemes for the study of electromagnetically induced transparency in an isolated system, an in-depth study of a cascade system within rubidium is carried out in this chapter. It is shown that under the correct conditions the hyperfine structure of the upper level is seen within the E.I.T. feature, and so the application of E.I.T. for high resolution spectroscopy is then discussed. With reference to the employment of E.I.T. to enhance nonlinear processes the effects of Zeeman splitting on E.I.T. within this cascade system are then considered.

5.1) An Outline Of Sub-Doppler E.I.T. Within The Cascade System

This chapter looks in greater detail at the employment of continuous-wave Ti:sapphire lasers for the study of E.I.T. within a cascade atomic level scheme of rubidium. These laser sources provide a useful range of power, thus producing Autler-Townes splittings from the order of the single photon linewidth (~ 528 MHz) down to that of the structure of the hyperfine levels (less than 20 MHz). This is significantly more than that induced in the diode laser experiments to date [1, 2] but still below those achieved for pulsed laser experiments [3]. Initially, it was believed that the sub-Doppler limit for observing E.I.T. was that the Rabi frequency induced by the coupling field

must be greater than the two photon linewidth of the system [4]. In Chapter 7 it will be shown that this is not in fact the limiting condition for observing sub-Doppler E.I.T. However, as is discussed below, the two photon linewidth limits the resolution that can be achieved when employing E.I.T. for spectroscopy. This discussion is followed by a series of theoretical and experimental results where the effects of the optical field geometry, coupling field power and coupling field detuning are considered. A further set of results follows where fluorescence has been employed to monitor the population levels in the upper state of the cascade system. This provides a direct contrast with the characteristics of the probe field transition absorption curves.

The effects of the influence of a magnetic field on this cascade system is of importance because this is the basis of the theoretical paper by Moseley et. al. [5]. The authors propose the employment of E.I.T. to enhance the generation of sum frequency mixing within a cascade system [6]. Introducing a magnetic field to a coherently prepared system is also of direct relevance to the design of a high sensitivity magnetometer, as proposed by Scully et al. [7]. Thus, a theoretical study of the effects of introducing a magnetic field to this system is presented. As well as this theoretical consideration, the effects are demonstrated experimentally, and it is shown that this provides a second method for spectroscopic analysis of the two photon transition between the lower and upper levels. The basic mechanism involved in this process is that the application of the magnetic field causes Zeeman splitting [8] of the energy levels within the rubidium atoms and so alters the three level nature of the relevant atomic levels. The effect on the E.I.T. window itself is then two-fold. The first is that the E.I.T. window splits into components associated with the different allowed transitions. These are dependent on the operative selection rules for Δm_ℓ which in turn are governed by the polarisations of the input fields with respect to the magnetic field. By varying the combinations of the input field polarisations the E.I.T. window can split into one, two or three clusters of components whose degeneracy is removed by the Zeeman splitting. Secondly, it is found that the Zeeman splitting of the ground state hyperfine levels, in conjunction with the Zeeman splitting of the allowed upper states, gives rise to a broadening of each Δm_ℓ component. It is shown theoretically and experimentally, that this leads to a dramatic reduction in the strengths of the E.I.T. effect in this counter-propagating, sub-Doppler geometry.

5.2) Two Photon Residual Doppler Width

The work in this paper is carried out on a cascade system within rubidium which employs the $5S_{1/2}$ - $5P_{3/2}$ - $5D_{5/2}$ levels as shown in Figure 5.1.

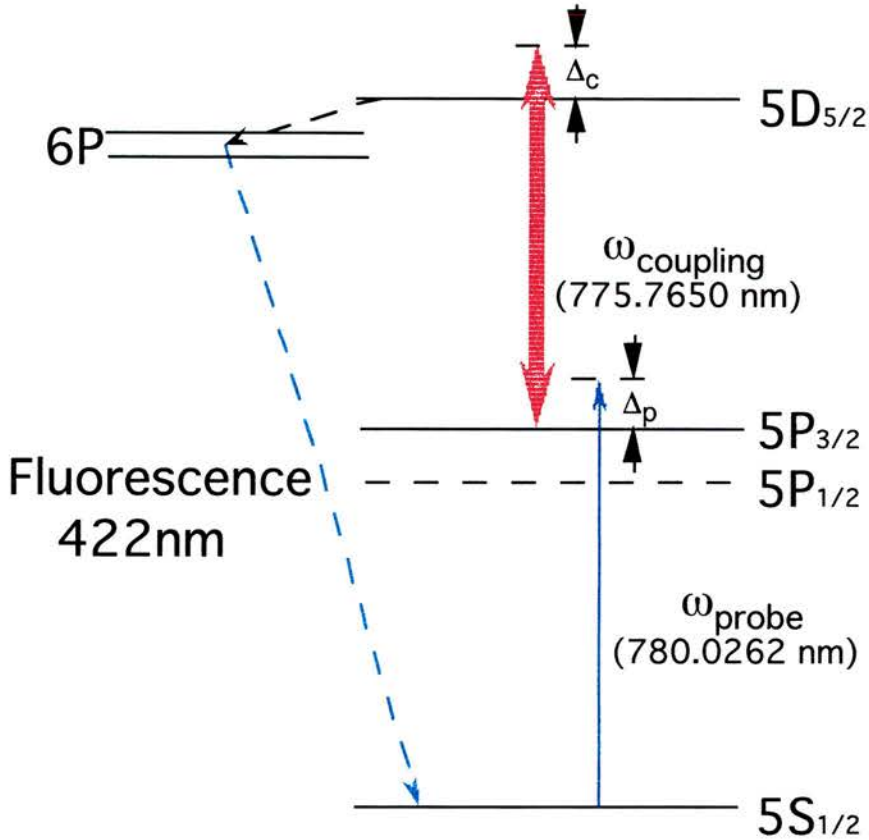


Figure 5.1:- A partial energy level diagram of rubidium showing the scheme employed for the cascade system experiment.

Since E.I.T. is a two photon resonant process the location of an E.I.T. resonance for a cascade system is given by the following expression:

$$\Delta_p + \Delta_c = 0 \quad (5.1)$$

where Δ_p and Δ_c are the detunings of the two applied optical fields, as defined in Figure 5.1. Hence, the location is independent of the structure and position of an intermediate level and it is the energy separations of the lower and upper levels, relative to the photon energies, that is the important parameter, i.e. in this rubidium cascade system E.I.T. is independent of the position and structure of the intermediate $5P_{3/2}$ level. However, for the E.I.T. effect to be physically observed it is required that the probe

field frequency falls within the absorption linewidth of the $5S_{1/2} - 5P_{3/2}$ probe transition. The individual detunings can be expressed as

$$\Delta_p = \Delta_p^0 - k_p V_z \quad (5.2)$$

$$\Delta_c = \Delta_c^0 - k_c V_z \quad (5.3)$$

where Δ_i^0 is the detuning of the applied optical field from the transition frequency of a stationary atom. The $k_i V_z$ term is the Doppler shift on the transition for an atom with velocity component V_z in the direction of beam propagation of the light with the z -component of the wavenumber k_i (positive for the same sense).

In order to observe sub-Doppler effects on the probe field it is necessary to reduce the two photon residual linewidth below that of the single photon probe Doppler width. The residual Doppler width of the two photon transition is :

$$\Delta v_D = \left| (k_p + k_c) u \right| \quad (5.4)$$

where

$$u = \sqrt{\frac{2k_B T}{M} \ln 2} \quad (5.5)$$

and k_B is the Boltzmann constant, T the temperature of the gas and M the atomic mass. The first requirement to minimise this broadening is that the transitions must be chosen such that they have nearly equal wavelengths i.e. $|k_p| \approx |k_c|$. If the two input waves are then counterpropagated (i.e. k_p and k_c are of opposite sign) the shifts on the individual transitions will be in opposite directions and the residual Doppler width will be low, similar to the situation occurring in Doppler free two photon spectroscopy [9]. For the cascade system considered, the co-propagating two photon width is 536 MHz while with counterpropagating fields it is only 1.38 MHz at 320 K. These compare with the single photon probe Doppler width of 528 MHz. From this argument it can be seen that the resolution of the E.I.T. spectroscopy technique will be of the order of a few megahertz if counterpropagating fields are employed.

It should be noted at this point that for Λ -type systems and V-type systems the two photon residual Doppler width is $|(k_p - k_c)u|$ and a co-propagating beam geometry minimises this for nearly equal transition wavelengths.

5.3) Varying The Optical Field Parameters

The experimental results described in this chapter were obtained employing the same procedures as outlined in Chapter 4 for the cascade system. However, unlike the results of Chapter 4 the results of Section 5.3.2 - 5.3.5 were obtained by focusing the optical fields into a 2 cm rubidium cell instead of a 10 cm cell. The coupling field was focused with a 20 cm lens and the probe with a 40 cm lens. This arrangement again ensured that the confocal parameters were longer than the cell and that the probe field was confined to the centre of the coupling field.

5.3.1) Effect Of The Orientation Of The Optical Fields

In this section the effects of the orientation of the two optical fields is examined. Figure 5.2 presents two theoretical curves which examine the effect of optical field orientation within a matched wavelength cascade system. Here two probe absorption curves are presented where the same field strengths have been employed but for (a) the fields co-propagate whereas in (b) the fields counterpropagate. Only in the latter trace is the an E.I.T. feature resolved within the Doppler broadened absorption curve. For co-propagating fields the Autler-Townes absorption regions for one particular velocity group overlap in frequency space with the transparency region of other velocity groups, with the net effect that no transparency is observed. A full explanation of this phenomenon and related effects is presented later in Chapter 7.

Experimentally an initial examination was carried out where the two fields co-propagate through the 10 cm rubidium cell. This was then followed by a study of the case where the field orientation was altered such that they counterpropagate through the cell. This allows confirmation of the fact that optical pumping does not play a significant role in the cascade system, and highlights the contribution of optical field orientation for observing E.I.T.

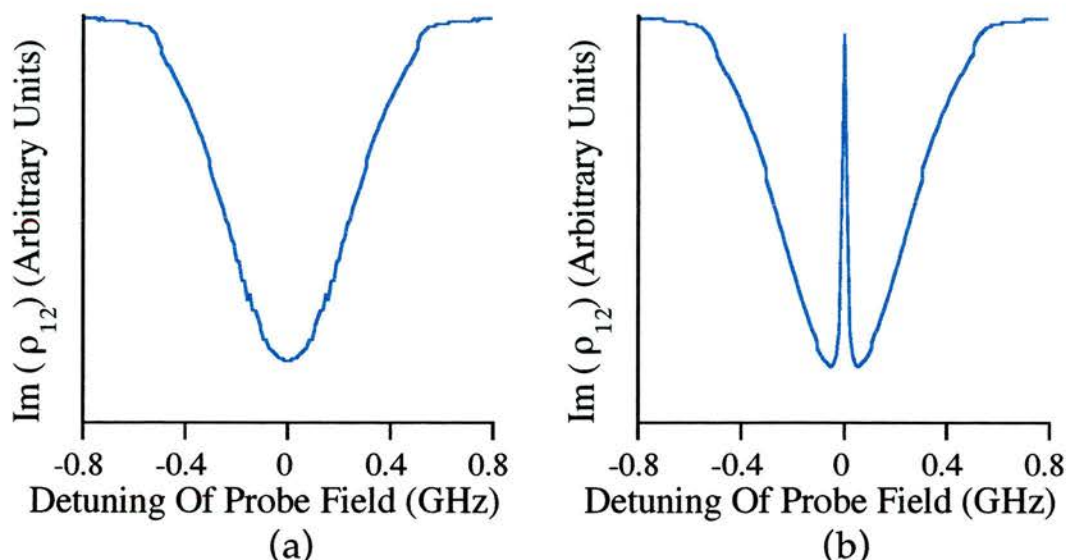
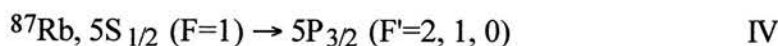
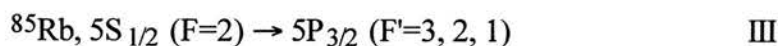
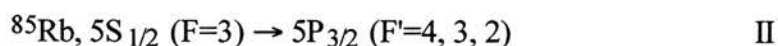
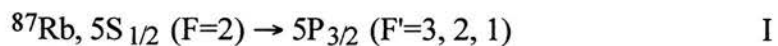
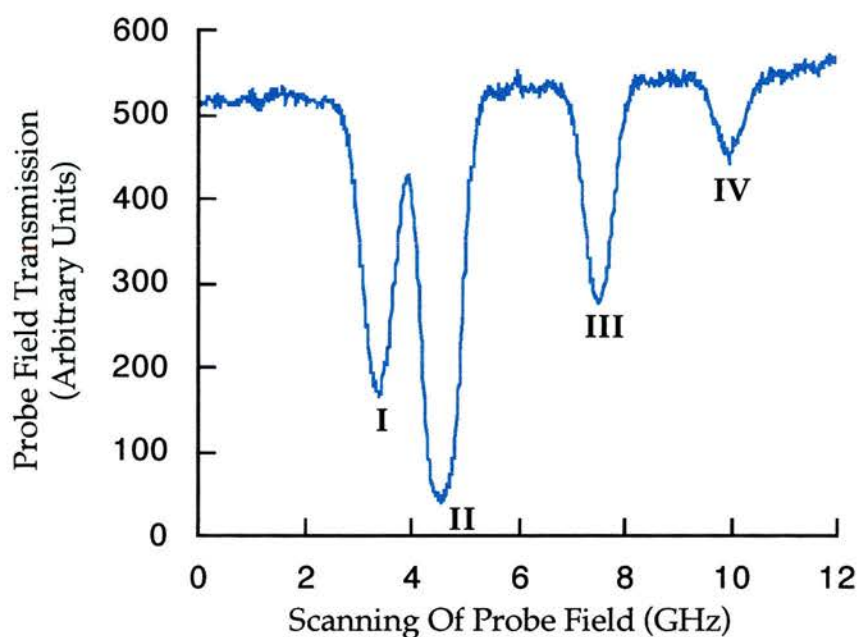


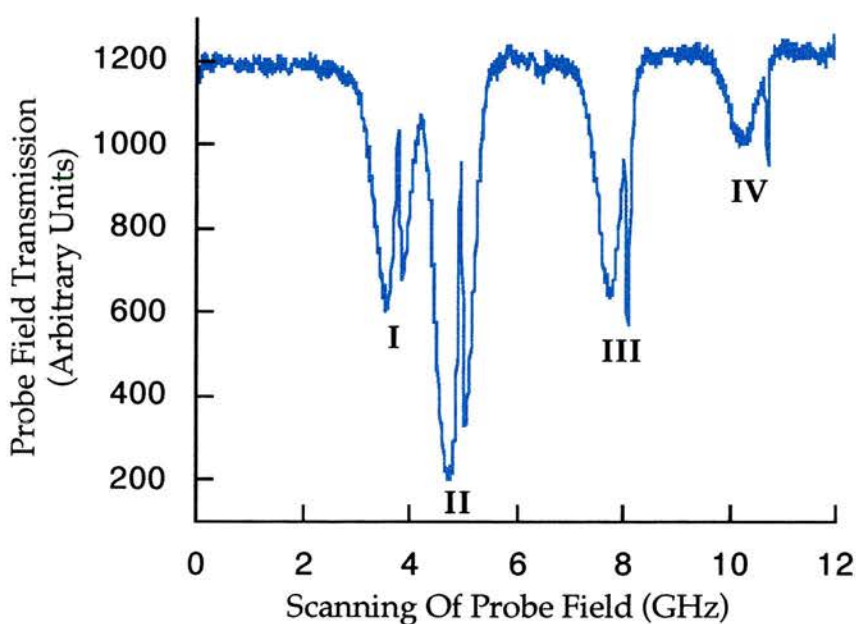
Figure 5.2:- Theoretical curves showing the imaginary component of ρ_{12} (which is proportional to the probe field absorption), including the effects of Doppler broadening, for: a) Co-propagating fields; b) Counterpropagating fields. ($\Omega_{12} = 1$ MHz, $\Omega_{23} = 50$ MHz and vapour temperature = 47 °C).

Since there are two naturally occurring isotopes of rubidium, both of which have hyperfine structure, there are four main Doppler broadened features which appear in the probe absorption curve, as seen in Figure 5.3. These correspond to the transitions (as labelled on Figure 5.3)





(a)



(b)

Figure 5.3:- Experimental cell transmission as the probe is tuned across the $5S_{1/2} - 5P_{3/2}$ transition with the coupling laser (a) co-propagating and (b) counterpropagating. The vapour temperature for both was $45\text{ }^{\circ}\text{C}$, coupling laser power 300 mW , probe laser power $<1\text{ mW}$ but not identical in (a) and (b). The traces were taken in a 10 cm cell with a 50 cm lens in the coupling laser beam and a 40 cm lens in the probe laser beam.

In the co-propagating case, Figure 5.3(a), the four lines are essentially identical to the absorption features seen in the absence of a coupling field. However, on the counterpropagating trace, Figure 5.3(b), strong reductions in absorption due to E.I.T., 60 to 70 % in these curves, are seen on peaks I and II with the E.I.T. appearing detuned on peaks III and IV due to the different F levels accessed from the ground state under the $\Delta F = \pm 1$ or 0 selection rule. As E.I.T. depends on the two-photon resonance condition the E.I.T. feature positions are determined on this scale solely by the lower level structure. There is no large scale hyperfine optical pumping process present in the cascade system as long as the probe field power is weak enough that it does not begin to saturate the $5S_{1/2} - 5P_{3/2}$ transition. The difference in the strength between the four transitions is accounted for by the fact that each has a different dipole matrix element and by the fact that the two isotopes have different abundances.

Although these were the maximum levels of E.I.T. achieved in this system within a 10 cm cell the E.I.T. features did keep increasing in width and depth up to the maximum power levels available from the Ti:sapphire lasers. This suggests that if more coupling field power could be obtained then the E.I.T. feature could be further enhanced. Improving the spatial overlapping between the two beams could also lead to improved E.I.T. windows in this system. If the two beams are not ideally overlapped some absorption of the probe field would occur in the regions lying outwith the coupling field. Also towards the edges of the coupling beam the Gaussian profile of the intensity distribution means that the Rabi splitting will be somewhat less than at the centre and some absorption will take place. This is further complicated by the effects of Electromagnetically Induced Focusing, and especially defocusing, which is the subject of Chapter 6. Due to these effects mode matching of the two beams cannot be guaranteed throughout the frequencies scanned. The comparison of these two traces does however clearly show the advantage of employing counterpropagating optical fields, instead of those which co-propagate, in order to experimentally observe E.I.T. within a cascade system.

5.3.2) Effect Of Coupling Field Power

The effects of varying the coupling field power are now characterised and it will be seen that this leads to a novel method for the spectroscopic analysis of the $5D_{5/2}$ upper

state. In order to allow a detailed analysis only the first two absorption lines (I and II) are displayed. Figure 5.4(a) displays four results taken with successive quartering of the coupling field power. Quartering of the coupling field power is equivalent to halving the corresponding Rabi frequency (see Chapter 2). The reduction in the Autler-Townes splitting is obvious from these curves as well as the reduction in the depth and width of the E.I.T. window.

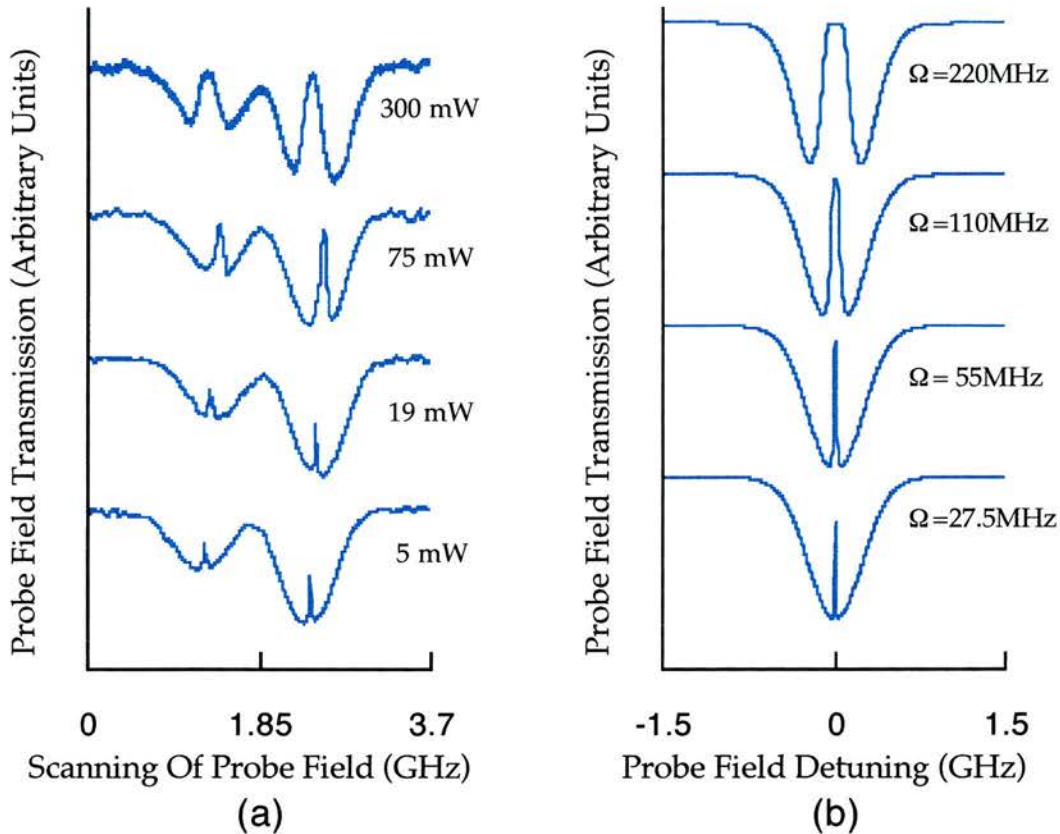


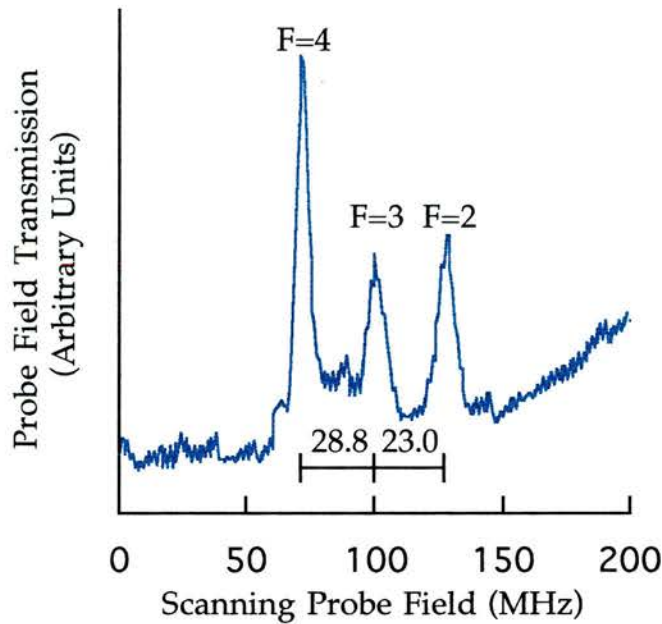
Figure 5.4:- (a) Experimental probe field transmission curves as the probe laser is scanned across the ^{87}Rb , $5S_{1/2}$ ($F=2$) and ^{85}Rb , $5S_{1/2}$ ($F=3$) to $5P_{3/2}$ transitions (peak I and II) for the stated coupling field powers. The probe field has a power of $3\ \mu\text{W}$, and the oven temperature is $\sim 47\ ^\circ\text{C}$. (b) Theoretical probe field transmission curves from density matrix calculations on a three level system including Doppler broadening (for $47\ ^\circ\text{C}$) at the coupling field Rabi frequencies stated.

A theoretical comparison for this system is presented in Figure 5.4(b) where a three level cascade model has been employed with Rabi frequencies chosen to match the observed Autler-Townes splitting. As can be seen the match to the experimental results

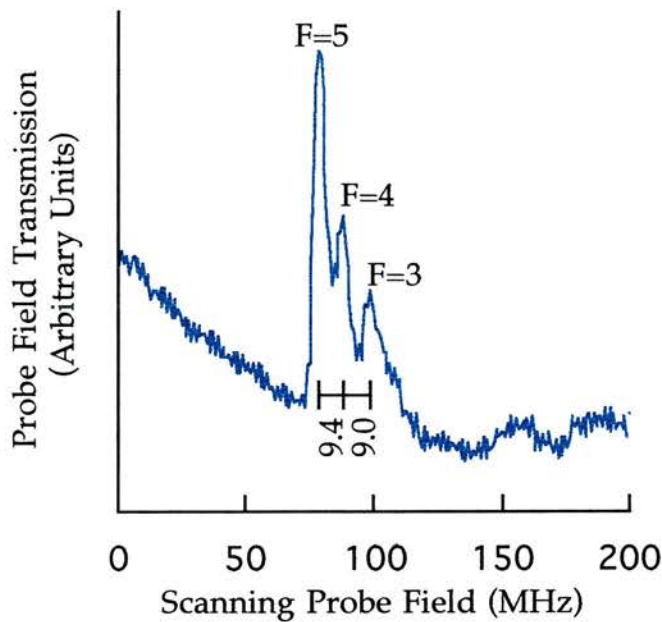
is good, although slightly less transparency is observed than theoretically predicted. The reasons for this discrepancy are the same as those given in the previous section, i.e. imperfect mode matching of the fields, absorption of the edges of the probe due to the coupling field Gaussian radial profile and effects of E.I.F. A further cause of the reduction in the observed transparency stems from the hyperfine structure of the $5D_{5/2}$ level which results in multiple E.I.T. resonance frequency positions. These are visible on careful inspection of the ^{87}Rb , $5S_{1/2}$ ($F=2$) \rightarrow $5P_{3/2}$ transition at 19 mW and 5 mW coupling field power. This phenomenon is the origin of the first method for employing E.I.T. as a spectroscopic technique which will be discussed in detail in the following section. A final point to note is that the dephasing rates in the experimental system will be higher than those predicted in the model due to atomic collisions and to the fact that the lasers have a finite linewidth. Nevertheless, the experimentally achieved transparency levels are high, in excess of 90% in the 300 mW power trace, despite the appreciable hyperfine structure of the atomic levels.

5.3.3) Employing E.I.T. As A Method Of Spectroscopy

As noted in the previous section there is transparency whenever two photon resonance occurs. This allows E.I.T. to be used for spectroscopic purposes, revealing the structure of the top level as well as the ground state. The ground state splitting is large enough (3 GHz or 6 GHz) such that the upper level structure is clearly resolvable, provided it is greater than the residual Doppler width. With good resolution two photon selection rules predict the presence of five allowed E.I.T. resonances within ^{85}Rb and four or three within ^{87}Rb depending on what ground state hyperfine level is employed [10]. The reason for difference in the number of allowed two photon transitions between the two isotopes of rubidium is a direct result of the fact that these isotopes have different nuclear spin values, I . Figure 5.5 shows the detail of the E.I.T. features within (a) ^{87}Rb and (b) ^{85}Rb achieved experimentally in this system. However, only three sub-levels can be resolved in both of these cell transmission curves, probably due to the small dipole matrix element for the highest frequency components. One noticeable difference between the two traces is the spacing of the three observed transmission peaks.



(a)



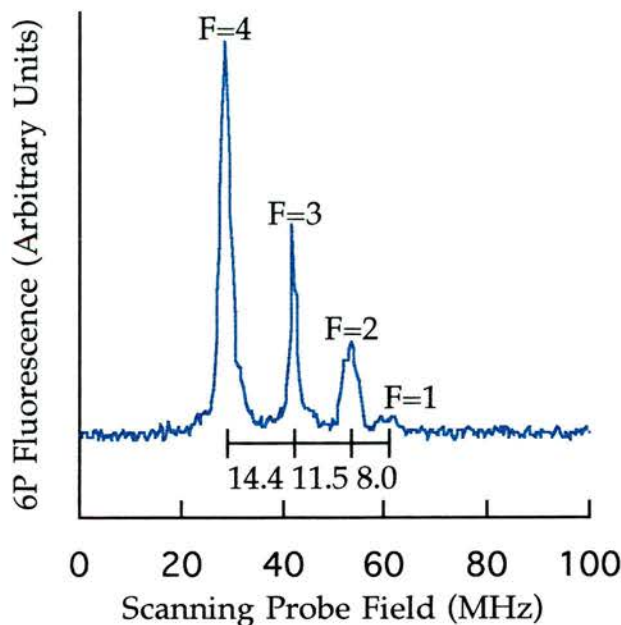
(b)

Figure 5.5:- Detail of (a) the ^{87}Rb , $5S_{1/2}$ ($F=2$) \rightarrow $5P_{3/2}$ probe absorption and (b) the ^{85}Rb , $5S_{1/2}$ ($F=3$) \rightarrow $5P_{3/2}$ probe absorption, with a coupling laser power of 75 mW. The three resolved E.I.T. peaks in (a) correspond to the two photon resonances from $5S_{1/2}$ ($F=2$) \rightarrow $5D_{5/2}$ ($F=4, 3, 2$) hyperfine levels as marked. The three resolved E.I.T. peaks in (b) correspond to the two photon resonances from $5S_{1/2}$ ($F=3$) \rightarrow $5D_{5/2}$ ($F=5, 4, 3$) hyperfine levels as marked. Probe laser power 2.5 μW , vapour temperature 47 $^{\circ}\text{C}$ and both beams are unfocused with approximately 1 mm beam radii.

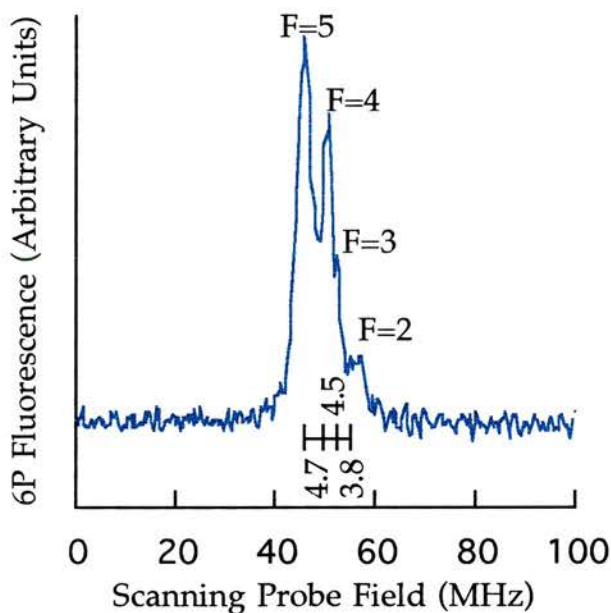
This reflects the different atomic splittings of the hyperfine components of the $5D_{5/2}$ upper state, the corresponding theoretical values for which are marked on the graphs. For ^{87}Rb the resolved peaks correspond to the two photon transitions from the $5S_{1/2}$ ($F=2$) ground state hyperfine level to the $5D_{5/2}$ ($F= 4, 3, 2$) upper state levels, with the $5D_{5/2}$ ($F= 1$) resonance remaining unresolved. The corresponding resolved ^{85}Rb peaks are the two photon transitions from the $5S_{1/2}$ ($F=3$) ground state hyperfine level to the $5D_{5/2}$ ($F= 5, 4, 3$) upper state levels, and again the highest frequency component $5D_{5/2}$ ($F= 2$) is unresolved. These traces were taken with both beams unfocused, with approximately 1 mm beam radii, and with a coupling field power of 75 mW. Spectroscopic accuracy is also limited in these results by the stability of the (unstabilised Schwartz Ti:sapphire) coupling laser but a resolution of less than 8 MHz is still displayed. It should also be noted that a similar E.I.T. experiment to the one described above has recently been reported by Jin et al. Here the authors employed diode lasers to generate the required coherence such that E.I.T. could be used as a spectroscopic technique to examine the $5D_{5/2}$ cascade upper state in ^{85}Rb [11].

As a means of comparison two photon Doppler-free spectroscopy was also performed on the $5S_{1/2} - 5D_{5/2}$ transition and the results are presented for both isotopes in the curves of Figure 5.6. A more detailed account of two photon spectroscopy on this transition is presented in the work of Nez et al [10]. The basic idea involves employing a single laser field which is split into two components such that these components counterpropagate through the rubidium cell. Two photon absorption is then experienced when this laser field has a frequency equal to half that of any of the allowed ground state to upper state two photon resonances. Monitoring the fluorescence from the upper $5D_{5/2}$ level provides spectroscopic details of the atomic levels involved.

The two photon absorption curves of Figure 5.6 again show the spectroscopic detail of the two photon transition. Figure 5.6(a) now includes the fourth previously unresolvable two photon resonance corresponding to the ^{87}Rb $5S_{1/2}$ ($F=2$) \rightarrow $5D_{5/2}$ ($F=1$) transition. An extra peak is also resolved for the ^{85}Rb isotope corresponding to the $5S_{1/2}$ ($F=3$) \rightarrow $5D_{5/2}$ ($F= 2$) transition, however the fifth predicted resonance ($5S_{1/2}$ ($F=3$) \rightarrow $5D_{5/2}$ ($F= 1$)) still remains unresolved due to it having such a weak dipole matrix element, a factor of 50 less than the $5S_{1/2}$ ($F=3$) \rightarrow $5D_{5/2}$ ($F= 5$) transition [10].



(a)



(b)

Figure 5.6:- Equal frequency Doppler free two photon spectroscopy results for (a) ^{87}Rb , $5S_{1/2}$ ($F=2$) \rightarrow $5D_{5/2}$ two photon absorption. The four resolved peaks correspond to the two photon resonances from $5S_{1/2}$ ($F=2$) \rightarrow $5D_{5/2}$ ($F= 4, 3, 2, 1$) hyperfine levels as marked. (b) ^{85}Rb , $5S_{1/2}$ ($F=3$) \rightarrow $5P_{3/2}$ two photon absorption. The three resolved peaks correspond to the two photon resonances from $5S_{1/2}$ ($F=3$) \rightarrow $5D_{5/2}$ ($F= 5, 4, 3$) hyperfine levels as marked. Input laser power 300 mW, 40 cm focusing lenses and vapour temperature 200 °C.

In comparing the two techniques it should be noted that the conventional two photon experiment was conducted at a greatly increased temperature, and thus particle density, compared to the E.I.T. experiment. This was necessary in order to achieve sufficient two photon absorption so as to enable fluorescence detection. However, the possible resolution is not limited by the first order Doppler effect due to the exact equality of the photon energies on the two photon transition. On the other hand the E.I.T. result has a limited resolution set by the residual Doppler broadening of the two photon field. This is 1.38 MHz in this experiment and depends on the near coincidence of the chosen transition wavelengths. The different resolving powers of the two techniques is evident in the fact that it was possible to resolve more of the allowed two photon resonances using two photon spectroscopy. The coupling field strength will also limit resolution in the E.I.T. technique, however a resolution approaching the laser linewidths and two photon residual Doppler width is attainable. In favour of the E.I.T. method is the fact that it relies on the single photon absorption levels and therefore can be conducted at greatly reduced particle densities, and hence temperatures. This greatly simplifies the detection of the signal which can be accomplished by the use of a simple photodiode. Therefore, under circumstances of low available particle densities, spectroscopy of a two photon transition by E.I.T. may be preferable. It is noted that high resolution spectroscopy via velocity selection [12] (as opposed to Doppler free techniques) could be used under similar conditions to E.I.T., however, this is sensitive to the intermediate level structure which may complicate the observed results, while E.I.T. is not.

As a final point it should be noted that the Λ -type and V-type systems could also be used for spectroscopic purposes and that the available resolution could be significantly higher than that shown here due to closer matching of transition wavelengths. As an example, a sub-natural linewidth feature was observed in the Λ -type system experiment of Akulshin et al. [13].

5.4) Effect Of Coupling Field Detuning

While examining the effects of optical field geometry it was seen that the E.I.T. feature did not always appear central within the four Doppler broadened features of Figure 5.3. This results from the fact that the coupling field is slightly detuned from

exact resonance for peaks III and IV. In this section a more systematic study of the effects of coupling field detuning is carried out. The behaviour with successive steps in coupling laser tuning is shown in Figure 5.7(a), with the corresponding theoretical traces for a three level atom displayed in Figure 5.7(b).

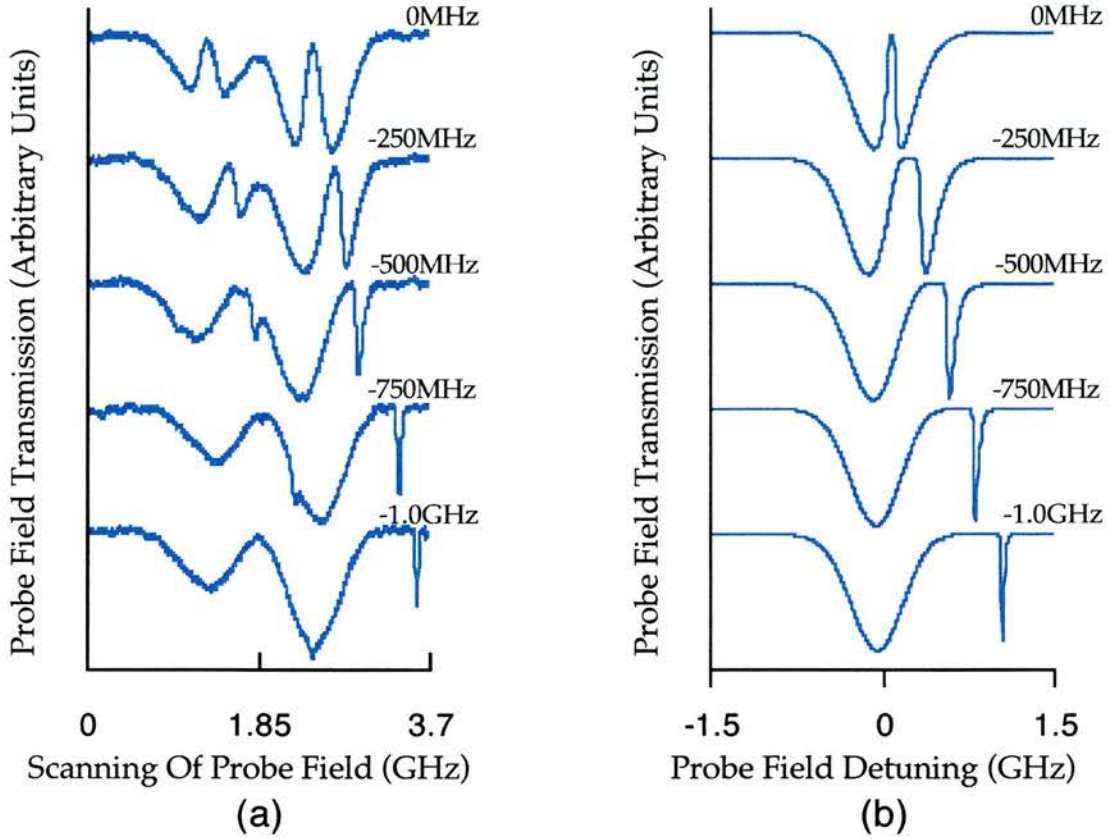


Figure 5.7:- (a) Experimental probe field transmission curves as the probe laser is scanned across the ^{87}Rb , $5S_{1/2}$ ($F=2$) and ^{85}Rb , $5S_{1/2}$ ($F=3$) to $5P_{3/2}$ transitions (peak I and II) as the coupling laser is detuned in successive 250 MHz steps. The coupling laser power is 300 mW, the probe laser power $3 \mu\text{W}$ and the oven temperature is $\sim 47^\circ\text{C}$. (b) Theoretical probe field transmission curves as the coupling field is detuned in 250 MHz steps. ($\Omega_{12} = 1 \text{ MHz}$, $\Omega_{23} = 220 \text{ MHz}$ and vapour temperature = 47°C).

As is clearly observed there is a sharpening of the inner edge of the transparency as the coupling field is tuned off exact resonance. This predicted sharpening of the inner edge is a hallmark of E.I.T. with a slightly detuned coupling field. As the detuning rises the two sub-components from each line take on markedly different characters. One remains Doppler broadened and does not move significantly, whereas the other narrows and

moves appreciably with the coupling laser tuning. Once the detuning is in excess of the on resonance Rabi splitting value the narrow peak may be identified as coming from two photon absorption (due to the low residual width on this transition), and the Doppler broadened peak as coming from single photon absorption. The two photon peak is surprisingly strong but this can be accounted for through resonant enhancement with the $5P_{3/2}$ intermediate level, without a corresponding population movement [14, 15, 16]. Figure 5.8 shows diagrammatically a simplified argument for the change in excitation conditions experienced within the experiment.

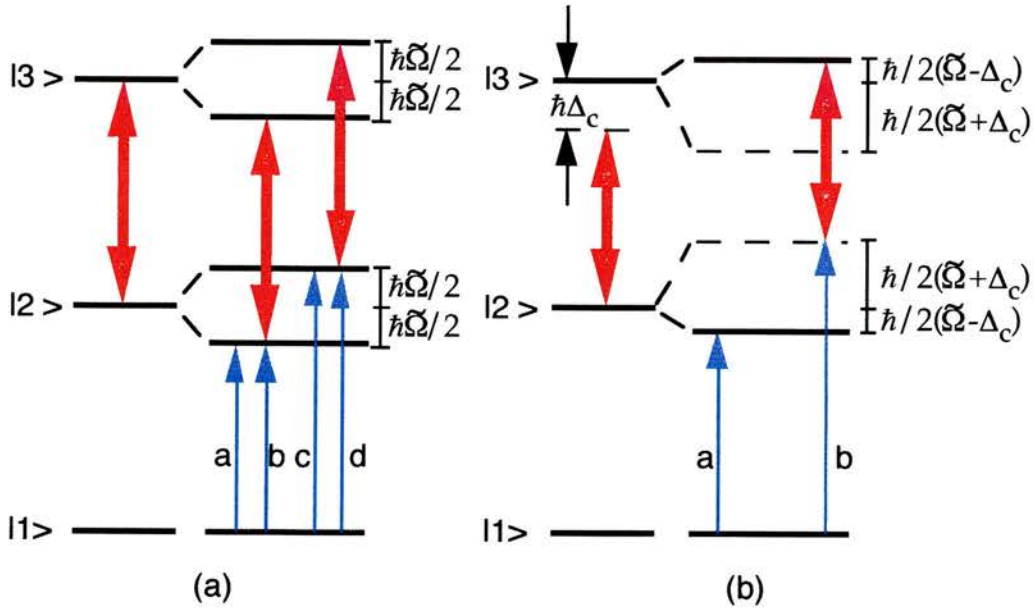


Figure 5.8:- A schematic representation of the atomic conditions when (a) the Rabi frequency of the coupling field, $\Omega_c = \mu_{23}E_c/\hbar$, is in excess of the detuning, and (b) when $\Omega_c < \Delta_c$. In the figure $\tilde{\Omega}$ denotes the generalised Rabi frequency given by $\tilde{\Omega} = \sqrt{\Omega_c^2 + \Delta_c^2}$.

Initially, when the Rabi frequency induced by a resonant coupling field is in excess of the detuning, the atom is in the condition of Figure 5.8(a). E.I.T. can be considered to be the complicated combination of four separate routes marked 'a' to 'd'. Two of these routes can be considered single photon, 'a' and 'c', while the other two, 'b' and 'd', are two photon excitation routes. Once the coupling laser is detuned in excess of the on resonance Rabi splitting then Figure 5.8(b) displays the atomic conditions. Due to an asymmetric splitting of the Autler-Townes sub-components the relative strengths of the

single photon transitions and of the two photon transitions alter. Considering the single photon transitions first, the route labelled 'a' dominates over the one labelled 'c' since the sub-component of the Autler-Townes splitting with which it interacts remains closer in energy to the original bare state $|2\rangle$. By a similar argument the two photon route labelled 'b' dominates in the detuned experiment because it interacts with the stronger weighted Autler-Townes sub-component of the original upper level bare state $|3\rangle$. An interesting point however is the fact that this two photon route is resonantly enhanced by maintaining exact resonance with the weaker Autler-Townes sub-component of level $|2\rangle$ under all conditions. The further that the coupling laser is detuned the clearer is the separation between single and two photon absorption within the experiment. Indeed the final two traces of Figure 5.7 have no E.I.T. character visible at all. A point to note is how the ^{87}Rb two photon feature moves in frequency over the ^{85}Rb single photon line with no interaction between the two as is to be expected for pathways of separate isotopes.

The above argument provides a somewhat over simplified picture of what is happening in the real atomic system in the presence of a detuned coupling field. It is presented merely to offer a phenomenological explanation for the differing effects between the cases where the coupling field is far from resonance or on exact resonance. It is not a complete description of the system since it does not adequately describe the process occurring at intermediate coupling field detunings (those of the order of the induced Rabi frequency for a resonant coupling field). A more complete description of these effects may be found in recent papers by Vemuri et al. [17, 18].

5.5) A Population Comparison

Another aspect of this cascade system is that it allows simultaneous measurement of the upper state population, $5D_{5/2}$, via cascade decay to the $6P$ levels. This provides a second diagnostic for examining the effects of E.I.T. on the probe field transition since excitation to the upper level depends directly on a two photon interaction, i.e. absorption of a probe field photon followed by a coupling field photon [12,14]. Fluorescence results recorded alongside the E.I.T. curves of Figure 5.4(a) are presented in Figure 5.9(a). Examination of these traces shows that the fluorescence features are sub-Doppler in nature due to the velocity selective excitation conditions, but are

strongly affected by power broadening. Also included in Figure 5.9(b) are theoretical calculations of the upper level population (ρ_{33}) for Rabi frequencies corresponding to the powers used in the experimental traces of Figure 5.9(a). It is seen from Figure 5.9 that the predicted fluorescence lineshapes match up well with those obtained experimentally. However, better E.I.T. is again obtained theoretically than is experimentally observed, as was to be expected from the discussion in Section 5.3.1. Good agreement is also seen between these fluorescence results and those of the earlier probe absorption curves of Figure 5.4.

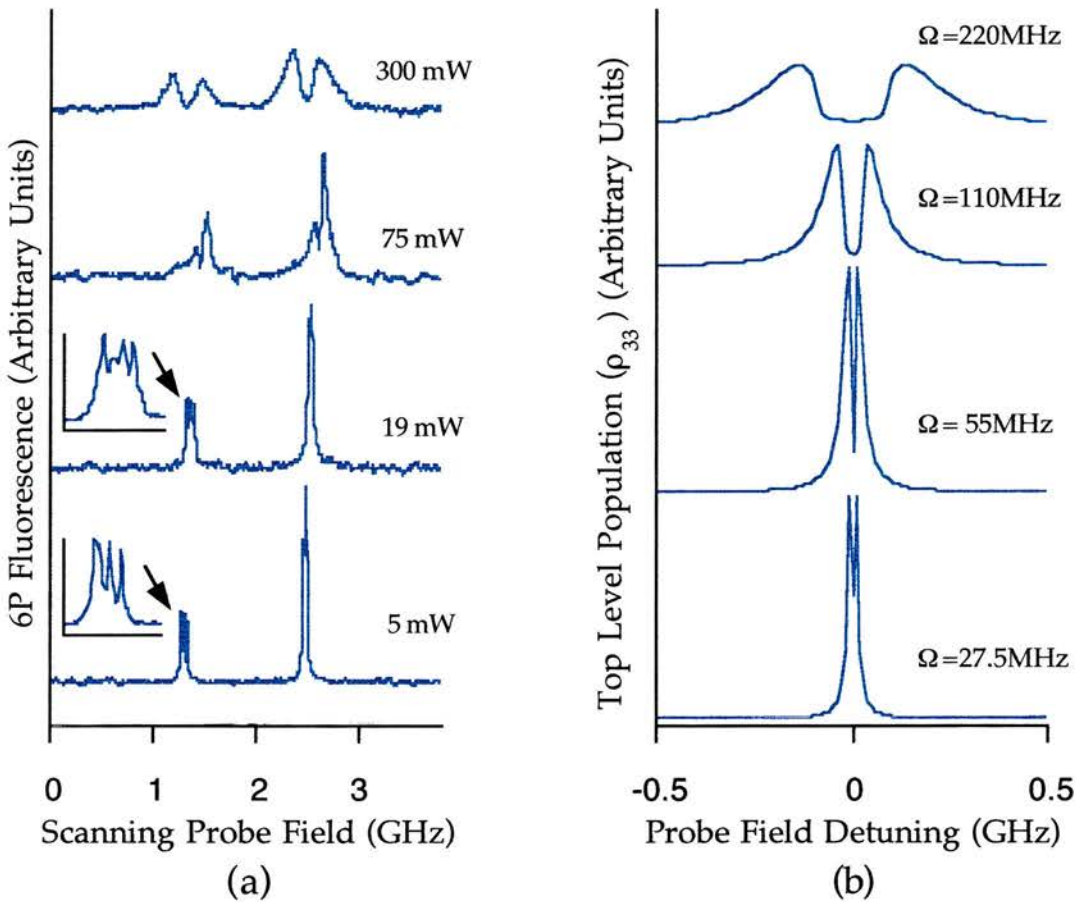


Figure 5.9:- (a) Experimental fluorescence from the $6P \rightarrow 5S_{1/2}$ spontaneous decay at 422 nm, which is proportional to the population of the $5D_{5/2}$ level, detected during the corresponding coupling field power traces of Figure 5.4. (b) Theoretical calculations of the upper level population from a three level density matrix model which includes Doppler broadening effects (for 47 °C) at the coupling field Rabi frequencies corresponding to the experimental traces of (a).

Experimental traces taken at 300 mW and 75 mW coupling field power show obvious Autler-Townes splitting characteristics. However the 75 mW trace appears a little asymmetric which is a result of the fact that the coupling laser was slightly detuned from exact resonance, as explained in the previous section. As expected the maximum excited population is observed to increase as the coupling laser power is lowered, thus reducing the effects of power broadening. This can be explained by the fact that since the probe laser intensity remains constant across all of these traces, the upper state population curve is effectively normalised. Therefore, as the coupling field power increases the fluorescence feature power broadens and so the magnitude of the peak maximum is reduced. Over and above this effect there is a second contribution to the maximum fluorescence at lower coupling field powers with the fact that as the coupling field power is reduced, the effect of E.I.T. is reduced and so greater excitation from the $5S_{1/2}$ ground state can take place. By the 19 mW and 5 mW traces the structure of the $5D_{5/2}$ level can be resolved, as shown by the insets of Figure 5.9(a). However, Autler-Townes splitting is still visible in the strongest (leftmost) component in both of these traces. A point to note is that the first E.I.T. feature in the 19 mW trace occurs at the frequency of the dip between the first two peaks of the fluorescence. This is a result of the fact that these two peaks are just two Autler-Townes components of the one hyperfine upper state. Autler-Townes shifts cause the other fluorescence peaks to be slightly offset from the relevant E.I.T. dips.

A final point to note is that the predicted and observed dip in population excitation is less than that predicted and observed due to E.I.T. on probe field absorption. This characteristic is observable in all of the fluorescence traces but is most obvious in the two lower powered coupling field traces. This phenomenon is not a result of the fact that the fluorescence is less affected by E.I.T. but is a misleading side effect due to the narrow Lorentzian lineshape of the fluorescence. The edges of the fluorescence lines which lie outside the E.I.T. feature are well below the level of the fluorescence maximum that would be observed in the absence of E.I.T. Thus the true reduction in the population is hard to accurately gauge. This in contrast to the probe absorption measurements since the absorption levels outside the E.I.T. window are close to the peak absorption levels in the absence of E.I.T. This is particularly true on the two lower powered traces where the upper state sub-levels show an Autler-Townes splitting on a similar scale to their hyperfine separation which only acts to add further complications to the results.

Fluorescence curves, obtained in the presence of a detuned coupling field, were also recorded along with the probe absorption curves of Figure 5.7. These are presented in Figure 5.10(a) along with the equivalent theoretical predictions of Figure 5.10(b). Both of these graphs again show excellent agreement with the experimental and theoretical curves obtained for the probe field transmission results of Section 5.4.

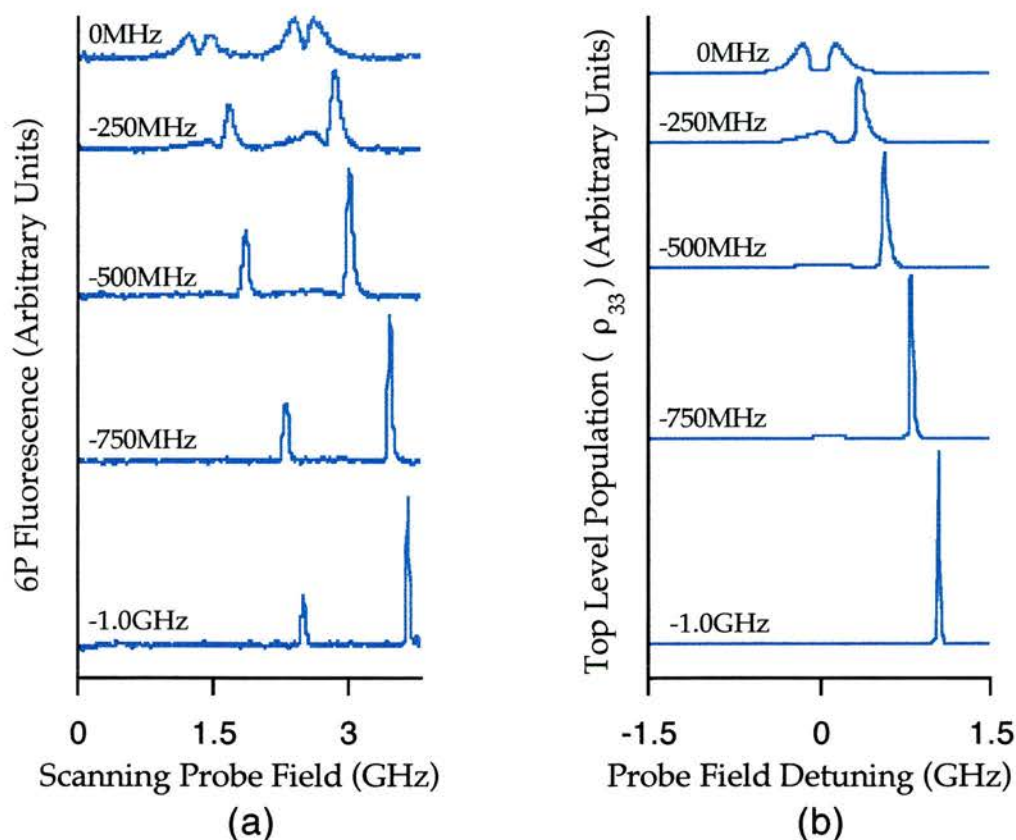


Figure 5.10:- (a) Experimental fluorescence from the $6P \rightarrow 5S_{1/2}$ spontaneous decay at 422 nm, which is proportional to the population of the $5D_{5/2}$ level, detected during the corresponding coupling field detuning traces of Figure 5.7. (b) Theoretical calculations of the upper level population from a three level density matrix model which includes Doppler broadening effects (for 47 °C) at the coupling field detunings stated.

The fluorescence traces again show the broadening and eventual disappearance of one sub-component along with the narrowing of the other. This is entirely consistent with the argument that a separation into single and two photon excitation routes occurs as was outlined in Figure 5.8. The increase in peak fluorescence during detuning is due to

the narrowing of the line and the asymmetry introduced during detuning which shifts the peak of the fluorescence to one side of the E.I.T. window.

5.6) A Theoretical Look At The Effects Of Introducing A Magnetic Field

The application of a magnetic field to an atomic system causes the levels to split due to the Zeeman effect [8]. When the applied magnetic field is of sufficient strength it allows previously degenerate atomic levels to be resolved. For example, J states each have $(2J+1)$ degenerate levels labelled from $m_J = J$ to $m_J = -J$ and similarly hyperfine levels have a $(2F+1)$ degeneracy labelled from $m_F = F$ to $m_F = -F$. The effect of the magnetic field can be characterised into three regions: a weak field region, an intermediate field region and a strong field (or Paschen Back) region [19, 20]. The weak field region is the one in which the splitting of the hyperfine components ($\propto \mu_B B$) is much less than the zero field splitting of the F components (twice ξ_{HF} , the hyperfine constant). It follows that the Paschen Back region is where the opposite is true and that the intermediate field region falls between these two regimes. In the weak field case Zeeman splitting can be perceived as being a small perturbation on the hyperfine interaction whereas in the Paschen Back region the hyperfine interaction is regarded as the small perturbation acting upon the Zeeman effect.

Since increasing the applied magnetic field strength causes atomic levels to pass through the three regions described above, it is not appropriate to use either m_F or m_J as the basis on which transitions between levels are traced as the eigenstate mixture within each level is not constant. Instead it is appropriate to employ the more fundamental quantum numbers m_ℓ and m_s . The quantum number m_ℓ takes the values from ℓ to $-\ell$, where ℓ is the orbital angular momentum. The value of m_s can be either $1/2$ (termed spin up) or $-1/2$ (termed spin down). During an atomic transition it is known that an electron cannot change its spin value and so only transitions to levels with the same spin value are allowed [21]. This gives the selection rule $\Delta m_s = 0$. The Δm_ℓ selection rule is dependent on the polarisations of the input optical fields and on the orientation of the applied magnetic field. In this experiment the applied magnetic field is perpendicular to the counter-propagating optical fields. For this set-up the presence of the applied magnetic field results in the single photon Δm_ℓ selection rules listed in Table 5.1:

Table 5.1:- Single photon Δm_ℓ selection rules

Optical Field Polarisation	Δm_ℓ
Parallel To The Magnetic Field	0
Perpendicular To The Magnetic Fields	± 1

How two photon electric dipole selection rules can be obtained through the combination of the above single photon selection rules is outlined by Bonin et al. [22]. Table 5.2 below shows the selection rules appropriate to the $5S_{1/2}$ - $5D_{5/2}$ two photon transition within this cascade system experiment.

Table 5.2: Two photon selection rules

	Probe field polarisation	Coupling field polarisation	Two photon selection rules	
			Δm_ℓ	Δm_s
(a)	Parallel	Parallel	0	0
(b)	Parallel	Perpendicular	± 1	0
(c)	Perpendicular	Perpendicular	$0, \pm 2$	0

Each of the fine and hyperfine levels are a mixture of spin $1/2$ and spin $-1/2$ eigenstates. The m_J and m_F quantum numbers are composed as follows:

$$m_J = m_\ell + m_s \quad (5.6)$$

$$m_F = m_I + m_J \quad (5.7)$$

For the $5S_{1/2}$ state $m_\ell = 0$, so $m_J = \pm 1/2$, therefore any m_F hyperfine state consists of two components related to both the spin eigenstates such that:

$$\begin{aligned}\Psi(n, \ell, m_F) &= C_1 \phi |m_\ell, m_s\rangle + C_2 \phi |m'_\ell, m'_s\rangle \\ &= C_1 \phi |m_F - \frac{1}{2}, \frac{1}{2}\rangle + C_2 \phi |m_F + \frac{1}{2}, -\frac{1}{2}\rangle\end{aligned}\quad (5.8)$$

Similarly, the m_J hyperfine states consist of two components related to both the spin eigenstates such that:

$$\begin{aligned}\Psi(n, \ell, m_J) &= C_1 \phi |m_\ell, m_s\rangle + C_2 \phi |m'_\ell, m'_s\rangle \\ &= C_1 \phi |m_J - \frac{1}{2}, \frac{1}{2}\rangle + C_2 \phi |m_J + \frac{1}{2}, -\frac{1}{2}\rangle\end{aligned}\quad (5.9)$$

The two coefficients C_1 and C_2 are the Clebsch-Gordan coefficients of the eigenstates. These coefficients describe the relative admixtures that constitute each sub-level. As a physical quantity, the squares of these values gives the probabilities of finding the electron in either of the spin states. In order that the wavefunction be normalised (i.e. $\Psi\Psi^* = 1$.) it is necessary that the Clebsch-Gordan coefficients satisfy the following condition:

$$(C_1)^2 + (C_2)^2 = 1 \quad (5.10)$$

These coefficients depend on the strength of the applied magnetic field, one increasing while the other decreases as the magnetic field grows. Employing the following expressions enables these coefficients to be calculated:

$$(C_1)^2 = \frac{Y^2}{Y^2 + Z^2} \quad (5.11)$$

$$(C_2)^2 = \frac{Z^2}{Y^2 + Z^2} \quad (5.12)$$

where for fine states

$$Z = Z_F = \frac{\xi_F}{2} \sqrt{\left(\ell + m_J + \frac{1}{2}\right)\left(\ell - m_J + \frac{1}{2}\right)} \quad (5.13)$$

$$Y = Y_F = \frac{\xi_F}{2} \left(m_J + \left(\frac{\mu_B B}{\xi_F} \right) \pm \frac{1}{2} \sqrt{x_F} \right) \quad (5.14)$$

$$x_F = 1 + 8m_J \left(\frac{\mu_B B}{\xi_F} \right) + 4 \left(\frac{\mu_B B}{\xi_F} \right)^2 + 4\ell(\ell + 1) \quad (5.15)$$

ξ_F - fine structure constant (35.5252 Hz), ℓ - orbital angular momentum, m_J - magnetic total angular momentum of electron, μ_B - Bohr magneton (in frequency units 14 GHz / T), B - applied magnetic field (Tesla). (All bracketed values refer to ^{85}Rb)

and for hyperfine states

$$Z = Z_{\text{HF}} = \frac{\xi_{\text{HF}}}{2} \sqrt{\left(I + m_F + \frac{1}{2} \right) \left(I - m_F + \frac{1}{2} \right)} \quad (5.16)$$

$$Y = Y_{\text{HF}} = \frac{\xi_{\text{HF}}}{2} \left(m_F + \left(\frac{(g_J - g_I)\mu_B B}{\xi_{\text{HF}}} \right) \pm \frac{1}{2} \sqrt{x_{\text{HF}}} \right) \quad (5.17)$$

$$x_{\text{HF}} = 1 + 8m_F \left(\frac{(g_J - g_I)\mu_B B}{\xi_{\text{HF}}} \right) + 4 \left(\frac{\mu_B B}{\xi_{\text{HF}}} \right)^2 + 4I(I + 1) \quad (5.18)$$

ξ_{HF} - hyperfine structure constant (1.0119Hz), I - nuclear intrinsic spin (5/2), m_F - magnetic total angular momentum of atom, g_J - Landé g value (2.0023 for $5S_{1/2}$ level or 1.20 for $5D_{5/2}$ level) and g_I nuclear g factor (0.0003) and other symbols as previously defined. (All bracketed values refer to ^{85}Rb)

The magnetic field used to produce the Zeeman splitting in this experiment had a strength of 8 mT. In this field region, the hyperfine I-J coupling for the $5S_{1/2}$ ground state does not significantly break down. The energy shifts of the (F, m_F) states are found by solving a 2x2 secular equation, the result of which is the following form of the Breit-Rabi formula shown below [19, 23]:

$$\Delta E_{\text{BR}} = -g_I m_F \mu_B B - \frac{\xi_{\text{HF}}}{4} \pm \frac{\xi_{\text{HF}}}{4} \sqrt{x_{\text{HF}}} \quad (5.19)$$

Let us consider the $5S_{1/2}$ ($F=3$) level of ^{85}Rb . Figure 5.11 shows the relative hyperfine Zeeman splitting of the m_F states within this level. It can be seen that the application of a magnetic field causes the degeneracy of the level to be lifted and the seven m_F states are clearly separated at a field value of 8 mT. At this magnetic field

seven m_F states are clearly separated at a field value of 8 mT. At this magnetic field value the total Zeeman splitting of the $5S_{1/2}$ ($F=3$) level is of the order of 225 MHz. The other three hyperfine ground states of rubidium split in a similar fashion.

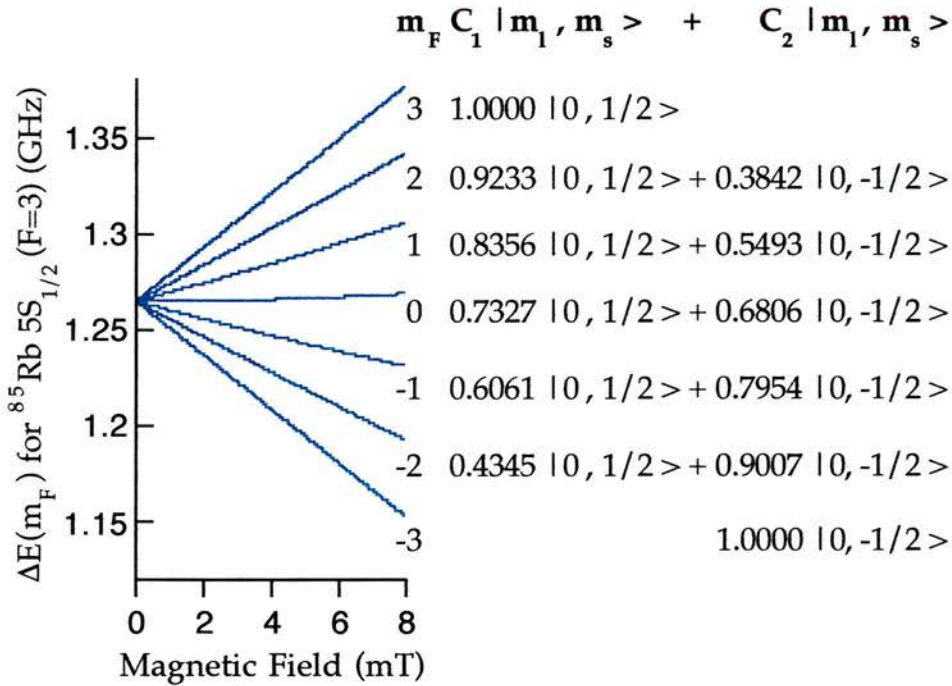


Figure 5.11:- An energy diagram showing the effects of an applied weak magnetic field on the $5S_{1/2}$ ($F=3$) state in ^{85}Rb . Shown on the right are the related $m_\ell - m_s$ basis eigenstates with the corresponding weak field Clebsch-Gordan coefficients, calculated at 8 mT. The observed offset on the zero field level position is due to the hyperfine splitting of the ground state.

For the upper state, $5D_{5/2}$, the hyperfine structure is small (~ 4 MHz) [24] and so, even for our relatively small applied magnetic fields, the hyperfine I-J coupling is effectively broken. A simplified linear approximation for the Zeeman splitting in L-S coupling is then appropriate [20]:

$$\Delta E = g_J m_J \mu_B B \tag{5.20}$$

Figure 5.12 shows the Zeeman splitting of the m_J states for the $5D_{5/2}$ level of ^{85}Rb . Application of the magnetic field again causes the degeneracy of the level to be

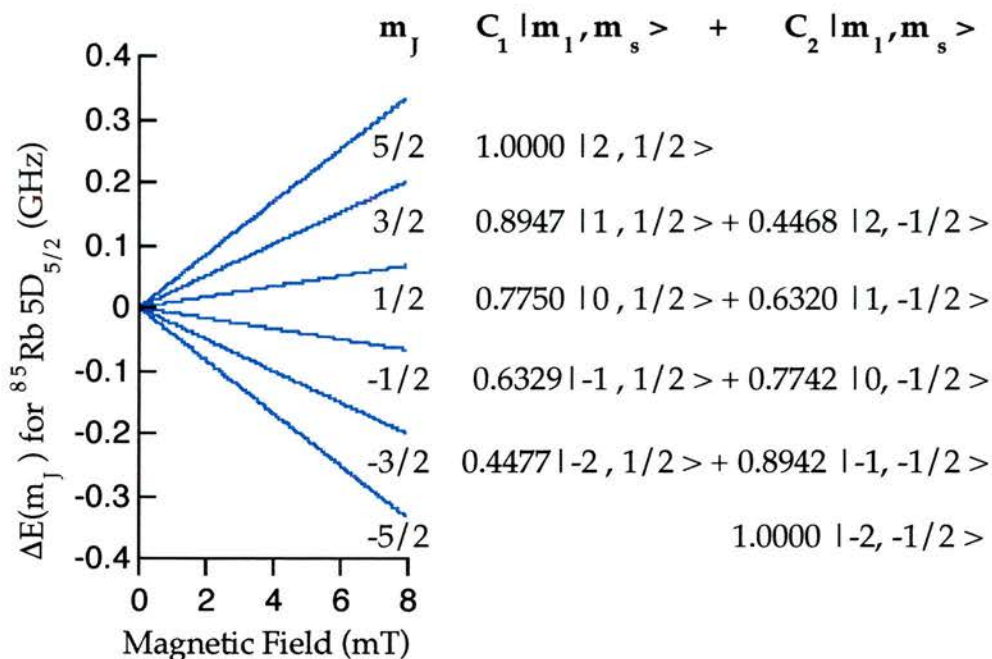


Figure 5.12:- An energy diagram showing the effects of an applied weak magnetic field on the $5D_{5/2}$ state in ^{85}Rb . Shown on the right are the related $m_\ell - m_s$ basis eigenstates with the corresponding weak field Clebsch-Gordan coefficients, calculated at 8 mT.

In order to calculate the Zeeman splittings of the levels involved in the two-photon, $5S_{1/2} - 5D_{5/2}$, transitions, it is necessary to identify all those that are dipole allowed. However, as has been previously discussed, the Zeeman splittings of the two levels are most conveniently described within different basis states: L-S eigenstates for the $5S_{1/2}$ level and I-J eigenstates for the $5D_{5/2}$ level. By choosing the $m_\ell - m_s$ basis to describe both levels, a picture of the allowed dipole transitions can be obtained. Shown on the right-hand side of the energy level diagrams in Figures 5.11 and 5.12 are the corresponding $m_\ell - m_s$ eigenstates along with their related Clebsch - Gordan coefficients, for the case when the applied magnetic field is 8 mT.

Initially with no applied magnetic field, the E.I.T. window produced will consist of a degenerate superposition of all the allowed two photon transitions within the $m_\ell - m_s$ basis. When a magnetic field is applied this degeneracy is removed. With reference to the selection rules listed in Table 5.2, it is predicted that, from a macroscopic view

point, it is possible to split the E.I.T. window into various clusters of $\Delta m_\ell = 0, \pm 1, \pm 2$ components. At most only three components will be seen at any one time, corresponding to the case where the probe and coupling fields both have linear polarisations perpendicular to the applied magnetic field.

This, however, is not the complete picture. Each Δm_ℓ component in fact consists of a cluster of lines. These lines correspond to all the allowed dipole transition routes, which simultaneously satisfy the two photon selection rule for a particular Δm_ℓ value. Each Δm_ℓ cluster can be regarded as a “comb” having “teeth” which correspond to each of the allowed sub-level transitions. E.I.T. will occur at each two-photon position as dictated by the Zeeman splitting. The applied magnetic field causes the formation of five clusters corresponding to the five possible Δm_ℓ selection rules as shown in Figure 5.13. Each cluster can be seen to consist of twelve sub-components.

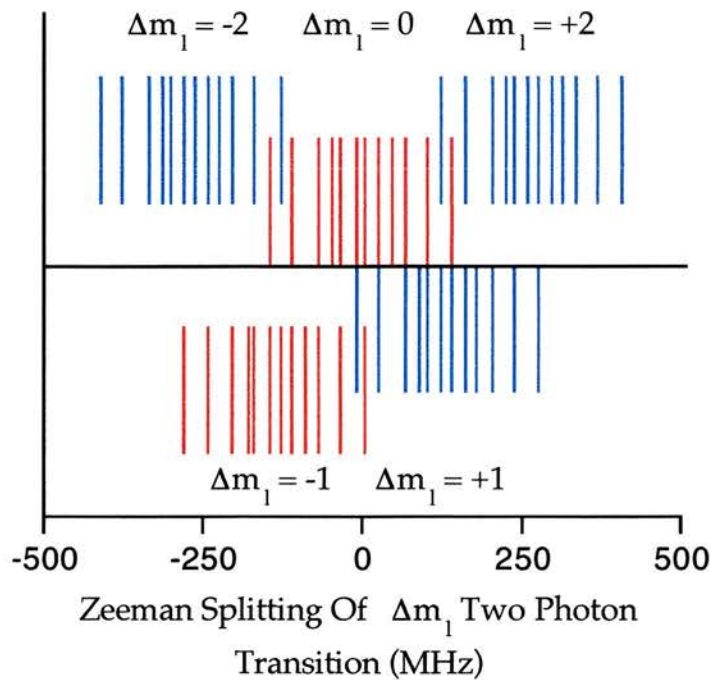


Figure 5.13:- Zeeman splitting, at 8 mT, of all the allowed Δm_ℓ two-photon transitions in the $m_\ell - m_s$ basis. Five clusters can be seen corresponding to $\Delta m_\ell = 0, \pm 1, \pm 2$ selection rules, each of which consists of twelve sub-components.

It is expected that the depths of the E.I.T. feature will be reduced, relative to that of the initial window, when the magnetic field is introduced. This is due to two processes which occur simultaneously as the applied magnetic field is increased. Consider the case when the applied optical fields are both perpendicularly polarised. The two-photon selection rule is that $\Delta m_\ell = 0, \pm 2$. Note that, the $\Delta m_\ell = 0$ state is composed of two alternative two-photon routes. An atom may be excited through the cascade system by a $\Delta m_\ell = +1, -1$ combination or by a $\Delta m_\ell = -1, +1$ combination, starting from the same ground state and achieving the same upper state. In this way it can be seen that the coupling field acts on four separate cascade systems. For the case of zero applied magnetic field these four cascade systems are degenerate and so the observed E.I.T. feature is the superposition of four E.I.T. windows observed at a central frequency. Turning to the case when an applied magnetic field is present, then the $\Delta m_\ell = \pm 2$ E.I.T. windows move in frequency space relative to the zero field position. Thus, at the frequency where the $\Delta m_\ell = -2$ transitions are transparent the $\Delta m_\ell = +2$ transitions are not, and vice versa. The two $\Delta m_\ell = 0$ clusters are still found at the central frequency position. Hence, the observed E.I.T. feature is now the superposition of four distinct E.I.T. windows, only two of which are at the same frequency position. From this argument it is expected that in applying a magnetic field we will see a marked reduction in the depth of the observed E.I.T. windows. For the $\Delta m_\ell = \pm 2$ clusters this reduction should be of the order of a factor of four, while the still degenerate $\Delta m_\ell = 0$ clusters should see only a factor of two reduction.

To complicate matters further each Δm_ℓ cascade system is not a true three level system but in fact consists of multiple systems. In the case of the $5S_{1/2} (F=3) - 5D_{5/2}$ system there are twelve simultaneous cascade systems. The magnetic field Zeeman splits all these systems by slightly different values, resulting in an overall broadening of each Δm_ℓ cluster as the applied magnetic field is increased. This broadening mechanism causes a reduction in the depth of the observed E.I.T window due to the corresponding increase of the effective linewidth of the system.

A third factor which must be considered is that each individual cascade system has its own dipole matrix elements. The Autler-Townes splitting connected with an E.I.T. window is directly proportional to the induced Rabi frequency produced by the coupling laser through the exact resonance relation:

$$\Omega = \frac{\mu E_0}{\hbar} \quad (5.21)$$

where Ω is the upper transition Rabi frequency, μ the upper transition dipole matrix element and E_0 the amplitude of the coupling field. Thus, referring to equation (5.21) it is seen that the upper Rabi frequencies differ between systems if the transition matrix elements differ. In Section 5.3.2 it was shown that the depth of an E.I.T window is dependent on the magnitude of the Rabi frequency. Therefore, systems with a smaller coupling field transition Rabi frequency will see an E.I.T. window of reduced depth. The superposition of all the sub-level transitions within each cluster, and the clusters themselves in the zero magnetic field regime, tend to mask out this subtle effect which becomes more apparent in the presence of a magnetic field.

A Grotrian diagram for the allowed coupling transitions between the $5P_{3/2}$ and $5D_{5/2}$ energy levels of rubidium is shown in Figure 5.14.

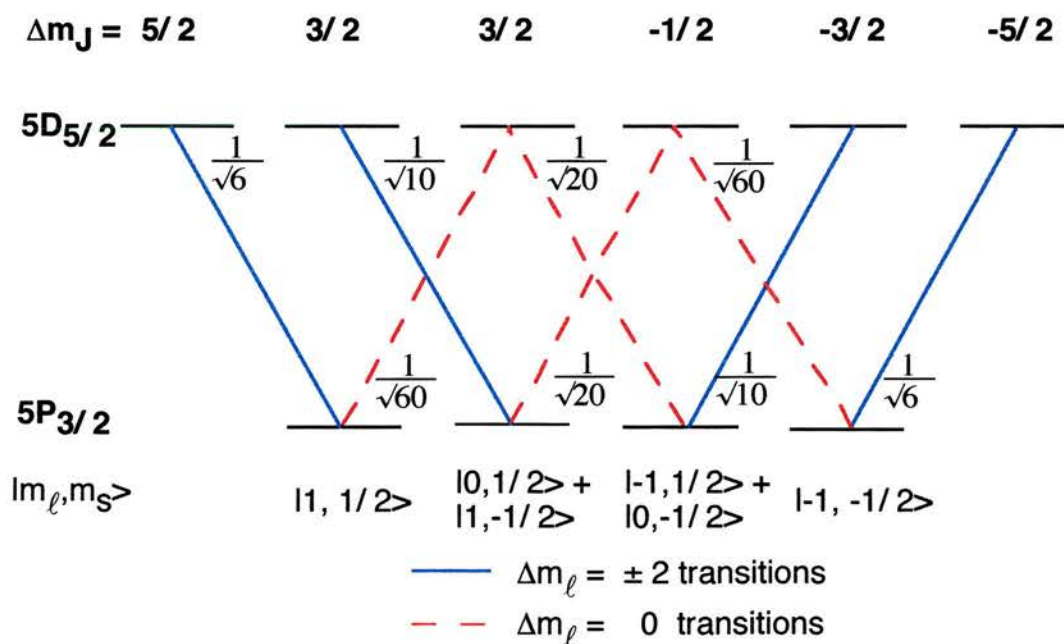


Figure 5.14:- A Grotrian diagram for the allowed transitions between the $5P_{3/2}$ and $5D_{5/2}$ energy levels of rubidium. This diagram shows the relative dipole matrix element strengths for the transitions possible when both fields are linearly polarised perpendicular to the magnetic field ($\Delta m_\ell = 0, \pm 2$).

This diagram shows the relative dipole matrix elements strengths for the transitions possible when both fields are linearly polarised perpendicular to the magnetic field ($\Delta m_\ell = 0, \pm 2$). As can be seen, the routes employed in the $\Delta m_\ell = 0$ two-photon transitions have much smaller dipole matrix elements than those employed in the $\Delta m_\ell = \pm 2$ transitions. The result of this is that the $\Delta m_\ell = 0$ systems are expected to have E.I.T. windows of reduced depths to those in the $\Delta m_\ell = \pm 2$ systems, due to the smaller Rabi frequencies induced by the same coupling field power.

5.7) An Experimental Look At The Effects Of Introducing A Magnetic Field

In this section experimental results are presented where the probe laser on the $5S_{1/2}-5P_{3/2}$ transition is scanned through the ^{87}Rb , $F=2$, and the ^{85}Rb , $F=3$, hyperfine levels. Two magnetic field regimes have been studied for the purpose of this experiment. The "low magnetic field" regime corresponds to the case when the applied magnetic field is ≤ 0.3 mT, while that of the "high magnetic field" has a magnetic field strength ~ 8 mT. Shown in Figure 5.15 is the $6P-5S_{1/2}$, 422 nm fluorescence signal for the case when both the applied optical fields have perpendicular polarisations (row (c) of Table 5.2). The low magnetic field regime, represented by the blue line in Figure 5.15, clearly shows E.I.T. effects induced by the coupling laser, within the fluorescence signal. When we move to the high magnetic field regime, red lines marked with crosses, the effects of the Zeeman splitting superimposed on the E.I.T. features are observed. A 300 MHz confocal signal is also included to give a frequency marker for the graph. There are now three E.I.T. features as predicted, and the $\Delta m_\ell = 0$ and $\Delta m_\ell = \pm 2$ clusters split by ~ 240 MHz, which corresponds to within 10% of the 250 MHz splitting predicted from Figure 5.13. The discrepancy arises due to the error within the experimentally measured magnitude of the applied magnetic field.

Probe field transmission curves for both the low and high applied magnetic field regimes are presented in Figure 5.16 for three different optical field polarisation combinations. Again a 300 MHz confocal signal is included in each as a frequency marker. Taking each graph in turn the varying E.I.T. features which occur can be explained in terms of the arguments presented in Section 5.6.

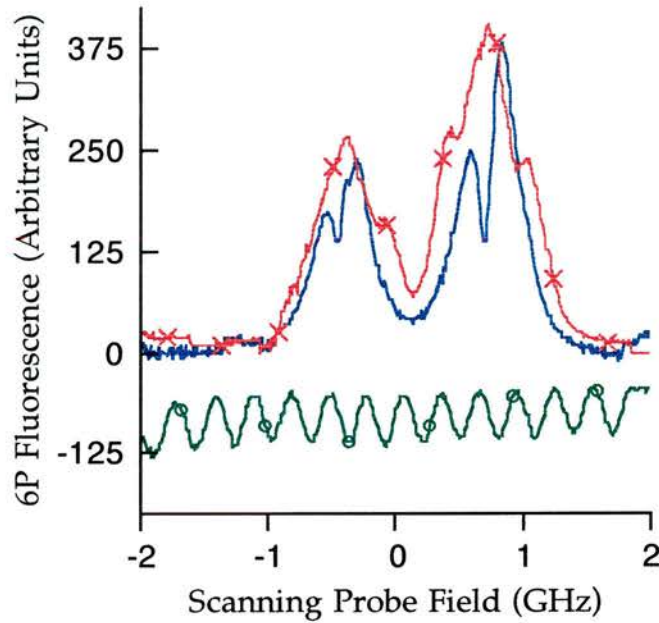


Figure 5.15:- Fluorescence signal from the $6P - 5S_{1/2}$ transition (442 nm), for the case when both applied optical fields had perpendicular polarisations ($\Delta m_\ell = 0, \pm 2$). The blue line represents the case of a low applied magnetic field (≤ 0.3 mT), the red line marked with crosses represents a high applied magnetic field (~ 8 mT). A 300 MHz confocal signal is presented as a frequency reference.

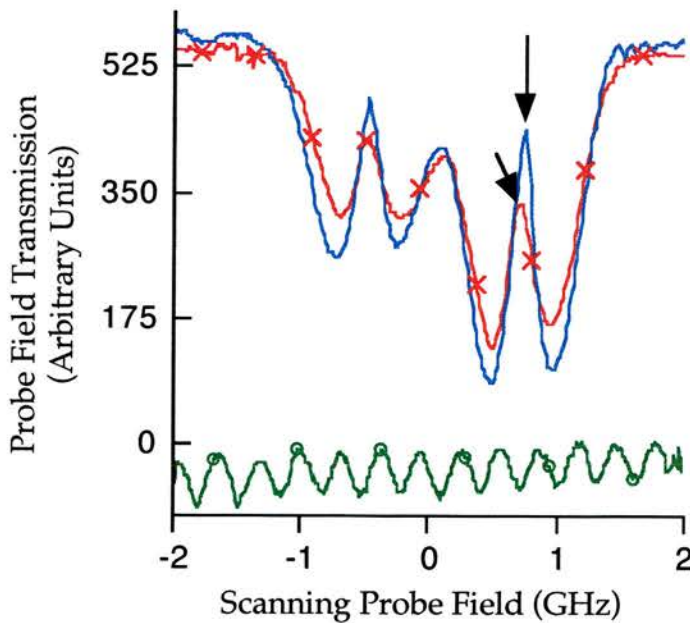
Figure 5.16(a) shows the case when both applied optical fields have parallel polarisation (row (a) of Table 5.2). In this case application of the magnetic field does not produce separate Δm_ℓ clusters. However, the applied magnetic field does cause Zeeman splitting of each sub-level which effectively increases the linewidth of the two photon transition. Hence, since the Rabi frequency is unaltered, the E.I.T. window is reduced. The reduction in the maximum absorption level of the probe laser when moving to the high magnetic field regime is consistent with the lower transition ($5S_{1/2} - 5P_{3/2}$) being spread out due to Zeeman splitting.

Figure 5.16 (b) (corresponding to rows (b) of Table 5.2) shows the E.I.T. window being split into two Δm_ℓ components by the application of a magnetic field. For this optical field configuration the $\Delta m_\ell = \pm 1$ components both split from the original central E.I.T. window position. The E.I.T. windows thus have a marked

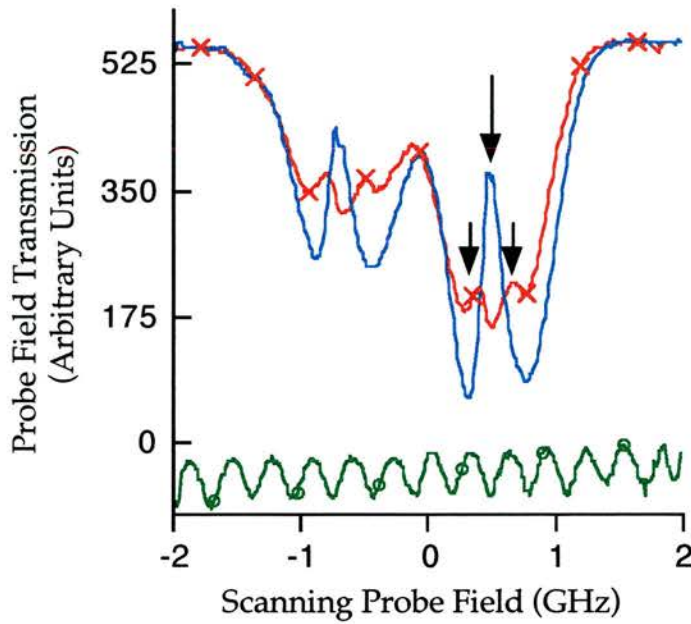
reduction compared to the previous case, due to the loss of degeneracy in frequency space induced by the Zeeman splitting.

Figure 5.16(c) shows the case described by the selection rules of Table 5.2 row (c), where the applied optical fields are both polarised perpendicular to the magnetic field. As predicted, in the high magnetic field regime the E.I.T. window is clearly seen to split into three Δm_ℓ components. Two of the components, $\Delta m_\ell = \pm 2$, split from the line centre leaving only the $\Delta m_\ell = 0$ component there. At ~ 8 mT the splitting of the $\Delta m_\ell = 0$ and $\Delta m_\ell = + 2$ clusters is ~ 225 MHz. This is again within 10% of the theoretically predicted splitting of Figure 5.13 and also of the experimental splitting observed on the fluorescence signal of Figure 5.15.

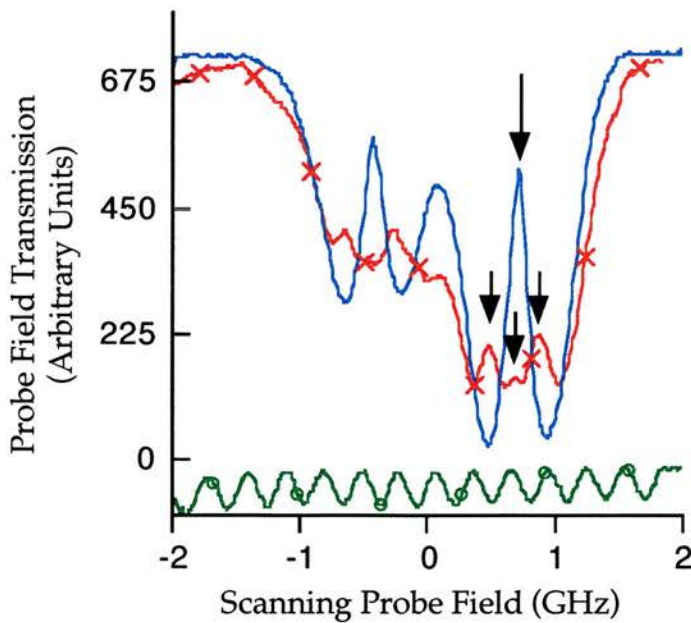
Figure 5.16:- The probe field transmission for the low (blue line) and high (red line marked by crosses) applied magnetic field regimes. A 300 MHz confocal signal is included as a frequency marker. The frequency positions of the E.I.T. features are shown by a long tailed arrow for the low magnetic field regime, and by a short tailed arrow for the high magnetic field regime. Three different polarisation combinations are considered:-



(a) Probe and coupling field having polarisations parallel to the applied magnetic field ($\Delta m_\ell = 0, \Delta m_s = 0$).



(b) Probe field polarised parallel, coupling field perpendicular, to the applied magnetic field ($\Delta m_\ell = \pm 1$, $\Delta m_s = 0$).



(c) Probe and coupling field having polarisations perpendicular to the applied the magnetic field ($\Delta m_\ell = 0, \pm 2$, $\Delta m_s = 0$).

Again it can be seen that there is a partial reduction in the maximum absorption level due to the Zeeman splitting on the lower transition.

The relative depths of all the Δm_ℓ E.I.T. windows do indeed fall off as expected. The $\Delta m_\ell = \pm 2$ components are $\sim 20\%$ of the original E.I.T. window. However, the $\Delta m_\ell = 0$ component is well down on the 50% value expected. One reason for the overall reduction in the E.I.T. windows is because of the broadening of each individual Δm_ℓ cluster, induced by the Zeeman splitting, as seen explicitly in the case of Figure 5.16(a). The loss of inter Δm_ℓ cluster degeneracy effectively reduces the depth of the E.I.T. features through the superposition, within clusters, of E.I.T. features located at different frequencies. A second contribution is that from the previously predicted effect due to the separation of Δm_ℓ components.

A further explanation for the lower than expected E.I.T. window depth of the $\Delta m_\ell = 0$ component is that this system employs $m_\ell - m_s$ levels which have dipole matrix elements that are much smaller than those in the $\Delta m_\ell = \pm 2$ system, see Figure 5.14. Therefore even although there are twice as many individual systems involved, each one has a Rabi splitting less than a corresponding $\Delta m_\ell = \pm 2$ system and so the total superposition has a smaller depth than originally predicted.

5.8) Implications Of Zeeman Splitting On Coherently Prepared Systems

The effect of Zeeman splitting on electromagnetically induced transparency has some fundamental consequences to the application of E.I.T. effects in magnetic field induced three-wave mixing experiments [5]. Introducing a magnetic field to allow the collinear generation of a second-harmonic signal, a sum-frequency signal or a difference frequency signal by rotation of the appropriate quadrupole moments, will produce less enhancement than expected in the presence of E.I.T. due to the Zeeman splitting effects described in this chapter. Thus high powered lasers should be employed, such that the Rabi frequencies are greater than the Zeeman splittings. Other methods for breaking the symmetry of the vapour region may be preferable if it is desired to incorporate E.I.T. to enhance second order nonlinear processes. i.e. non-collinear beams (but these will also reduce induced transparencies) [25] or the use of high power pulses [26].

With regards to non-inversion laser systems [27] it would be beneficial to shield the experiment from surrounding background magnetic fields such that Zeeman splitting will not reduce the prepared coherence within the proposed lasing medium. This shielding need not be of such a level to exclude the earth's magnetic field since at ~ 0.06 mT it falls well within the low field regime and so will not significantly destroy any induced coherence.

Finally the design of a high-sensitivity magnetometer [7] has as its basis the effects of Zeeman splitting. In a weak magnetic field regime the proposed design should not experience any difficulties due to the effects of Zeeman splitting, and so should be capable of accurately measuring very weak magnetic fields as predicted. However, in the presence of strong magnetic fields the Zeeman splitting will match or exceed the upper transition Rabi frequency. Therefore, the E.I.T feature will itself split and the interferometric method of detection will lose its sensitivity. Thus, the upper limit of the high-sensitivity magnetometer will be limited by the effects of Zeeman splitting. Measurement of the E.I.T. splitting in the strong magnetic field regime (~ 8 mT) may prove to be a possible optical magnetometer in its own right. However, this will not provide the accuracy of the proposed high-sensitivity magnetometer.

As has been shown in the Sections 5.6 and 5.7, the introduction of a magnetic field to an E.I.T. system provides a mechanism for carrying out sub-Doppler, two-photon spectroscopy within that system. This spectroscopic analysis is again free from any complicating factors introduced by the intermediate $5P_{3/2}$ energy level and as such provides a useful method for examining the two-photon structure. Thus this magnetic field study has further highlighted the fact that in E.I.T. processes the level structures normally revealed by two-photon spectroscopy (ground to upper state) are imprinted, as E.I.T. features, upon the single-photon absorption profile associated with the lower transition (ground to intermediate state).

5.9) Concluding Remarks

This chapter has presented a study of electromagnetically induced transparency employing continuous wave lasers with an emphasis on the two photon excitation conditions associated with this process. Theoretical results obtained by employing density matrix models for three level atoms have been compared with those results

obtained experimentally. Even although the experimental system had appreciable hyperfine structure in all of its corresponding levels the theoretical models predicted the principle features well. These included the effects of optical field geometry, coupling field power and coupling field detuning. Simultaneously measurements of the upper state population (via fluorescence) were recorded which allowed their velocity selected lineshapes to be contrasted with those of the probe field transmission. An initial novel two photon spectroscopy technique was also presented whereby E.I.T. was used to imprint the upper and lower levels structure on the probe transmission curve, taking advantage of the reduced two photon Doppler width to achieve good resolution. A theoretical and experimental examination of the affect of applying a magnetic field on an E.I.T. system was then presented. This showed that an E.I.T. window will split into clusters, the number of which depends directly on the operative two photon selection rules which are themselves directly related to the polarisation of the optical fields. This then provided a second novel, though lower resolution, method of spectroscopic analysis of the two photon structure. Overall it was found that a magnetic field acts to reduce, or mask, an E.I.T. window. The depth of each component of the induced transparency is reduced relative to the zero magnetic field case while simultaneously undergoing frequency shifting and broadening processes.

References

- [1] **W. F. Buell and M. Fink**, *On Experiments To Observe Gain Without Inversion And High Index Without Absorption In Rubidium*, Proc. International Conference On Lasers, 438 (1992).
- [2] **J.G. Banacloche, Y. Li, S. Jin and M. Xiao**, *Electromagnetically Induced Transparency In Ladder Type Inhomogeneously Broadened Media: Theory And Experiment*, Phys. Rev. A 51, 576 (1995).
- [3] **J.E. Field, K.H. Hahn and S.E. Harris**, *Observation Of Electromagnetically Induced Transparency In Collisionally Broadened Lead Vapour*, Phys. Rev. Lett. 67, 3062 (1991).
- [4] **R.R. Moseley, S. Shepherd, D.J. Fulton, B.D. Sinclair and M.H. Dunn**, *Two Photon Effects In Continuous Wave Electromagnetically Induced Transparency*, Optics Commun. 119, 61 (1995).
- [5] **R.R. Moseley, B.D. Sinclair and M.H. Dunn**, *Enhanced Conversion Efficiency In Three Wave Mixing Via Electromagnetically Reduced Fundamental Wave Absorption*, Opt. Commun. 101, 139 (1993).
- [6] **S. Shepherd, R.R. Moseley, B.D. Sinclair and M.H. Dunn**, *Effects Of Different Phase-Matching Conditions In Sum Frequency Mixing Systems In Vapours*, Phys. Rev. A 49, 3002 (1994).
- [7] **M.O. Scully and M. Fleischhauer**, *High Sensitivity Magnetometer Based On Index Enhanced Media*, Phys. Rev. Lett. 69, 1360 (1992)
- [8] **E.U. Condon and G.H. Shortley**, *The Theory Of Atomic Spectra*, (Cambridge University Press, Cambridge (1953)).
- [9] **V.S. Letokhov and V.P. Chebotayev**, *Nonlinear Laser Spectroscopy*, Springer-Verlag, (Berlin Heidelberg New York (1977)).

- [10] **F. Nez, F. Biraben, R. Felder and Y. Millerioux**, *Optical Frequency Determination Of The Hyperfine Components Of The $5S_{1/2}$ - $3D_{3/2}$ Two-Photon Transitions In Rubidium*, *Optics Commun.* 102, 432 (1993).
- [11] **S. Jin, Y. Li and M. Xiao**, *Hyperfine Spectroscopy Of Highly Excited Atomic States Based On Atomic Coherence*, *Optics Commun.* 119, 90 (1995)
- [12] **J.E. Bjorkholm and P.F. Liao**, *Line Shape And Strength Of Two Photon Absorption In An Atomic Vapour With A Resonant Or Nearly Resonant Intermediate State*, *Phys. Rev. A* 14, 751 (1976).
- [13] **A.M. Akulshin, A.A. Celikov and V.L. Velichansky**, *Optics. Commun.* 84, 139 (1991).
- [14] **R.R. Moseley, S. Shepherd, D.J. Fulton, B.D. Sinclair and M.H. Dunn**, *Interference Between Excitation Routes In Resonant Sum Frequency Mixing*, *Phys. Rev. A* 50, 4339 (1994).
- [15] **J.E. Bjorkholm and P.F. Liao**, *Line Shape And Strength Of Two-Photon Absorption In An Atomic Vapour With A Resonant Or Nearly Resonant Intermediate State*, *Phys. Rev. A* 14, 751 (1976).
- [16] **P. R. Berman**, *Effects Of Collisions On Linear And Non-Linear Spectroscopic Line Shapes*, *Phys. Rep.* 43, 101 (1978).
- [17] **G. Vemuri, G.S. Agarwal and B.D.N. Rao**, *Sub-Doppler Resolution In Homogeneously Broadened Media Using Intense Control Fields*, *Phys. Rev. A* 53, 2842 (1996).
- [18] **G. Vemuri, G.S. Agarwal and B.D.N. Rao**, *Analysis Of Sub-Doppler Linewidths In Inversionless Amplification*, *Phys. Rev. A* 54, 1 (1996).
- [19] **S. Shepherd**, *Use And Development Of A CW Titanium Sapphire Laser For Nonlinear Optics*, PhD thesis, University of St. Andrews (1993).

- [20] **G.K. Woodgate**, *Elementary Atomic Structure*, Second Edition, Oxford Science Publications, (Oxford (1992)).
- [21] **B.W. Shore**, *The Theory Of Coherent Atomic Excitation*, Vol. 1 and 2, (J. Wiley and Sons, New York (1990)).
- [22] **K.D. Bonin and T.J. McIlrath**, *Two Photon Electric Dipole Selection Rules*, J. Opt. Soc. Am. B 1, 52 (1984).
- [23] **G. Breit and I.I. Rabi**, *Measurement Of Nuclear Spin*, Phys. Rev. 38, 2082 (1931).
- [24] **E.Arimondo, M. Inguscio and P.Violino**, *Experimental Determinations Of The Hyperfine Structure In The Alkali Atoms*, Rev. Mod. Phys. 49, 31 (1977).
- [25] **D.S. Betune, R.W. Smith and Y.R. Shen**, *Optical Quadrupole Sum-Frequency Generation In Sodium Vapour*, Phys. Rev. Lett. 37, 431 (1976)
- [26] **R.D. Freeman, R. Panock and J.E. Bjorkholm**, *Optical S.H.G. In Atomic Sodium*, IEEE Digest Of Technical Papers, Conference On Laseres And Electro-Optics (IEEE / OSA Washington D.C) IEEE J. Quantum Elect QE-17, 10. (1981).
- [27] **P. Mandel**, *Lasing Without Inversion: A Useful Concept ?*, Contemp. Phys. 34, 235 (1993).

Chapter 6

Electromagnetically Induced Focusing

This chapter considers the spatial consequences of employing Gaussian profiled cw optical fields within an experiment to study E.I.T. It is shown that the radial intensity profile of the strong coupling field results in significant cross focusing effects on the weak probe field. These focusing effects are dubbed Electromagnetically Induced Focusing (E.I.F.) in recognition of their inherent connection with E.I.T. and to distinguish them from self focusing and related phenomena.

6.1) An Introduction To The Spatial Consequences Of E.I.T.

The previous two chapters have discussed in detail the changing absorption profile of a weak probe field due to the presence of a strong coupling field on a connected transition. Accompanying this variation in the transmitted probe field amplitude is a variation in the phase delay or refractive index experienced by the probe. Figure 6.1 presents a density matrix calculation of the frequency dependent refractive index experienced by the probe field in the absence of a coupling field (solid blue line marked with crosses) or in the presence of a 100 MHz coupling field (solid red line). It is clearly seen that the normal dispersive refractive index curve is radically altered by the introduction of a coupling field, as predicted by Scully in 1991 [1].

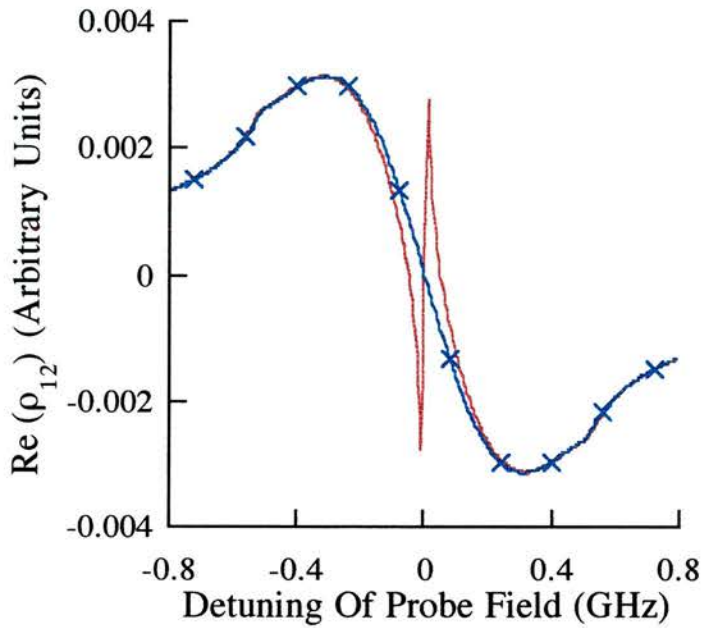


Figure 6.1:- Theoretical curves showing the real component of ρ_{12} (which is proportional to the refractive index experienced by the probe field), including the effects of Doppler broadening, for the case of no coupling field (shown by a blue solid line marked with crosses) and the case when a 100 MHz coupling field is present (shown by a red solid line). ($\Omega_{12} = 1$ MHz, and vapour temperature = 45 °C).

The coherently created dispersion properties of these systems have generated a great deal of interest in their own right: Harris and co-workers have theoretically predicted a reduction in the group velocity of a pulsed probe beam [2,3] due to the rapidly varying refractive index near line centre and experimentally confirmed this phenomenon in a later publication [4]. A similar cw experiment has been carried out within atomic rubidium by Xiao et al [5]. The authors employed the same cascade system as discussed in this chapter to experimentally observe E.I.T. and simultaneously measure the rapidly varying refractive indices. A reduction in the group velocity for an on resonance probe beam ($v_g = c / 13.2$) is inferred from the measured dispersion curve, with a 52.5% absorption suppression experienced by the probe field; Scully and co-workers have theoretically discussed the possibilities of creating a medium of enhanced refractive index and low absorption, dubbed "phaseonium" [6], in order to develop a novel atomic magnetometer [7]. Lately, these authors have also reported the first experimental demonstration of this effect within atomic rubidium [8].

The refractive index profile change discussed above is directly related to the strength of the coupling field induced Rabi frequency and to the dephasing on the uncoupled transition in exactly the same manner as was outlined for E.I.T. in Chapter 4. It is this fact that is the underlying principle for observing Electromagnetically Induced Focusing (E.I.F.) [9,10], the process for which is outlined schematically in Figure 6.2.

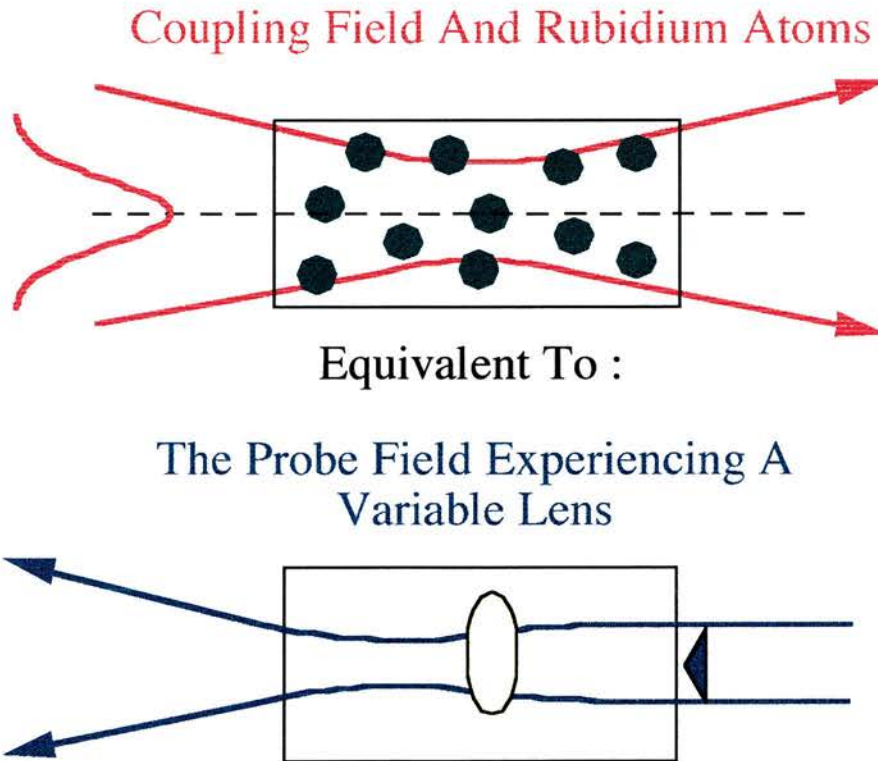


Figure 6.2:- Schematic representation of the process involved in producing Electromagnetically Induced Focusing.

Consider a typical cascade system E.I.T. experiment where the focusing of the two counter propagating optical fields is such that the probe field is radially contained within the coupling field along the length of the interacting medium. Since the coupling field has a Gaussian radial intensity there will be a radial variation in the induced transparency depth and refractive index change as experienced by a resonant probe field. Both these effects will be strongest on axis and will fall off as we move radially outwards across the coupling field. Therefore, a radially varying refractive index profile will be induced upon the probe field due to the interaction of the coupling field

with the rubidium atoms. This is simply the principle of an optical lens, thus focusing of the probe field is to be expected.

It should be noted that the control of the path of an optical field by another has been demonstrated by Tam and Happer via an optical pumping mechanism [11]. However, in the work of this chapter the control is mediated by the E.I.T. conditions altering the atomic susceptibilities produced in the vapour. As such, E.I.F. is effectively non-dissipative in terms of the coupling radiation, since large scale population transfers are not involved. Further, unlike self-focusing effects [12,13] there is the potential for using this mechanism for focusing, trapping, and defocusing without accompanying absorption of the weak probe radiation.

E.I.F. cannot however be completely explained in terms of a spatially varying refractive index as first suggested [9]. It is found that radially varying E.I.T. effects also play a significant role in the resultant spot size of the probe field. Various experimental parameters also alter the final spot size, in particular the detuning of the probe field from exact resonance, but also: the relative focal position of the probe field; the temperature of the cell; and the initial relative spot sizes of the two optical fields. This chapter will present results from a detailed calculation for the propagation of the probe field within a cascade system. The model includes the radial change in both refractive index and absorption, and highlights the fact that focusing and defocusing induced on the probe field are due to the combination of both of these effects. Experimental confirmation of all of these theoretical results will follow, with a final section outlining the production of novel optical writing techniques of the coupling field on the probe field being presented.

The motivation behind the study of E.I.F. lies with its relevance to the design of any experiment in the field of atomic coherence. Not only will E.I.T. experiments cause this form of cross focusing, but also experiments in inversionless lasing [14,15 and reference therein], where strong coupling fields are used to prepare the atomic conditions. Thus E.I.F. may prove problematic, and as such the design of inversionless laser cavities may have to include E.I.F. compensation. Furthermore, access to ultrahigh refractive index without absorption [1,6] will give rise to lensing on the probe fields in a similar manner. The majority of theories in these areas have dealt with plane wave approximations, and as such have so far neglected the effects of spatial variations. E.I.F. is also of fundamental interest in its own right since it allows laser induced lenses

to be created, whose sign and focal power can be varied. This "Focusing of Light by Light" was the topic of a recent paper by Marangos [16].

6.2) Modelling Electromagnetically Induced Focusing

In order to theoretically analyse the effects of E.I.F. a model has to be derived which is capable of dealing with the radial variations induced in the medium's susceptibility by the Gaussian profile of the coupling field. With this radial profile in place the spatial effects upon the probe field as it propagates through the medium have to be evaluated. Following the coupling field induced medium, the effects of free space propagation to the observation plane upon the probe must then be considered. It is the combination of all of these complex processes which gives the resultant spot profile at the detector. However, this calculation holds for only one specific probe field frequency. Thus, the model must be executed for a range of probe field detunings in order to appreciate how the spot size at the detector varies as the probe field frequency is scanned through resonance.

6.2.1) Calculating The Radially Varying Atomic Susceptibility

The calculation of the radial variations in the atomic conditions within the cell is achieved by employing a standard density matrix model as detailed in Chapter 2. The relevant density matrix model for E.I.F. studies is a three level cascade system (Matrix 2.1) which incorporates the effects of Doppler broadening. The population decay rates (Γ_{ij}) are set to be $\Gamma_{12} = 40$ MHz, $\Gamma_{32} = 1.6$ and $\Gamma_{31} = 2.6$ MHz, and the corresponding coherence decay rates (γ_{ij}) are

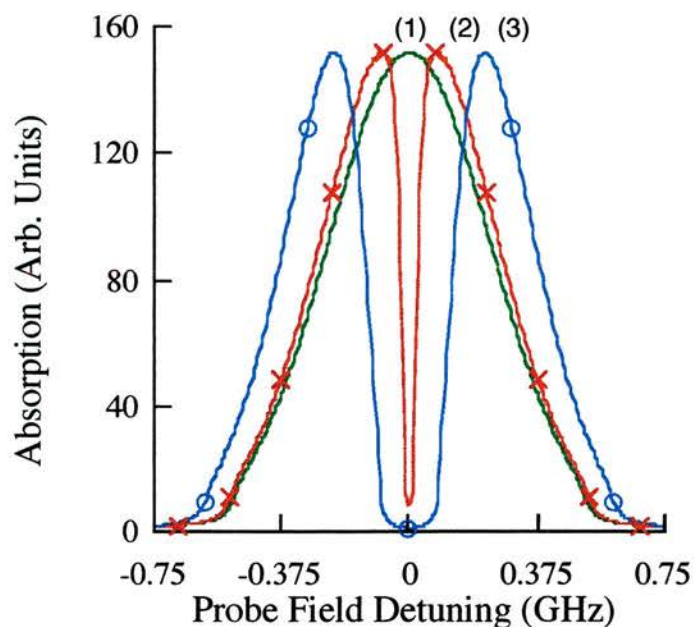
$$\gamma_{12} = \frac{1}{2}\Gamma_{21} \quad (6.1)$$

$$\gamma_{23} = \frac{1}{2}(\Gamma_{21} + \Gamma_{31} + \Gamma_{32}) \quad (6.2)$$

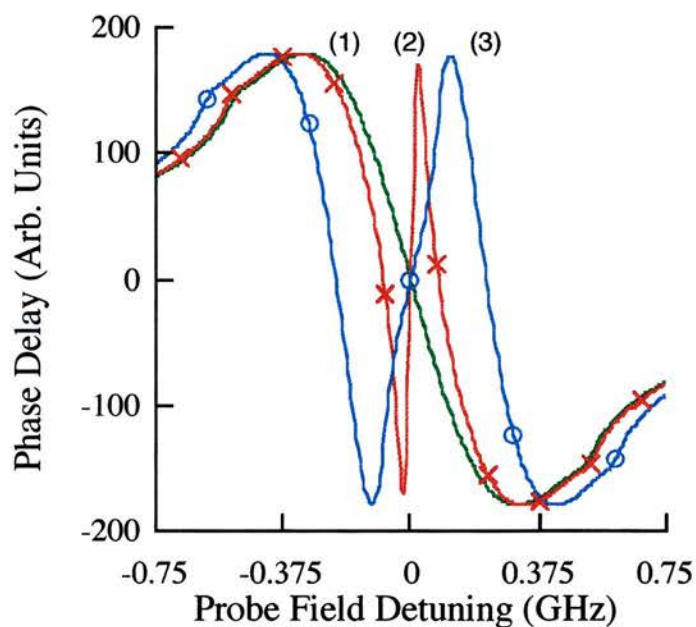
$$\gamma_{13} = \frac{1}{2}(\Gamma_{31} + \Gamma_{32}) \quad (6.3)$$

At first glance the inclusion of a Γ_{31} spontaneous decay term contradicts the non-dipole allowed nature of the uncoupled transition as described in Chapter 2. However, the justification for the inclusion of this term lies in the fact that it makes the model physically more realistic. The $5S_{1/2}$ - $5P_{3/2}$ - $5D_{5/2}$ cascade system is not a truly isolated three level system. Population can leak out of the three level system from the $5D_{5/2}$ level by spontaneous decay to the $6P$ level. This population always re-enters the three level system via the $6P$ - $5S_{1/2}$ relaxation and so is accounted for in this model by the inclusion of a Γ_{31} term in the density matrix and as an extra dephasing rate. It is this very decay route which allows the experimental observation of the 422 nm fluorescence in previous chapters.

An initial employment of the standard density matrix model allows a phenomenological picture of the radially varying susceptibility to be obtained. Figure 6.3 presents some typical results from the density matrix calculation for three different coupling field Rabi frequencies. Part (a) shows the absorption experienced by the probe field (from the imaginary part of ρ_{12}) and part (b) the corresponding phase delay or refractive index experienced by the probe field (from the real part of ρ_{12}), both plotted against probe field detuning. Curve (1), shown by a green solid line, corresponds to a coupling field Rabi frequency (Ω_{23}) of zero and hence represents the conditions in the vapour outside of the coupling laser. The red curve marked with crosses, curve (2), is the calculation carried out at edge of the waist of the coupling field and as such has $\Omega_{23} = 162$ MHz. Curve (3) is calculated at the centre of the coupling field Gaussian profile with $\Omega_{23} = 440$ MHz and is represented by the blue curve marked with circles. From these curves the radial change in the conditions within the cell can be deduced. For example, with the probe field tuned to line centre, the middle of the probe beam will experience low absorption, but the wings, if they extend outside of the coupling laser profile, will be absorbed. The converse situation occurs when the probe field has a detuning of 0.25 GHz from line centre. At this frequency significant absorption levels are predicted on axis with less absorption at the edges of the probe beam.



(a)



(b)

Figure 6.3:- The absorption (a) (calculated from the imaginary part of the off-diagonal matrix element ρ_{12}) and phase delay or refractive index (b) (calculated from the real part of the off-diagonal matrix element ρ_{12}) plotted against probe field detuning. Three sets of curves are presented corresponding to coupling field strengths of:- (1) $\Omega_{23} = 0$ MHz, green solid curves, (2) $\Omega_{23} = 162$ MHz, red curves marked with crosses, (3) $\Omega_{23} = 440$ MHz, blue curves marked with circles. The counter propagating beams have 780 nm and 776 nm probe and coupling field wavelengths, respectively. The coupling field has $\Delta_c = 0$ and the cell temperature is 320 K.

To help clarify the picture Figure 6.4 displays a set of curves obtained from a similar density matrix model to that above, except for the fact that now the probe frequency is set and it is the radial position across the coupling field that is scanned. Again graph (a) corresponds to probe field absorption and (b) to the phase delay but in this case both experience a Gaussian induced Rabi frequency profile of waist size ω_0 . Individual curves within Figure 6.4 correspond to different probe detunings relative to line centre, as noted in the caption. However, the basic trend is that curve (1) corresponds to line centre and the rest follow a progression of increased detunings in steps of 0.05 GHz. Beginning with the absorption conditions it can be seen that there is a relatively wide transparency window for the probe to propagate through at line centre, but this progressively narrows and becomes less pronounced as the probe tuning changes. Thus, it is to be expected that a probe beam of similar waist to that of the coupling beam will experience clipping of its edges. As the detuning increases to around the value of the peak Rabi frequency of the coupling field, the situation reverses, as predicted above, and the absorption actually becomes greater on axis, favouring the propagation of the outer edges of the probe beam. The refractive index also changes over this same detuning range. Initially, on line centre the refractive index has no radial variation (as noted in [9]), but in curve (2) there is already a strong radial variation. While $-1 < r / \omega_0 < 1$, the curve displayed gives less phase delay on axis and so imposes a diverging curvature on the probe wave front. In later curves this is observed to reverse and a converging curvature is imposed. However, the behaviour of a probe beam in case (2) and (3) will be strongly dependent on the relative initial coupling and probe waist sizes due to the change in curvature with radial position. Therefore, distinct non-Gaussian probe output beams are to be expected.

As well as producing non-Gaussian probe output beams it can be deduced from Figure 6.5 that the probe spot size is also dependent on the sign of the probe field detuning. Figure 6.5 presents similar graphs to those of Figure 6.4, however this time the detuning step intervals are - 0.05 GHz instead of + 0.05 GHz. Examination of Figure 6.5(a) quickly reveals that the absorption profiles vary exactly as before. Thus, the contribution of absorption effects to the overall probe spot size can be seen to be symmetrical about the probe field resonance frequency. This however, is not found to be the case for the refractive profiles, shown in Figures 6.4 (b) and 6.5(b).

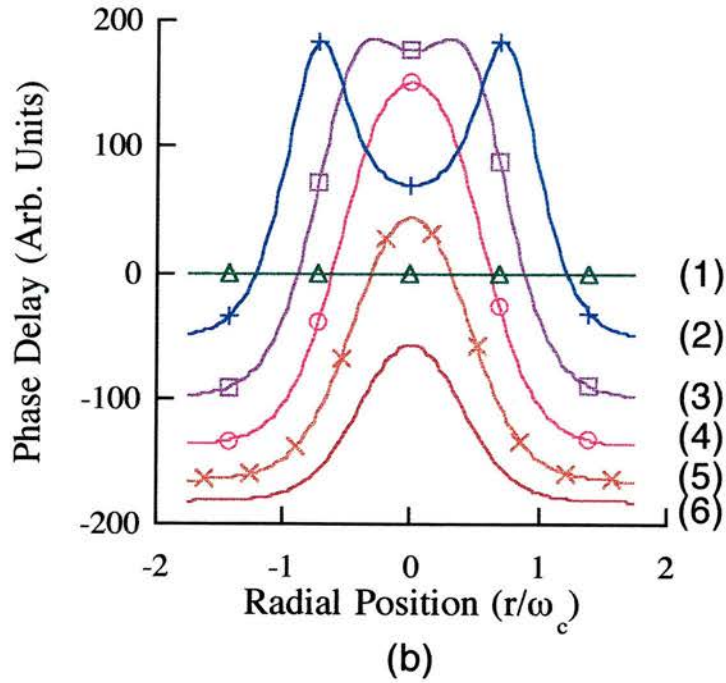
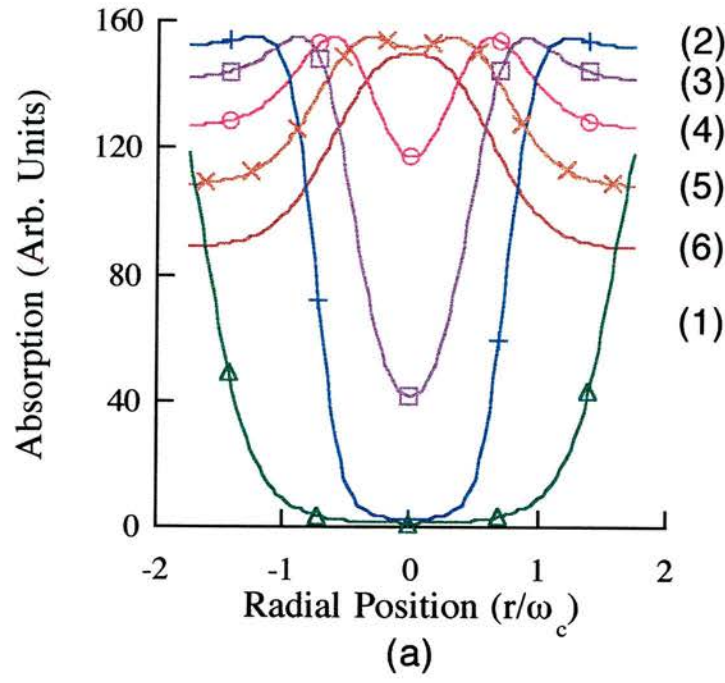
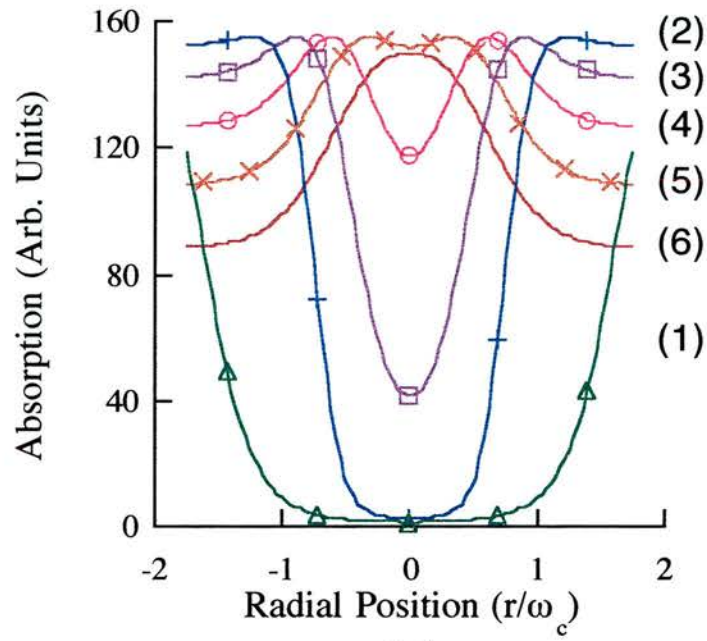
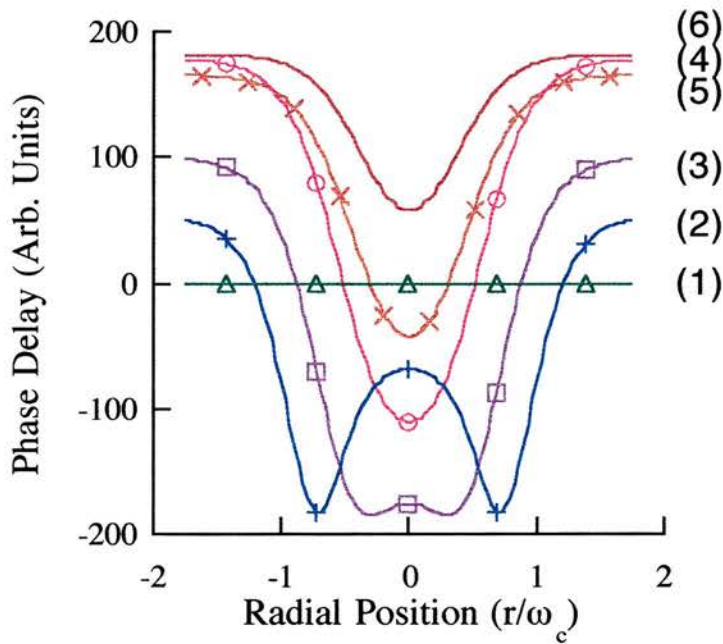


Figure 6.4:- The absorption (a) and phase delay (b) plotted against radial position with respect to the centre of the Gaussian coupling field profile. Curves (1) to (6) correspond to probe detunings of 0.0, 0.05, 0.10, 0.15, 0.20, and 0.25 GHz respectively. The radial position is scaled in units of the coupling field waist size ω_c . The peak coupling field Rabi frequency is 440 MHz and all other parameters are as in Figure 6.3.



(a)



(b)

Figure 6.5:- The absorption (a) and phase delay (b) plotted against radial position with respect to the centre of the Gaussian coupling field profile. Curves (1) to (6) correspond to probe detunings of -0.0 , -0.05 , -0.10 , -0.15 , -0.20 , and -0.25 GHz respectively. The radial position is scaled in units of the coupling field waist size ω_c . The peak coupling field Rabi frequency is 440 MHz and all other parameters are as in Figure 6.3.

It can be seen that a +100 MHz detuned probe (curve (3) Figure 6.4(b)) experiences a converging phase delay curvature imposed upon it, for $-1 < r / \omega_0 < 1$, whereas inspection of Figure 6.5(b) (curve (3)) shows that a -100 MHz detuned probe has imposed upon it a diverging phase delay curvature. Therefore, since the overall spot size depends on the combination of the absorption and refractive index profiles it is expected that this will be non-symmetrical about the probe field resonance frequency.

6.2.2) Calculating The Effects Of Probe Field Propagation

In order to calculate the combined effects of these unusual radial variations in the refractive index and absorption on the propagation of a probe beam through a cell prepared in this way by the coupling field, a matrix solution of the Maxwell equations was followed as detailed by McDuff [17]. To simplify matters this treatment proceeds in only one transverse dimension, but this is a valid approximation for circularly symmetric conditions and is sufficient to provide significant insight into E.I.F. phenomena. The method involves resolving the spatial information of the input beam and that of the medium's susceptibility into a linear combination of Gaussian-Hermite modes. Employing the properties of these Gaussian-Hermite modes allows the recasting of the wave equation into a form which enables numerical solutions to be calculated. Therefore, the complex electric probe field amplitude, $E_p(x,z)$, is expressed as:

$$E_p(x,z) = \sum_{k=0}^{n=\infty} f_k(z) \psi_k(x) \quad (6.4)$$

and the complex susceptibility of the medium, $\sigma(x,z)$, by

$$\sigma_m(x,z) = \sum_{k=0}^{n=\infty} N_k(z) \psi_k(x) \quad (6.5)$$

where

$$\psi_k = C_k H_k \left(\frac{\sqrt{2x}}{r_o} \right) \exp \left[- \left(\frac{x}{r_o} \right)^2 \right] \quad (6.6)$$

is the Gaussian-Hermite polynomial or mode of order k , H_k is the k -th order Hermite polynomial and C_k is a constant. In order to express the probe field, and the susceptibility of the medium as a linear combination of Gaussian-Hermite polynomials, ψ_k , the latter must form a complete set. Siegman has shown that this is in fact true [18]. It is also convenient if these Gaussian-Hermite modes form a set of orthogonal and orthonormal functions. McDuff [17] shows that for this to be the case C_k must satisfy the following relation

$$C_k = \left[\sqrt{\pi} r_0 2^{(k-1/2)} k! \right]^{1/2} \quad (6.7)$$

The factor r_0 in the above expressions is simply a scaling constant. This constant is chosen to match the Gaussian-Hermite mode sizes to roughly the beam waist of the profile being decomposed, in order to ensure swift convergence of the modes to form the beam profile. From this orthogonality relationship the coefficients of the linear combinations f_k and N_k can be determined from

$$f_k(z) = \int_{-\infty}^{\infty} E(x,z) \psi_k dx \quad (6.8)$$

$$N_k(z) = \int_{-\infty}^{\infty} \sigma(x,z) \psi_k dx \quad (6.9)$$

The propagation of the mode weights $f_k(z)$, is then given by equation (10) of reference [17]

$$\frac{df_k}{dz} = -\underline{\mathbf{E}}(z) f_k \quad (6.10)$$

where $\underline{\mathbf{E}}(z)$ is the propagation matrix as described by equation (11) of reference [17]. This propagation matrix takes into account spreading of the beam due to diffraction and the variation in absorption and refractive index experienced by the probe beam. Equation (6.10) is a simple first-order matrix differential equation which has the solution:

$$\mathbf{f}_k(\mathbf{z}) = \exp \left[-\int_0^z \underline{\mathbf{E}}(\mathbf{z}) dz \right] \mathbf{f}_k(\mathbf{z} = \mathbf{0}) \quad (6.11)$$

where $\mathbf{f}_k(\mathbf{z}=\mathbf{0})$ is the initial field expressed as a column vector of amplitudes of Gaussian-Hermite polynomials. Making the assumption that $\underline{\mathbf{E}}$ is independent of z the solution (6.11) can be simplified to:

$$\mathbf{f}_k(\mathbf{z}) = \exp[-\underline{\mathbf{E}}] \mathbf{f}_k(\mathbf{z} = \mathbf{0}) \quad (6.12)$$

Physically this assumption requires that the coupling laser beam be uniform throughout the cell. This is a fair approximation if the coupling beam is sufficiently collimated so as not to spread appreciably due to diffraction during propagation through the cell, and that the probe field is sufficiently weak such that the propagation of the coupling beam is unaffected by the interaction medium. These assumptions could be removed by numerical integration along the beam paths within the cell, but that complication is not necessary here in order to gain an understanding of the nature of E.I.F. In the implementation, the matrix exponential function is computed by a (4,4) Padé approximation [19], and decomposition up to the 40 th order of Gaussian-Hermite modes ($n = 40$) is used. This is extended however, up to the 60 th mode ($n = 60$) if the coupling and probe waists are of widely different sizes (e.g. in Figure 6.14 below). Since all the experimental observations of the beam spot size changes are made some distance back from the cell end, because of the counter propagating arrangement, the calculation is extended to include propagation across a set distance after the cell end through a homogeneous medium (air). This is achieved by propagating each of the Gaussian-Hermite modes excited at the cell end for the chosen distance through air [20], and then recombining them with the appropriate weights, $f_k(z)$ as calculated above, at the observation plane.

6.2.3) Acknowledgement

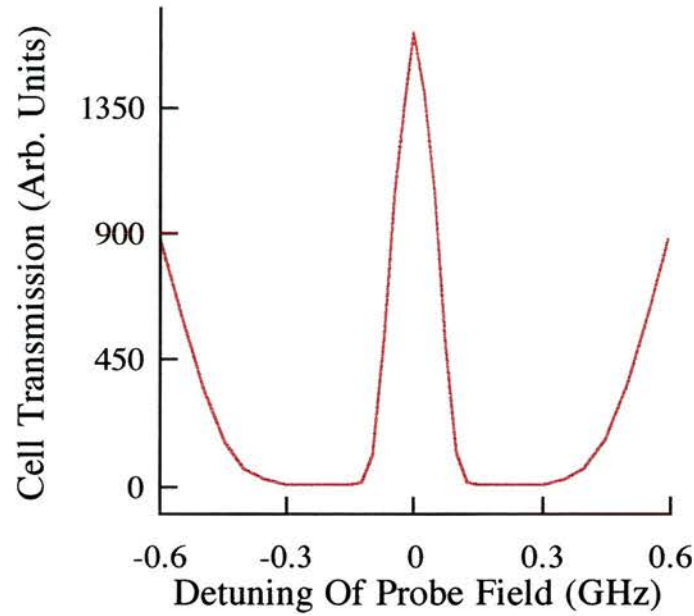
At this point I would like to acknowledge the work of R.R. Moseley who was the principle worker in the design and coding of the above E.I.F. model. The model was implemented in C in a UNIX environment on Sun SPARC workstations. As will be shown below, this model has proved itself an invaluable tool for dissecting the mechanisms involved in E.I.F. and as such has provided great insight into this phenomenon.

6.2.4) Theoretical Predictions Of The E.I.F. Model

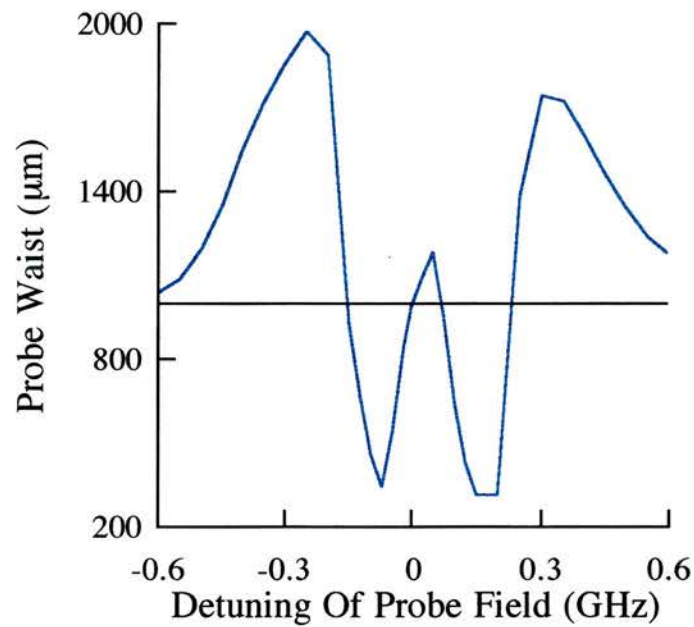
6.2.4.1) E.I.F. Within a 10 cm Rubidium Medium

Implementing the model described above produces the graphs shown in Figure 6.6 for a probe field of initial waist size 1 mm and a coupling field of waist 2 mm. The rubidium medium is chosen to be 10 cm long (as was the case for the original E.I.F. experiments [9]) and the observation plane is set to be 50 cm after the end of the cell. These relatively large beam waist sizes were chosen so as to avoid significant diffraction within these propagation distances and so allow the behaviour of E.I.F. to be unambiguously observed. Figure 6.6(b) shows the calculated probe beam waist at the $1/e$ point as a function of probe detuning while Figure 6.6(a) shows the calculation of the corresponding intensity of the transmitted light. As can be seen the behaviour is predominantly one of defocusing in the highly absorbing wings and focusing within the E.I.T. window. The overall behaviour significantly differs from that predicted from the simple method employed in the original work [9]. This is due to the spatially varying absorption conditions also present within the cell which were not previously accounted for.

To illustrate the contributions to the overall probe field spot size of the real and imaginary components of the mediums susceptibility the model is run with the same parameters but ignoring first the refractive index information, Figure 6.7(a), and then secondly ignoring the absorption information, Figure 6.7(b). The refractive index only calculation shows equal regions of focusing and defocusing around the zero detuning point. However, the absorption contribution is notably different and can be seen to be symmetric about the zero detuning point. These two results confirm the predictions made from the simpler density matrix calculations of Figures 6.4 and 6.5. The focusing behaviour near probe resonance is due to good E.I.T. being experienced at the high intensity regions of the coupling field and poor E.I.T. being experienced by the wings. This results in the probe field being clipped and hence a smaller transmitted spot. The defocusing in the off resonance regions corresponds to the opposite absorption variation. When the probe detuning is of the order of the coupling field Rabi frequency, the centre of the probe beam experiences high absorption because the Autler-Townes component has shifted to be resonant with the probe.

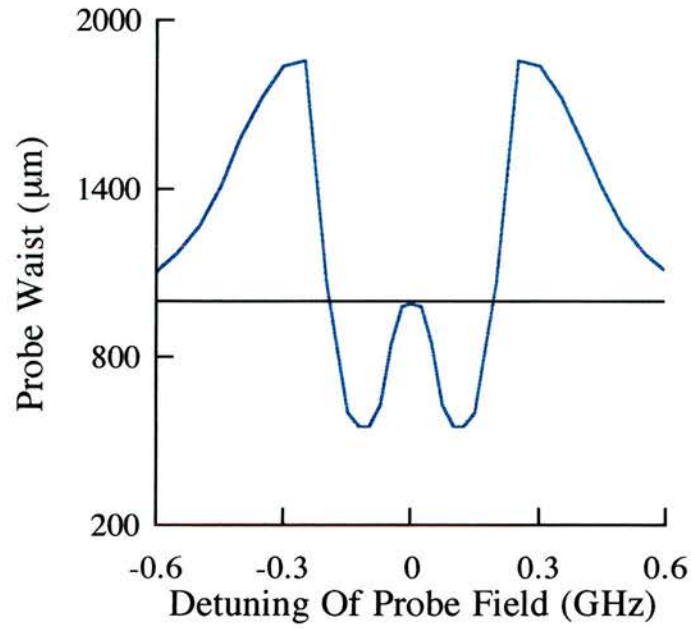


(a)

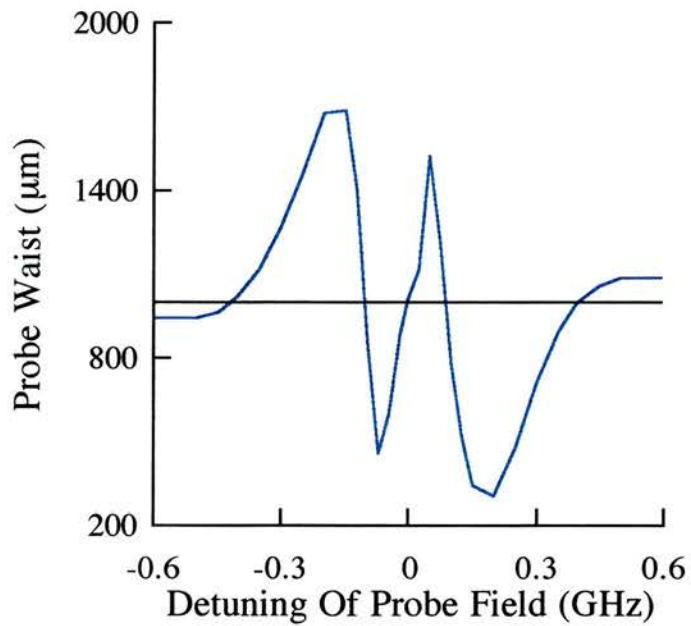


(b)

Figure 6.6:- The calculated probe transmitted irradiance (a) and waist size at the $1/e$ point (b) for the probe field after propagation through a 10 cm rubidium cell, followed by 50 cm through air. Initially the probe field waist size is set to be 1 mm, the coupling field waist 2 mm, and the peak Rabi frequency is 440 MHz. The counter propagating beams have 780 nm and 776 nm probe and coupling field wavelengths, respectively. The coupling field is assumed resonant such that $\Delta_c = 0$ and the cell temperature is set to equal 320 K. The horizontal reference line in plot (b) is the undisturbed waist size for propagation over the same distance.

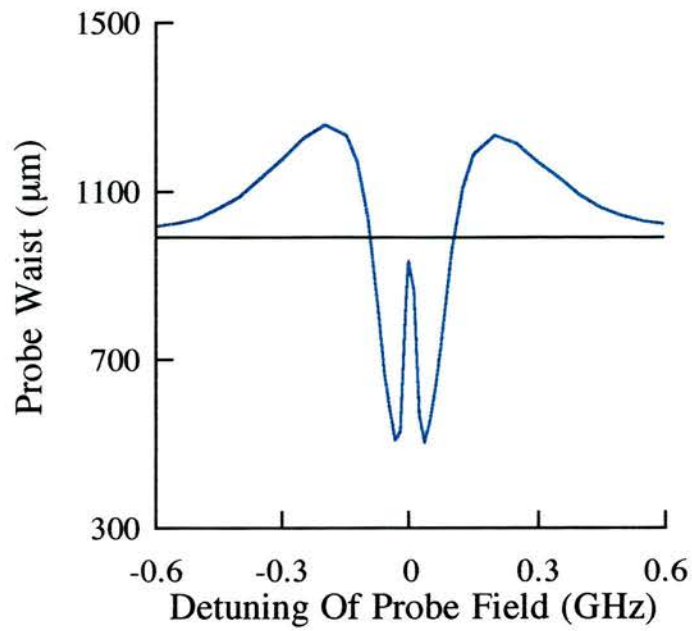


(a)

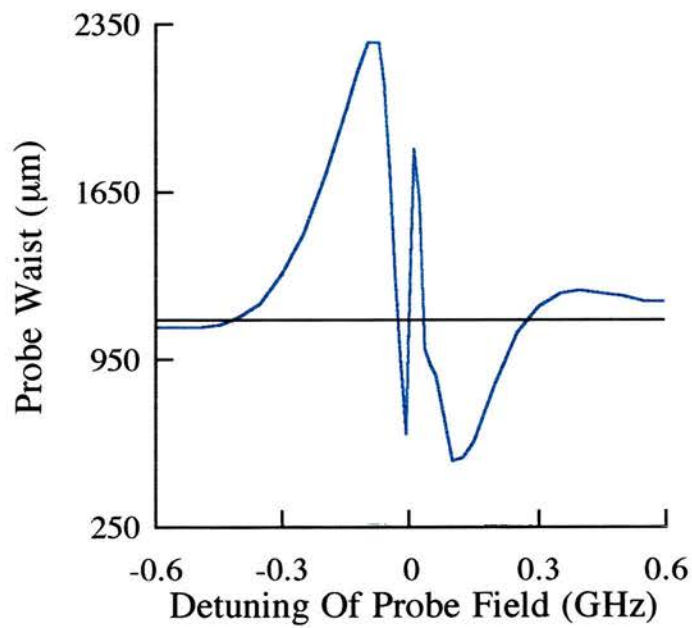


(b)

Figure 6.7:- The calculated probe waist size for the propagation conditions of Figure 6.6 but with (a) only the presence of the absorption information of the coherently prepared medium and (b) only the presence of the refractive index information of the coherently prepared medium. The horizontal reference lines again represent the undisturbed waist size for propagation over the same distance.



(a)



(b)

Figure 6.8:- The calculated probe transmitted waist size at the 1/e point (a) observed at the cell end and (b) observed after propagating a further 200 cm through air. All other parameters are as for Figure 6.6. The horizontal reference lines again represent the undisturbed waist sizes for propagation over the same distances.

The edge of the probe beam, on the other hand, has less absorption because the Autler-Townes splitting is less and the probe detuning puts it in the wings of the absorption feature. This effect is clearly observed within the graphs of Figures 6.3 to 6.5.

How these two contributions combine to give the resulting output depends on the propagation conditions after the cell. If the probe beam profile is interrogated at the end of the cell, Figure 6.8(a), it follows the absorption conditions very closely. The wave fronts have had a phase modulation impressed on them by the refractive index changes, but only after propagation over a distance will this translate into a focused or defocused beam. In Figure 6.8(b) the propagation distance after the cell has been increased by a factor of four to 200 cm. It is seen that the phase modulation imposed on the wave fronts now dominates over the absorption effects resulting in the probe beam profile now following closely the refractive index contribution. Thus the result of Figure 6.6(b) consists of an equal mixture of the two contributions, since the refractive index contributions have led to an effect of roughly the same magnitude as the absorption contributions over the 50 cm propagation distance. Therefore, there are different regimes for the observation of E.I.F.: the near field, where absorption effects dominate; the far field, where the refractive index effects dominate; and an intermediate regime, where both are important.

6.2.4.2) E.I.F. Within a 2 cm Rubidium Medium

With this understanding in place, the parameters for the model were now chosen to reflect the experimental conditions more closely. A cell length of 2 cm was employed with a charge-coupled device (C.C.D.) placed approximately 20 cm after the cell end, and these values were entered into the model. The probe waist size was reduced to 55 μm , with the focus at the cell centre, and the coupling field waist size was similarly reduced to a value of 110 μm . With these relatively small waists, which give confocal parameters for the beams less than the overall propagation distance, diffraction effects are important at the observation plane. The theoretical prediction for the variation in the probe full width at half maximum (F.W.H.M.), as measured in the following experiments, is presented in Figure 6.9. Immediately it can be seen that this result is very different to that of Figure 6.6(b), where the probe does not experience a tight focus. Under these conditions, focusing within the cell from E.I.F. will tighten the

probe waist and result in a larger spot size observed on the camera plane. In a similar fashion, defocusing produces a larger probe waist in the cell and so a smaller spot in the observation plane. To examine the relative contributions of the absorption and refractive index profiles upon the final spot size this calculation was repeated initially ignoring the refractive index contribution, Figure 6.10 (a), and then secondly ignoring the absorption contribution, Figure 6.10(b). These graphs show that the overall variation is different from either of these and that the inclusion of the spatially varying absorption to the calculation is vital.

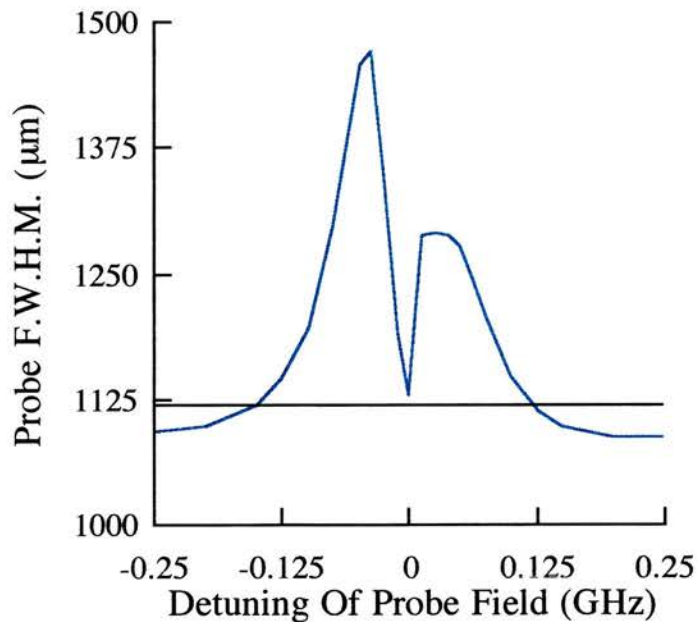
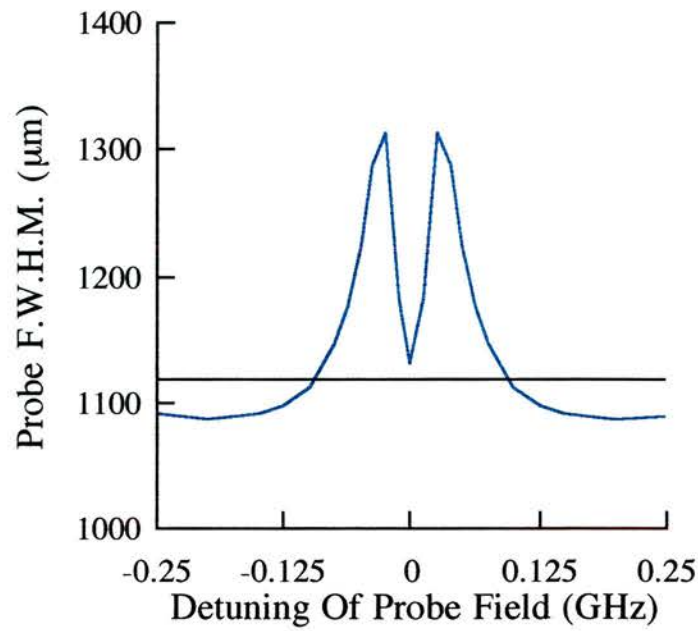
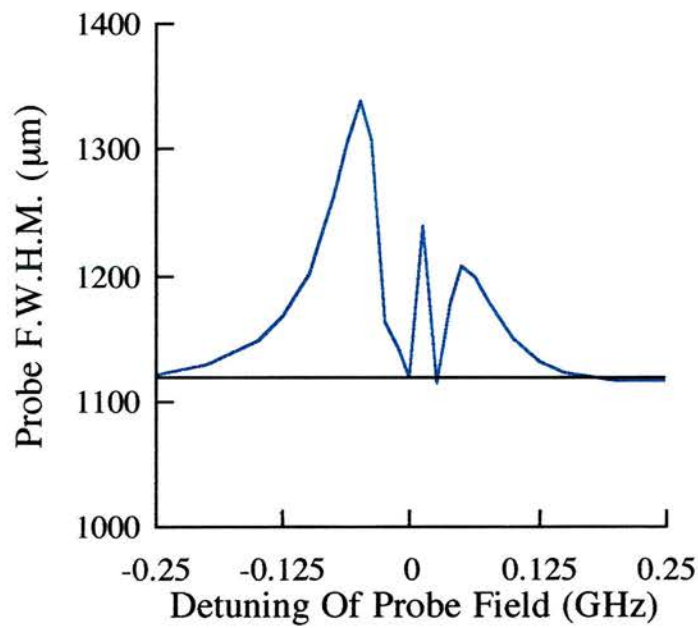


Figure 6.9:-The calculated probe F.W.H.M. after propagation through a 2 cm rubidium cell followed by 20 cm of air. The horizontal line denotes the waist size under diffraction-limited propagation conditions. The undisturbed probe beam waist is 55 mm, with the focus located at the cell centre. The coupling field waist size is 110 mm with a peak Rabi frequency of 220 MHz. The counter propagating beams have 780 nm and 776 nm probe and coupling field wavelengths, respectively. The coupling field is assumed resonant such that $\Delta_c = 0$ and the cell temperature is set to equal 320 K.



(a)



(b)

Figure 6.10:- The calculated probe F.W.H.M. for the propagation conditions of Figure 6.9 but with (a) the presence of the absorption information of the coherently prepared medium only and (b) the presence of the refractive index information of the coherently prepared medium only. The horizontal reference lines again represent the undisturbed waist sizes for propagation over the same distance.

An important and interesting point to note is that for a resonant probe field there is still a finite change in the probe spot size and that this is entirely due to the presence of the variation in the absorption radial profile. If the absorption information had been neglected, free space propagation would be predicted on line centre. With the appreciation of the radial change in absorption, this will not be the case unless the probe field is restricted to only a small portion of the coupling field profile, where there is essentially no change in the spatial conditions, or else a coupling field is generated which exhibits a "top hat" radial intensity profile.

6.2.4.3) Theoretical Effect Of Varying E.I.F. Parameters

There are a large number of physical parameters which can be varied in order to change the properties of the probe spot size at the observation plane. One of the most dramatic is that of the focal position of the probe field within the cell. Figure 6.11 shows the predicted spot size variation for (a) the probe focused at the input window of the cell and (b) the probe focused at the output window of the cell. Immediately it is seen that these two cases differ radically from the situation where the probe field was focused at the centre of the cell, Figure 6.9. A closer inspection reveals that these profiles are almost the mirror images of each other. Experimental confirmation of this change in conditions is given later in the results of Section 6.3.1.

A second experimental parameter which is easily varied is the temperature of the rubidium in the cell. Figure 6.12 shows the result of running the model for various cell temperatures using the same parameters as for Figure 6.9 except for the fact that the free space propagation distance after the cell is now 50 cm. With a cell temperature of 315K (green dashed line) and 320K (blue solid line) the lineshape of the probe F.W.H.M. curves are similar to those obtained in Figure 6.9. The overall spot sizes are larger due to greater free space propagation distance. As is to be expected the 315K curve shows less focusing effects on the probe spot size than the 320K curve since the lower temperature results in a lower density within the cell and so the effects of E.I.F. are reduced. An interesting effect occurs as the temperature is still further increased to 325K (purple dashed curve with x markers) and 330K (solid red line marked by crosses).

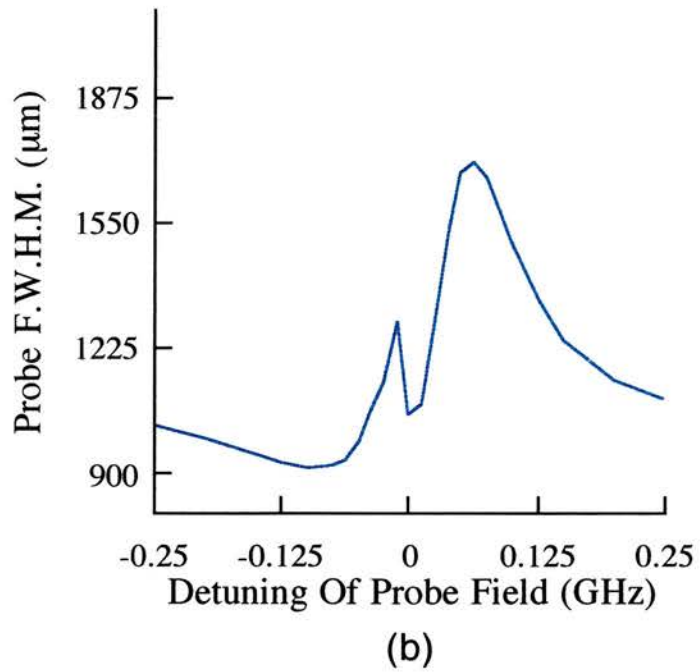
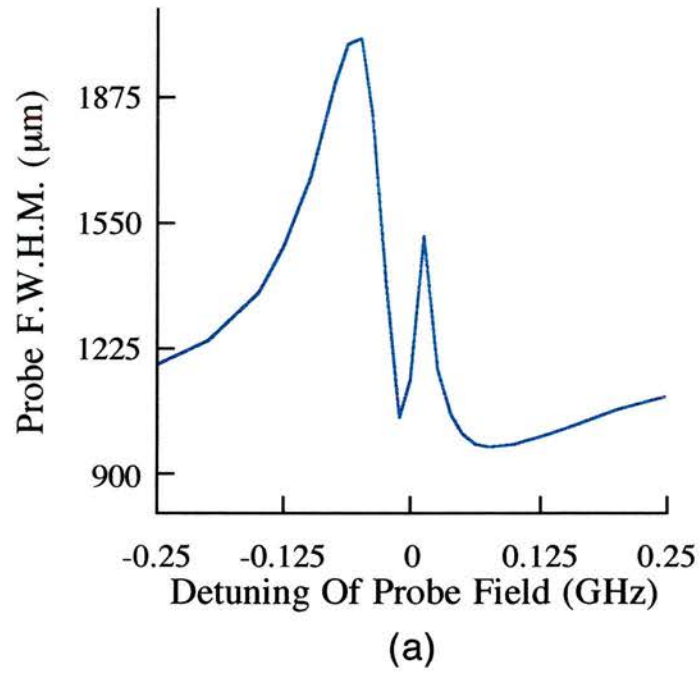


Figure 6.11:- The calculated probe F.W.H.M. for the propagation conditions of Figure 6.9 but with the undisturbed probe field focus located (a) at the input window of the cell and (b) at the output window of the cell.

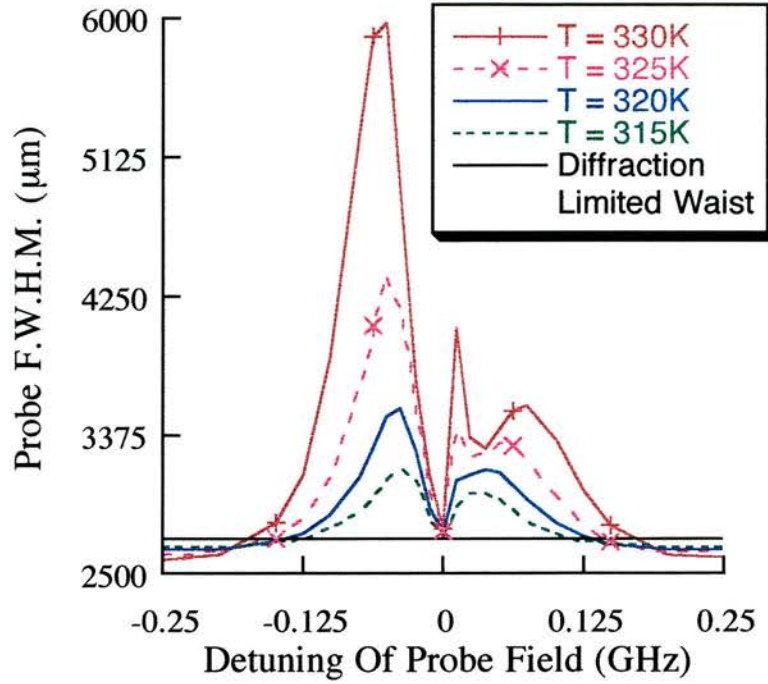


Figure 6.12:- The calculated probe F.W.H.M. for the propagation conditions of Figure 6.9 but with the propagation distance after the cell being 50 cm and the temperature of the rubidium cell set to 315K (green dashed line), 320K (blue solid line), 325K (purple dashed line marked by crosses) and 330K (red solid line marked with crosses). The 320K curve is also included for reference (red dashed line).

The second peak breaks into two components: a sharp region of defocusing and refocusing of the probe F.W.H.M. followed by a shallower less pronounced region of probe field defocusing and refocusing. This resembles the lineshape of Figure 6.10(b) where only the presence of the refractive index information was considered. Thus, it is seen that increasing the cell temperature enhances the refractive index contribution to the overall probe spot size at a higher rate than the equivalent absorption contribution, as is to be expected from the increase in particle density. Therefore, as the cell temperature is increased the probe spot size profile changes from one which is dominated by the absorption contribution to a regime where the refractive index contribution dominates. This provides the possibility of employing cell temperature as a second method for experimentally distinguishing the contribution of these two effects. A further point of interest is that Figure 6.12 shows that the structure of an E.I.F. probe

spot size profile has better temperature stability on the low probe frequency side of resonance than on the high frequency side. Therefore, if the fundamental focusing properties of E.I.F. are to be employed as a means of optical switching or path control it is favourable to work in the low frequency detuning region of the probe field since here the effects of temperature stabilisation will not be as problematic.

The properties of the coupling field can also be easily altered within this experiment, these include coupling field power, detuning, spot size etc. Figure 6.13 considers just one of these, the detuning of the coupling field. The profile presented is generated by leaving the probe field on resonance and scanning the coupling field, with all other parameters set to be the same as Figure 6.9. Here it is seen that the probe field spot size follows a very similar lineshape to that of Figure 6.9. The probe spot size again experiences two distinct regions of defocusing and then refocusing, one on either side of coupling field resonance. However, for this situation the magnitude of the focusing effects are not as strong as those for the case when the coupling field is set to be on resonance and the probe field is scanned in frequency.

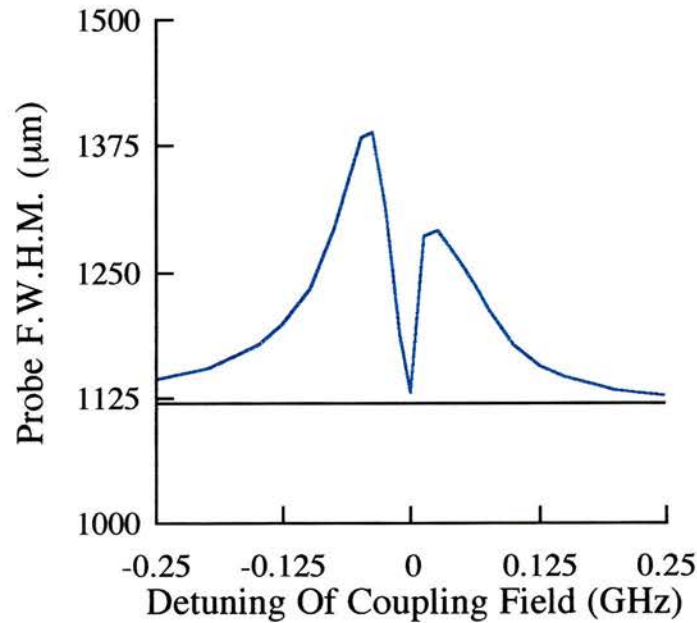
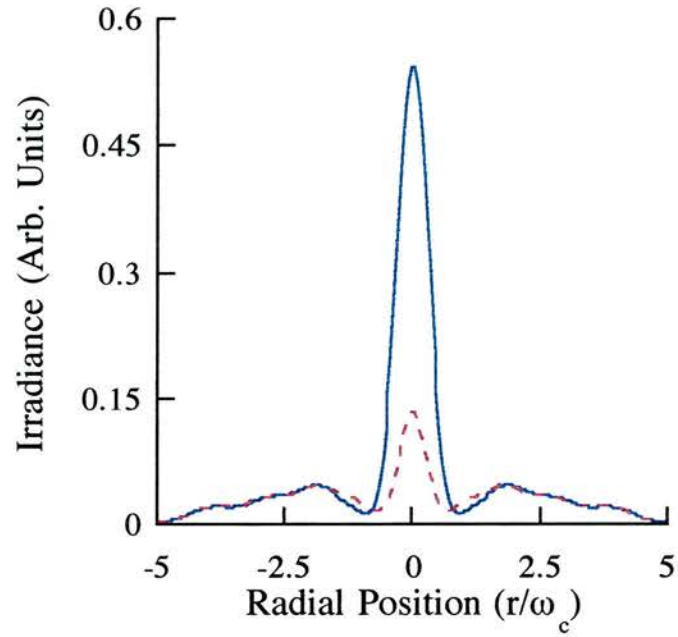
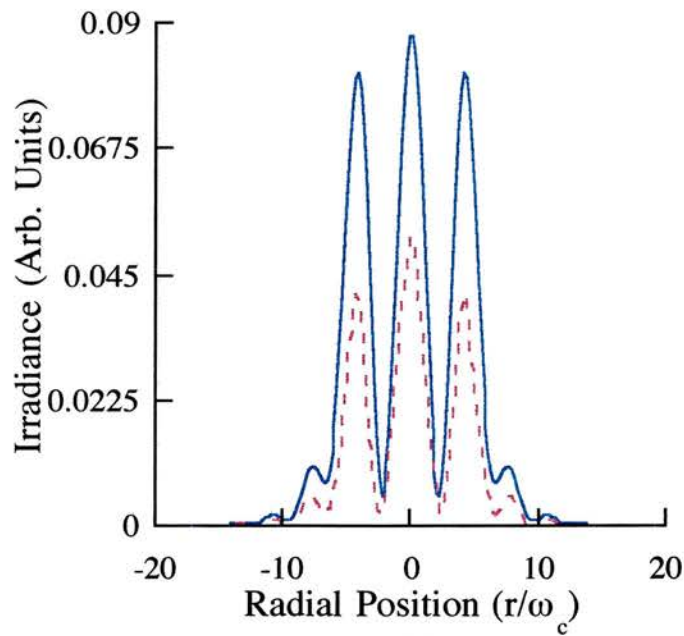


Figure 6.13:-The calculated probe F.W.H.M. of an on resonance probe field as a function of coupling field frequency. All other parameters remain as set for Figure 6.9. The horizontal reference line again represents the undisturbed waist size for propagation over the same distance.

Finally consider the situation in which the probe field waist size is initially greater than that of the waist of the coupling field. This condition is opposite to those discussed above and to those in most E.I.T. experiments because of the requirement for good transmission of the probe field. This situation is of interest however since the probe field effectively "sees" a soft-edged pinhole in the vapour at line centre, with low absorption on axis and high absorption off axis. Figure 6.14 shows the result for the probe field profile at (a) the exit of the cell and (b) after a further 20 cm propagation through air, where the initial probe waist size is 500 μm , five times that of the coupling field waist. Distinct diffractionlike rings can be observed on the probe profile, mirroring those seen for propagation through a traditional pinhole. It is predicted that the radius of these rings will change as the transparency window changes size with probe detuning. Experimental observation of these novel diffraction like rings is given in Section 6.3.2 along with further non-circularly symmetric diffractionlike fringes.



(a)



(b)

Figure 6.14:- The calculated probe radial intensity profile (a) at the end of the 2 cm cell and (b) after propagating a further 20 cm through air. The blue solid lines represent a probe detuning of 100 MHz, and the red dashed lines represent a probe detuning of 150 MHz. The radial position is scaled in units of the coupling field waist size ω_c . The input probe field waist size is 500 mm, the coupling field waist size is 100 mm and the peak Rabi frequency is 440 MHz. All other parameters are as in Figure 6.9.

6.3) Experimental E.I.F. Results

The following experiments on the effects of E.I.F. were all carried out within a 2 cm cell of rubidium vapour, following a similar procedure to that previously outlined in Section 4.3. The cell was typically heated to around 50 °C to give appreciable absorption of the focused probe field ($\geq 60\%$). The $5S_{1/2}$ - $5P_{3/2}$ - $5D_{5/2}$ cascade system was again employed with the two Ti:Sapphire lasers once more generating the applied optical fields. Figure 6.15 presents a schematic representation of (a) the atomic system employed, and (b) the experimental setup employed.

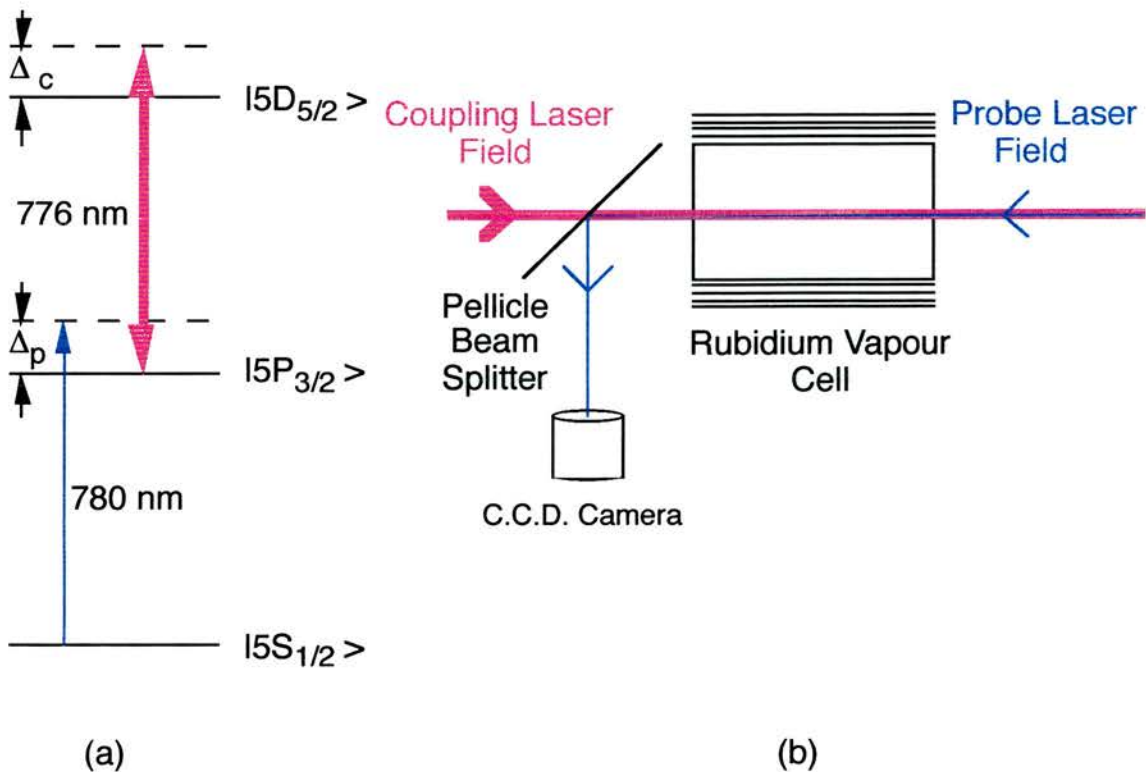


Figure 6.15:- A schematic representation of (a) the atomic cascade system employed for this experiment and (b) the experimental setup, showing the arrangement of the laser beams, vapour cell and C.C.D. camera.

The coupling laser provided up to 500 mW of power, however the probe laser power was attenuated to $< 300 \mu\text{W}$ in order to insure that the effects of self-focusing, which

would distort the results, were removed. After the cell a sample of the probe field was picked off by a pellicle beam splitter and then directed onto a C.C.D. array at a distance 20 cm from the cell end. The total intensity of the light was found by integration over the pixel values, and the F.W.H.M. of the probe field was measured directly in order to study the effects of E.I.F.

6.3.1) A Fully Contained Probe Field

The following results correspond to the case where the probe field is contained fully within the coupling field over the duration of the rubidium cell. This is achieved by focusing the coupling field with a 40 cm lens to give a waist size of around 150 μm . The confocal parameter is therefore nine times the cell length, providing a roughly constant axial intensity. The probe field is focused to a 55 μm waist, giving a confocal parameter of 2.4 cm which is of the same order as the cell length.

The above arrangement enables the profile of the probe field waist size to be experimentally observed after propagation through a coherently prepared E.I.F. medium. Therefore, it has proved possible to compare experimental E.I.F. with the previously generated theoretical profiles of Section 6.2. The variation in the probe waist size due to E.I.F. is found to be a good fit to the theoretical model in the cases where the probe field is focused on the ends of the rubidium cell. Figure 6.16 shows these two experimental traces (a) where the probe field is focused at the input window of the cell and (b) where the probe field is focused at the output window of the cell, corresponding to those generated for Figure 6.11(a) and (b) respectively. In Figure 6.16(a) the probe field can be seen to experience a wide frequency region of defocusing prior to the E.I.T. peak before it is quickly made to focus, defocus and then refocus over the E.I.T. region itself. For the case when the probe field is focused at the output window of the cell, Figure 6.16(b), the opposite occurs. As the E.I.T. feature is approached from the low frequency side the probe field is made to defocus, focus and then it enters its wide defocused region, now centred over the absorption after the E.I.T. window. This is exactly the phenomena predicted for both of these cases from the E.I.F. model.

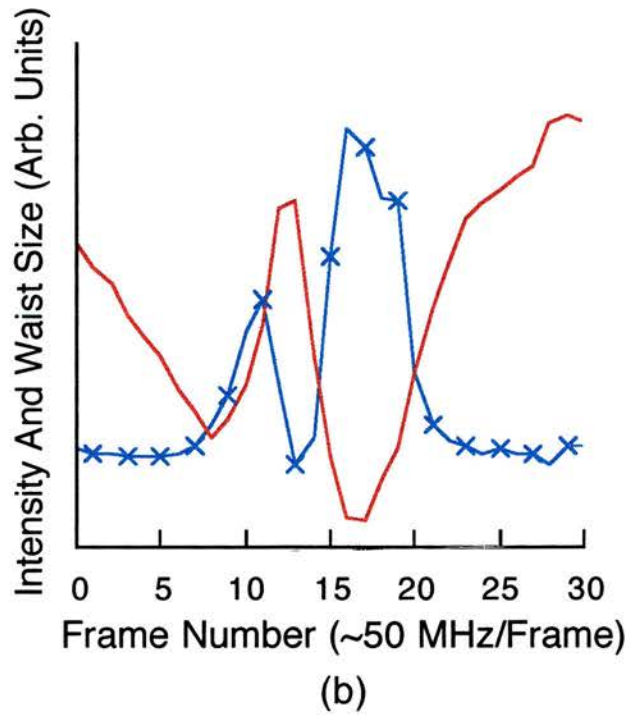
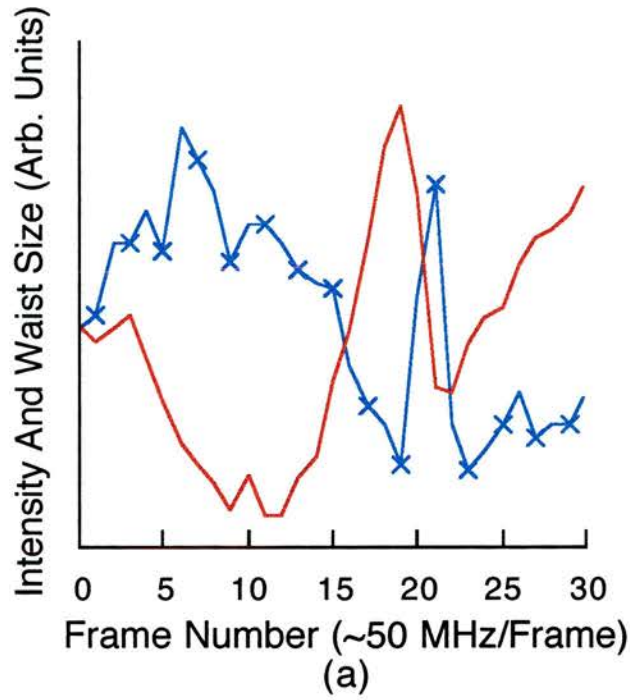
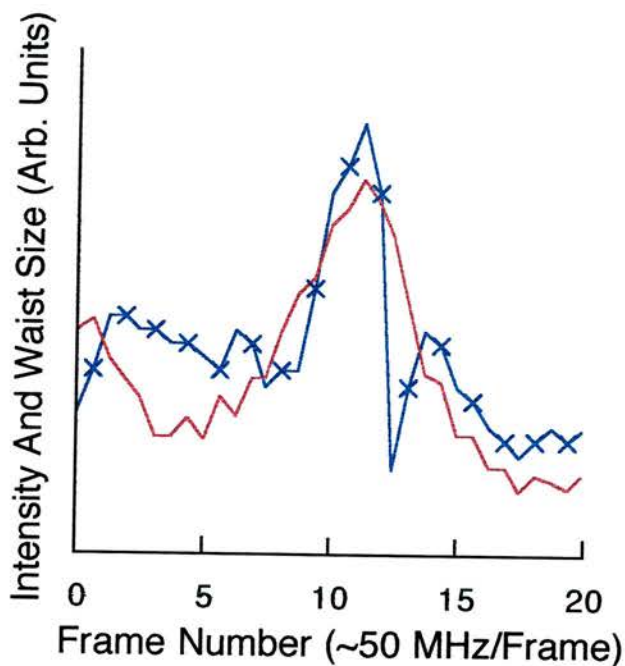


Figure 6.16:-The experimental variation of the probe F.W.H.M.(blue solid line marked by crosses) and intensity (red solid line) when the probe is focused (a) at the input window of the cell and (b) at the output window of the cell. Initially the probe field is focused to a 55 μm waist whereas the coupling field has a waist of 150 μm . The temperature of the cell is ~ 50 $^{\circ}\text{C}$.

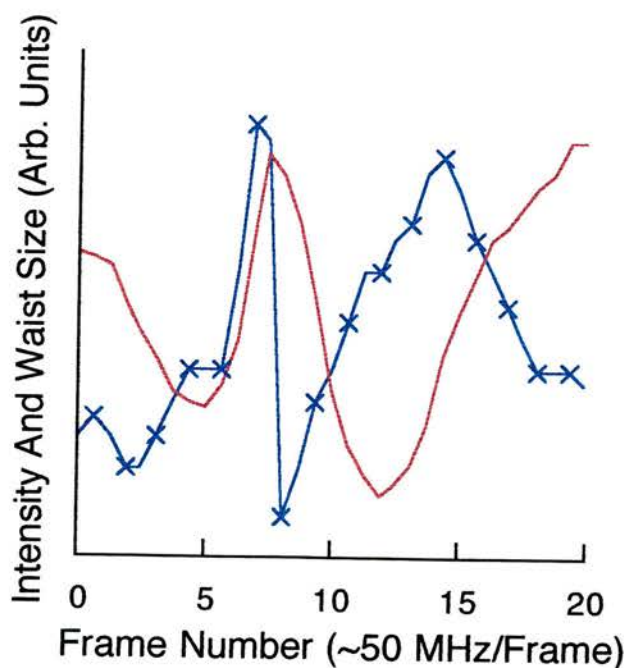
The results for the case when the probe field is focused at the centre of the cell are not quite as good. The behaviour of the probe field is found to vary between different experimental traces. In general the experimentally measured beam waists followed the behaviour predicted by the E.I.F. model, see Figure 6.17(a). On the whole the probe field experiences two defocusing regions both of which lie within the frequency range of the E.I.T. window. The strong focusing at the transmission peak is always observed. This is a very abrupt feature, typically occurring over a probe tuning range of 25-50 MHz at these coupling field powers. However, the relative height of the two peaks is found to vary between experimental traces, and the peak edges are sometimes blurred by defocusing at the transparency edges. Figure 6.17(b) and (c) represents two of these anomalous results where the structure of the second peak in particular is seen to differ from the theoretically predicted curve of Figure 6.9. This may not be too surprising, since from day to day the exact field focal positions will not always coincide and it has been shown that a 1 cm change in the focal position of the probe field in either direction leads to a radical change in the output waist sizes. Furthermore, changes in cell temperature have been shown theoretically to significantly affect the probe beam profile, see Figure 6.12, specifically in the probe field frequency region of the second peak. Therefore better temperature stabilisation of the rubidium cell would help in the reproducibility of Figure 6.17(a). A final experimental parameter that can not always be held constant from day to day is the overlap of the two optical fields. It is found that the observed probe field behaviour is very sensitive to the beam overlap and so this again contributes to the difficulty in reproducing the exact form of Figure 6.17(a).

The general good fit to the theoretical treatment outlined in Section 6.2 for the three different focal positions within the cell shows that both the refractive index and absorption properties must be considered to correctly predict E.I.F. behaviour. Ignoring either of these contributions leads to far different behaviour, which is unable to be matched to the experimental profiles taken in what is effectively the intermediate region between absorptive and refractive domination.

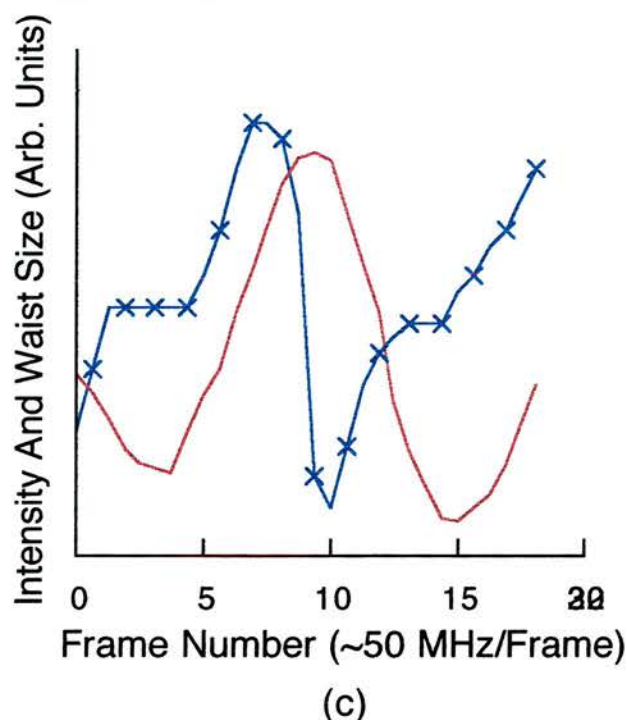
Figure 6.17:-The experimental variation of the probe F.W.H.M. (blue solid lines marked by crosses) and intensity (red solid lines) when the probe is focused at the centre of the rubidium cell. The three curves differ in the fact that in (a) the profile agrees well with the theoretical model, whereas (b) and (c) show profiles of poorer agreement. The experimental parameters are believed the same for all traces with the probe field initially focused to a $55\ \mu\text{m}$ waist whereas the coupling field has a waist of $150\ \mu\text{m}$. The temperature of the cell is $\sim 50\ ^\circ\text{C}$.



(a)



(b)



6.3.2) A Non Contained Probe Field: Novel Diffraction Techniques

Turning now to the case where the probe field is no longer contained fully within the coupling field over the length of the rubidium cell produces a novel effect associated with E.I.F. The probe field is now left unfocused and as such has a waist size of approximately 2 mm, much bigger than that of the coupling field waist, around 150 μm . Figure 6.18 shows the probe field after propagation through the cell at a frequency tuning close to that of the transparency peak. Clear diffraction-like rings can now be seen on the probe field intensity profile as predicted earlier in Figure 6.14 by the E.I.F. model. These rings are seen to contract as the probe is scanned upwards in frequency through resonance. The change in the ring structure is shown in Figure 6.19 for different probe frequency detunings within the E.I.T. region. It should be noted that this diffraction-like pattern cannot simply be a diffraction effect, as the rings would then both expand and contract as the aperture changed shape.

This behaviour follows directly from the circularly symmetric nature of the coupling field intensity profile and as such can be changed by inserting a cylindrical lens into the coupling field. The effect of this cylindrical lens was to produce a slitlike focus within the cell, hence fringes rather than rings were expected at the observation plane. This is indeed the case as shown in Figure 6.20.

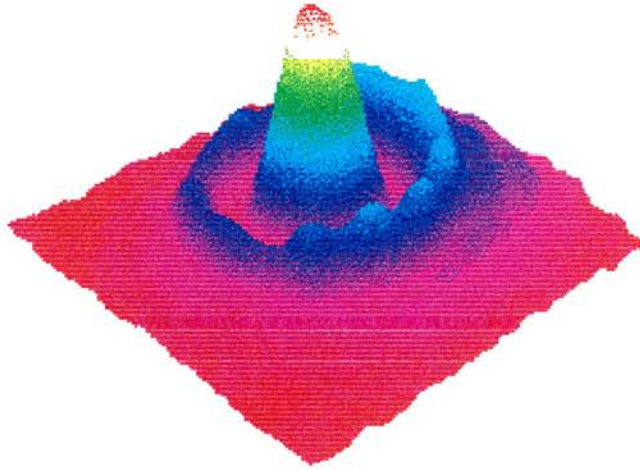


Figure 6.18:- A three dimensional plot of the probe field as it appears on the C.C.D. camera after being transmitted through a much smaller circular transparency. The probe field has a 2 mm waist, the coupling field a 150 μm waist and the cell is at a temperature $\sim 50^\circ\text{C}$.

Radial Intensity Variation With Probe Frequency:- Ring Contraction

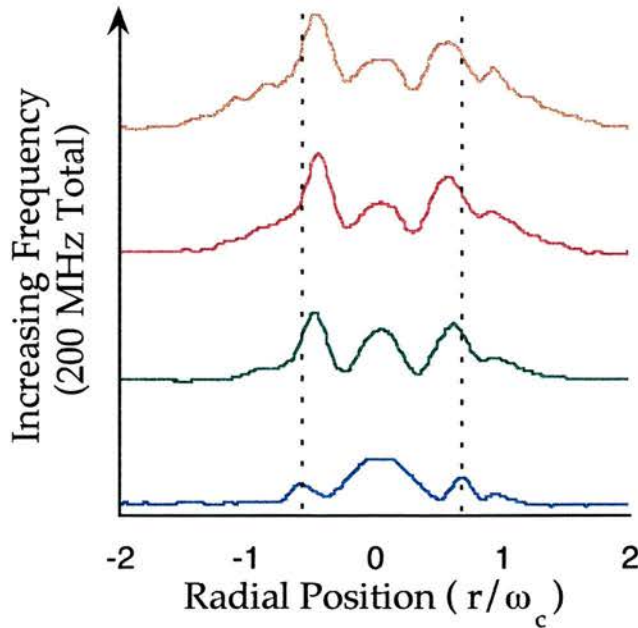


Figure 6.19:- The variation with frequency of the ring pattern observed in Figure 6.18.

The probe field now diffracts into a series of linear fringes after propagating through the transparency slit coherently induced within the rubidium cell.

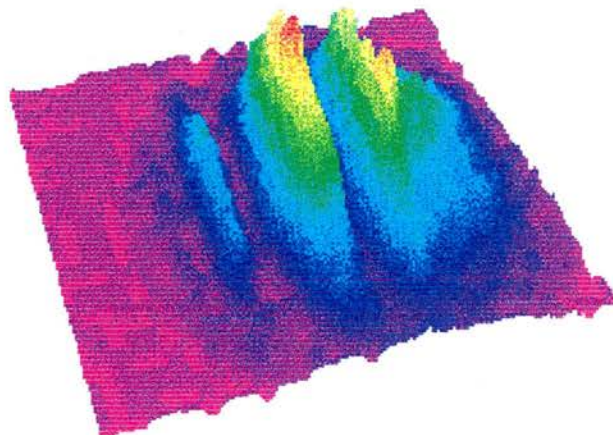


Figure 6.20:-*A three dimensional plot of the probe field as it appears on the C.C.D. camera after being transmitted through a slitlike transparency imposed on the vapour by a cylindrical lens. The probe field has a 2 mm waist, the coupling field a 150 μm waist and the cell is at a temperature $\sim 50^\circ\text{C}$.*

6.4) Concluding Remarks On E.I.F.

Electromagnetically Induced Focusing (E.I.F.) is a novel non-dissipative cross-focusing effect whereby an atomic medium, coherently prepared by a coupling field, acts as a variable lens to a connected probe transition. It is noted that self focusing within an E.I.T. experiment has previously been discussed in the context of E.I.T. systems by Rathe et al. [21], arising through the dependence of the third order susceptibility on the field of the probe laser. However, it is emphasised that this effect is not a self induced one, but rather the modification of one beam by the other. This can be verified by the use of a lower vapour temperature, such that the probe is not completely attenuated outside of the transparency region. Under these conditions the probe field waist size changes are only seen during the transparency region. Furthermore, a reduction of probe field power does not lead to any reduction in the lensing effects, as would be expected if E.I.F. was a self induced phenomena. It has

also been shown theoretically that higher temperatures lead to greater lensing action as expected.

The mechanism for E.I.F. has been shown to be the result of the complex combination of the spatially varying absorption and refractive index profiles induced through E.I.T. effects. Regions of focusing and defocusing are caused by these conditions which are shown to vary with many experimental parameters, including relative spot sizes, probe field focal positions, cell temperature and coupling field detuning. An indepth theoretical model has been developed which correctly predicts many of these features including the emergence of diffraction-like rings on the probe field when an initially large probe field waist, relative to the coupling field waist, is employed. Experiments were carried out in this regime in which the coupling field imprints a transparency aperture upon the medium, of either a circular or slit like nature. The probe field then treats this light induced aperture in much the same way as it would a solid aperture, with ring or fringe diffraction-like patterns evident in the probe field observation plane.

Electromagnetically Induced Focusing has critical implications for future experiments in the area of atomic coherence. Mode matching of coupling laser and the circulating laser modes in inversionless lasers schemes will be affected, as will all E.I.T. experiments, including those to enhance nonlinear processes. Of particular interest will be the susceptibility of this lensing within the various schemes proposed for enhanced refractive index mediums which do not exhibit significant absorption. Experiments designed to avoid E.I.F. may utilise either a "top-hat" coupling field laser mode, or ensure that the probe is contained within a sufficiently small area of the coupling laser to avoid a spatial variation in the susceptibility.

As well of being of consequence to future atomic coherence experiments, E.I.F. is of fundamental interest in its own right. It provides a mechanism whereby an optical field can be controlled by the properties of a second field. Thus, modulation of the coupling field intensity or frequency will induce a rapidly varying lens upon the probe field. The time scale for these effects is of the same order as the response times of E.I.T effects, a few hundred nanoseconds as discussed in Section 4.2.2. In addition to the observed changes in spot size, deflections of the probe field due to non-perfectly overlapped lasers have been observed. Therefore, E.I.F. may be employed as a non-dissipative optical switch, or waveguide if doughnut coupling field modes were

employed. Whether E.I.F. is considered as a problematic feature to be circumvented within future atomic coherence experiments or as an interesting and useful tool in the control and manipulation of optical fields, it is an inherent feature of E.I.T. experiments and as such cannot simply be ignored.

References

- [1] **M.O. Scully**, *Enhancement Of The Index Of Refraction Via Quantum Coherence*, Phys. Rev. Lett. 67, 1855 (1991).
- [2] **S.E. Harris, J.E. Field and A. Kasapi**, *Dispersive Properties Of Electromagnetically Induced Transparency*, Phys. Rev. A 46, R29 (1992).
- [3] **S.E. Harris**, *Normal Modes For Electromagnetically Induced Transparency*, Phys. Rev. Lett. 72, 52 (1994).
- [4] **A. Kasapi, M. Jain, G.Y. Yin and S.E. Harris**, *Electromagnetically Induced Transparency : Propagation Dynamics*, Phys. Rev. Lett. 74, 2447 (1995).
- [5] **M. Xiao, Y. Li, S. Jin and J. Gea-Banacloche**, *Measurement Of Dispersive Properties Of Electromagnetically Induced Transparency In Rubidium Atoms*, Phys. Rev. Lett. 74, 666 (1995).
- [6] **M. Fleischhauer, C.H. Keitel and M.O. Scully**, *Resonantly Enhanced Refractive Index Without Absorption Via Atomic Coherence*, Phys. Rev. A 46, 1468 (1992).
- [7] **M.O. Scully and M. Fleischhauer**, *High Sensitivity Magnetometer Based On Index Enhanced Media*, Phys. Rev. Lett. 69, 1360 (1992).
- [8] **A.S. Zibrov, M.D. Lukin, L. Hollberg, D.E. Nikonov, M.O. Scully, H.G. Robinson and V.L. Velichansky**, *Experimental Demonstration Of Enhanced Index Of Refraction Via Quantum Coherence In Rb*, Phys. Rev. Lett. 76, 3935 (1996).
- [9] **R.R. Moseley, S. Shepherd, D.J. Fulton, B. D. Sinclair and M.H. Dunn**, *Spatial Consequences Of Electromagnetically Induced Transparency: Observation Of Electromagnetically Induced Focusing*, Phys. Rev. Lett. 74, 670 (1995).
- [10] **R.R. Moseley, S. Shepherd, D.J. Fulton, B. D. Sinclair and M.H. Dunn**, *Electromagnetically Induced Focusing*, Phys. Rev. A. 53, 408 (1996).

- [11] **A.C. Tam and W. Happer**, *Long-Range Interactions Between Cw Self-Focused Laser Beams In An Atomic Vapour*, Phys. Rev. Lett. 38, 278 (1977).
- [12] **A. Javan and P.L. Kelley**, *Possibility Of Self-Focusing Due To Intensity Dependent Anomalous Dispersion*, IEEE J. Quantum Electron. QE-2, 470 (1966).
- [13] **J.E. Bjorkholm and A. Ashkin**, *Cw Self-Focusing And Self Trapping Of Light In Sodium Vapour*, Phys. Rev. Lett. 32, 129 (1974).
- [14] **O. Kocharovskaya**, *Amplification And Lasing Without Inversion*, Phys. Rep. 219, 175 (1992).
- [15] **P. Mandel**, *Lasing Without Inversion: A Useful Concept ?*, Contemp. Phys. 34, 235 (1993).
- [16] **J. Marangos**, *Focusing Light With Light*, Nature 374, 679 (1995).
- [17] **R. McDuff**, *Matrix Method For Beam Propagation Using Gaussian Hermite Polynomials*, Appl. Opt. 29, 802 (1990).
- [18] **A.E. Siegman**, *Lasers* (Oxford U.P., London, 1986)
- [19] **Y.Y. Lin and L.P. Hwang**, *Efficient Computation Of The Matrix Exponential Using Padé Approximation*, Comput. Chem. 16, 285 (1992).
- [20] **A. Yariv**, *Optical Electronics*, 4th ed. (Saunders, Philadelphia, 1991).
- [21] **U. Rathe, M. Fleischhauer, S.Y. Zhu, T.W. Hänsch and M.O. Scully**, *Nonlinear Theory Of Index Enhancement Via Quantum Coherence And Interference*, Phys. Rev. A 47, 4994 (1993).

Chapter 7

Wavelength Dependence Of Coherently Induced Transparency in a Doppler-Broadened Medium

The work of this chapter involves the examination of the effect of changing the coupling laser transition, and hence the wavelength, on the coherently induced transparency experienced by a probe beam in Doppler-broadened E.I.T. systems. This examination includes the theoretical study of cascade, lambda and V-type systems within atomic rubidium and is backed up with experimental results from various cascade systems. The transparency of the vapour is shown to be an effect not just of E.I.T., but of the velocity group dependent Autler-Townes splitting within the vapour. Consequently, the best overall transparency for Rabi splittings less than the Doppler width is not at the position of matched coupling and probe wavelengths, but for coupling field wavelengths less than that of the probe.

7.1) An Introduction To Coupling Field Wavelength Effects

Various E.I.T. systems within atomic rubidium have been discussed in the previous chapters of this work and within the various papers referenced therein. The wavelengths involved in the configurations of most of these rubidium cascade, lambda and V-type systems are in the near infrared, and therefore easily covered by both diode

and Ti: sapphire laser sources. Since the wavelengths of the probe and coupling fields in these configurations are similar, the proper choice of co or counter-propagating beams can reduce the Doppler broadened vapour to a virtually Doppler-free medium. To date, all schemes in rubidium, including that of the first cw inversionless laser [1], have taken advantage of these Doppler-free schemes. It had been thought that the use of a Doppler free medium was a necessary requirement for the observation of coherent transparency since it was believed that these reduced the power requirements on the coupling field laser. In this chapter it will be shown, both theoretically and experimentally, that this is in fact not the case. Instead, for all three configurations, if the wavelength of the coupling field is less than that of the probe, there is no disadvantage in using mismatched wavelengths. This result is found theoretically to extend further within the V-type system. When the wavelength mismatch is such that the coupling field has a larger wavelength than that of the probe field there is still no significant reduction in the depth of an induced transparency feature.

Wavelength mismatching has been previously discussed theoretically for a homogeneously broadened cascade system in a paper by Geo-Banacloche *et al* [2]. Within their theoretical analysis the authors show that it is advantageous for the observation of E.I.T. if an atomic system is chosen such that the coupling field is lower in wavelength than that of the probe field. However, the work of this chapter extends these theoretical ideas and provides the first experimental confirmation of these effects in the regime where the wavelength mismatch between the two optical fields is of the order of hundreds of nanometers. In so doing a physical explanation of induced transparency is obtained where the relative roles of Autler-Townes splitting and E.I.T. are highlighted. This picture also highlights the inherent nature of these two mechanisms within a vapour and so emphasises the fact that in a vapour the two cannot be treated separately. The real significance of this work lies in the prospect of inducing cw inversionless gain in Doppler-broadened media where the coupling wavelength is no longer similar to that of the probe, allowing new lasing wavelengths in the blue or U.V. to be generated.

7.2) Modelling The Effects Of Wavelength Mismatch Within E.I.T. Systems

The three basic systems for the observation of E.I.T. are again considered in this chapter with relation to the effect of changing the coupling field wavelength in each. Figure 7.1 presents schematics of these three systems and the corresponding optical fields, the coupling and probe fields are shown by red double headed arrows and blue single headed arrows, respectively.

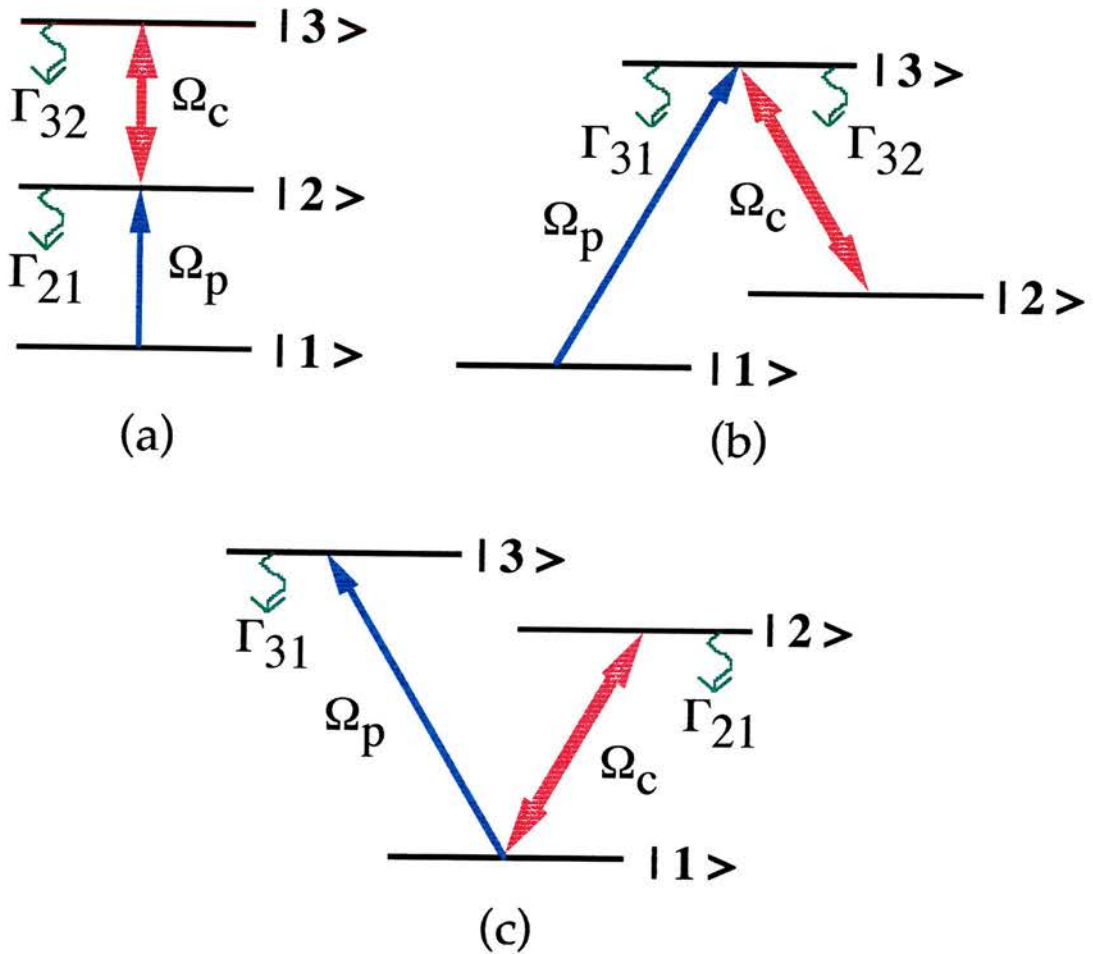


Figure 7.1:- Schematic energy level diagrams for (a) the cascade, (b) the lambda and (c) the V-type systems. Red double headed arrows correspond to coupling field transitions and blue single headed arrows correspond to probe field transitions.

7.2.1) E.I.T. Versus Autler-Townes Splitting In a Doppler Broadened Medium

In a Doppler broadened medium the E.I.T. position (corresponding to two-photon resonance between the uncoupled transitions of Figure 7.1) shifts across the velocity groups, v , such that :

$$\Delta_p = (k_p \pm k_c)v - \Delta_c \quad (7.1)$$

where the + or - correspond to either co or counter propagating optical fields, $k_p = 1/\lambda_p$, $k_c = 1/\lambda_c$, Δ_p - the detuning of probe field, Δ_c - the detuning of coupling field and v - the magnitude of the relevant velocity group. If the wavevectors k_p and k_c have the same magnitude, and the beams are counter-propagating for the cascade system, as in two-photon spectroscopy, or co propagating for the lambda or V-type systems, then the position of two-photon resonance is the same for all velocity groups, and the medium can be considered as Doppler-free. For real atomic systems this is not generally the case, and so any model which approximates an atomic vapour must take into account Doppler broadening. The integration over all velocity groups is a standard procedure in the simulation of cw E.I.T. effects in rubidium vapour [1, 2, 3, 4] as outlined in Chapter 2. However, a clearer picture of the physical processes involved in coherent transparency can be found by examining individual velocity groups, each of finite width, centred at different points across the Doppler profile. Chapters 4 and 5 discussed the importance of the dephasing on the uncoupled transitions to the levels of transparency obtained. Consider the cascade system of Figure 7.1(a). For each velocity group the amount of transparency at the E.I.T. point is set by the dephasing on the uncoupled transition, γ_{13} , which in turn is determined by several factors, including the population decay from level $|3\rangle$ and the linewidth of the coherent sources used in the experiment [5]. If γ_{13} were zero, then the two-photon E.I.T. position would be the point of maximum transparency for each velocity group. However, in reality this is not the case since experimentally, this term is always greater than zero for cascade systems.

In addition to the effect of E.I.T. on the probe absorption in the cascade system, the coupling field also induces Autler-Townes splitting of the levels $|2\rangle$ and $|3\rangle$, which are near resonance with the coupling field [6, 7]. The absorption of the probe by any one atom, travelling with a velocity, v , will consequently split into two components separated by the generalised Rabi frequency, $\tilde{\Omega}_R$, of the coupling laser. The transparency at any point between these two absorptions is also dependent on γ_{13} . The

transparency at any point between these two absorptions is also dependent on γ_{13} . The frequency positions of the two absorptions change for each velocity group within the vapour and the overall probe absorption is the integral over all velocity groups.

The position of maximum transparency for any one velocity group is affected by both of the effects described above; the interference E.I.T. effect, and the Autler-Townes splitting effect. The magnitude of γ_{13} determines the exact frequency position of the maximum transparency. Figure 7.2 illustrates this fact.

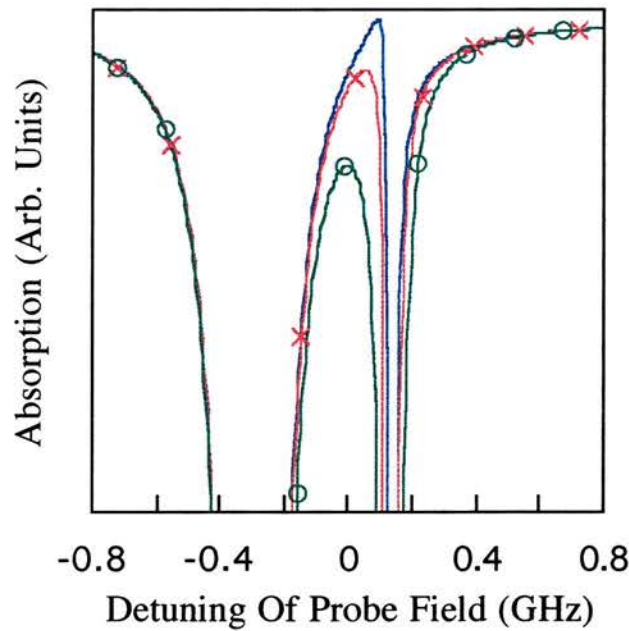


Figure 7.2:- Probe absorption experienced by the $-220 \text{ ms}^{-1} \rightarrow -180 \text{ ms}^{-1}$ velocity group within a cascade system where $\lambda_p = 780 \text{ nm}$ and $\lambda_c = 572 \text{ nm}$ for (a) $\gamma_{13} = 0 \text{ MHz}$ (blue curve), (b) $\gamma_{13} = 3.4 \text{ MHz}$ (red curve marked with crosses) and (c) $\gamma_{13} = 20 \text{ MHz}$ (green curve marked with open circles). The probe field Rabi frequency $\Omega_p = 1 \text{ MHz}$, the coupling field Rabi frequency $\Omega_c = 250 \text{ MHz}$, $\Delta_p = \Delta_c = 0$ and the cell temperature = $47 \text{ }^\circ\text{C}$.

γ_{13} values, the maximum transparency is near (or at, for $\gamma_{13}=0$) the E.I.T. point. However, the higher the dephasing, the less effective are the interference effects, resulting in the maximum transparency shifting to lie nearer the centre of the two Autler-Townes split levels. (In the following models, based on atomic rubidium systems, appropriate values of γ_{13} are used which are consistent with the definitions based on the lifetimes of the relevant states within rubidium as outlined fully in Chapter 2 and reference [3]. For these dephasing values, the maximum transparencies are still close to the E.I.T. points, as shown above in Figure 7.2(b)).

For good transparency it is therefore important to ensure that the absorbing Autler-Townes components for any one velocity group do not overlap with the maximum transparency frequency points of other velocity groups. In order to assess the relative roles of E.I.T. and Autler-Townes splitting in the overall induced transparency, the contribution of individual velocity groups is now considered. The frequency at which the probe experiences absorption due to the Autler-Townes split components of a level is affected by the velocity dependent detunings of both the coupling and probe fields. The probe field propagation direction is defined as always being positive and the velocities of the atoms are positive if they move in the same direction. The coupling field propagates either co or counter to this direction. For a counter-propagating coupling beam the magnitude of the Autler-Townes splitting for each velocity group, v , is the generalised Rabi frequency for that group, $\tilde{\Omega}_R$, and is related to the velocity dependent detuning of the coupling laser, $\Delta_c(v)$ such that:

$$\tilde{\Omega}_R = \sqrt{\Omega^2 + (\Delta_c(v))^2} = \sqrt{\Omega^2 + \left(\Delta_c + \frac{v}{\lambda_c}\right)^2} \quad (7.2)$$

where

$$\Omega = \frac{\mu E}{\hbar} \quad (7.3)$$

and μ is the dipole matrix element of the coupling field transition, E the magnitude of the coupling electric field and \hbar is related to Planck's constant ($\hbar = h/2\pi$).

As well as the atomic levels connected by the coupling field splitting as described above it is found that the central frequency position of the two peaks is shifted away from the unperturbed levels. In relation to the probe field these frequency shifts are given in Table 7.1 below:

Table 7.1

System	Shift From Level	Frequency Shift
Cascade	$ 2\rangle$	$-\frac{1}{2}\left(\Delta_c + \frac{v}{\lambda_c}\right)$
Lambda	$ 3\rangle$	$+\frac{1}{2}\left(\Delta_c + \frac{v}{\lambda_c}\right)$
V-type	$ 1\rangle$	$+\frac{1}{2}\left(\Delta_c + \frac{v}{\lambda_c}\right)$

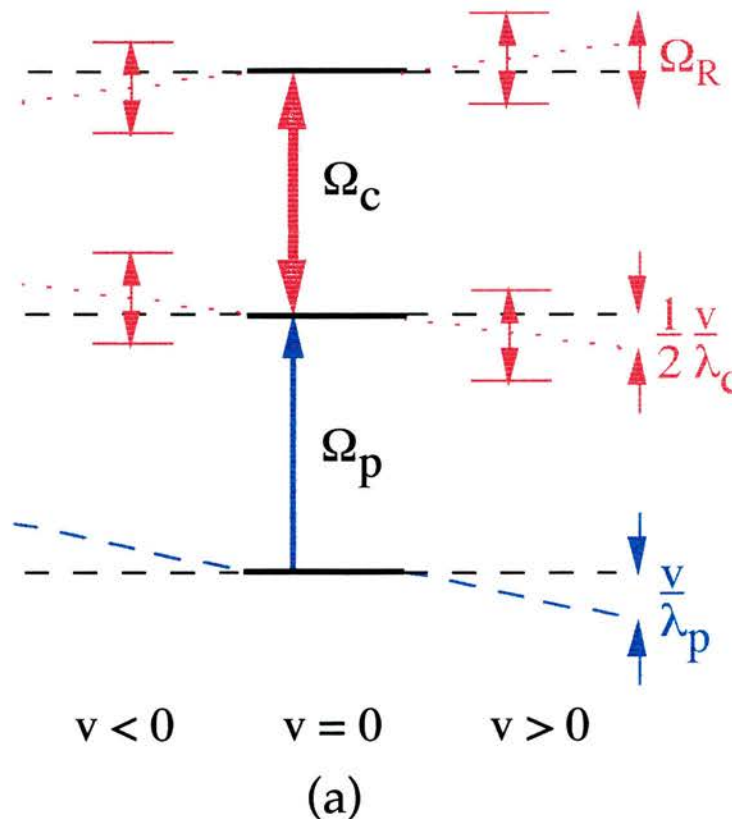
The probe field is itself also frequency shifted within all three systems by an amount $-v/\lambda_p$. The overall effect of these three velocity dependent effects is that the probe is absorbed at frequencies around the uncoupled resonant absorption position such that:

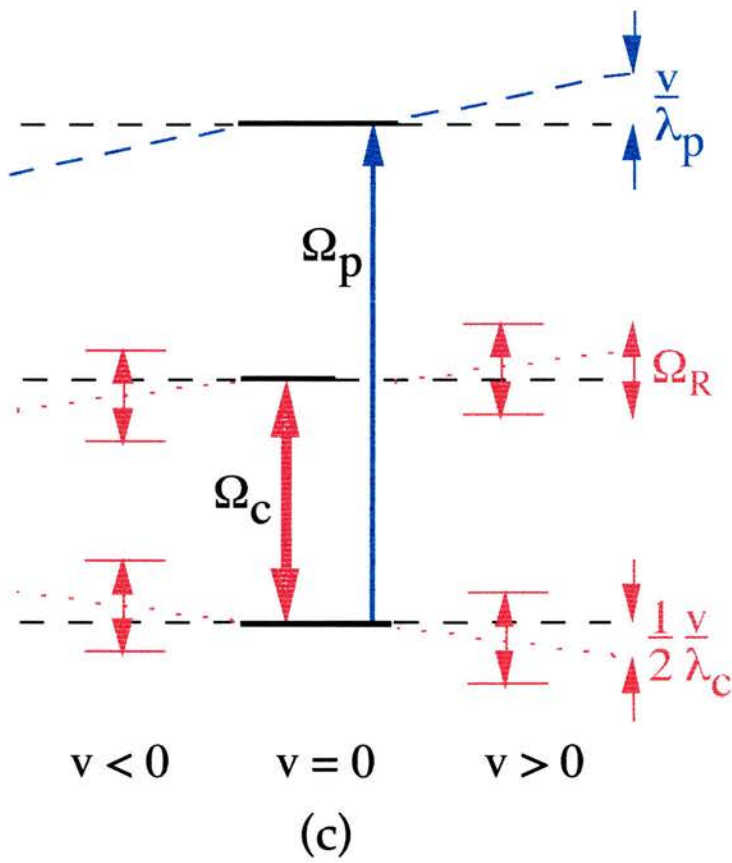
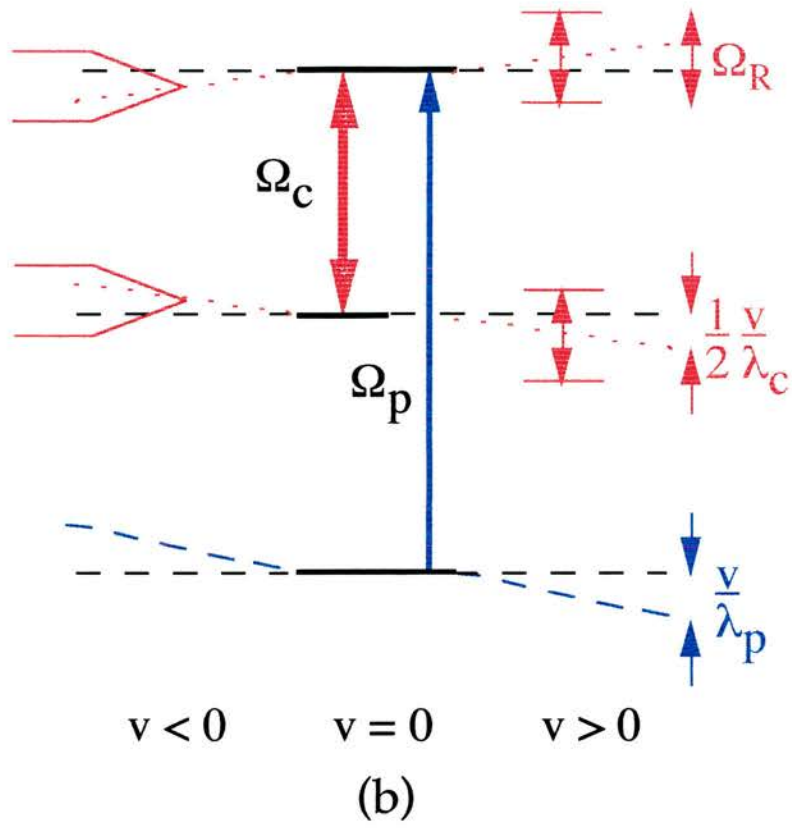
$$\Delta v_{\text{probe abs}} = \frac{v}{\lambda_p} \mp \frac{1}{2}\left(\Delta_c + \frac{v}{\lambda_c}\right) \pm \frac{1}{2}\sqrt{\Omega^2 + \left(\Delta_c + \frac{v}{\lambda_c}\right)^2} \quad (7.4)$$

The negative sign in front of the second term of equation (7.4) corresponds to the cascade system while the positive sign to that of the lambda or V-type systems. For the case where the coupling field co propagates, as is normal for the lambda and V-type systems, the λ_c terms of equation (7.4) should be substituted with $-\lambda_c$ terms. Figure 7.3 presents schematic energy level representations of the frequency shifts involved in equation (7.4) at line centre ($\Delta_p = \Delta_c = 0$) for (a) the cascade, (b) the lambda and (c) the V-type systems, respectively. Looking first at the cascade system shown in Figure 7.3(a), and considering the positive velocity groups (shown on the right of the zero velocity energy levels), all three frequency shifting effects can be observed. The requirement of a higher probe frequency due to the probe Doppler shift (first term of equation (7.4)) is represented by the lowering in energy of level $|1\rangle$, as shown by the blue dashed line. The shift in the central frequency position of the Autler-Townes components (second term of equation (7.4)) is represented by the lowering in energy of level $|2\rangle$ and raising of level $|3\rangle$, shown by dotted red lines. Now for one particular velocity the Autler-Townes splitting around the central frequency shifted point is shown schematically by solid red lines. It is the complicated combination of these three effects which determines the overall frequency shift in the probe absorption for one particular velocity group v . The corresponding frequency shifts for the negative velocity groups

level $|2\rangle$ and raising of level $|3\rangle$, shown by dotted red lines. Now for one particular velocity the Autler-Townes splitting around the central frequency shifted point is shown schematically by solid red lines. It is the complicated combination of these three effects which determines the overall frequency shift in the probe absorption for one particular velocity group v . The corresponding frequency shifts for the negative velocity groups are also shown on the left hand side of the central zero velocity energy levels. All the same effects can be observed in either the lambda, (Figure 7.3(b)) or the V-type (Figure 7.3(c)) systems. The reason for the sign change on the second term of equation (7.4) should now be obvious from these diagrams.

Figure 7.3:- Schematic energy level representations of the frequency shifts involved in equation (7.4) at line centre ($\Delta_p = \Delta_c = 0$) for (a) the cascade, (b) the lambda and (c) the V-type systems, respectively. Probe Doppler shifts (first term of equation (7.4)) are represented by blue dashed lines. Shifts in the central frequency positions of the Autler-Townes components (second term of equation (7.4)) are represented by dotted red lines. For one particular positive and negative velocity the Autler-Townes splitting around the central frequency shifted point is shown schematically by solid red lines.





In the cascade system, the shift of the central frequency position of the Autler-Townes components causes a reduction in the requirement of the probe field frequency to maintain resonance, in the lambda and V-type systems it is required that the probe field frequency be increased to maintain resonance.

A final but significant point to note is the nature of the Autler-Townes component, as seen by the probe field, frequency shifted furthest from the unperturbed energy level. The cascade and lambda systems both have two-photon resonance processes as well as the single photon processes contributing to the overall probe absorption, however the V-type system does not. Thus, the *weaker* Autler-Townes components (i.e. the one frequency shifted furthest from the unperturbed energy level, [8] or see Chapter 5) will therefore experience significantly higher absorption levels in the cascade and lambda systems than in the V-type system. This means that even if the weaker Autler-Townes component of the higher velocity groups within the V-type system overlap with the maximum transparency points of the lower velocity groups the effect will not be as detrimental to the transparency window as would be the case for the cascade or lambda systems. This point discussed further in the V-type system analysis of Section 4.2.3 below.

7.2.2) Theoretical Cascade Systems

Consider a cascade system which has a probe field wavelength of 780 nm corresponding to the $5S_{1/2} - 5P_{3/2}$ transition within rubidium. Figure 7.4(a) shows the variation in overall transparency versus coupling laser wavelength, within this cascade system, at line centre ($\Delta_p = \Delta_c = 0$) for four different Rabi frequencies as outlined in the legend of the graph. It can be seen that the trade-off between absorption and transparency across the velocity groups results in the best overall transparency occurring within the cascade system when the wavelengths satisfy the condition that $\lambda_c < \lambda_p$, for the case where the Rabi frequency (Ω_R) is less than the Doppler width (ν_D), (as is usually the case for cw E.I.T. experiments) and the dephasing term of the uncoupled transition is greater than zero. These curves were calculated using the standard density matrix analysis appropriate to the three level system shown in Figure 7.1(a) and described in Chapter 2, with integration over all the velocity groups contributing to the probe Doppler width of ≈ 530 MHz (FWHM).

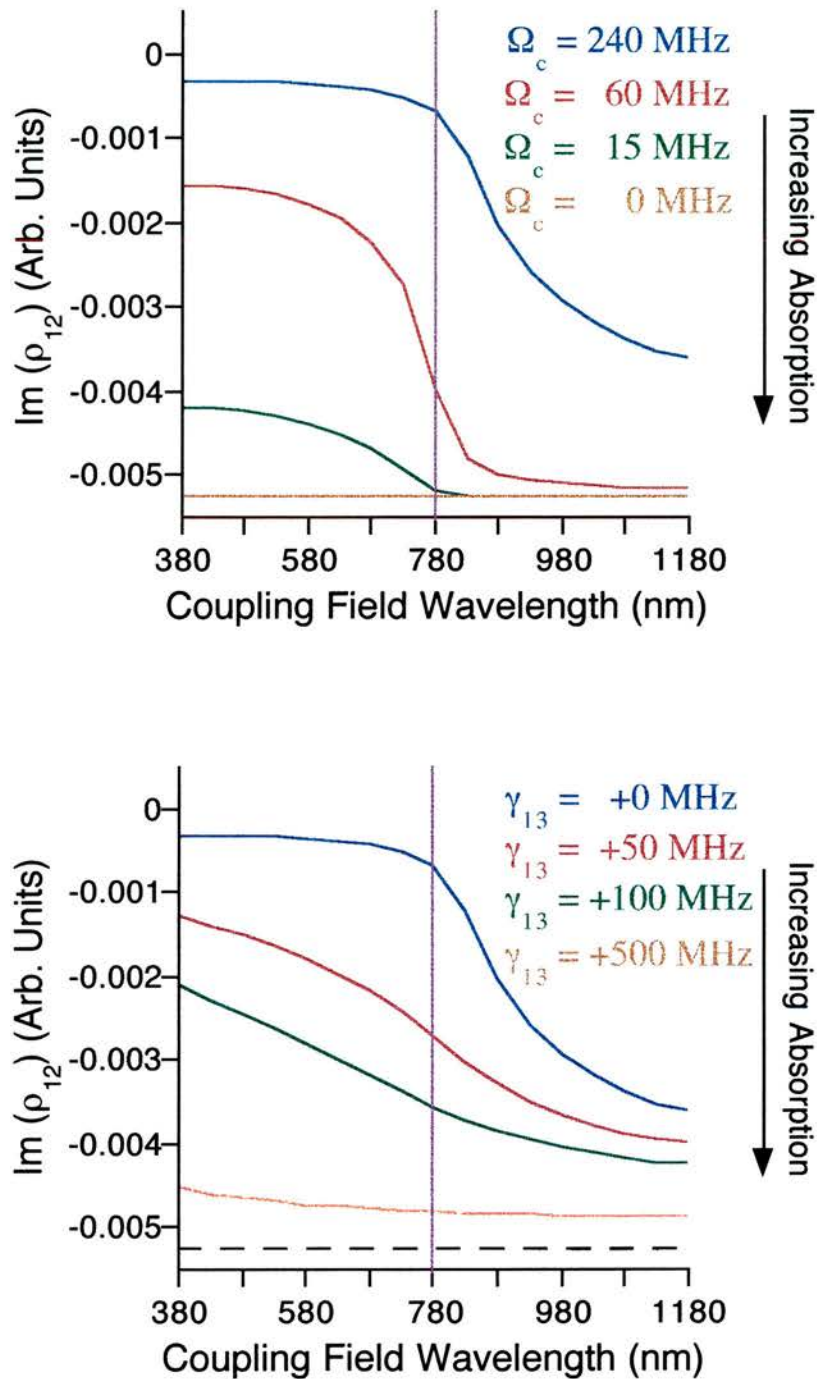


Figure 7.4:- Probe absorption within a cascade system versus coupling field wavelength as a function of (a) coupling field power and (b) the dephasing on the uncoupled transition, for the values indicated on the graphs. The curves in (b) were calculated for $\Omega_c = 240$ MHz. All other parameters are as given for Figure 7.2. Shown for reference is the probe field transmission in the absence of the coupling field (dashed line).

The shift in maximum transparency from where $\lambda_c = \lambda_p$ is clearly visible. The magnitude of this shift is dependent on the value of the dephasing term, γ_{13} . For $\lambda_c < \lambda_p$ the transparency level is seen to be enhanced by the wavelength mismatch. This is most evident for the case where $\Omega_c = 60$ MHz. In all cases the transparency level is observed to fall off as the wavelength of the coupling field increases past that of the probe field.

The effect of artificially dephasing the coherence on the uncoupled transition in this cascade system is shown in Figure 7.4(b). Four curves are presented, the value of γ_{13} for each being indicated in the legend of the graph. Also shown for reference is the probe field transmission in the absence of the coupling field (dashed line). It is seen that as γ_{13} increases the overall transparency level decreases and tends towards the value obtained in the absence of a coupling field. The lineshape of the curves can also be seen to alter, changing from the characteristic bent knee profile to that of a straight line.

Further insight into the physical mechanism involved in the cascade system is achieved by plotting the frequency positions of the Autler-Townes split absorptions (described by equation (7.4)), and the E.I.T frequency positions, (described by equation (7.1)) as a function of group velocity. These calculations are shown in Figure 7.5 where the probe field was again set to be resonant with the $5S_{1/2} - 5P_{3/2}$, 780 nm transition with the coupling field taking various wavelengths and orientations as depicted in the figure caption. The coupling field Rabi frequencies were always set such that $\Omega_c = 250$ MHz. Figure 7.5(a) shows the case for $\lambda_c = 572$ nm, given counter propagating optical fields. It can be seen that there is a frequency region of 220 MHz around zero detuning in which there is no absorption for any velocity group, but there is E.I.T. For $\lambda_c = 776$ nm, Figure 7.5(b), this region has shrunk to 62 MHz, and at $\lambda_c = 980$ nm is non-existent. These graphs clearly show the advantage in having $\lambda_c < \lambda_p$ within the cascade system, as the absorbing Autler-Townes components are frequency shifted and so do not obscure E.I.T., resulting in a better overall transparency region. Figure 7.5(d) shows the case for $\lambda_c = 572$ nm for co instead of counter propagating optical fields. The advantage of having a short coupling wavelength has now been lost, as the Autler-Townes absorptions of one velocity group always encroach on the transparency regions of other velocity groups.

Townes absorptions of one velocity group always encroach on the transparency regions of other velocity groups.

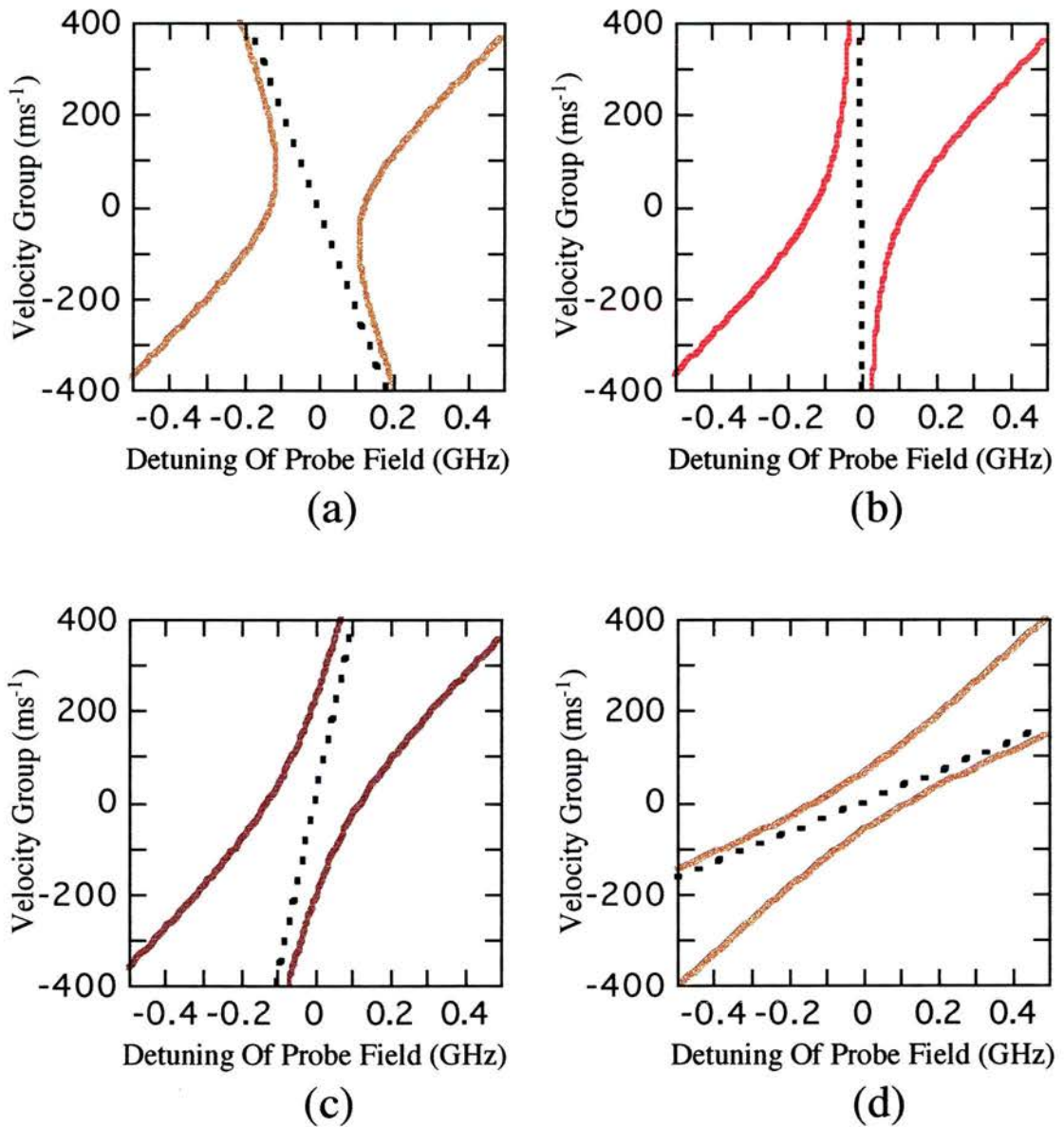
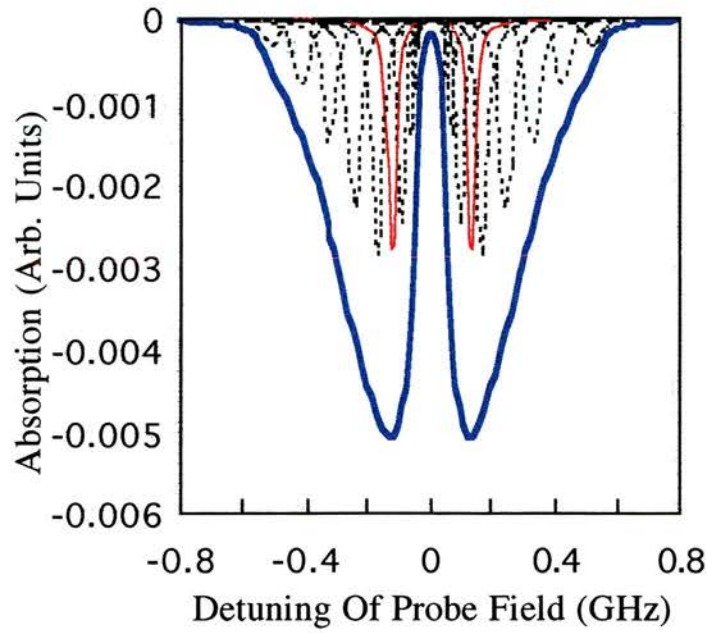


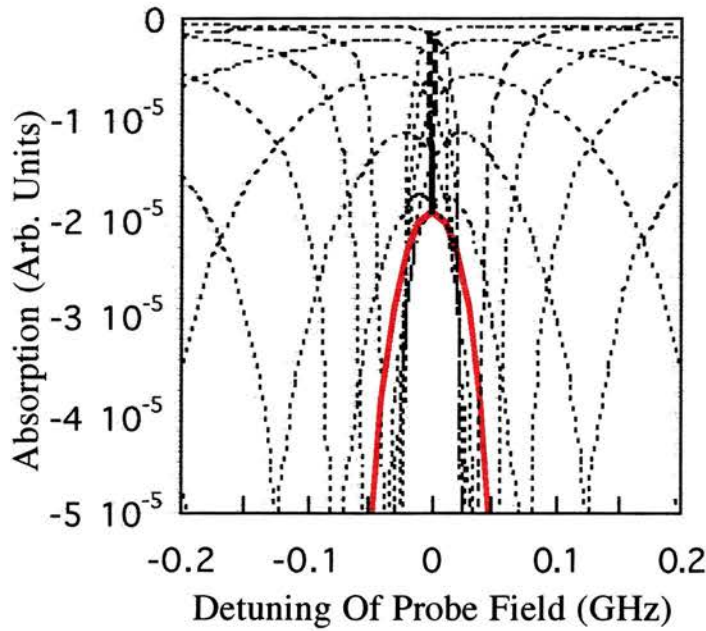
Figure 7.5:- Variation in frequency of the Autler-Townes absorption components (solid lines) and E.I.T. positions (dotted lines) versus probe frequency across the velocity groups within the cascade system. Figures 7.5(a), (b) and (c) are for counter propagation to a 780 nm probe field wavelength with (a) $\lambda_c = 572$ nm, (b) $\lambda_c = 776$ nm and (c) $\lambda_c = 980$ nm. Figure 7.5 (d) shows the case for $\lambda_c = 572$ nm co propagating with a $\lambda_p = 780$ nm probe field. The overlap of absorption with E.I.T. across the velocity groups can be seen to get progressively worse from (a) to (d).

This graph does not change significantly for any coupling wavelength, showing why counter propagating beams are the preferred geometry for observing transparency in a Doppler broadened cascade medium.

Although Figure 7.5 shows the positions of the Autler-Townes absorptions, the magnitude of each absorption also varies. The higher the velocity group the smaller are the absorptions of that group, due to the Maxwellian distribution. Also, for a particular group, the Autler-Townes component closer to the unperturbed position experiences more absorption. However, as discussed above, since the cascade scheme has a two-photon as well as the single-photon process contributing to the overall probe absorption, the weaker Autler-Townes component for each velocity group is still significant even at large frequency shifts. A complete picture of the absorptions of the velocity groups is given for $\lambda_c = 776$ nm, $\Omega_c = 250$ MHz in Figure 7.6(a). The velocity groups are each 40 ms^{-1} wide and are shown by dotted lines, except for the group centred about zero velocity (-20 $\text{ms}^{-1} \rightarrow 20$ ms^{-1}) which is marked by a red solid line. The thick blue line represents the standard resultant over all velocity groups. Figure 7.6(b) is a close-up of the overlapping of the velocity bands near resonance, where the solid red line again corresponds to the group centred about zero velocity (-20 $\text{ms}^{-1} \rightarrow 20$ ms^{-1}). A dashed line is also included which simply connects the frequency positions of the two-photon E.I.T. points of each velocity grouping. A similar picture for $\lambda_c = 572$ nm is given in Figure 7.7. These pictures illustrate how, despite the position of maximum transparency (which is near the E.I.T. position) shifting less with velocity band for 776 nm than for 572 nm, the resultant is a deeper, wider transparency window in the latter case since the Autler-Townes absorptions are shifted further away from the mid resonance point for $\lambda_c = 572$ nm. In short, the absorptions in the 572 nm case do not erode into the transparency region as much as they do for longer coupling wavelengths and so the transparency window appears deeper and wider. As previously discussed the idea that a negative residual Doppler width should enhance transparency in cascade configurations was previously mentioned in the mathematical analysis of Geo-Banacloche *et al*, [2], but to date no experiments have been carried out in this region, and the role of Autler-Townes absorption in association with E.I.T. as a means of reducing transparency has not been addressed.

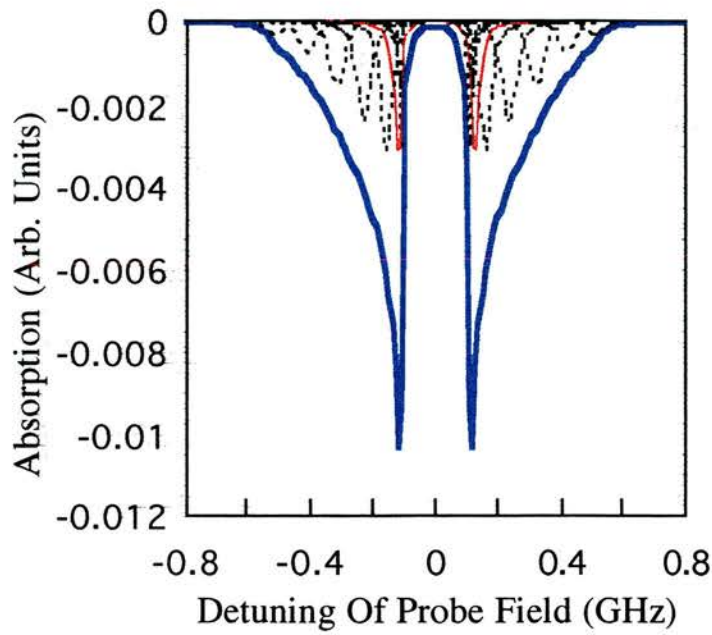


(a)

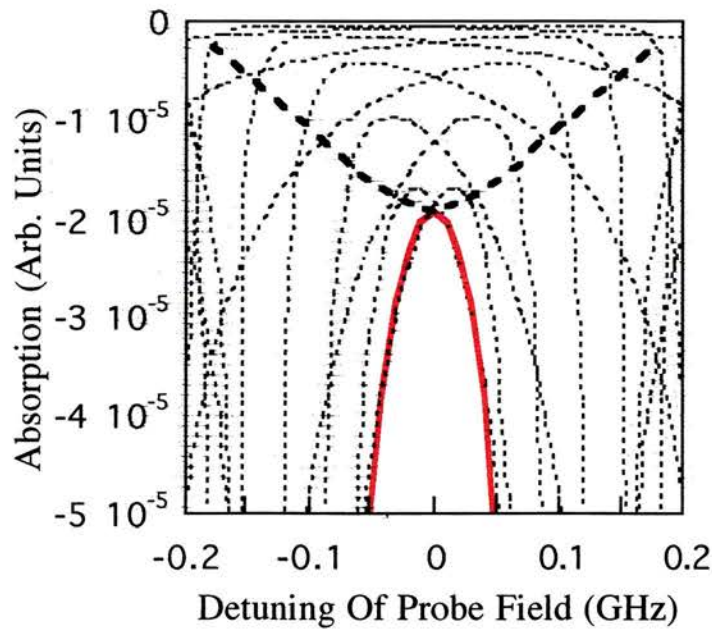


(b)

Figure 7.6:- (a) Variation of absorption of a 780 nm probe field, within a cascade system with a counter propagating 776 nm coupling field ($\Omega_c = 250$ MHz), versus probe frequency for velocity groups 40 ms^{-1} wide spread across the Doppler profile. Each velocity group is marked by a dotted line, except for the group centred about zero velocity ($-20 \text{ ms}^{-1} \rightarrow 20 \text{ ms}^{-1}$) which is marked by a solid red line. The thick blue line shows the absorption for an integration over all velocity groups. (b) Close up of the velocity groups shown in (a) at the resonance point. The dashed line connects the two-photon (E.I.T.) positions for each velocity group.



(a)



(b)

Figure 7.7:- (a) Variation of absorption of a 780 nm probe field, within a cascade system with a counter propagating 572 nm coupling field ($\Omega_c = 250$ MHz), versus probe frequency for velocity groups 40 ms^{-1} wide spread across the Doppler profile. Each velocity group is marked by a dotted line, except for the group centred about zero velocity ($-20 \text{ ms}^{-1} \rightarrow 20 \text{ ms}^{-1}$) which is marked by a solid red line. The thick blue line shows the absorption for an integration over all velocity groups. (b) Close up of the velocity groups shown in (a) at the resonance point. The dashed line connects the two-photon (E.I.T.) positions for each velocity group.

7.2.3) Theoretical Lambda and V-type Systems

Similar density matrix calculation were carried out for the lambda and V-type systems of Figure 7.1(b) and (c) respectively. Plotted in Figure 7.8(a) is the transparency experienced by the probe field on line centre, within the lambda system, as a function of coupling field wavelength for three different coupling field Rabi frequencies. At higher coupling field Rabi frequencies the probe absorption curves are similar to that of the cascade system discussed above. However, at lower coupling field Rabi frequencies the transparency levels can be seen to fall quite dramatically as the coupling field wavelength is reduced. As seen for the cascade system, when $\lambda_c > \lambda_p$ the transparency levels fall away rapidly with wavelength mismatch. To confirm that these enhanced transparency effects are not due to optical pumping of the ground state population into level $|2\rangle$ the populations of the three levels for the 15 MHz coupling field case are plotted as a function of coupling field wavelength in Figure 7.8(b). As is clearly seen for all coupling field wavelengths, more than 90% of the population remains in level $|1\rangle$ (blue curve with x markers) and so these enhanced transparency effects within the lambda system at mismatched wavelengths are not the result of optical pumping.

Turning to the V-type system of Figure 7.1(c) similar density matrix calculations have been carried out. The results of the transparency levels experienced by the probe field versus coupling field wavelength as a function of coupling field Rabi frequency are plotted in Figure 7.9(a). The most surprising result about the V-type system is that unlike the cascade and lambda systems the enhanced transparency level is insensitive to the relative direction of the wavelength mismatch. The coupling field can be taken to a higher wavelength than the probe field with no obvious deterioration of the transparency depths. A check was again carried out on the population levels to make sure that these enhanced transparency levels within the V-type system were not due to coupling field saturation effects, as discussed in Chapter 3. For a coupling field power of 240 MHz it can be seen that more than 60% of the population remains in level $|1\rangle$ at all times, and that no significant population ever appears in level $|3\rangle$. These facts confirm that it is atomic coherence effects and not population movement that is the source of the observed transparency effects.

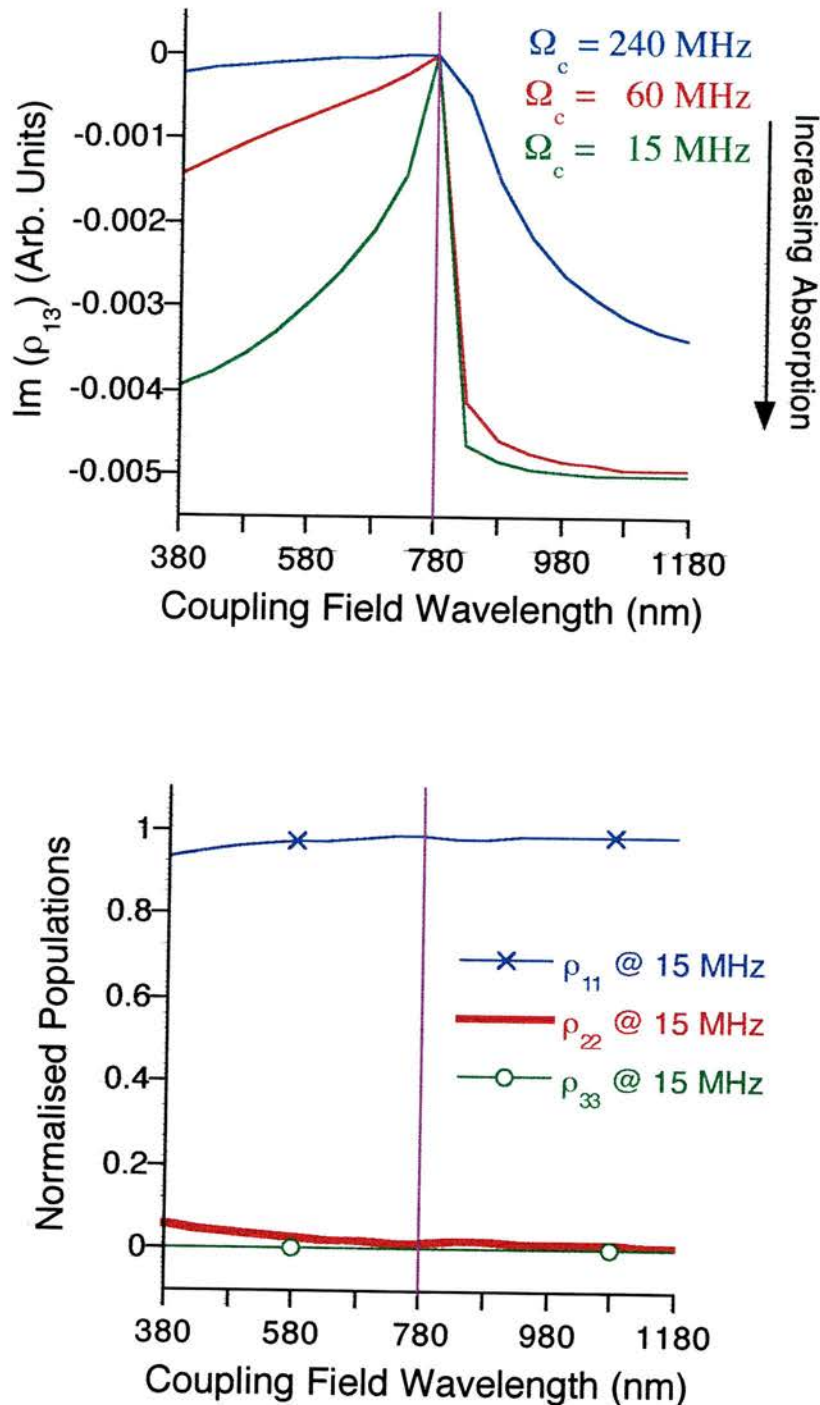


Figure 7.8:- (a) Probe absorption within a lambda system versus coupling field wavelength as a function of coupling field power $\Omega_c = 240$ MHz (blue curve), $\Omega_c = 60$ MHz (red curve) and $\Omega_c = 15$ MHz (green curve) (b) the corresponding populations within the three levels for the case where $\Omega_c = 15$ MHz. ρ_{11} shown in blue with x markers, ρ_{22} shown in red and ρ_{33} shown in green with circle markers. All other parameters are as given for Figure 7.2.

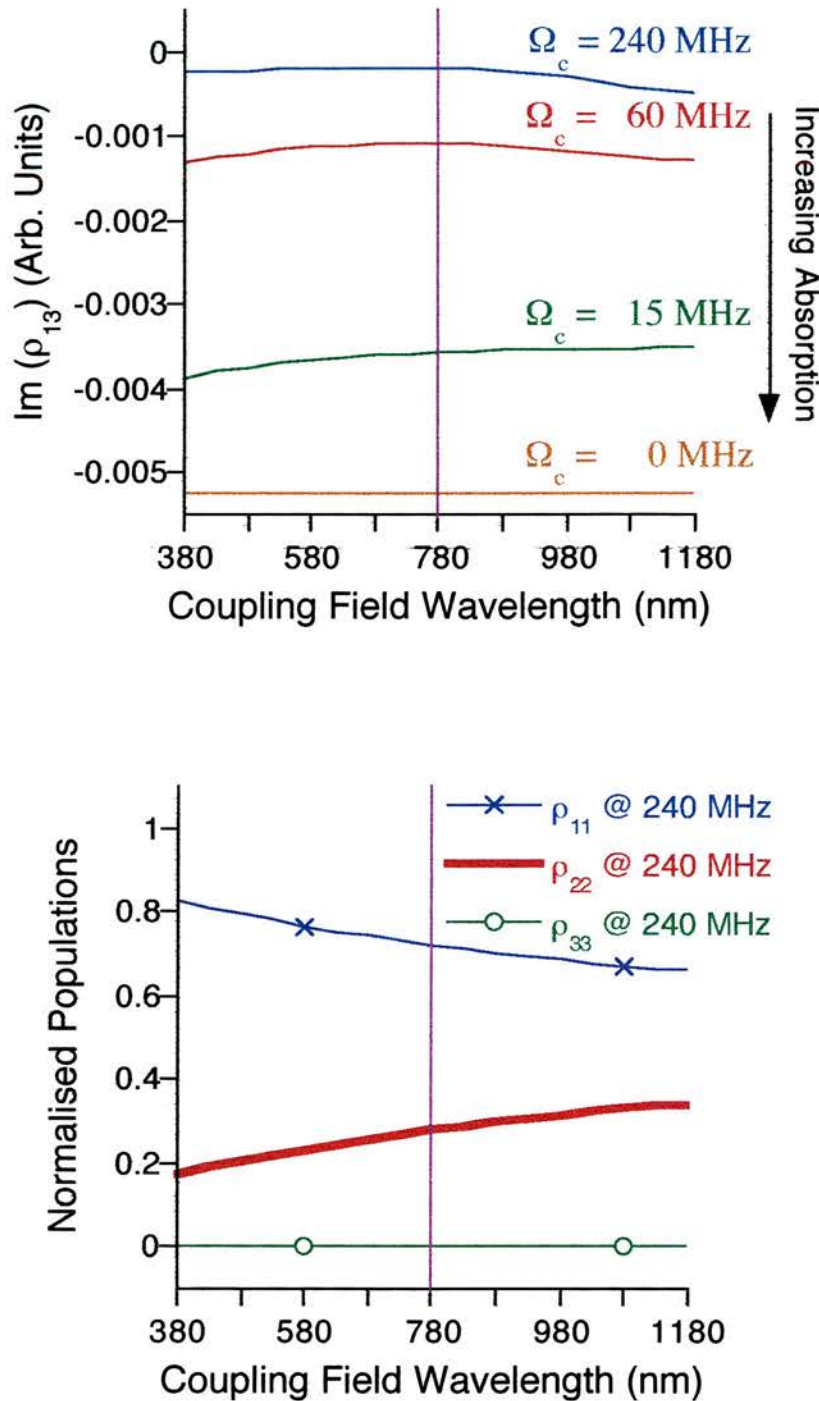


Figure 7.9:- (a) Probe absorption within a V-type system versus coupling field wavelength as a function of coupling field power $\Omega_c = 240$ MHz (blue curve), $\Omega_c = 60$ MHz (red curve), $\Omega_c = 15$ MHz (green curve) and $\Omega_c = 0$ MHz (orange curve) (b) the corresponding populations within the three levels for the case where $\Omega_c = 15$ MHz. ρ_{11} shown in blue with x markers, ρ_{22} shown in red and ρ_{33} shown in green with circle markers. All other parameters are as given for Figure 7.2.

The frequency positions of the Autler-Townes split absorptions and of the E.I.T positions (described by equations (7.4) and (7.1) respectively) are by definition identical in the lambda and V-type systems if the probe and coupling fields are set to have the same wavelength in each system. Figure 7.10 shows the frequency positions of these features as a function of the velocity groups for various coupling field wavelengths. A probe field set resonant with the $5S_{1/2} - 5P_{3/2}$, 780 nm transition is employed and the co propagating coupling field ($\Omega_c = 250$ MHz) takes various wavelengths values:- (a) $\lambda_c = 572$ nm, (b) $\lambda_c = 776$ nm (c) $\lambda_c = 980$ nm and (d) $\lambda_c = 572$ nm but counter propagates with the probe field. As with the cascade system results of Figure 7.5 it can be seen that for $\lambda_c = 572$ nm a wide frequency region ~ 220 MHz exists around the zero detuning point within which there is no absorption of any velocity group. As the coupling field wavelength is increased the width of this frequency region reduces to ~ 62 MHz for the matched wavelength case. By the time $\lambda_c > \lambda_p$, as is the case for Figure 7.10(c), there is significant absorption overlap across the velocity groups. The result of Figure 7.10(d) shows why the power requirement to observe transparency when the optical fields counter propagate are significantly higher since no transparency window remains due to the overlap of the highly absorbing low velocity groups.

From these graphs it can be seen that the same argument which was presented for the cascade system holds for the lambda and V-type systems when $\lambda_c < \lambda_p$. The higher velocity groups experience large enough Autler-Townes splitting such that their components are shifted away from the frequency region of the zero velocity group transparency window and so E.I.T. remains observable. However, when $\lambda_c > \lambda_p$ it is the absorption levels of the individual velocity group Autler-Townes components, which overlap with the zero velocity group transparency window, which determines if any transparency remains at line centre. As shown above for the cascade system and for the lambda system in Figure 7.11 these overlapping velocity group components have significant absorption levels and so, quickly erode into the central transparency region masking the presence of E.I.T. However, for the V-type system the secondary Autler-Townes components are significantly smaller than in the cascade or lambda systems, since there is no two-photon absorption contribution.

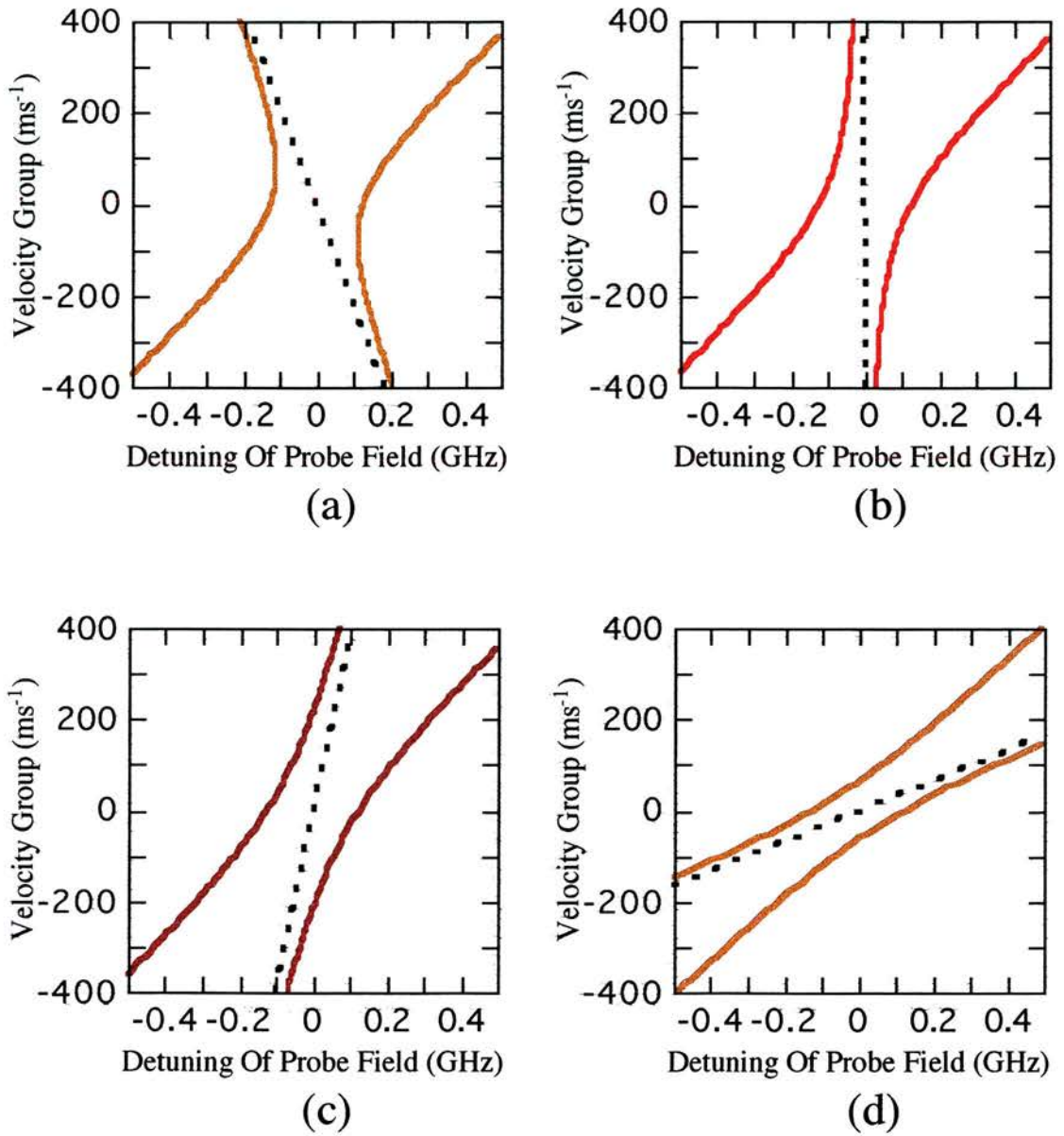
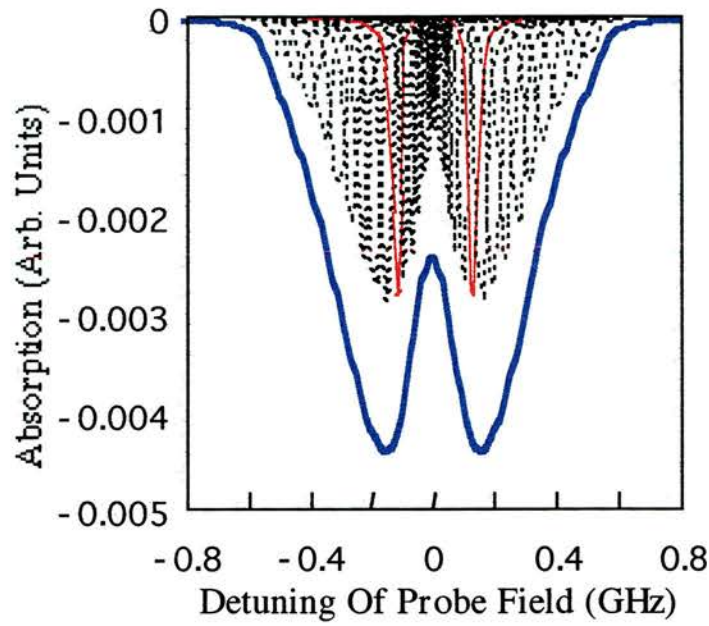
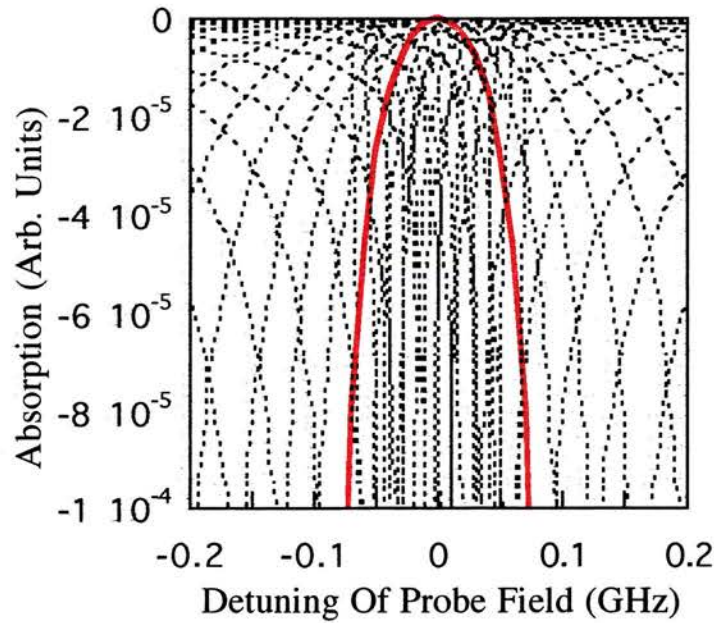


Figure 7.10:- Variation in frequency of the Autler-Townes absorption components (solid lines) and E.I.T. positions (dotted lines) versus probe frequency across the velocity groups within the lambda and V-type systems. Figures 7.10(a), (b) and (c) are for co propagation to a 780 nm probe field wavelength with (a) $\lambda_c = 572 \text{ nm}$, (b) $\lambda_c = 776 \text{ nm}$ and (c) $\lambda_c = 980 \text{ nm}$. Figure 7.5(d) shows the case of $\lambda_c = 572 \text{ nm}$ counter propagating with a $\lambda_p = 780 \text{ nm}$ probe field. The overlap of absorption with E.I.T. across the velocity groups can be seen to get progressively worse from (a) to (d).



(a)

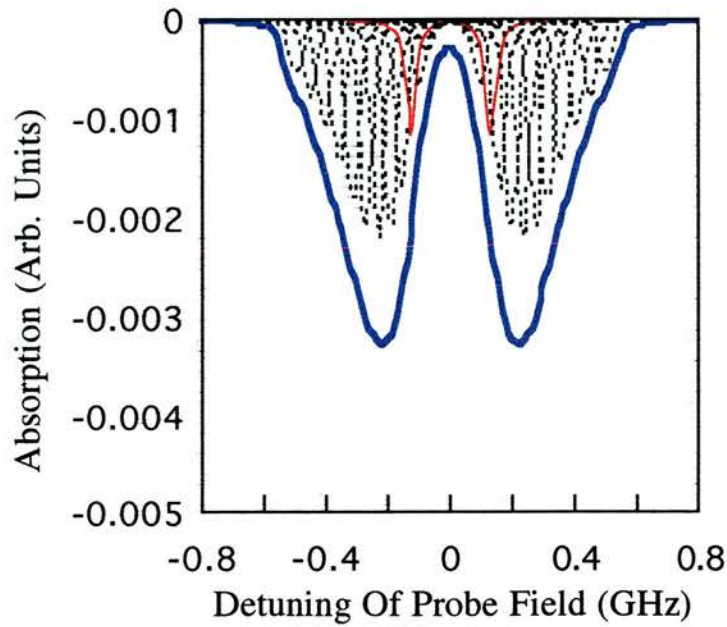


(b)

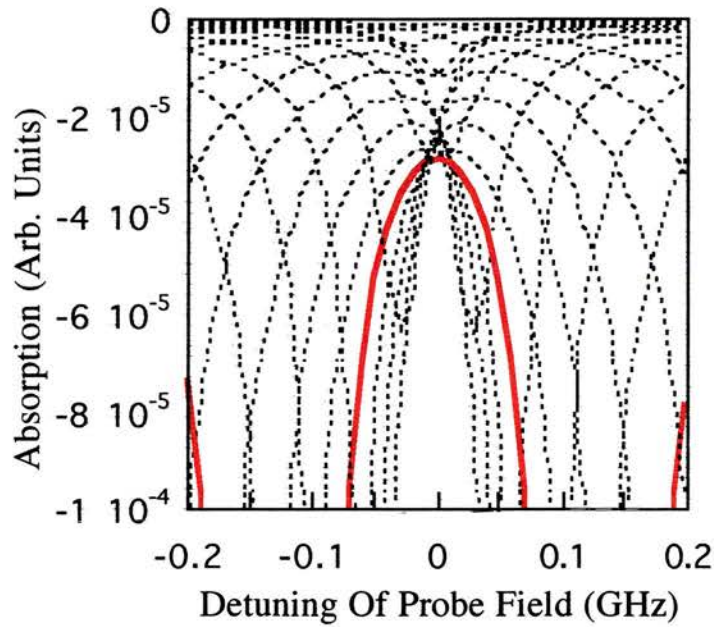
Figure 7.11:- (a) Variation of absorption of a 780 nm probe field, within a lambda system with a co propagating 980 nm coupling field ($\Omega_c = 250$ MHz), versus probe frequency for velocity groups 40 ms^{-1} wide spread across the Doppler profile. Each velocity group is marked by a dotted line, except for the group centred about zero velocity ($-20 \text{ ms}^{-1} \rightarrow 20 \text{ ms}^{-1}$) which is marked by a solid red line. The thick blue line shows the absorption for an integration over all velocity groups. (b) Close up of the velocity groups shown in (a) at the resonance point. The dashed line connects the two-photon (E.I.T.) positions for each velocity group.

Therefore, when $\lambda_c > \lambda_p$, the secondary Autler-Townes components that lie within the frequency region of the zero velocity group transparency window exhibit such small levels of absorption that the transparency window still remains, as shown in Figure 7.12. This is the reason that the curves of Figure 7.9(a) do not exhibit the bent knee profiles of the cascade and lambda systems but remain relatively constant in their transparency depths.

The requirement of co propagating optical fields for the observation of sub-Doppler transparency within the lambda and V-type systems is confirmed by Figure 7.13. Here the resultant probe field absorption curves (blue curves) in the presence of a counter propagating coupling field of Rabi frequency $\Omega_c = 250$ MHz are plotted for (a) a lambda system with $\lambda_c = 572$ nm and (b) a V-type system with $\lambda_c = 572$ nm. As expected for the lambda and V-type systems of Figure 7.1(b) and Figure 7.1(c) respectively, the presence of any transparency feature is masked by the overlap of transparency regions of the lower velocity groups with the higher velocity group absorption components, and vice versa. Therefore, the resultant is just a Doppler broadened absorption profile.

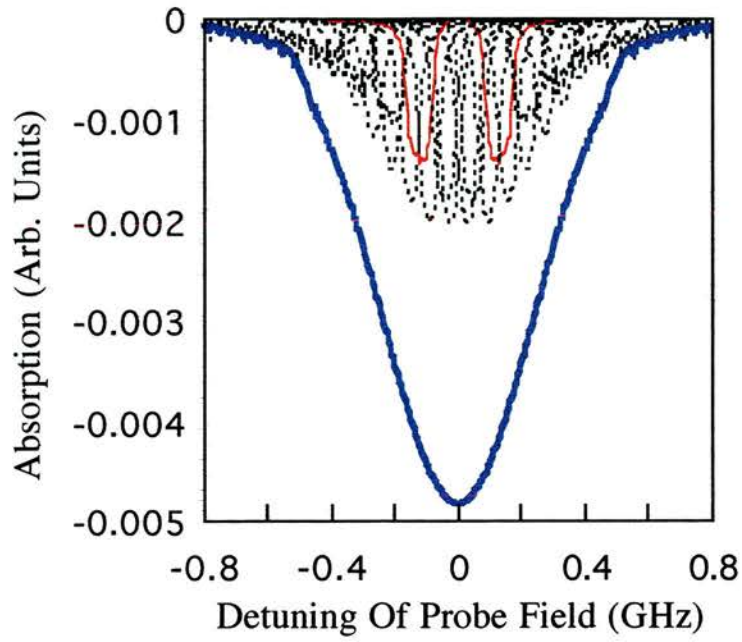


(a)

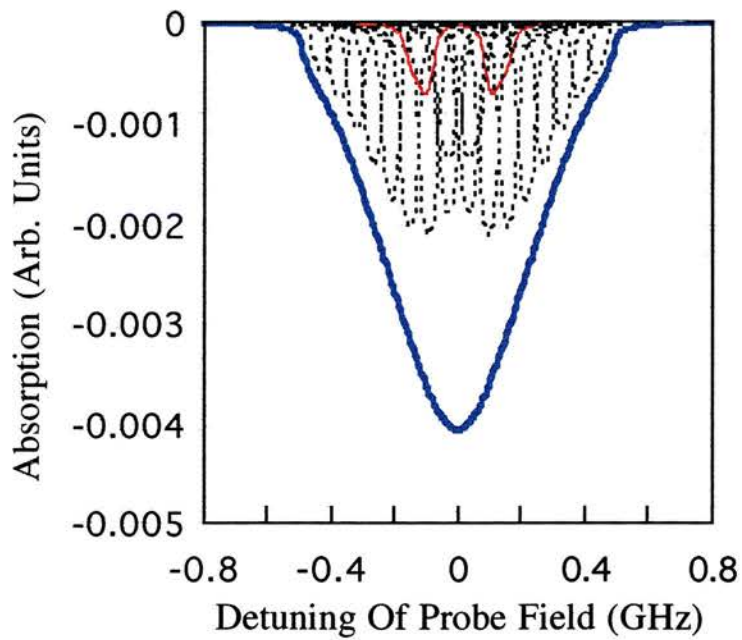


(b)

Figure 7.12:- (a) Variation of absorption of a 780 nm probe field, within a V-type system with a co propagating 980 nm coupling field ($\Omega_c = 250$ MHz), versus probe frequency for velocity groups 40 ms^{-1} wide spread across the Doppler profile. Each velocity group is marked by a dotted line, except for the group centred about zero velocity ($-20 \text{ ms}^{-1} \rightarrow 20 \text{ ms}^{-1}$) which is marked by a solid red line. The thick blue line shows the absorption for an integration over all velocity groups. (b) Close up of the velocity groups shown in (a) at the resonance point. The dashed line connects the two-photon (E.I.T.) positions for each velocity group.



(a)



(b)

Figure 7.13:- Resultant probe absorption (blue solid lines) in the presence of a counter propagating coupling field of Rabi frequency $\Omega_c = 250$ MHz for (a) a lambda system with $\lambda_c = 572$ nm and (b) a V-type system with $\lambda_c = 572$ nm. The contributing velocity groups, 40 ms^{-1} wide, are again shown by the dotted lines.

7.3) Experimental Effects Of Varying The Coupling Field Wavelength

In order to obtain confirmation of the theoretical results predicted above a series of experiments were carried out within rubidium cascade systems. Figure 7.14 shows schematic energy level diagrams of the actual rubidium energy levels used in the experiments described in this section. Figure 7.14(a) describes those for a probe field wavelength resonant with the $5S_{1/2}$ - $5P_{3/2}$ transition (780 nm), while the coupling field wavelength was resonant with either of the $5P_{3/2}$ - $5D_{5/2}$ (776 nm), $5P_{3/2}$ - $7S_{1/2}$ (741 nm), or the $5P_{3/2}$ - $7D_{5/2}$ (572 nm) transitions. Figure 7.14(b) however, describes those for a probe field wavelength resonant with the $5S_{1/2}$ - $5P_{1/2}$ transition (795 nm), while the coupling field wavelength was resonant with either the $5P_{1/2}$ - $5D_{3/2}$ (762 nm) transition or the $5P_{1/2}$ - $7S_{1/2}$ (728 nm) transition.

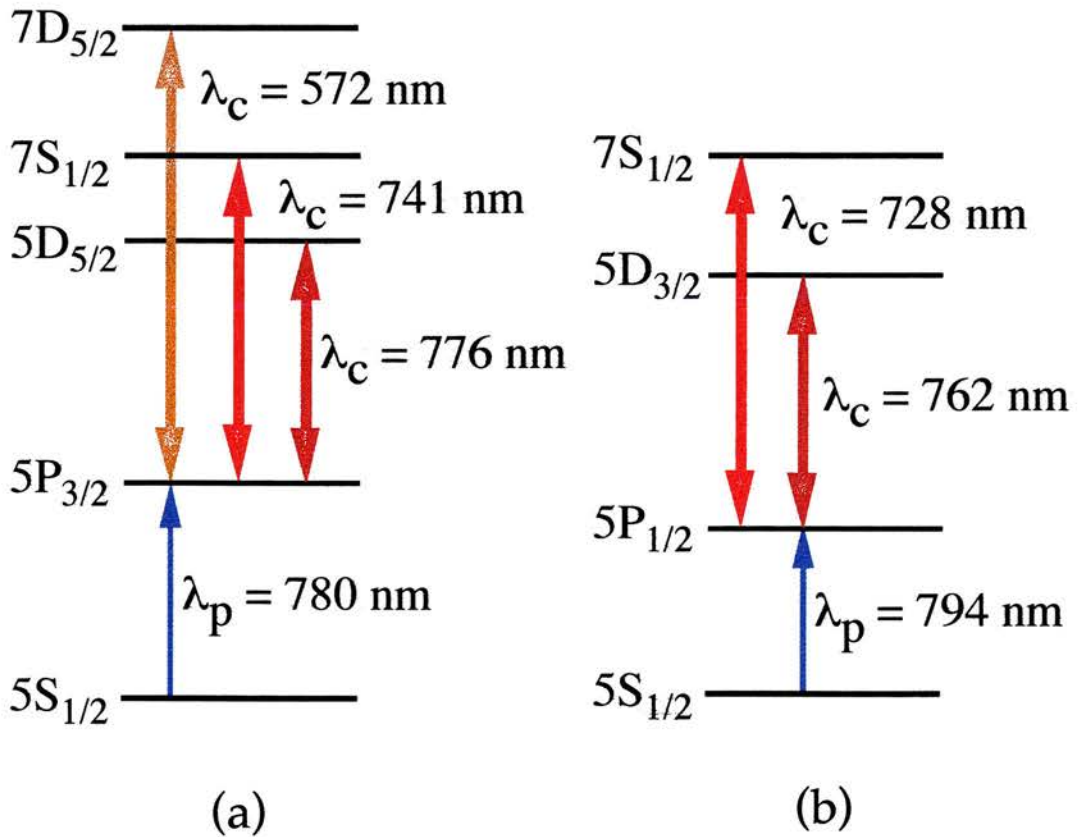


Figure 7.14:- Atomic energy levels in rubidium employed for the study of the effects on an induced transparency of the coupling field wavelength. The probe field was resonant with (a) the $5S_{1/2}$ - $5P_{3/2}$ transition (780 nm) or (b) $5S_{1/2}$ - $5P_{1/2}$ transition (795 nm), while the coupling field transition, and hence wavelength, was varied to be resonant with different atomic transitions.

In general results recorded with the $5S_{1/2}$ - $5P_{3/2}$ transition probe field (780 nm) were better than those taken with $5S_{1/2}$ - $5P_{1/2}$ transition probe (795 nm). The reason for this is that the dipole transition strengths on the relevant coupling field transitions are stronger in the former probe field systems than in the latter. Also more experimental systems were available from the former probe field transition since more coupling field wavelengths, corresponding to allowed transitions, could be generated with the lasers available, see Chapter 3 for more detail on the laser sources. The probe field wavelengths were provided by the Microlase MBR 110 scanning Ti:sapphire laser, with the output power filtered to 4 μ w. The coupling field wavelengths were provided by either the Schwartz Ti:sapphire or a Spectra-Physics 380D Dye laser running on rhodamine 6G, depending on the wavelength required. The beams were all linearly polarised, and the polarisations of coupling and probe fields were parallel. As each transition has a different transition strength [9], the coupling laser intensity was varied to give equal r.m.s. Rabi frequencies on each transition. (There are a number of degenerate transitions excited by the coupling laser, with different Rabi frequencies, but the r.m.s. value is a fair indicator of the overall Rabi frequency). This was done by satisfying the following relation [10]:

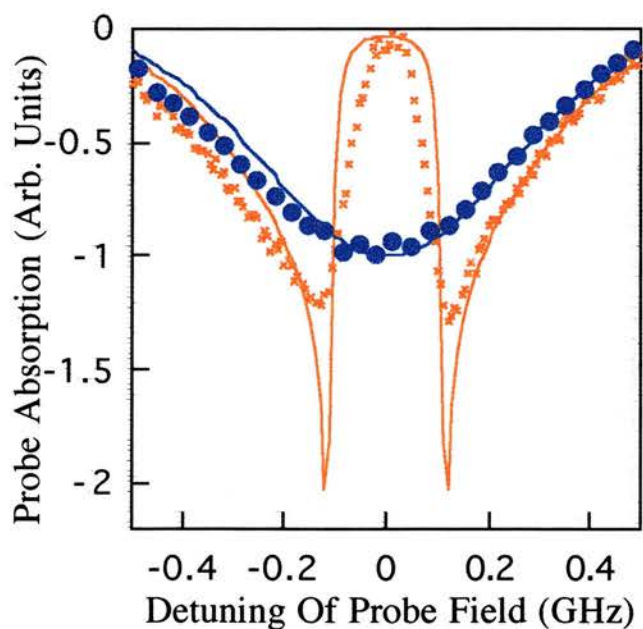
$$\Omega_{\text{r.m.s}} \propto \sqrt{\lambda_c A_{\text{coeff}} \overline{\omega} I} = \text{Constant} \quad (7.5)$$

where λ_c - coupling field wavelength (m), A_{coeff} - coupling field transition strength (10^8 s^{-1}), $\overline{\omega}$ - the degeneracy of the upper level and I - coupling field intensity (Wm^{-2}). The probe was focused to a 50 μm waist within the 2 cm cell of rubidium vapour heated to 50 $^\circ\text{C}$, while the coupling laser was focused to a waist of 135 μm . A wide area photodiode and phase sensitive detection were used to monitor the probe radiation. When on resonance with the $5S_{1/2}$ ($F = 3$) - $5P_{3/2}$ ($F = 4, 3, 2$), ^{85}Rb transition, the absorption of the probe, in the absence of the coupling laser, was $\sim 60\%$.

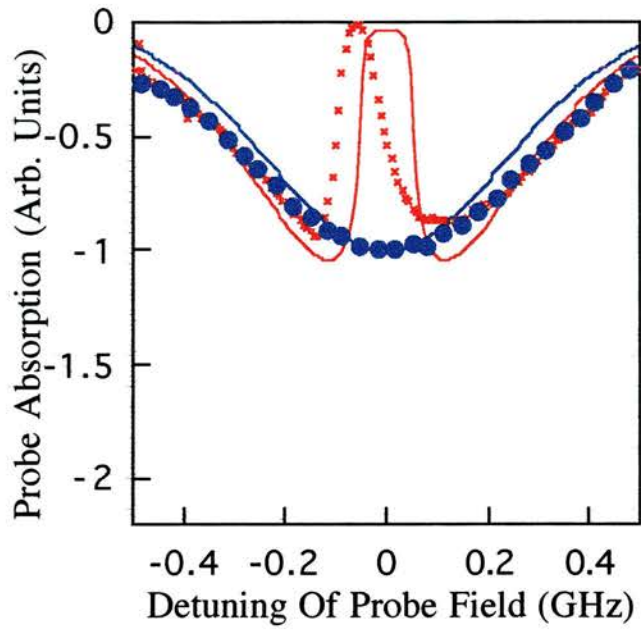
Figure 7.15 shows the induced transparency on the $5S_{1/2}$ - $5P_{3/2}$ probe (780 nm) for a coupling laser wavelength of (a) 572 nm, (b) 741 nm and (c) 776 nm. In each of the graphs the red crosses and blue dots show the probe absorption in the presence and absence of the coupling laser, respectively. The solid lines show theoretical fits to the three cases above based on a Rabi frequency of 250 MHz. (This is in reasonably good agreement with the calculated Rabi frequency components for this transition, see Chapter 3 for more detail. For the $m_J = 3/2 \rightarrow m_J = 3/2$ and $m_J = 1/2 \rightarrow m_J = 1/2$

Chapter 3 for more detail. For the $m_J = 3/2 \rightarrow m_J = 3/2$ and $m_J = 1/2 \rightarrow m_J = 1/2$ transitions these are 338.5 MHz and 414.5 MHz respectively). There are obvious differences between the three graphs of Figure 7.15. The first is that the frequency region of transparency for $\lambda_c = 572$ nm is larger than for either $\lambda_c = 741$ nm or $\lambda_c = 776$ nm and it covers almost the entire range between the 250 MHz Autler-Townes split components of the $5P_{3/2}$ level. The second is the enhanced absorption on the wings of the transparency in the 572 nm case. Both features are experimentally quite obvious, though not as pronounced as expected, due probably to the range of Rabi frequencies present.

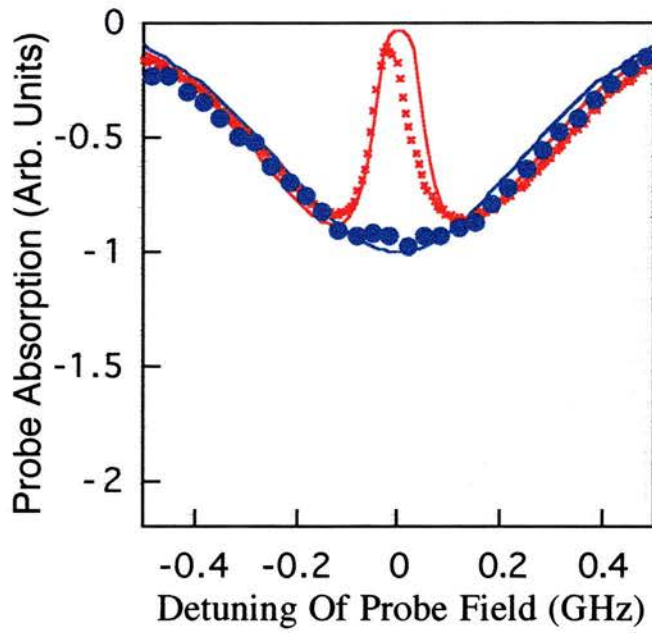
Figure 7.15:- Experimental absorption of the $5S_{1/2} - 5P_{3/2}$ probe field (780 nm) in the presence (red crosses) and absence (blue dots) of a 250 MHz coupling field of wavelength (a) 572 nm, (b) 741 nm and (c) 776 nm. The solid lines represent the theoretical fits to the same parameters.



(a)



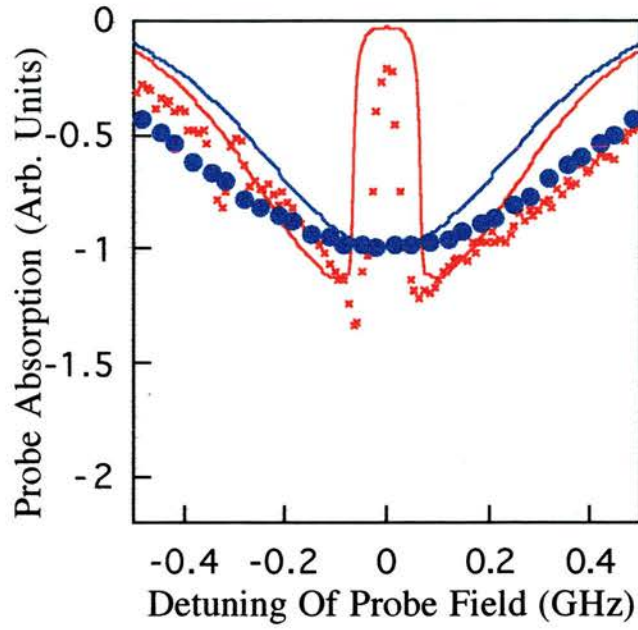
(b)



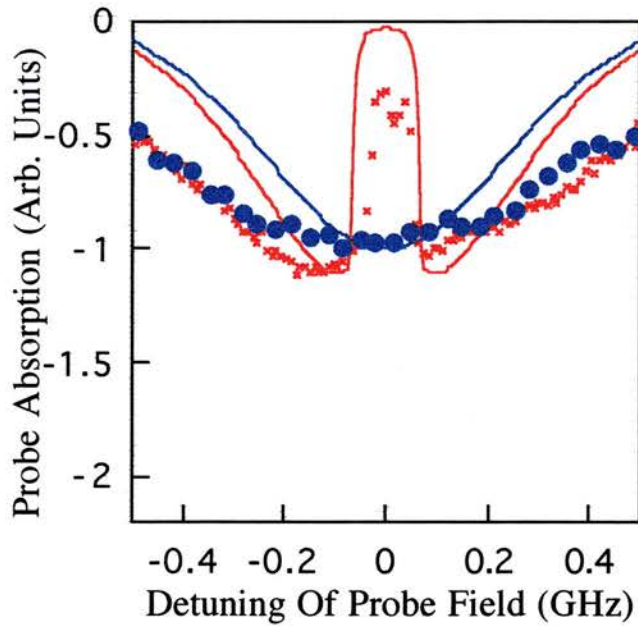
(c)

Similar results are presented in Figure 7.16 for the case of a $5S_{1/2}$ - $5P_{1/2}$ probe (795 nm) and coupling field wavelengths of (a) 728 nm and (b) 762 nm. Moving from the 762 nm coupling field to the 728 nm coupling field the transparency can again be seen to widen and the same characteristic enhancement of the absorption curve can be observed. These effects are not as pronounced as the curves of Figure 7.15 but this is to be expected since the wavelength mismatch is not as great in these systems.

It is interesting to note that along with these features in the absorption spectrum, an increase in the variation of the dispersion of the probe for the case of $\lambda_c = 572$ nm is predicted due to the increased absorption in the wings of the transparency. Figure 7.17 directly compares the theoretical curves for the 572 nm and 776 nm coupling field systems. The enhanced levels of absorption and refractive index at the Autler-Townes splitting frequency can be clearly seen in Figures 7.17(a) and 7.17(b), respectively. This phenomenon may be experimentally harnessed to induce stronger phaseonium effects [11, 12] through the employment of systems which have lower wavelength coupling fields.

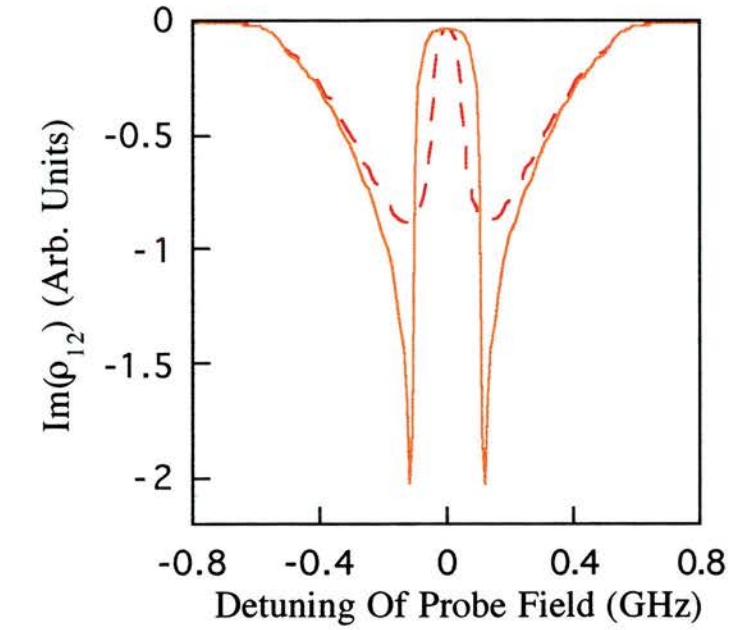


(a)

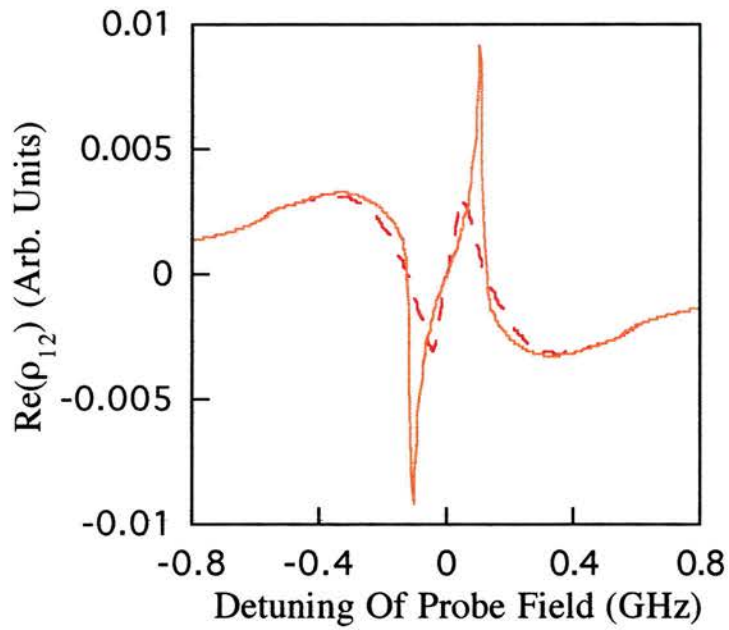


(b)

Figure 7.16:- Experimental absorption of the $5S_{1/2} - 5P_{1/2}$ probe field (795 nm) in the presence (red crosses) and absence (blue dots) of a 250 MHz coupling field of wavelength (a) 728 nm and (b) 761 nm. The solid lines represent the theoretical fits to the same parameters.



(a)



(b)

Figure 7.17:- (a) Theoretical plots of the absorption experienced by a 780 nm probe field in the presence of a 572 nm coupling field (orange line) and a 776 nm coupling field (red dashed line). (b) Corresponding theoretical refractive index curves for the same parameters as in (a).

The final experimental verification of the variation of induced transparency with wavelength is shown in Figure 7.18. The transparency depth at line centre for the $5S_{1/2}$ - $5P_{3/2}$ probe (780 nm) have been plotted against coupling field wavelength for two different Rabi frequencies, 250 MHz (blue open triangles) and 88.5 MHz (red closed triangles). Also included on this graph are the theoretically predicted curves corresponding to the above two Rabi frequencies. The general trend at both Rabi frequencies can be seen to be quite good. However, the agreement is better at the higher Rabi frequency, where the blurring effect of the variation in Rabi frequencies does not affect the maximum transparency as much as for the case of lower powers.

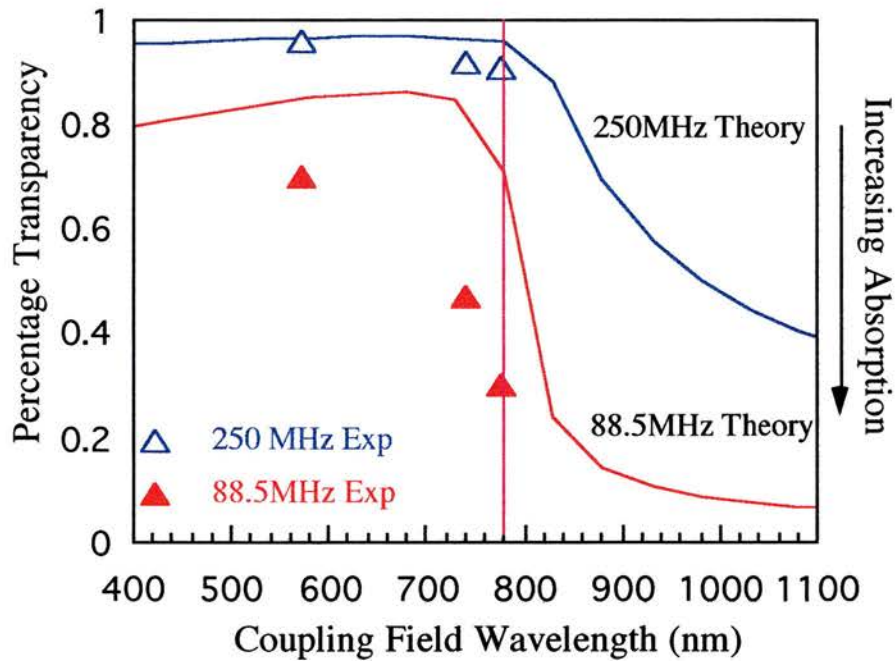


Figure 7.18:- Experimental and theoretical variation of percentage transparency of the $5S_{1/2}$ - $5P_{3/2}$ probe (780 nm) plotted against coupling field wavelength. The solid lines represent the theoretical variation for $\Omega_c = 250$ MHz and $\Omega_c = 88.5$ MHz. The solid red triangles correspond to the experimental variation at $\Omega_c = 88.5$ MHz, and the open blue triangles correspond to the experimental variation at $\Omega_c = 250$ MHz for $\lambda_c = 572$ nm, 741 nm and 776 nm. The vertical line shows the matched wavelength position.

7.4) Concluding Remarks

In conclusion, it has been shown that coherent transparency in a Doppler-broadened medium depends not just on the two-photon E.I.T. position, but on the positions of the Autler-Townes components across the velocity groups. The position of maximum transparency for any one velocity group is determined by the amount of dephasing present on the uncoupled transition i.e. γ_{13} within a cascade system. An expression for the frequency shift of an on resonance probe field, in the presence of a coupling field of wavelength λ_c , has been derived for all three systems. This expression takes account of the Doppler shifts experienced by the probe and coupling fields as well as the contribution of the power dependent Autler-Townes splitting. By employing density matrix models the overall transparency was obtained by integrating over all of these velocity groups. However, by breaking this model into smaller velocity group components it was seen that the depth of transparency for any individual velocity group is set by the dephasing, but the width is controlled by the Autler-Townes splitting. By trading off the Autler-Townes absorption positions against the maximum transparency position across the velocity groups, it is possible to maintain or even increase the overall transparency at low coupling field powers by altering the coupling field wavelength. For the cascade and lambda systems this involves moving to the wavelength regime where $\lambda_c < \lambda_p$, but for a V-type system it has been shown that the transparency depth is relatively insensitive to the direction of the wavelength mismatch. This is accounted for through the lack of a two-photon contribution to the probe absorption within the V-type system. The contribution of the individual velocity groups also explains the requirement of counter propagating optical fields for the cascade system, and co propagating optical fields for the lambda and V-type systems in order to observe sub-Doppler coherent transparency effects. To extend the experimental work of this chapter to include the lambda and V-type systems requires a third laser source to remove the complicating contributions of optical pumping, as outlined in Chapter 4. To date this laser source is not yet available.

The significance of the results of this chapter lie in the fact that E.I.T. without Autler-Townes splitting within a Doppler broadened medium is almost impossible to observe. In order to improve the isolation of E.I.T. it is necessary to find a Doppler free medium such as an atomic beam or trap. However, the search for systems to produce

coherent transparency regions and hence, phaseonium media or non-inversion lasing systems can now be extended to include mismatched wavelength schemes. To date cw non-inversion lasing systems have employed matched wavelength systems in proof of principle style experiments [1,13]. The lifting of this restriction opens up the opportunity of the employment of I.R. laser sources to generate non-inversion lasing in the blue, a wavelength shift of some 350 nm, (see Chapter 8 for such a theoretical system). Further study of atomic or solid state media may extend this wavelength shift still further and result in lasing media at U.V, or X-ray wavelengths.

References

- [1] **A.S. Zibrov, M.D. Lukin, D.E. Nikonov, L. Hollberg, M.O. Scully, V.L. Velichansky and H.G. Robinson**, *Experimental Demonstration Of Laser Oscillation Without Population-Inversion Via Quantum Interference In Rb*, Phys. Rev. Lett. 75, 1499 (1995).
- [2] **J. Geo-Banaoche, Y.Q. Li, S.Z. Jin and M. Xaio**, *Electromagnetically Induced Transparency In Ladder-Type Inhomogeneously Broadened Media: Theory And Experiment*, Phys Rev. A. 51, 576, (1995).
- [3] **D.J. Fulton, S. Shepherd, R.R. Moseley, B.D. Sinclair and M.H. Dunn**, *Continuous-Wave Electromagnetically Induced Transparency: A Comparison of V, A and Cascade Systems*, Phys. Rev. A. 52, 2302 (1995).
- [4] **Y.Q. Li, S.Z. Jin and M. Xaio**, *Observation Of An Electromagnetically Induced Change Of Absorption In Multilevel Rubidium Atoms*, Phys. Rev. A. 51, R1754 (1995).
- [5] **B. J. Dalton and P. L. Knight**, *Population Trapping And Ultranarrow Raman Lineshapes Induced By Phase-Fluctuating Fields*, Opt. Commun. 42, 411 (1982).
- [6] **P.L. Knight and P.W. Milonni**, *The Rabi Frequency In Optical Spectra*, Physics Reports 66, 21 (1980).
- [7] **H.R. Gray and C. R. Stroud. Jr**, *Autler-Townes Effect In Double Optical Resonance*, Opt. Commun. 25, 359 (1978).
- [8] **R.R. Moseley, S. Shepherd, D.J. Fulton, B.D. Sinclair and M.H. Dunn**, *Two-Photon Effects In Continuous-Wave Electromagnetically-Induced Transparency*, Opt. Commun. 119, 61 (1995).
- [9] **A. Lindgård and S. E. Nielsen**, *Atomic Data and Nuclear Data Tables*, Vol. 19 (Academic Press, New York and London (1977)).

- [10] **B. Shore**, *The Theory of Coherent Atomic Excitation*, Vol. 2 (Wiley, New York, (1990)).
- [11] **M. Fleischhauer, C.H. Keitel, M.O. Scully, C. Su, B.T. Ulrich and S.Y. Zhu**, *Resonantly Enhanced Refractive Index Without Absorption Via Atomic Coherence*, Phys Rev. A. 46, 1468, (1992).
- [12] **A.S. Zibrov, M.D. Lukin, L. Hollberg, D.E. Nikonov, M.O. Scully, H.G. Robinson and V.L. Velichansky**, *Experimental Demonstration Of Enhanced Index Of Refraction Via Quantum Coherence In Rb*, Phys. Rev. Lett. 76, 3935 (1996).
- [13] **G.G. Padmabandu, G.R. Welch, I.N. Shubin, E.S. Fry, D.E. Nikonov, M.D. Lukin and M.O. Scully**, *Laser Oscillation Without Population Inversion In A Sodium Atomic Beam*, Phys. Rev. Lett. 76, 2053 (1996).

Chapter 8

Development Of A 422 nm Inversionless Gain System And Other Future Experiments

This chapter presents theoretical analyses of various systems being considered for future experimental work. The main content involves the study of a novel five level system, based on atomic rubidium, which exhibits inversionless gain in the blue wavelength region of the electromagnetic spectrum. The analysis is built up in various simplified stages which help to highlight some of the key features of this newly proposed system. A second section then follows which discusses the practicalities of other future experiments. These include extending the mismatched wavelength work to carry out atomic coherence experiments where the coupling field is replaced by an R.F. coupling source. Finally, a brief discussion is presented on the possibilities of other non-Doppler broadened atomic coherence experiments. It is proposed to realise these non-Doppler broadened media through the employment of an atomic beam or trap.

8.1) A Theoretical 422 nm Inversionless Gain System Within Atomic Rubidium

8.1.1) Coherently Induced 422 nm Inversionless Gain In A Closed V-type System

The starting point for the discussion on 422 nm inversionless gain within atomic rubidium is to introduce inversionless gain in a closed three level V-type system, shown

schematically in Figure 8.1. This system is the basis of the more complicated six level system, outlined in Section 8.1.3, which is required to be experimentally employed due to the atomic structure and allowed transitions within rubidium. Although a simplistic view, this three level system provides initial evidence that inversionless gain can be produced at the blue wavelength.

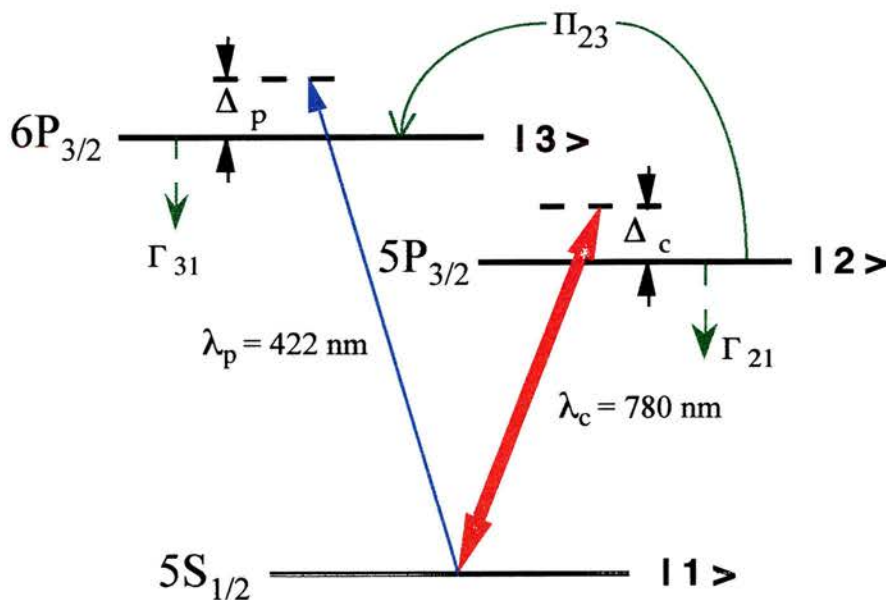


Figure 8.1: A closed three level V-type system with a 422 nm probe field and a 780 nm coupling field. An incoherent pump, Π_{23} , is present to move population from level $|2\rangle$ to level $|3\rangle$ in a non-reversible manner, so as to produce inversionless gain.

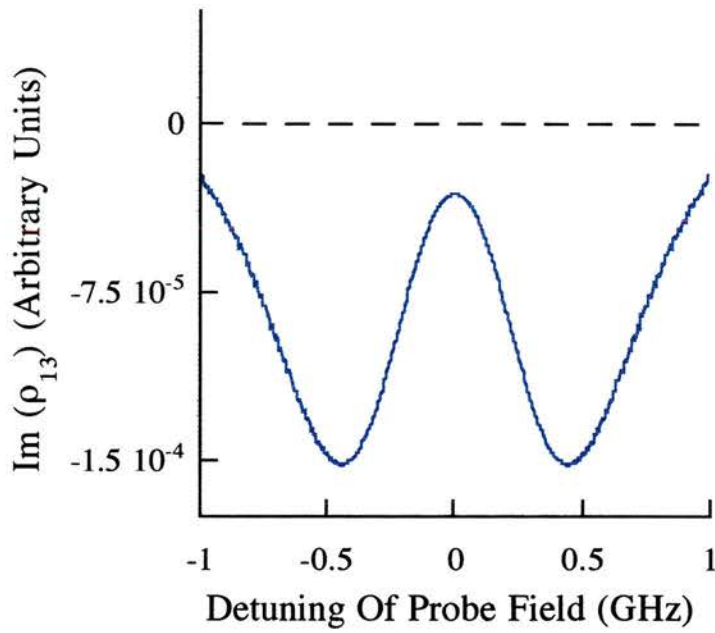
In Chapter 7 the effects of wavelength mismatch within a V-type system were extensively examined. It was shown that there was no disadvantage for the observation of coherently induced transparency if the probe field was several hundred nanometers shorter in wavelength than the coupling field (for reference see Figure 7.9). Therefore, by employing the appropriate system matrix, Matrix 8.1, it should prove possible to modify an induced transparency feature to provide gain by the simple introduction of an Π_{23} incoherent pump. A non-reversible incoherent pump term is employed in this system since in the full 422 nm inversionless gain system the mechanism for population transfer takes advantage of a spontaneous decay route into level $|3\rangle$, thus population can not be transferred back from level $|3\rangle$ to level $|2\rangle$.

Matrix 8.1: A closed three level V-type system employed to produce 422 nm inversionless gain.

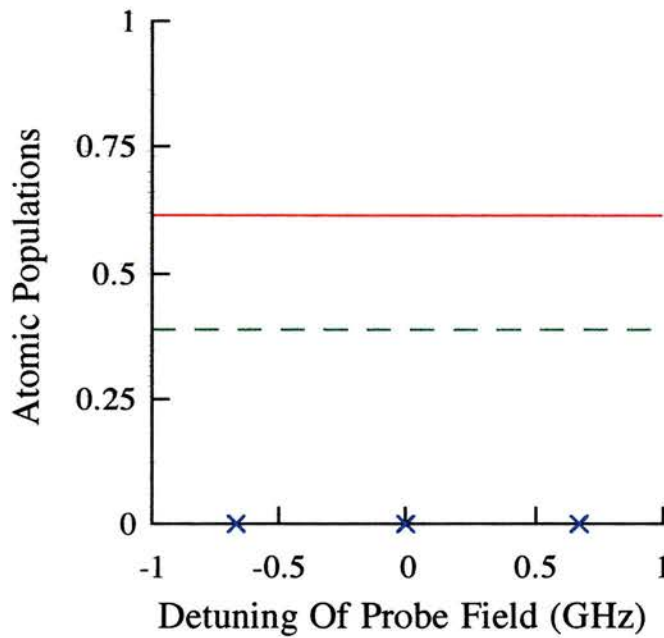
$$\begin{bmatrix}
 (\Gamma_{21} + \Pi_{23}) & 0 & 0 & 0 & 0 & 2\Omega_p & 0 & 0 \\
 -\Pi_{23} & \Gamma_{31} & 0 & 0 & 0 & 0 & 2\Omega_c & 0 \\
 0 & 0 & \gamma_{12} & 0 & 0 & -\Delta_p & 0 & -\Omega_c \\
 0 & 0 & 0 & \gamma_{13} & 0 & 0 & -\Delta_c & \Omega_p \\
 0 & 0 & 0 & 0 & \gamma_{23} & \Omega_c & \Omega_p & -(\Delta_c - \Delta_p) \\
 -2\Omega_p & -\Omega_p & \Delta_p & 0 & -\Omega_c & \gamma_{12} & 0 & 0 \\
 -\Omega_c & -2\Omega_c & 0 & \Delta_c & -\Omega_p & 0 & \gamma_{13} & 0 \\
 0 & 0 & \Omega_c & -\Omega_p & (\Delta_c - \Delta_p) & 0 & 0 & \gamma_{23}
 \end{bmatrix}
 \begin{bmatrix}
 \rho_{22} \\
 \rho_{33} \\
 \rho_{12}^r \\
 \rho_{13}^r \\
 \rho_{23}^r \\
 \rho_{12}^i \\
 \rho_{13}^i \\
 \rho_{23}^i
 \end{bmatrix}
 =
 \begin{bmatrix}
 0 \\
 0 \\
 0 \\
 0 \\
 0 \\
 -\Omega_p \\
 -\Omega_c \\
 0
 \end{bmatrix}$$

Figure 8.2(a) plots the 422 nm probe absorption against probe field detuning in the presence of a coupling field of Rabi frequency 250 MHz. The corresponding populations are shown in Figure 8.2(b) where ρ_{11} is shown as a red solid line, ρ_{22} as a green dashed line, and ρ_{33} as a blue solid line marked with crosses. For these graphs no Π_{23} incoherent pump was present and the decay rates are chosen to mimic those of the appropriate levels within atomic rubidium. As is clearly observed in the probe field absorption curve a coherently induced transparency at 422 nm is present due to the quantum interference effects induced by the I.R. coupling field.

If an incoherent field is now introduced as in Figure 8.3, then it is shown that the induced transparency feature can be enhanced to provide inversionless gain on the 422 nm probe field, Figure 8.3(a). Confirmation of the inversionless nature of this gain feature is confirmed by examining the associated population of the three levels as shown in Figure 8.3(b), where again ρ_{11} is shown as a red solid line, ρ_{22} as a green dashed line, and ρ_{33} as a blue solid line marked with crosses. As can be seen, there is no inversion in the population on the probe field transition even in the presence of the Π_{23} incoherent pump.



(a)



(b)

Figure 8.2 : (a) 422 nm probe field absorption curve showing a coherently induced transparency with (b) the corresponding population levels, for the density matrix model corresponding to Matrix 8.1. Population in ρ_{11} shown as a red solid line, ρ_{22} as a green dashed line and ρ_{33} as a blue solid line marked with crosses. $\Omega_c = 250$ MHz, $\Omega_p = 0.1$ MHz, $\Delta_c = 0$ MHz. and $\Gamma_{23} = 0$ MHz.

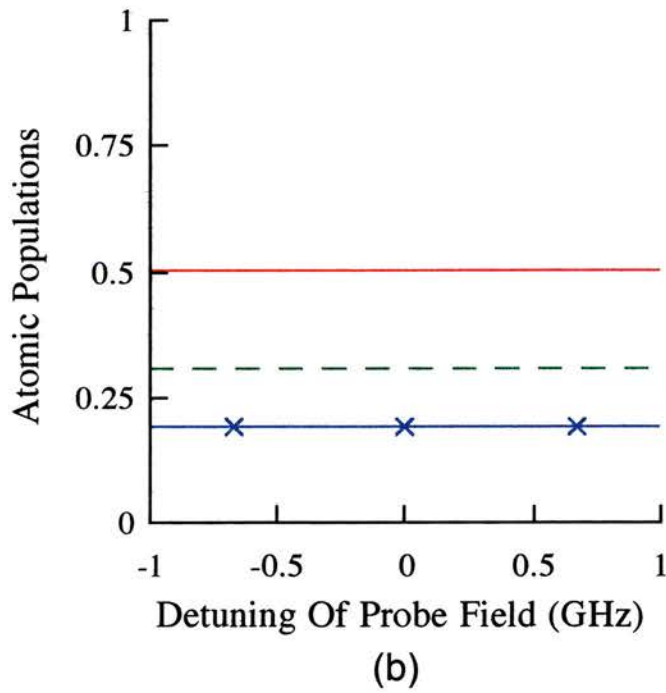
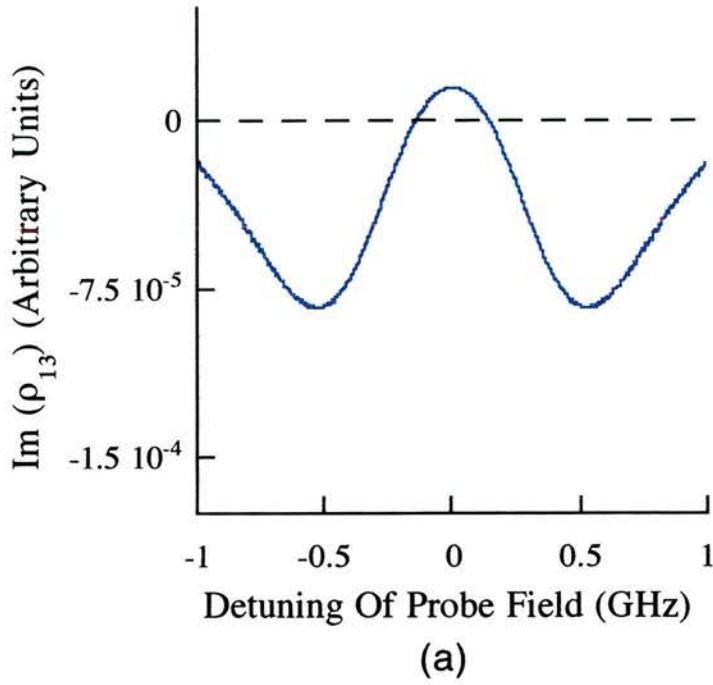


Figure 8.3 : (a) 422 nm probe field absorption curve showing inversionless gain. and (b) the corresponding population levels, for the density matrix model corresponding to Matrix 8.1. Population in ρ_{11} shown as a red solid line, ρ_{22} as a green dashed line and ρ_{33} as a blue solid line marked with crosses. $\Omega_c = 250$ MHz, $\Omega_p = 0.1$ MHz, $\Delta_c = 0$ MHz. and $\Pi_{23} = 5$ MHz.

It should be noted however that the $5P_{3/2} - 6P_{3/2}$ ($|2\rangle - |3\rangle$) transition, with which the incoherent pump interacts, is dipole forbidden. As such it would prove difficult to experimentally move population between these levels, since higher poled transition elements would have to be employed which are orders of magnitude weaker than dipole transition elements. A more feasible mechanism for moving the required small amount of population to the higher energy state of the inversionless gain transition must be obtained.

A mechanism for population movement is also required to reduce the effects of ground state hyperfine optical pumping. Two possible mechanisms are initially discussed and then compared below, in Section 8.1.2. One involves employing a coherent optical field while the second an incoherent field. The comparison provides information about the feasibility of employing either incoherent or coherent pumps within atomic coherence experiments. The same arguments hold when discussing moving atomic population for the purpose of producing inversionless gain. This can be seen to be the case in Section 8.1.3 where coherent pumps and then incoherent pumps are employed to produce 422 nm inversionless gain within atomic rubidium.

8.1.2) Introducing The Effects Of The Ground State Hyperfine Structure

Before going on to discuss the mechanisms involved in converting the above 422 nm system to an experimentally realisable inversionless gain system, the problematic effects of the ground state hyperfine structure must be addressed. As outlined in detail in Chapter 4, V-type systems which employ a coupling field which is resonant with the ground state of rubidium suffer from the detrimental process of ground state hyperfine optical pumping. This optical pumping mechanism was neglected in the above model since a simplified single level ground state was assumed. Lifting this assumption requires the derivation of a model for the system outlined in the schematic energy level diagram of Figure 8.4.

The problem of optical pumping is overcome by the introduction of a third optical field, as in the Zibrov inversionless gain system [1] outlined in Chapter 2. A four level density matrix model allows an initial analysis of the relevant features of employing either a coherent or incoherent source as the third optical field. The appropriate density matrix for this system can be found in Matrix A.2 in Appendix A. Both incoherent,

R_{pmp} , and coherent, Ω_{pmp} , pump terms have been included on the $5S_{1/2}$ ($F=3$) - $5P_{3/2}$ transition for completeness, however only one is actually employed at any one time, the other being set equal to zero.

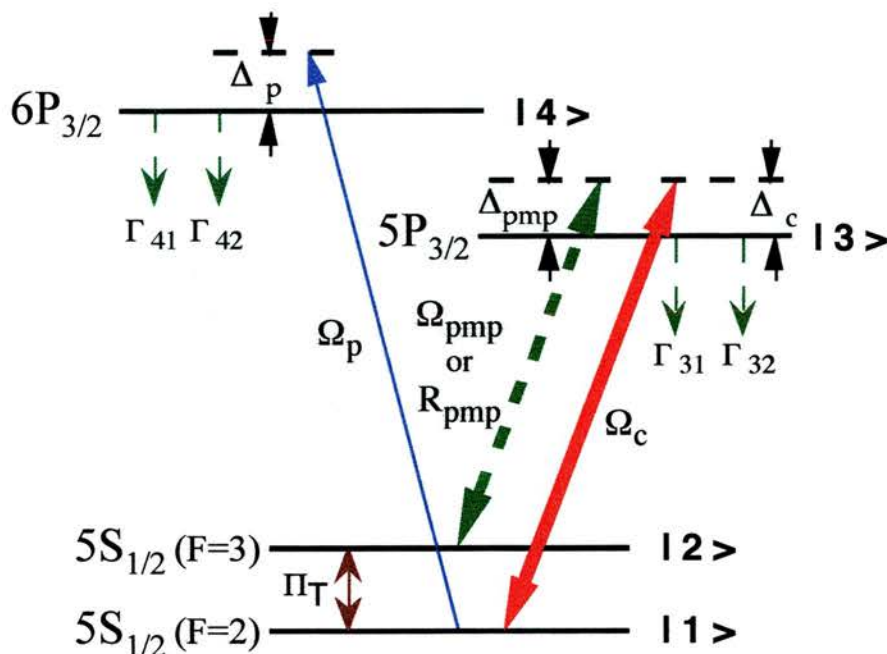


Figure 8.4: A closed level V-type system with a ground state doublet employed to produce a coherently induced transparency on a 422 nm probe field.

The model is initially executed with no pump field present on the $|2\rangle - |3\rangle$ transition to highlight the effects of optical pumping. Figure 8.5(a) shows the absorption experienced by the 422 nm probe in the presence (blue solid line) and absence (red dashed line) of a 250 MHz coupling field. The corresponding population traces for the case where the coupling field was present are also shown, Figure 8.5(b). As can clearly be seen the majority of the population becomes optically pumped between the ground state hyperfine levels, the majority of which, $\sim 98\%$, ends up in level $|2\rangle$. For this reason there is significantly less population left in level $|1\rangle$, $\sim 1\%$, with which the probe field interacts and so the absorption experienced by the probe field is far less than would be expected in the absence of this optical pumping mechanism. In fact for these particular atomic parameters the probe field absorption is more or less zero.

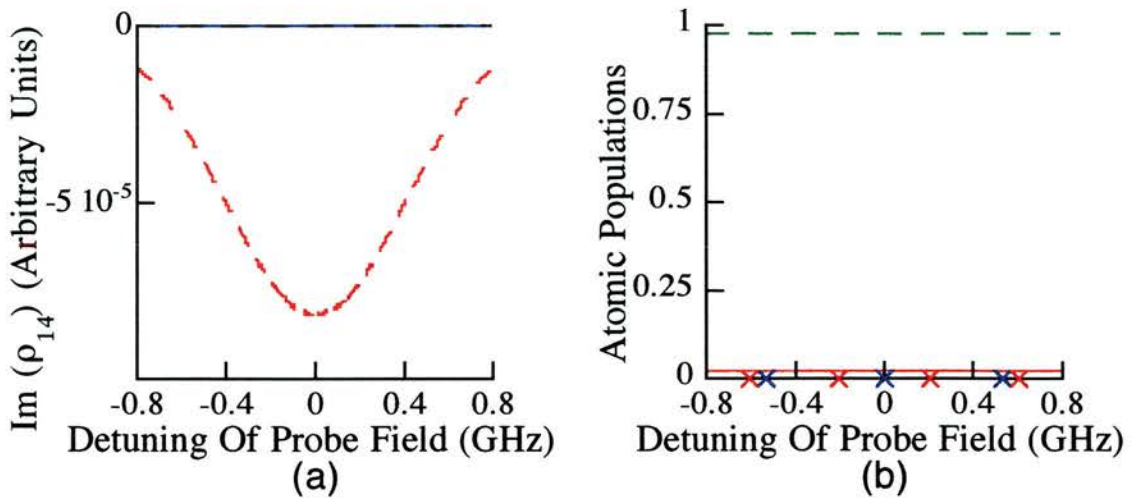


Figure 8.5 : (a) 422 nm probe field absorption curve in the presence (blue solid line) and absence (red dashed line) of a 250 MHz coupling field for the model described by Matrix A.2. when no pump field was present i.e. $R_{pmp} = \Omega_{pmp} = 0$. (b) Corresponding populations for the case where the coupling field was present. ρ_{11} shown as a red solid line, ρ_{22} as a green dashed line, ρ_{33} as a blue solid line marked with crosses and ρ_{44} as a red solid line marked with crosses. $\Omega_p = 0.1$ MHz and $\Delta_c = \Delta_{pmp} = 0$ MHz.

The picture of Figure 8.5 changes somewhat if a pump field is introduced which is resonant with the $|2\rangle - |3\rangle$ transition. Figure 8.6(a) shows the probe field absorption curve in the presence of a 250 MHz coherent pump field, while that of Figure 8.6(c) is obtained in the presence of a 50 MHz incoherent pump field. The corresponding atomic populations are presented in Figure 8.6(b) and (d) respectively. These two Rabi frequency values were chosen so as to produce probe field absorption levels of the same order as that achieved in the absence of either a pump or coupling field (red dashed lines). Further confirmation of the reduced level of ground state hyperfine optical pumping is given by examination of the populations present in each system. As can be seen the population in levels $|1\rangle$ and $|2\rangle$ (red solid and green dashed lines respectively) are now of the same order of magnitude, as is to be expected if the effects of ground state optical pumping have been reduced.

From the absorption curves of Figure 8.6(a) and (c) it can be seen that there are obvious side effects of introducing these pump fields.

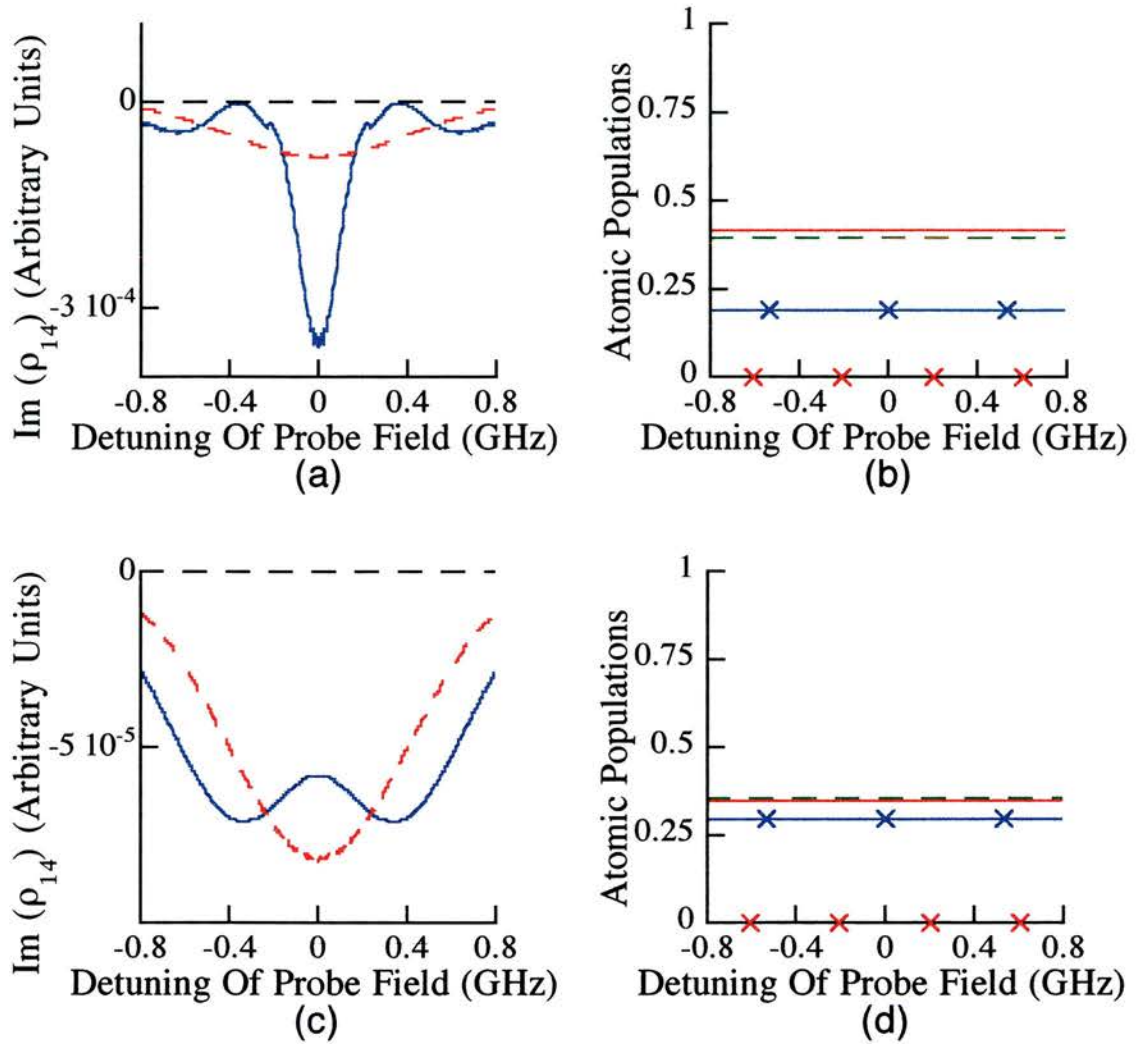


Figure 8.6 : 422 nm probe field absorption curves with the corresponding population levels generated by the model corresponding to Matrix A.2. ρ_{11} shown as a red solid line, ρ_{22} as a green dashed line, ρ_{33} as a blue solid line marked with crosses and ρ_{44} as a red solid line marked with crosses. $\Omega_c = 250$ MHz, $\Omega_p = 0.1$ MHz and $\Delta_c = \Delta_{pmp} = 0$ MHz. In (a) $R_{pmp} = 0$ MHz, $\Omega_{pmp} = 250$ MHz, and (c) $R_{pmp} = 50$ MHz, $\Omega_{pmp} = 0$ MHz with the red dashed lines again representing probe field absorption in the absence of either a pump or coupling field.

For the case of a coherent pump field the maximum transparency is now present at two separate frequencies, one either side of line centre, instead of appearing as just one centralised feature at probe resonance. Here the probe field absorption curve can be considered as a normal induced transparency curve with an extra absorption component overlaid at line centre. Turning to the case where the pump is of an incoherent nature the absorption profile resembles that of the simplified closed three level system trace of

Figure 8.2(a). However, the level of induced transparency is significantly lower in this system than in the three level system.

The reason for the difference between the traces of Figure 8.6(a) and (c) lies within the explanation of single atom E.I.T. of Section 4.2.1. In this section E.I.T. within a V-type system was explained in terms of state amplitude oscillation across the coupling field and probe field transitions which, at line centre, were of equal and opposite phase. Therefore, after a short period of time (on the order of the natural lifetimes within the atom) the probe field polarisation averages to zero and so no net absorption of the probe field occurs. It is this delicate balance between the phase of the various amplitude states, induced by the ρ_{34} coherence within this system, which leads to this phenomenon. The presence of a coherent pump field can, from an examination of Matrix A.2, be seen not only to move the required population between atomic states but also to drive a coherence between levels $|2\rangle$ and $|3\rangle$. This ρ_{23} coherence provides significant feedback to the ρ_{34} coherence and as such acts to destroy the delicate state amplitude phase balance between levels $|3\rangle$ and $|4\rangle$. This effect is strongest when the probe field is on exact resonance, thus explaining why there is more absorption at line centre than at small detuned probe frequencies within the absorption profile of Figure 8.6(a). Now the presence of an incoherent pump field also acts to move a small amount of population between atomic states, this time disturbing the ρ_{34} coherence through the fact that R_{pmp} terms appear in the dephasing terms and population equations, ρ_{kk} , of Matrix A.2. These terms do not alter the probe absorption profile as radically as when a coherent pump field is present but they do have a strong enough influence so as to significantly reduce the induced transparency feature.

The solution to the problem of hyperfine optical pumping is found by employing the $5P_{1/2}$ level as the upper state of the pump field transition as outlined in Figure 8.7. This level decays to the ground states at similar rates to the $5P_{3/2}$ level but since it is not directly connected to either level on the coupling field transition it should not significantly disturb the important uncoupled transition coherence (ρ_{45} in Figure 8.7). Due to computing power restrictions a complete model of this system is not possible. However, by running the previous model with R_{pmp} terms neglected from the coherence dephasing rates it is possible to approximate the five level atomic system.

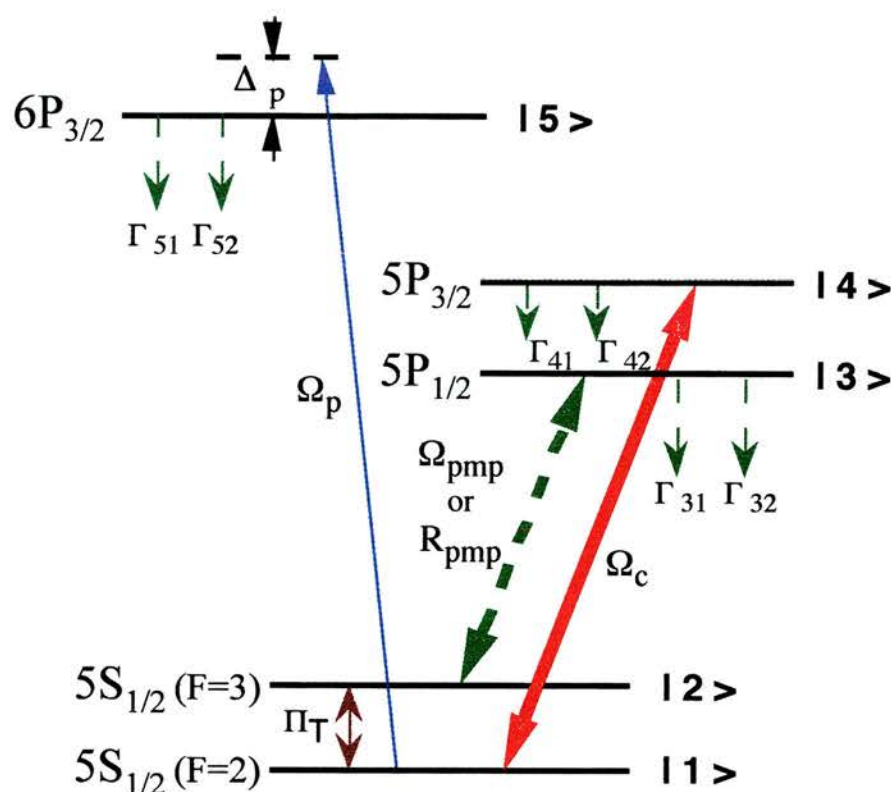


Figure 8.7: A closed level V-type system with ground state and first excited state doublets. This system is employed to reduce ground state hyperfine optical pumping and so produce coherently induced transparency on a 422 nm probe field resonant with the $|1\rangle - |4\rangle$ transition.

The results from this model are shown in Figure 8.8. As seen in Figure 8.8(a) the probe field absorption curve (shown by a blue solid line) again has a significant level of induced transparency. Included for reference on this graph is the probe field absorption, experienced in the presence of a similar coupling field, for the three level system of Figure 8.1 (red dashed line). The presence of the incoherent pump field has resulted in a reduction of the ground state optical pumping, and so the absorption level is now of the order obtained in the simpler three level system. This reduction in the optical pumping is further confirmed by examining the population levels of Figure 8.8(b). It can be seen that the population in level $|1\rangle$ is now greater than in level $|2\rangle$. This is a direct result of the reduction in optical pumping and of quantum interference effects acting to reduce absorption on the probe field transition.

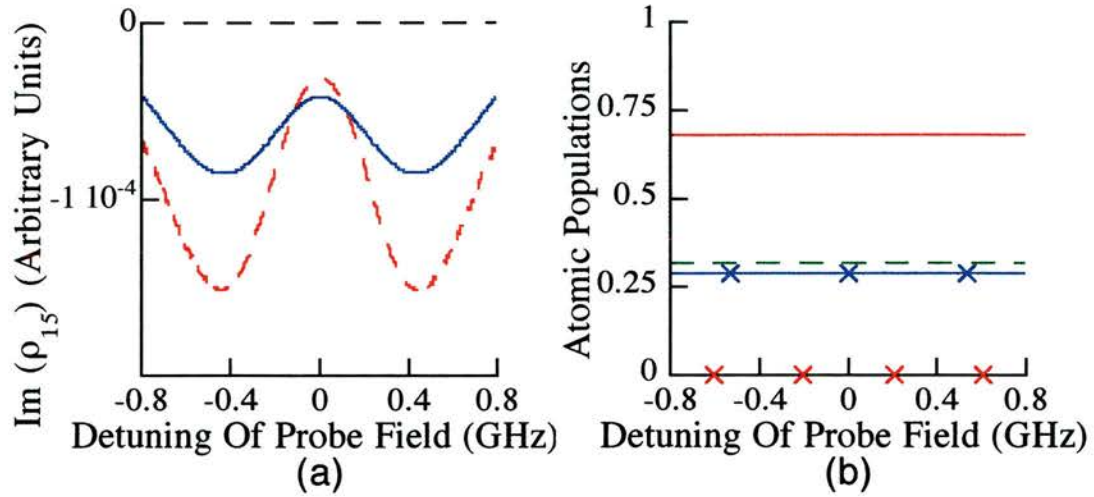


Figure 8.8 : (a) 422 nm probe field absorption curve with the corresponding population levels generated by the model corresponding to Matrix A.2, where the R_{pmp} terms have been neglected in the coherence dephasing rates. (b) Corresponding populations, ρ_{11} shown as a red solid line, ρ_{22} as a green dashed line, ρ_{33} as a blue solid line marked with crosses and ρ_{44} as a red solid line marked with crosses. $\Omega_c = 250$ MHz, $\Omega_p = 0.1$ MHz, $R_{pmp} = 100$ MHz, $\Omega_{pmp} = 0$ MHz with the red dashed line representing probe field absorption, for similar parameters, in the simplified system of Figure 8.1.

8.1.3) A 422 nm Inversionless Gain System And A Four Level Approximation

This section introduces the complete six level, four optical field system proposed for the generation of 422 nm inversionless gain. The system is outlined schematically in Figure 8.9. The basic mechanism of the system is to employ three I.R. optical fields in order to generate inversionless gain on the 422 nm probe field which is resonant with the $5S_{1/2}$ (F=2) - $6P_{3/2}$ transition. The first I.R. source is a 780 nm coupling field which is resonant with the $5S_{1/2}$ (F=2) - $5P_{3/2}$ transition. The other two I.R. optical fields, which can be either coherent or incoherent in nature, act as population pump fields. One is resonant with the $5S_{1/2}$ (F=3) - $5P_{1/2}$ transition (794 nm) and is employed to negate the effects of optical pumping as described previously in Section 8.1.2, while the second is resonant with the $5P_{3/2}$ - $5D_{5/2}$ transition (776 nm) and is present to move the required small population to the higher energy state of the gain transition. This complete scheme results in a 36x36 system matrix equation.

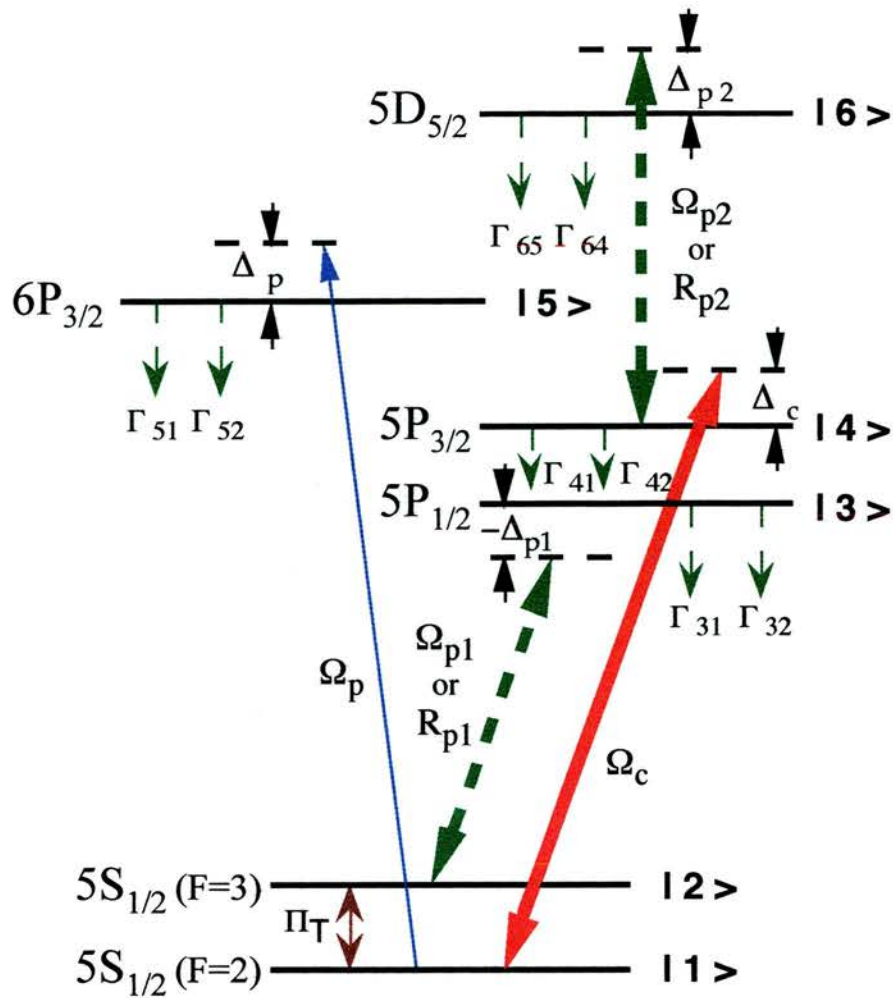


Figure 8.9: A closed six level V-type system employed to produce inversionless gain on a 422 nm probe field resonant with the $5S_{1/2} (F=2) - 6P_{3/2}$ transition. A 780 nm coupling field is resonant with the $5S_{1/2} (F=2) - 5P_{3/2}$ transition. Two pump fields are also present, the first is resonant with the $5S_{1/2} (F=3) - 5P_{1/2}$ transition (794 nm) while the second is resonant with the $5P_{3/2} - 5D_{5/2}$ transition (776 nm).

However, the computer power needed to solve this complete system is not available to the group and as such a four level approximation to this system has had to be made. This approximated system is shown in the schematic energy level diagram of Figure 8.10, where the basic assumption has been to neglect the effects of ground state hyperfine optical pumping. It previously proved possible to negate these optical pumping effects with the introduction of an optical field on the $5S_{1/2} (F=3) - 5P_{1/2}$ transition, as outlined in Section 8.1.2, thus the above assumption is not an unreasonable

first approximation to make. The system matrix for this four level approximation can again be found in Appendix A, shown as Matrix A.3.

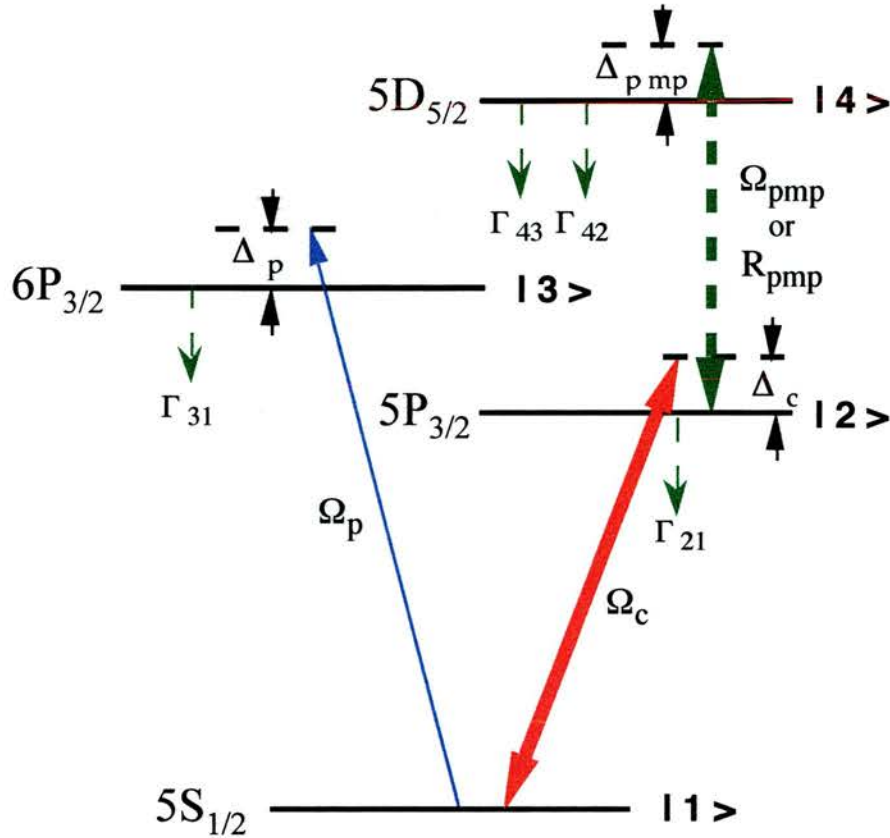


Figure 8.10: A closed four level approximation to the six level V-type system of Figure 8.9. A 422 nm probe field is again resonant with the $5S_{1/2}$ ($F=2$) - $6P_{3/2}$ transition along with a 780 nm coupling field set to be resonant with the $5S_{1/2}$ ($F=2$) - $5P_{3/2}$ transition. Only one pump field is now present and is set to be resonant with the $5P_{3/2}$ - $5D_{5/2}$ transition (776 nm).

An expression for the gain coefficient for a weak probe field on the $|1\rangle - |3\rangle$ transition in the presence of a coherent pump field on the $|2\rangle - |4\rangle$ transition has been derived for the four level system of Figure 8.10. The starting point for this derivation is the definition of the gain coefficient, G , as defined by Siegman [2]:

$$G = \frac{\alpha_{\text{gain}} z}{2} = \frac{\pi \nu \chi'' z}{c} \quad (8.1)$$

where α_{gain} is the small gain coefficient, z the length of the gain medium, ν is frequency of the gain transition, χ'' the imaginary component of the susceptibility (as defined in Chapter 2) and c the speed of light. Examination of equation (8.1) shows that α_{gain} can be written as:

$$\alpha_{\text{gain}} = \frac{2\pi}{\lambda} \chi'' = k \chi'' \quad (8.2)$$

where λ is the gain transition wavelength and k the associated wavevector. Shore [3] provides the following relation between the Einstein, A_{ji} , coefficient and the electric dipole matrix element, μ_{ij} , for a particular transition:

$$|\mu_{ij}|^2 = \frac{3}{4} A_{ji} \frac{\hbar}{k^3} \bar{\omega}_j \quad (8.3)$$

where \hbar is related to Planck's constant and $\bar{\omega}_j$ is the statistical weight of the level $|j\rangle$. Therefore, substituting equation (8.3) into the expression for χ'' from Chapter 2 (equation (2.23)) and substituting the resultant, along with equation (8.2), in equation (8.1) results in an expression for the gain coefficient, G , in terms of the density matrix element ρ_{ij} :

$$G = \frac{3}{4} \frac{A_{ji} N \bar{\omega}_j z}{k^2 \epsilon_0} \frac{\rho_{ij}^i}{\Omega_{ij}} \quad (8.4)$$

Examination of the system density matrix, Matrix A.3, allows an algebraic expression for ρ_{ij}^i to be obtained solely in terms of atomic populations, population decay rates, coherence decay rates and Rabi frequencies. This solution is achieved in the weak probe field limit under the condition of exact resonance and is represented by equation (8.5). It can be seen that the first term in the numerator of equation (8.5) contributes to gain only in the presence of a population inversion such that $\rho_{33} > \rho_{11}$. However, the important factor in terms of quantum interference effects and the production of inversionless gain are the second two terms of the numerator, which are directly proportional to the squared Rabi frequencies induced by the coupling and pump fields. Inspection shows these terms contribute to the gain only when $\rho_{11} > \rho_{22} > \rho_{44}$. Therefore, if the first term in the numerator is smaller than the contribution of both the

second and third terms it is predicted that gain will be produced in this system even in the absence of a population inversion.

$$\rho_{ij}^i = \frac{\left\{ \begin{array}{l} \left(\gamma_{12} \gamma_{14} \gamma_{23} \gamma_{24} \gamma_{34} + \gamma_{12} \gamma_{23} \gamma_{34} \Omega_c^2 \right) \\ + \left(\gamma_{12} \gamma_{14} \gamma_{24} + \gamma_{23} \gamma_{24} \gamma_{34} + \gamma_{24} \right) \Omega_{pmp}^2 \\ + \gamma_{12} \Omega_c^2 \Omega_{pmp}^2 \end{array} \right\} (\rho_{11} - \rho_{33})}{-\Omega_p \left\{ \begin{array}{l} - \Omega_c^2 \left(\gamma_{14} \gamma_{24} \gamma_{34} + \gamma_{34} \Omega_c^2 - \gamma_{24} \Omega_{pmp}^2 \right) (\rho_{11} - \rho_{22}) \\ - \Omega_c^2 \Omega_{pmp}^2 (\gamma_{12} + \gamma_{34}) (\rho_{22} - \rho_{44}) \end{array} \right\}} \quad (8.5)$$

$$\left\{ \begin{array}{l} \gamma_{12} \gamma_{13} \gamma_{14} \gamma_{23} \gamma_{24} \gamma_{34} \\ + \Omega_c^2 \left(\gamma_{12} \gamma_{13} \gamma_{23} \gamma_{34} + \gamma_{12} \gamma_{14} \gamma_{24} \gamma_{34} + \Omega_c^2 \gamma_{12} \gamma_{34} \right) \\ + \Omega_{pmp}^2 \left(\gamma_{12} \gamma_{13} \gamma_{14} \gamma_{24} + \gamma_{13} \gamma_{23} \gamma_{24} \gamma_{34} + \Omega_{pmp}^2 \gamma_{13} \gamma_{24} \right) \\ + \Omega_c^2 \Omega_{pmp}^2 (\gamma_{12} \gamma_{13} + \gamma_{24} \gamma_{34}) \end{array} \right\}$$

This is exactly the case shown in Figure 8.11(a) where the probe field absorption curve (blue solid line) is presented in the presence of a 500 MHz coupling field and a 500 MHz coherent pump field. The absorption in the absence of both of these fields is again included for reference (red dashed line). As can clearly be seen the gain feature appears in two different frequency regions, one either side of probe resonance. The explanation of this phenomenon is exactly analogous to the explanation given in Section 8.1.2 for the splitting of the E.I.T. feature, in the presence of a coherent pump field, into two similar frequency regions. There the coherent pump field was employed to remove the effects of optical pumping but in this case it is employed to move a small amount of population to the top level of the gain transition. The presence of the coherent pump field also acts to drive a ρ_{24} coherence and so disturbs the all important ρ_{23} coherence generated by coupling field. This results in the extra absorption feature observed at line centre. Confirmation of the inversionless nature of the gain is shown in the atomic population traces of Figure 8.11(b). As can be observed the population ρ_{11} is greater

than ρ_{22} or ρ_{44} and is significantly greater than ρ_{33} thus confirming that the gain present is of a non inverted nature.

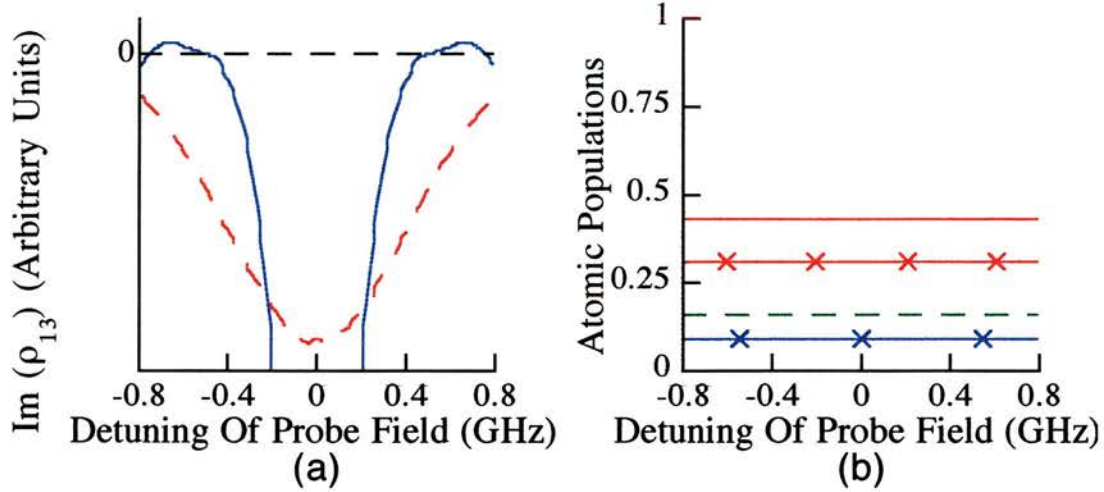


Figure 8.11 : (a) 422 nm probe field absorption curve in the presence (blue solid line) and absence (red dashed line) of a coupling and coherent pump field, (b) the corresponding population levels for the density matrix model corresponding to the system matrix of Matrix A.3 in the presence of a coupling and a coherent pump field. ρ_{11} shown as a red solid line, ρ_{22} as a green dashed line, ρ_{33} as a blue solid line marked with crosses and ρ_{44} as a red solid line marked with crosses. $\Omega_c = \Omega_{pmp} = 500$ MHz, $\Omega_p = 0.1$ MHz and $\Delta_c = \Delta_{pmp} = 0$ MHz.

The benefit of employing an incoherent pump to move population around an atomic system is highlighted in Figure 8.12. Here the incoherent pump field is resonant with the $|2\rangle - |4\rangle$ transition and gain is again observed on the probe field curve, Figure 8.12(a). This curve, unlike the previous probe field curve of Figure 8.11(a), resembles a coherently induced transparency curve which has been raised to produce gain at line centre. The probe absorption curve in the absence of any other field is once more present for reference (red dashed curve).

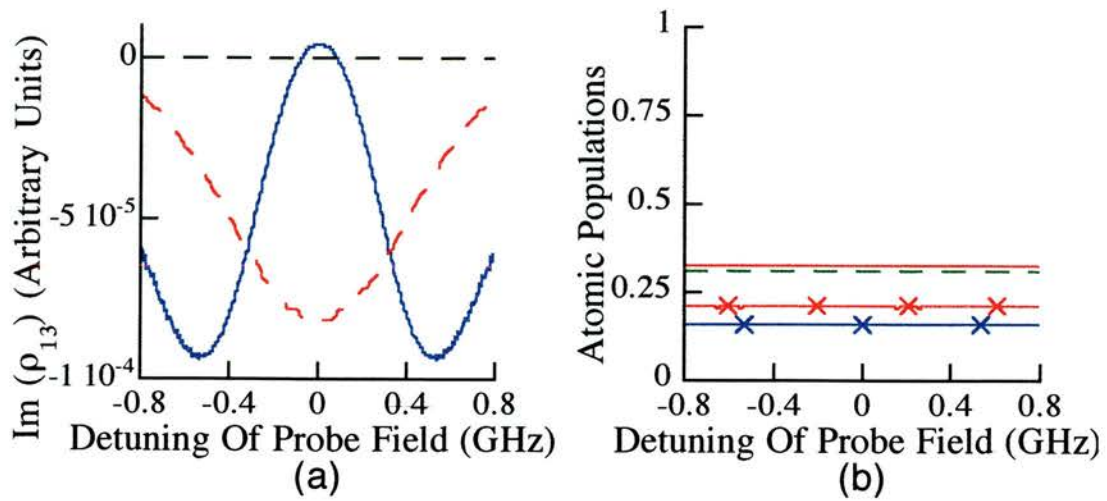


Figure 8.12: (a) 422 nm probe field absorption curve in the presence (blue solid line) and absence (red dashed line) of a coupling and incoherent pump field, (b) the corresponding population levels for the density matrix model corresponding to the system matrix of Matrix A.3 in the presence of a coupling and a coherent pump field. ρ_{11} shown as a red solid line, ρ_{22} as a green dashed line, ρ_{33} as a blue solid line marked with crosses and ρ_{44} as a red solid line marked with crosses. $\Omega_c = 400$ MHz, $R_{pmp} = 50$ MHz, $\Omega_p = 0.1$ MHz and $\Delta_c = \Delta_{pmp} = 0$ MHz..

As with the case of optical pumping, Section 8.1.2, the strength of the Rabi frequency required by an incoherent pump is significantly less than that required when a coherent pump field was employed, 50 MHz as compared with the previously employed value of 500 MHz. The explanation for this lies in the fact that gain is observed at line centre, where quantum interference effects are strongest, for the incoherent pump field case rather than at two separate frequencies either side of line centre as for the case of coherent pump field.

8.1.4) The Future Production Of Experimental 422 nm Gain

The theoretical work of this section has provided a solid basis for believing that a 422 nm inversionless gain medium will be generated in future experiments within the laboratory. A 422 nm probe source is presently under development for use in such experiments [4]. This involves the frequency doubling of the scanning Microlase MBR-

110 Ti:sapphire laser using a crystal of potassium niobate (KNbO_3). Although the above system will involve the ground state doublet of rubidium it has been theoretically predicted above, and shown previously experimentally [1], that the effects of ground state hyperfine optical pumping can be negated by the presence of an pump field. A further optical field source will also be required in the above experiment of Figure 8.7, since a second pump field is needed to move population between levels $|2\rangle$ and $|3\rangle$. A Ti:sapphire laser is presently under construction for this purpose. A means of broadening the linewidths of the pump fields is also required so as to provide a facility which allows switching between coherent and incoherent pump fields. This can be achieved by the employment of acoustic-optic modulators which have noise generated signals incorporated into their driving voltages. At present such a system is under development and so, with all the above equipment available, the St. Andrews group will be in a position to try and reproduce the above theoretical curves within the laboratory. Initial comparisons suggest that the levels of gain predicted for this system are at least as high, if not better, than those achieved within the Zibrov system [1], studied extensively in Section 2.3.2. This lends further weight to the hope that it will prove possible to produce blue inversionless gain.

8.2) Other Future Experimental Work

8.2.1) Radio-Frequency (R.F.) Effects in E.I.T.

The employment of a microwave source [5] is a second proposed area of new experimental work. So far E.I.T. experiments have used only lasers as the coherent coupling source, with wavelengths typically in the 500 - 1000 nm region. This is a major restriction on the systems which can be studied, particularly for solid state or semiconductor materials where previous experiments on the related effects of Autler-Townes splitting have usually employed both laser and microwave sources [6]. A future proposed experiment is to study the effects of employing R.F. sources within E.I.T. style experiments. An R.F. field may be employed in two distinct fashions within an atomic coherence experiment. Firstly, it can be employed as a means of removing the complicating effects of ground state hyperfine optical pumping or secondly, it may be employed as the coupling source in itself for the coherent preparation of the medium.

Two such schemes for this second use of the R.F. source are highlighted schematically in Figure 8.13.

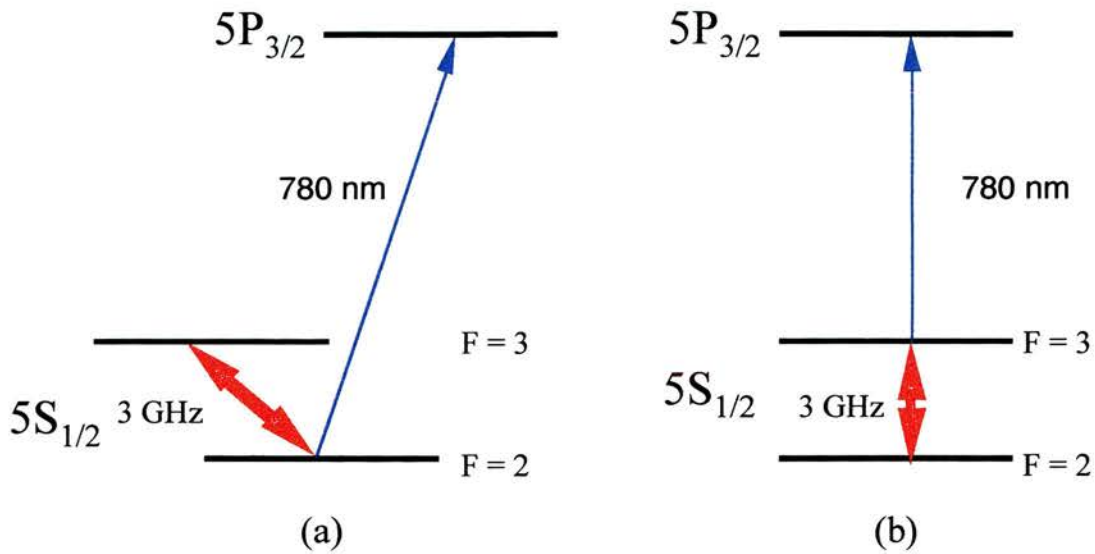


Figure 8.13: Possible (a) V-type and (b) cascade systems in which to observe R.F. control of an optical field in an E.I.T., type experiment.

Although the work of Chapter 7 has shown that the effects of Doppler broadening are not as restrictive as previously thought, some preliminary modelling of these systems suggest that because of the exceptionally large wavelength difference (10 cm and 780 nm) between these two fields the observation of E.I.T. would be masked. It is therefore proposed to employ either the atomic beam, described in Section 3.3.4.1, or an atomic trap in order to provide a Doppler-free medium. Initial work has already been carried out on the development of an R.F. source, tuneable from 1 - 8 GHz, for use in these experiments [5]. In order to provide the appropriate microwave field configurations for coupling into the optically probed atomic beam, microwave resonant cavities fed by tuneable microwave radiation from travelling-wave tubes will be employed. The intention of exploring R.F. field induced E.I.T. effects in a rubidium atomic beam with clearly identified energy levels is to establish the basic physical principles involved with a view to the possible subsequent extension to schemes in the solid state, including semiconductor media.

8.2.2) Doppler-Free Configurations For E.I.T.

A third area of proposed continued research is in Doppler-free experimental configurations, while still employing optical fields. In many circumstances, especially in the Doppler-broadened vapour systems of this work, a coherent transparency induced by a coupling field is not just pure E.I.T. As outlined in Chapter 7, for any scheme where there is significant Autler-Townes splitting, there is a region of transparency between the two Autler-Townes absorption components. The interference effect of E.I.T. also lies within this frequency region, at the frequency determined by two photon resonance. Therefore, pure E.I.T. can only be observed unambiguously in a system in which there is no Doppler-broadening as found in a vapour or lattice broadening as in a solid. Such systems can be produced by again employing a rubidium atomic beam or trap. This should provide a means for investigation of pure E.I.T. effects without the complications of velocity shifting of the position of the interference, or the obscuring effects of velocity shifted Autler-Townes components. This is exactly the case shown in Figure 8.14 where a homogeneously broadened theoretical curve is shown for a cascade medium which has been rendered Doppler free.

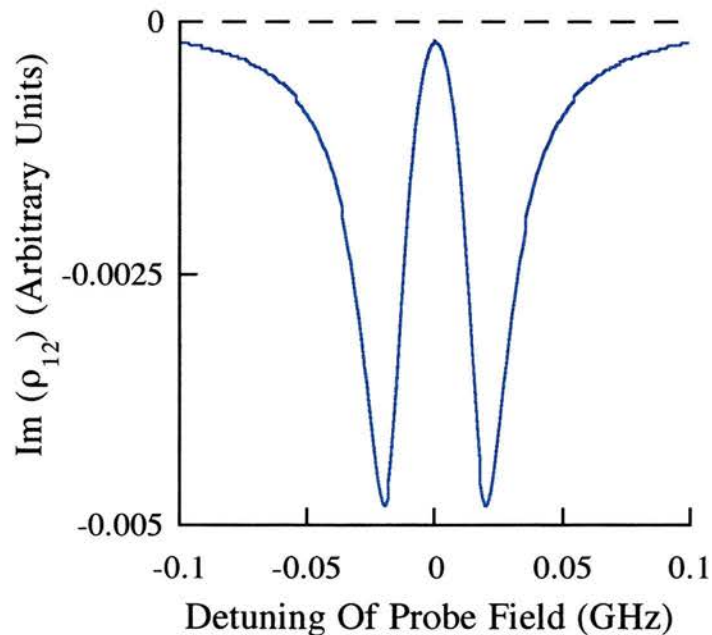


Figure 8.14: Homogeneously broadened E.I.T. within a cascade system. $\Omega_c = 20$ MHz, $\Omega_p = 0.1$ MHz and $\Delta_c = 0$ MHz

It should be noted that the power requirements on the coupling field in order to induce observable transparency in a Doppler-free system are much less than in a vapour. This means that observable pure E.I.T. effects should be observed where much larger coupling field Rabi frequencies can be generated. This will allow a new range of high powered cw atomic coherence experiments to be carried out.

References

- [1] **A.S. Zibrov, M.D. Lukin, D.E. Nikonov, L. Hollberg, M.O. Scully, V.L. Velichansky and H.G. Robinson**, *Experimental Demonstration Of Laser Oscillation Without Population-Inversion Via Quantum Interference In Rb*, Phys. Rev. Lett. 75 , 1499 (1995).

- [2] **A.E. Siegman**, *Lasers*, (Oxford U.P., London (1986)).

- [3] **B. Shore**, *The Theory Of Coherent Atomic Excitation*, (John Wiley & Sons, New York (1990)).

- [4] **J. Boon**, *Electromagnetically Induced Transparency And Related Effects: A Move Towards The Visible*, First Year Report, University of St. Andrews (1996).

- [5] **L. Zekou**, *A Study Of Coherently Induced Transparency, Inversionless Gain And R.F. Control Of Optical Fields*, First Year Report, University of St. Andrews (1996).

- [6] **C. Wei, N.B. Manson and J.P.D. Martin**, *Experimental Investigation Of Absorption And Dispersion Of A Strongly Driven Transition: V-Shaped Three-Level System With A Strong Probe* , Phys. Rev. A 51 , 1438 (1995).

Conclusions

The work contained in this thesis presents a significant contribution to the ever growing field of quantum interference, many aspects of which were discussed in the introduction. The majority of this work concentrated on continuous-wave phenomena within Doppler broadened media. Thus, extensive modelling through semi-classical density matrix analysis was carried out to help explain observed effects, and also to predict new ones within future proposed experiments. Although most of the previous chapters ended with their own conclusions, it is appropriate to gather some of the more significant points together here in this final section.

Two numerical methods for modelling quantum interference effects were discussed. The first, a state amplitude model, was presented which allowed the study of the interaction effects of coherent fields with single atoms. This model provided great insight into the mechanisms involved within E.I.T. in the three most popularly discussed systems: the V-type, lambda and cascade systems. It highlighted the fact that E.I.T. within the lambda and cascade systems involved the trapping of population in a superposition of states, while within the V-type system the mechanism involved was a complex combination of quantum oscillations across the probe and coupling field transitions. Moving to a large ensemble of atoms ($\sim 10^{17}$ atoms m^{-3}) required the introduction of the more powerful density matrix model. This model allowed the simple introduction of phenomenological terms to describe spontaneous decay,

coherence dephasing and incoherent movement of atomic population, as well as allowing the incorporation of Doppler Broadening through numerical integration. Although some physical insight was lost, on the single atom scale, the density matrix provided an ideal and accurate means for modelling quantum interference effects within rubidium vapour.

A theoretical and experimental study of E.I.T. in V-type, lambda and cascade systems within atomic rubidium was then carried out. Simple three level models predicted that the greatest depth of induced transparency should occur in the lambda system, and the poorest in the V-type system. However, experimentally it was found that optical pumping mechanisms drastically altered the observed probe field transmission profiles, particularly within the lambda and V-type systems, since these both had their coupling field resonant with the $5S_{1/2}$ ground state of rubidium. Therefore, it proved easiest to observe E.I.T. within the experimental cascade system, since this was effectively non-dissipative to both optical fields, and transparencies $>90\%$ were reported.

Following on from the previous work on the $5S_{1/2} - 5P_{3/2} - 5D_{5/2}$ cascade system within rubidium, a fundamental study of E.I.T. was carried out. The width and depth of an induced transparency was found to depend critically on the coupling field power, detuning and orientation relative to the probe field. E.I.T. was shown to depend on the two photon resonance condition, and so provided a novel method of spectroscopy whereby the relevant two photon transitions were seen imprinted upon a single photon probe field absorption trace. This E.I.T. spectroscopy technique was compared experimentally to the more traditional two photon spectroscopy technique. Although the E.I.T. technique was of poorer resolution it had the advantage of being able to be carried out at much lower vapour temperatures, since it relied only on single photon probe field absorption. The effect of Zeeman splitting on E.I.T. was also studied within this system. E.I.T. has historically been proposed to enhance nonlinear sum frequency mixing processes, which also employ magnetic fields to break the symmetry of the wave-mixing medium. However, this study showed that a magnetic field caused an E.I.T. feature to break up into clusters of windows, the exact number of which depending on operative two photon selection rules, which were themselves directly related to the polarisation of the input optical fields.

It was during similar experiments to those described above that the novel non-dissipative cross-focusing effect, named Electromagnetically Induced Focusing, was discovered. This phenomenon was shown to be a direct result of the Gaussian intensity profile of the optical fields. Since the radial intensity profile of the coupling field varied, so did the spatial effects of E.I.T. Therefore, the probe field experienced focusing due to the coherent interaction of the coupling field with the atomic medium. The sign of these focusing effects varied tremendously with many of the experimental parameters, including: probe field focusing, field detunings, vapour temperature and relative waist sizes. Therefore, as well as being of fundamental interest in its own right, since E.I.F. provided a means of optically controlling one field with another, it is believed to be of fundamental concern in the design of future atomic coherence experiments.

The relative role of the optical field wavelengths was then studied theoretically in all three systems, although experiments were limited to just cascade systems. These experiments disproved the belief that induced transparencies within Doppler broadened media required the employment of atomic systems that had wavelength matched optical transitions. In fact, for certain cases within the lambda and cascade systems, it was found that the depth and width of a coherently induced transparency was enhanced with wavelength mismatch. This mismatch was achieved by employing a coupling field transition of smaller wavelength than that of the probe field transition. These studies also highlighted the relative roles of Autler-Townes splitting and E.I.T. within a coherently induced transparency, and showed that the two are almost inseparable within a Doppler broadened medium. It was found that the depth of such a transparency was set by the effects of E.I.T. while the width was controlled by Autler-Townes splitting effects.

The removal of this restriction on wavelength matching has allowed a whole new range of atomic systems to be considered for future quantum interference experiments. In particular, the employment of the $5S_{1/2} - 5P_{3/2} - 6P_{3/2}$ system within rubidium has been proposed for the observation of blue E.I.T., with the extension thereafter to a 422 nm inversionless gain experiment. Two fundamental problems existed in this system. The first involved overcoming the complicating effects of ground state hyperfine optical pumping. It was proposed to achieve this by introducing a third laser source on the $5S_{1/2} - 5P_{1/2}$ transition. The second problem involved moving the required population

to the upper level of the lasing transition, in this case the $6P_{3/2}$ level. Two methods were put forward. Both involved pumping population from the $5P_{3/2}$ level into the $5D_{5/2}$ level, which in turn spontaneously decayed to populate the $6P_{3/2}$ level. However, it was the nature of the pump that moved this population which differed. The first method involved employing a coherent pump source, and so generated two regions of gain either side of line centre, while the second employed an incoherent source, generating one region of gain at line centre. By line broadening a Ti:sapphire laser with an acoustic-optic modulator, it was proposed to convert a coherent field to one that was incoherent in nature. Thus, it is hoped that it will be possible to generate both of the gain profiles described above in future experiments. Other future experiments have also been considered. These include the R.F. control of an optical field and the study of homogeneously broadened E.I.T. within an atomic beam or trap.

Appendix A

Density Matrix Equations For Four Level Atomic Systems

Appendix B

Publications, Conference Proceedings And Reviewed Papers

Publications

R.R. Moseley, S. Shepherd, D.J. Fulton, B.D. Sinclair and M.H. Dunn, *Interference Between Excitation Routes In Resonant Sum-Frequency Mixing*, Phys. Rev. A 50 , No. 5, 4339 (1994).

R.R. Moseley, S. Shepherd, D.J. Fulton, B.D. Sinclair and M.H. Dunn, *Spatial Consequences Of Electromagnetically Induced Transparency: Observation Of Electromagnetically Induced Focusing*, Phys. Rev. Lett. 94 , No. 5, 670 (1995).

D.J. Fulton, R.R. Moseley, S. Shepherd, B.D. Sinclair and M.H. Dunn, *Effects of Zeeman Splitting On Electromagnetically Induced Transparency*, Opt. Commun. 116 , 231 (1995).

R.R. Moseley, S. Shepherd, D.J. Fulton, B.D. Sinclair and M.H. Dunn, *Two-Photon Effects In Continuous-Wave Electromagnetically Induced Transparency*, Opt. Commun. 119 , 61 (1995).

D.J. Fulton, R.R. Moseley, S. Shepherd, B.D. Sinclair and M.H. Dunn, *Continuous-Wave Electromagnetically Induced Transparency: A Comparison Of Vee, Lambda, and Cascade Schemes*, Phys. Rev. A 52 , No. 3, 2302 (1995).

R.R. Moseley, S. Shepherd, D.J. Fulton, B.D. Sinclair and M.H. Dunn, *Electromagnetically Induced Focusing*, Phys. Rev. A 53 , No. 1, 408 (1996).

S. Shepherd, D.J. Fulton and M.H. Dunn, *Wavelength Dependence Of Coherently Induced Transparency In A Doppler Broadened Cascade Medium*, Phys. Rev. A (accepted).

Conference Proceedings

R.R. Moseley, S. Shepherd, D.J. Fulton, B.D. Sinclair and M.H. Dunn, *Interference Between Excitation Pathways In Resonant Sum-Frequency Mixing In Vapours*, Paper QMH2, IEEE Technical Digest, 5th European Quantum Electronics Conference (1994).

R.R. Moseley, S. Shepherd, D.J. Fulton, B.D. Sinclair and M.H. Dunn, *Spatial Consequences Of Electromagnetically Induced Transparency: Observation Of Electromagnetically Induced Focusing*, Post-Deadline Paper, IEEE Technical Digest, 5th European Quantum Electronics Conference (1994).

R.R. Moseley, S. Shepherd, D.J. Fulton, B.D. Sinclair and M.H. Dunn, *Cross Focusing In Electromagnetically Induced Transparency*, Paper QTuL1, QELS, Baltimore U.S.A. (1995).

S. Shepherd, D.J. Fulton, R.R. Moseley, B.D. Sinclair and M.H. Dunn, *A Study Of Electromagnetically Induced Transparency Schemes Within Rubidium Vapour*, Paper QTuL2, QELS, Baltimore U.S.A. (1995).

D.J. Fulton, R.R. Moseley, S. Shepherd, B.D. Sinclair and M.H. Dunn, *A Theoretical And Experimental Analysis Of Electromagnetically Induced Focusing*, Paper 6-5, QE-12, Southampton U.K. (1995).

D.J. Fulton, S. Shepherd and M.H. Dunn, *Wavelength Dependence Of Coherently Induced Transparency In A Doppler Broadened Cascade Medium*, Paper QThF2, QELS, Anaheim U.S.A. (1996).

Reviewed Papers

N. Wang, H. Rabitz, A.S. Manka and C.M. Bowden, *Optimal Control Of Piezophotonic And Magnetophotonic Switching In A Dense Medium Of Three-Level Atoms*, Phys. Rev. A 53, 2940 (1996).

D.A. Cardimona, K. Koch and P.M. Alsing, *Field-Cancellation By A Two- Level Atom In A Multimode Cavity Driven By A Time-Dependent Field*, (accepted Phys. Rev. A 55, (1997)).